Photoinduced electron transfer within heterometallic assemblies of [Ru(bpy)3]2+ linked to bisterpyridine complexes of Fe(II), Co(III) and Cr(III)

Rajaa Farran

UNIVERSITÉ GRENOBLE ALPES

THÈSE

pour obtenir le grade de

DOCTEUR DE L'UNIVERSITÉ DE GRENOBLE

Spécialité : **Chimie Inorganique et Bio Inorganique**

Arrêté ministériel : 7 août 2006

Présentée par
Rajaa FARRAN

Thèse dirigée par **Jérôme CHAUVIN**
et codirigée par **Frédérique LOISEAU**
et coencadrée par **Damien JOUVENOT**
préparée au sein du département de Chimie Moléculaire (DCM)
dans **l'École Doctorale Chimie et Sciences du Vivant (EDCSV)**

Transfert d'électron photoinduit au sein d'assemblages hétérométalliques associant le $[Ru(bpy)_3]^{2+}$ à des complexes bisterpyridine du Fe(II), Co(III) et Cr(III)

Thèse soutenue publiquement le **11 septembre 2015**,
devant le jury composé de:

M. Jean WEISS
Directeur de Recherche CNRS, Président
M. Marc ROBERT
Professeur, Université Paris Diderot, Rapporteur
M. Nathan D. MCCLENAGHAN
Directeur de Recherche CNRS, Rapporteur
M. Damien JOUVENOT
Maître de Conférences, Université Joseph Fourier, Co-encadrant
M^me^ Frédérique LOISEAU
Professeur, Université Joseph Fourier, Co-directeur
M. Jérôme CHAUVIN
Maître de Conférences, Université Joseph Fourier, Directeur de thèse

"You are what you dream to be"
My Mom

Acknowledgement

This thesis wouldn't have been possible without the help of so many people in so many ways. It is the results of a large measure of work, curiosity and determination that changed the course of both my academic and personal life to which I will be forever grateful.

As a start I would like to thank the CIRe group for accepting me as part of their family for three unforgettable years in a remarkable scientific environment during which I was lucky to work with three supervisors. No words can express my gratitude to all three of you. Jerôme thank you for giving me the opportunity to do this thesis with your patience to provide me with all the knowledge, time, expertise I needed as a scientist and consult as a friend. Damien, I am the scientist I am today because of your knowledge. Frederique, thank you for providing me with all the support in all my science depression, it would have been very difficult without you. Although technically not my supervisor, I would also like to thank Alain Deronzier, my God Father in chemistry, for all his valuable scientific and personal contribution to this work and to my life.

I would also like to express my gratitude to the members of the jury Mr. Jean Weiss, Mr. Marc Robert and Mr. Nathan D. Mcclenaghan for their time and interest in my work.

During these years I have probably bothered every member of the CIRe group with my countless questions and discussions which I enjoyed and will always remember, so thank you each and everyone of you. In particular I would like to thank Fabrice Thomas and Florian whom I worked in close contact with, along with all the interns especially Remi Vallet, Long and Yves Alexandres.

Away from science, I have spent a remarkable time with discussions, gossip, tears, laughter and memories that will always be part of me in the future thanks to amazing friends Deborah, Mat, Bertrand, Selim and Elina. I was also blessed to have Fatima and Zeinab tolerate all my nagging and ups and downs on lunch making this journey unique in all measures.

My parents are my secret recipe of who and where I am today. My mother an exquisite woman who struggled to teach me that there are no boundaries for dreams and no matter how hard life breaks us and tears us we will always pave our road by determination. Without you I would have never dared to dream. My father and friend, you have always been my shelter, you have loved and believed in me, you are forever my strength and inspiration. Wael, you are my companionship in success, you are the true definition of determination, and of a brother. Louay, you are my hope for a better future. Manar, you are my refuge for a brighter life. Mona your friendship has enlightened and guided me in so many different ways during all the stages of my life, you share a great deal of this success.

To this end I would like to thank my Mohammad, my home, my partner in life, dreams and success, everything is possible in your company and nothing is worth in your absence.

List of Abbreviations

A: Acceptor
AFM: Atomic Force Microscopy
ArN^{2+}: Diazonium Salt
AQ: 9,10-anthraquinone
Au: Gold Electrode
bpy: 2,2'-bipyridine
BISC: Back Intersystem Crossing
CSS: Charge Separated State
CV: Cyclic Voltammetry
D: Donor
DQ^{2+}: N,N'-diquaternary-2,2'-bipyridinium
ESI-MS: Electrospray Mass Spectroscopy
ET: Electron Transfer
E_nT: Energy Transfer
EDTA: Ethylenediaminetetraacetic Acid
GC: Gas Chromatography
GS: Ground State
HOMO: Highest Occupied Molecular Orbital
ITO: Indium Tin Oxide
ISC: Intersystem crossing
IC: Internal Conversion
ICPE: Incident Photon-to-Electron Conversion Efficiency
k_{ET}: Rate Constant of Kinetic Electron Transfer
L.B: Langmuir Blodget Films
LC: Ligand Centered
LUMO: Lowest Unoccupied Molecular Orbital
MC: Metal Centered
MLCT: Metal to Ligand Charge Transfer
Nbr: Number
NR: Non Radiative Decay
NMR: Nuclear Magnetic Resonance
Ox: Oxidation
PPh_3: Triphenyl Phosphine
PET: Photoinduced Electron Transfer
PSI: Photosystem I
PSII: Photosystem II
P: Photosensitizer
PTZ: Phenothiazine
Q: Quencher
Red: Reduction
RDE: Rotating Disc Electrode
SiO_2: Silicon Oxide
SAMs: Self Assembled Monolayers
TAA: Triarylamine
tpy: 2,2';2",6'-terpyridine
ttpy: 4'-(p-Tolyl)-2,2';2",6'-terpyridine

TEOA: Triethanolamine
TFA: Trifluoroacetic acid
TON: Turnover Number
TBAP: Tetrabutyl Ammonium Perchlorate
UV: Ultra Violet
Vis: Visible
V: Viologen
τ: Lifetime
ϕ: Quantum yield
ΔG: Variation of Free Enthalpy
Γ: Surface Coverage
ν: Scan Rate
ε: Molar Extinction Coefficient

CONTENTS

General Introduction

Résumé:

Les systèmes photosynthétiques naturels représentent le modèle le plus efficace pour la transformation de la lumière en énergie chimique. Ce processus photo-induit repose sur l'assemblage d'une unité chromophore capable d'absorber la lumière et de plusieurs cofacteurs redox (donneurs et accepteurs) qui agissent comme relais d'électrons. En effet, ce transfert d'électrons en plusieurs étapes entre le donneur D, le photosensibilisateur P et l'accepteur A est essentiel pour le transport d'électrons vectoriel, et la limitation de la recombinaison de charge non désirée.

Dans ce contexte, nous voulons construire des assemblages autour d'un noyau photosensible $[Ru(bpy)_3]^{2+}$ associé à différentes sous-unités métalliques servant comme relais d'électrons pour la transformation de la lumière en énergie chimique. En particulier, nous nous intéressons aux complexes terpyridyl de Fe(II), Co(III) et Cr(III).

Le chapitre 1 présente le travail effectué sur la synthèse et la caractérisation de fragments $[Ru(bpy)_3]^{2+}$ fonctionnalisés par une ou deux unité(s) terpyridine(s). Ceux-ci représentent une plate-forme pour accéder à des complexes trimétalliques de formule générale P-Q-P. La synthèse et la caractérisation détaillée de complexes trinucléaires de fer ou de cobalt sera présentée. Ces assemblages seront utilisés comme outils afin d'examiner la nature du quenching entre les différents centres métalliques (Fe^{2+}/Co^{3+}) et $[Ru(bpy)_3]^{2+*}$.

Dans le chapitre 2, discutons de l'immobilisation des différents assemblages de $[Ru(bpy)_3]^{2+}$, $[Co(ttpy)_2]^{3+}$, $[Fe(tpy)_2]^{2+}$ et $[Zn(tpy)_2]^{2+}$ de formules (DP, AP, DPA) sur des électrodes. De plus, nous présentons la possibilité de générer un courant électrique dans ces systèmes sous irradiation par la lumière visible et en présence d'un réactif sacrificiel. Cela nous permettra d'étudier les facteurs qui influent sur l'efficacité de la génération de photocourant.

Le chapitre 3 étudie la possibilité de quenching entre $[Ru(bpy)_3]^{2+*}$ et $[Cr(tpy)_2]^{3+}$ au sein d'un système bimoléculaire ou d'assemblages trinucléaires de type Ru-Cr-Ru. En outre, les résultats préliminaires portant sur l'activité catalytique potentielle de complexes de chrome terpyridyl pour la réduction des protons seront exposés.

Enfin dans le chapitre 4, nous allons démontrer la possibilité d'utiliser le métalloligand ruthénium bisterpyridine afin d'accéder à des polymères de coordination alternés de structure $\{[Ru(bpy)_3]^{2+}/[M(tpy)_2]^{n+}\}$ (M = Fe(II) et Cr(III)). Ces polymères seront synthétisés, entièrement caractérisés et leurs électro- et photo-activités seront examinées attentivement.

CHAPTER 0

GENERAL INTRODUCTION

0.1 Photochemical Conversion of Solar Energy

Energy appears as one of the most controversial issues of the 21^{st} century.[1] So far, most of our energy resources were governed by fossil fuels stocks. These finite stocks are unevenly distributed under the Earth's surface, thus threatened by depletion under continuous use.[2] Moreover, fossil fuel combustion is also associated with detrimental effects on both humans and the environment.[1] These energy crisis and environmental emergencies require seeking alternatives which will provide for man's needs. Solar energy is considered a promising clean and abundant energy source, for our earth receives a fairly distributed and inexhaustible power from the sun. Nonetheless, this energy can not be employed as such; it must be harvested and converted into useful forms of energy.[3]

Nature's photosynthetic machinery is the most efficient example for the photochemical conversion of solar energy **figure 1**.[4] Under irradiation, this system efficiently induces a series of short electron transfers between photosystem I (PSI) and photosystem II (PSII) *via* spatially organized electron carriers in the thylakoid membrane of green plants. This process generates a charge-separated state (CSS) where the electron is then used to reduce $NADP^+$ to NADPH, while the hole is used to oxidize the H_2O into O_2 and H^+ providing the latter for the ATP synthase that fuels an organism. In order to convert solar energy into chemical energy on the molecular level, we will have to reproduce the role of the different compartments found in the photosynthetic machinery. This will thus require the synthesis of molecular models that are capable of absorbing light namely photosensitizer (P), as well as electron carriers that can either serve as electron donors (D) or acceptors (A). In the thylakoid membrane, these entities are placed in close proximity without strong coupling interaction as governed by hydrogen bonding

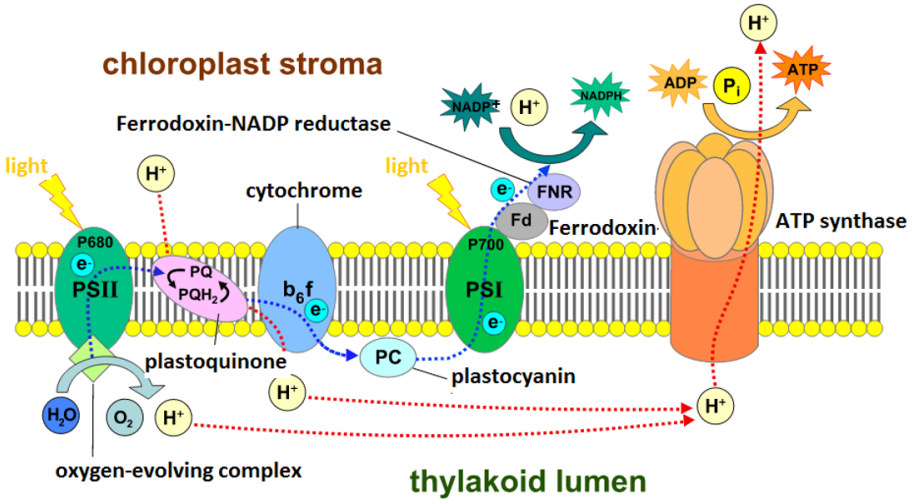

Figure 1: A drawing of the photosynthetic machinery.

and protein interaction, however on the molecular level, it is quite challenging to reconstitute this complex chain of interactions. One alternative, is to link these compartments by covalent bonds. These assemblies of D-P-A can generate the CSS upon light irradiation denoted by D^{+}-P-A^{-}, which in turn can be invested in two different approaches: This flow of electrons can be funneled directly on an electrode to produce current, or stored in the form of an energy vector like H_2 by the aid of a catalyst.

0.2 $[Ru(bpy)_3]^{2+}$: The Prototype of Redox Photochemistry

A photosensitizer (P) by definition is a chromophore that absorbs light, leading to electronic transitions, which bring the molecule into an electronically excited state with a lifetime long enough to allow a chemical interaction with the surrounding media. This transition is only possible if the photon energy (hν) matches the energy gap between the highest occupied molecular orbital (HOMO) and lowest unoccupied molecular orbitals (LUMO).

The prototype $[Ru(bpy)_3]^{2+}$ (bpy = 2,2'-bipyridine) **figure 2** is one of the most explored photosensitizers.

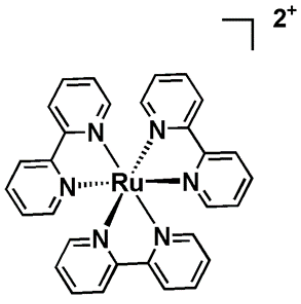

Figure 2: Molecular structure of $[Ru(bpy)_3]^{2+}$.

Ru^{2+} is a d^6 metal and the polypyridine ligands are usually colorless molecules possessing σ donor orbitals localized on the nitrogen atoms and π donors and π^* acceptor orbitals more or less delocalized on aromatic rings as described by Balzani et al.[5] It is notable, that in a $[Ru(bpy)_3]^{2+}$ complex, the bipyridine are high field ligands and thus induce the configuration shown in **figure 3.(a)**, where the valence electrons are distributed on the t_{2g} orbital. Upon absorption of light in the visible region of the spectrum, a singlet metal to ligand charge transfer (^{1}MLCT) state is populated which corresponds to the transfer of an electron from the metal centered t_{2g} orbital (**HOMO**) to the ligand centered π^* orbital **(LUMO) figure 3.(a)**. This electron transfer is accompanied by fast inter-system crossing (change of spin state) to the first triplet state ^{3}MLCT with a quantum efficiency of 1 made possible by strong spin-orbit coupling due to the presence of the metal center. This new excited state can be deactivated either by emission of a photon "phosphorescence" or non-radiative decay (loss of heat), or through the population of a metal centered ^{3}MC state which is non-emissive in nature and can give rise to ligand loss **figure** 3.(b).[6]

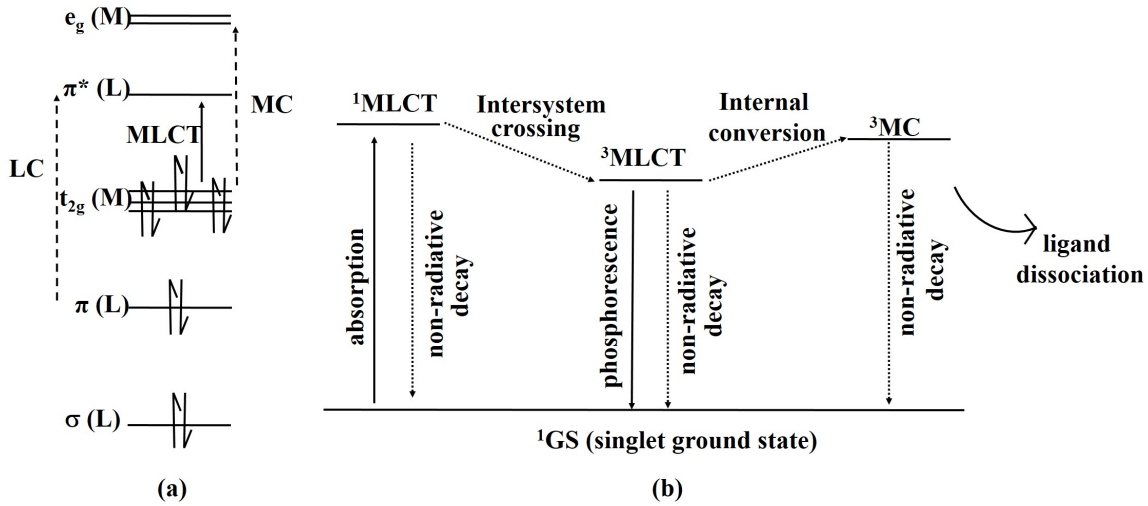

Figure 3: (a) Schematic molecular orbital diagram of a d^6 complex in an octahedral environment underlining metal centered (MC) and metal-to-ligand charge transfer (MLCT); (b) A simplified Perrin-Jablonski diagram indicating radiative and non radiative transitions for Ru^{2+} polypyridyl complexes.

At this level it is crucial to introduce two important terms that describe the excited state which are lifetime (τ) and emission quantum yield (ϕ). These quantities can be expressed by the following **equations 1 and 2**:[7]

$$\tau = \frac{1}{k_r + k_{nr}} \tag{1}$$

$$\phi = \frac{k_r}{k_r + k_{nr}} \tag{2}$$

where $\not{k}_r$ and $\not{k}_{nr}$ are the rate constants of radiative and non-radiative decay (internal conversion, intersystem crossing) respectively.

The absorption and emission spectra of $[Ru(bpy)_3]^{2+}$ are shown in **figure 4** along with proposed assignments.[8] In the absorption spectrum, there are three types of transitions. The band at 285 nm is assigned to spin allowed LC $\pi \rightarrow \pi^*$ transition, the broad band at 450 nm is attributed to a MLCT $d \rightarrow \pi^*$ transition and the shoulders at 322 and 344 nm are assigned to be MC $d \rightarrow d$ transitions. Excitation of $[Ru(bpy)_3]^{2+}$ in any of its absorption bands first decays to the emitting ^{3}MLCT. This emission is centered around 600 nm where its energy, intensity and lifetime are dependent on the temperature and the solvent. In deaerated acetonitrile and at room temperature the lifetime of this luminescence is estimated to be around 1 μs with a quantum yield of $\phi_{em} = 0.06$.

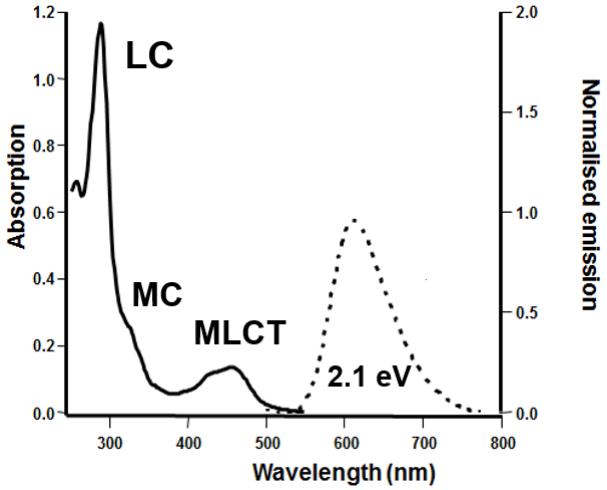

Figure 4: Electronic absorption and emission spectra of $[Ru(bpy)_3]^{2+}$ in CH_3CN at room temperature.

0.3 Mechanism of Quenching of the Excited State of $[Ru(bpy)_3]^{2+}$

In the presence of suitable donors and acceptors (quenchers), the ^{3}MLCT excited state of $[Ru(bpy)_3]^{2+}$ can take part in bimolecular reactions. The quenching reaction is dictated by the nature of the quencher, and can be energy **equation 3.a** and/or electron transfer **equation 3.b and 3.c**.

$^*[Ru(bpy)_3]^{2+} + Q \rightarrow [Ru(bpy)_3]^{2+} + {}^*Q$ Energy transfer (3a)

$^{*}[Ru(bpy)_3]^{2+} + Q \rightarrow [Ru(bpy)_3]^{3+} + Q^{-}$ Oxidative Quenching (3b)

$^{*}[Ru(bpy)_3]^{2+} + Q \rightarrow [Ru(bpy)_3]^{+} + Q^{+}$ Reductive Quenching (3c)

(3)

The three processes may proceed in parallel, but some information are important to help distinguish between them and to estimate the most favorable one:

1. Energy and nature of the emitting excited state of the photosensitizer (^{3}MLCT for Ru)
2. Absorption spectrum of the quencher.
3. Redox potentials of all systems

0.3.1 Energy Transfer

Energy transfer can be described by different mechanisms that can be either radiative or radiationless transition between two excited states. For energy transfer pathway to take place we should satisfy the condition which states that the energy of the excited state of the donor $^{*}E_D$ should be higher than that of the acceptor $^{*}E_A$. This energy transfer process can take part in two different mechanism: Förster[9] and Dexter[10] type as depicted in **figure 5**.[7]

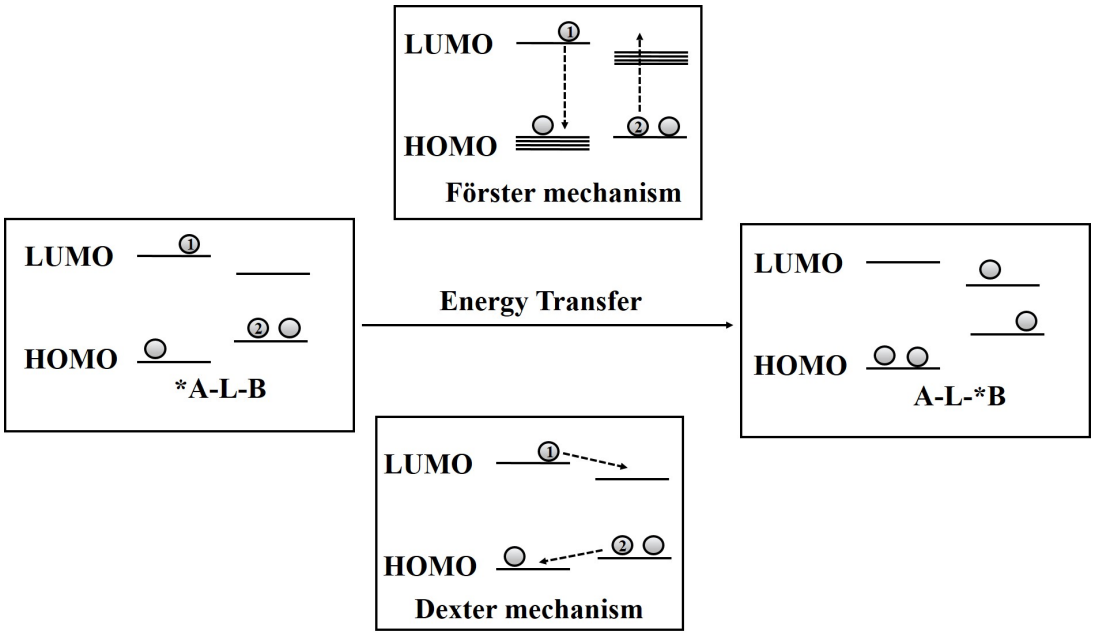

Figure 5: A Representation of the Förster and Dexter type mechanisms.

Regarding the Dexter mechanism, also known as the exchange mechanism, it involves a double electron exchange between the donor and the acceptor. During this mechanism an electron moves from the LUMO of the donor to the LUMO of the acceptor , accompanied by a simultaneous electron injection from the HOMO of the acceptor to the HOMO of the donor. This electron exchange necessitates a strong overlap between the orbitals of the donor and the acceptor and thus are dependent on the nature of the bridge connecting both entities. The dependence of the rate constant of energy transfer process with the distance between the donor and the acceptor is described by **equation 4**:

$$k_{EnT} \propto \mathrm{KJe}^{-\beta r} \tag{4}$$

In this expression, K is related to specific orbital interactions, J is the normalized spectral overlap integral, r expresses the distance between the donor and the acceptor and β refers to the attenuation factor which is specific for each bridge.
The Förster mechanism , which is also called coulombic mechanism, or through space, can be described as a long range mechanism, meaning that there is no requirement of a physical contact between both the donor and the acceptor. In other words, the electronic nature of the bridge between the donor and the acceptor, if present, doesn't influence the energy transfer rate, and the main contribution comes from the dipole-dipole interaction between the donor and the acceptor. The rate constant of the energy transfer is expressed by **equation** 5:

$$k_{EnT} \propto \frac{J\phi_D}{\tau_D r^6} \tag{5}$$

where ϕ_D and τ_D are the emission quantum yield and luminescence lifetime of the donor and r the distance between the donor and the acceptor.

Several di/trinuclear metal complexes containing $[Ru(bpy)_3]^{2+}$ were investigated and showed evidence of energy transfer, by which the ruthenium moiety can act either as a donor or as an acceptor depending on the counter metallic complex. We don't want to review the field, but we intend to highlight few examples which will serve for the following of the thesis, for further information one can refer to several review papers which deal with energy transfer in transition metal complexes.[5;11;12]

One of the most explored examples are based on Ru(II) and Os(II) bipyridyl complexes bridged with oligophenylene spacers **figure 6**.[13–15] In these dinuclear complexes, the $[Ru(bpy)_3]^{2+}$ plays the role of an energy donor, and the $[Os(bpy)_3]^{2+}$ acts as an energy acceptor. Thus excitation of the $[Ru(bpy)_3]^{2+}$ part is followed by an energy transfer to the $[Os(bpy)_3]^{2+}$ complex. The energy transfer in these examples proceeds through a Dexter mechanism and the rate constants were obtained for different systems based on varying the length, position and nature of the bridge in a series of publications. It was concluded, that there is a strong correlation be-

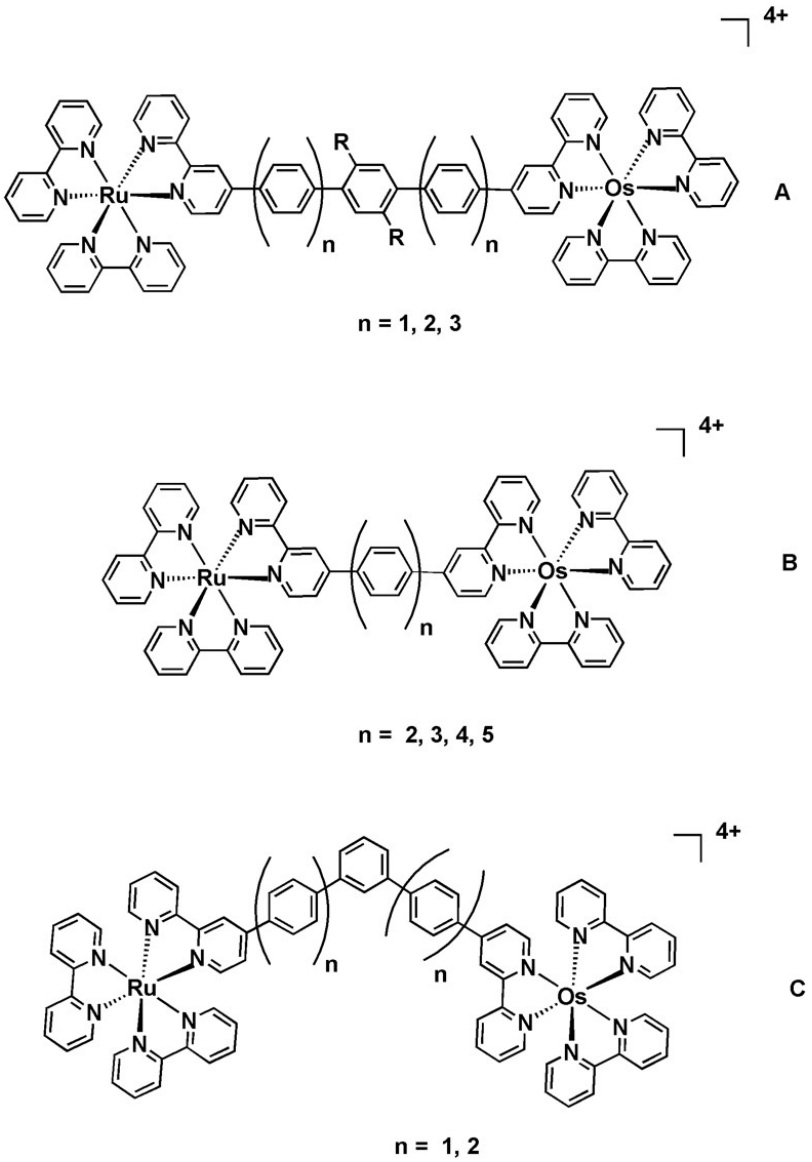

Figure 6: Different assemblies of Ru(II)/Os(II) with different bridges.

tween the length of the bridge and the efficiency of quenching. For instance, it was proven that the transfer rate constants decrease from 6.7×10^8 s^{-1} to 1.0×10^7 s^{-1} to 1.3×10^6 s^{-1} with increasing the length of the oligophenylene spacer from 3 to 5 to 7 units respectively, with an attenuation coefficient of 0.32 $Å^{-1}$ **figure 6.A**.[13] It was also established that the nature of the bridge plays a significant role in modulating the electronic coupling between the donor and acceptor, thus influencing the rate of the energy transfer. For instance it has been proven that for dyads containing bridges made of a total of three non- substituted phenyl spacers **figure 6.B** , the rate constants were 3.4×10^7 s^{-1} which is approximately three times higher than that recorded in the case of the phenylene with a β around 1 $Å^{-1}$ **figure 6.A**.[14] This was attributed to minimized communication between the two metallic centers as imposed by the twist angle of the methyl groups on the phenyl spacers. It has also been evidenced that the position of the substitution can significantly modulate the communication between the different compartments.

For example, phenyl spacers substituted on the para substitution **figure 6.B** showed more efficient energy transfer of a value of 2.77 $\times$ 10^{10} s^{-1} compared to the meta with a value of 1.32 $\times$ 10^{9} s^{-1} for a total of three phenylenes **figure 6.C**.[15]

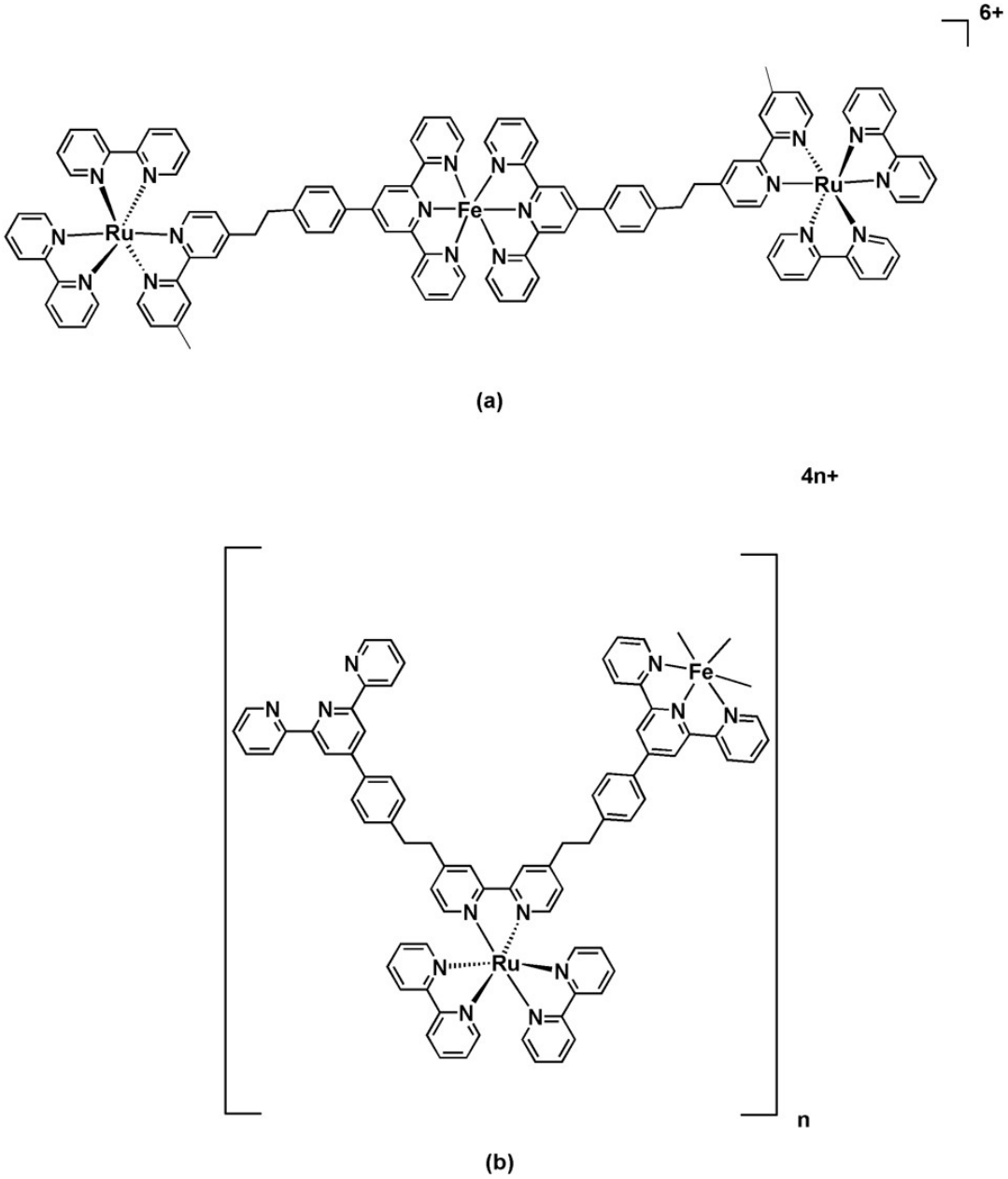

Figure 7: **(a)** Trimetallic complex based on Ru(II) and Fe(II) ;**(b)** coordination polymer based on alternating Ru(II) and Fe(II) subunits.

Similarly, complexes of Ru(II) and Fe(II) showed evidence of energy transfer, by which $[Ru(bpy)_3]^{2+*}$ acts as a donor while the $[Fe(tpy)_2]^{2+}$ (tpy = 2,2';6',2"- terpyridine) acts as an acceptor in trimetallic or polymeric assemblies **figure 7**.[16;17] While $[Ru(bpy)_3]^{2+}$ emits around 600 nm the $[Fe(tpy)_2]^{2+}$ absorbs largely around 590 nm. This overlap between the emission spectrum of the ruthenium complex, and absorption of the Fe part governs energy transfer from the former to the latter. This transfer is accompanied by the formation of the

MLCT state of the Fe subunit which in turn decays back to the ground state with non-radiative decay.

$[Ru(bpy)_3]^{2+}$ can also play the role of an energy acceptor when connected to Ir(III) complexes **figure 8**.[18] In this example the $[Ru(bpy)_3]^{2+}$ accepts energy from the excited state of the Ir-based chromophore. On the contrary to previously stated examples, increasing the distance between both entities slightly decreases the energy transfer rate passing from 8.3×10^{11} s^{-1} for two phenyl spacers to 3.3×10^{11} s^{-1} for a total of five phenyl spacers. This presumed attenuation parameter β is calculated to be 0.07 $Å^{-1}$. However, analyzing the MLCT excited state of the Ir center showed an increasing L.C character involving the bridge orbitals as the number of phenyls increased. Consequently, the metal- metal separation is not a reflection of the real distance between the donor and the acceptor. This lead to the assumption that energy transfer in this case passes by a hopping mechanism instead of a Dexter mechanism which was observed for previously stated complexes, and is the reason of the low β values.

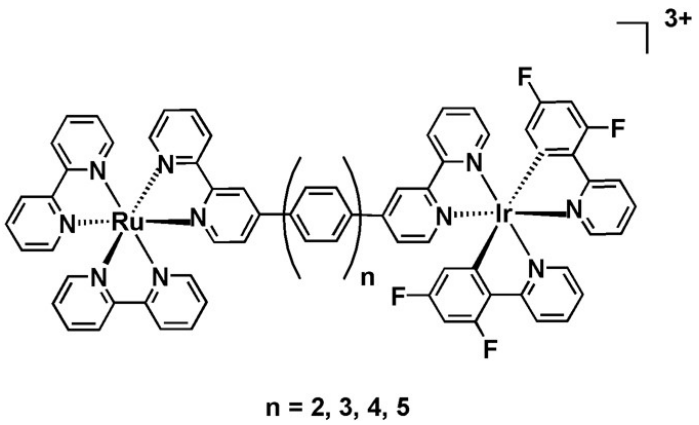

Figure 8: Dinuclear Ru(II) and Ir(III) dyads.

0.3.2 Photoinduced Electron Transfer Processes PET

Electron transfer is an exchange of electrons between two molecules by which the first is oxidized while the other is simultaneously reduced. PET reactions are only possible along well-designed redox gradients. In other words, this quenching path is dependent on the redox potentials of both the quencher and the excited state of the photosensitizer. One crucial perquisite is that the process should be thermodynamically allowed ($\Delta G < 0$). Therefore, we have to determine the excited state potentials of P. This can be done following the Rhem-Weller **equation 6**.[19]

$$E^*_{1/2}{}^{red} = E_{1/2}{}^{red} + E_{00} \qquad E^*_{1/2}{}^{ox} = E_{1/2}{}^{ox} - E_{00} \tag{6}$$

$E^*_{1/2}$ represents the reduction or oxidation potential of the excited state, $E_{1/2}$ is the reduction or oxidation potential of the ground state and can be extracted experimentally from a cyclic voltammetry (CV) experiment, E_{00} represents the difference in energy between the zeroth vibrational states of the ground and excited states. The zero-zero excitation energy, E_{00} is usually approximated by the emission energy of the compound at 77 K as illustrated in **figure 9**. This method allows calculation of approximate excited-state redox potentials from more easily measured ground-state redox potentials and spectroscopic data.

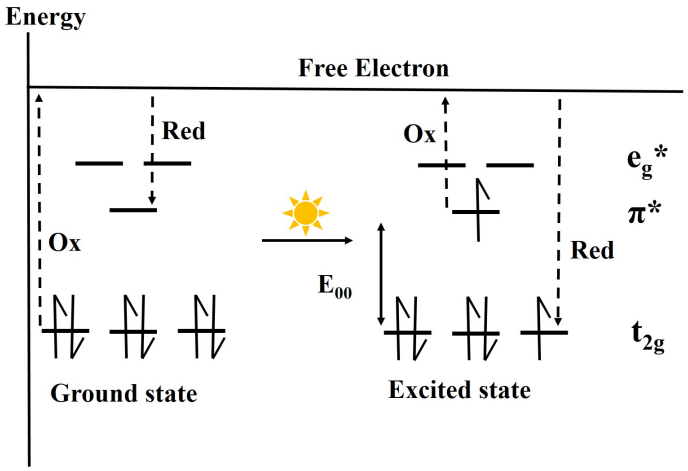

Figure 9: The redox properties of the excited state of a d^6 metal in terms of molecular orbitals.

After measuring and calculating the potentials of all the redox couples which could be involved, a first approximation of the exoergonicity of the processes can be evaluated using **equation 7** derived by Weller[20]:

$$\Delta G = e[E_{ox}(D) - E_{red}(A)] - E_{00} - \frac{e^2}{4\pi\varepsilon_0\varepsilon_s R_c} - \frac{e^2}{8\pi\varepsilon_0}\left(\frac{1}{r_{D^+}} + \frac{1}{r_{A^-}}\right)\left(\frac{1}{37.5} - \frac{1}{\varepsilon_s}\right) \quad (7)$$

In this equation ΔG represents the free enthalpy of the reaction, $E_{ox}(D)$ and $E_{red}(A)$ are the oxidation potential of the donor and the reduction potential of the acceptor, ε_s is the solvent dielectric constant, r_{D^+} and r_{A^-} are the ionic radii and R_C is the center-to-center separation distance between the donor and the acceptor. E_{00} is the singlet or triplet state energy determined by the emission maximum at 77 K. The third term represents the Coulombic interaction between the two charged moieties. The last term corrects the difference in the ion-pair solvation in which the redox potentials were measured. This expression can be also written in a more simplified form as shown in **equation 8**:

$$\Delta G = -nF\,[E^{ox}_{(1/2)} - E^{red}_{(1/2)}] \quad (8)$$

If ($\Delta G < 0$) then the reaction is thermodynamically favorable.

As formerly mentioned, $[Ru(bpy)_3]^{2+*}$ can take part in oxidative and/or reductive quench-

ing. Several bimetallic systems based on $[Ru(bpy)_3]^{2+}$ and several transition metals which act as quenchers were reported in the literature.[21–24] Nonetheless, it remains more tempting to link this Ru moiety to two subunits, by which one will act as an electron donor while the other will act as an acceptor in order to mimic the charge separated state found in Nature. Despite the remarkable properties of $[Ru(bpy)_3]^{2+}$, only few triads with the formula (D-P-A) were previously reported.

The first examples of triads based on $[Ru(bpy)_3]^{2+}$ which were reported in the literature lack symmetry and contain either two donor or acceptor units connected to different bipyridine ligands **figure 10**.[25;26] The first problem associated with this approach is that when D and A motifs are attached to different bipyridine ligands, resulting in a mixture of isomers (Λ/Δ, fac/mer) which complicates the study of the quenching mechanism. Moreover, the lack of linearity in such assemblies leads to the inefficient formation of the CSS. Triad in **figure 10**.**(a)** consists of

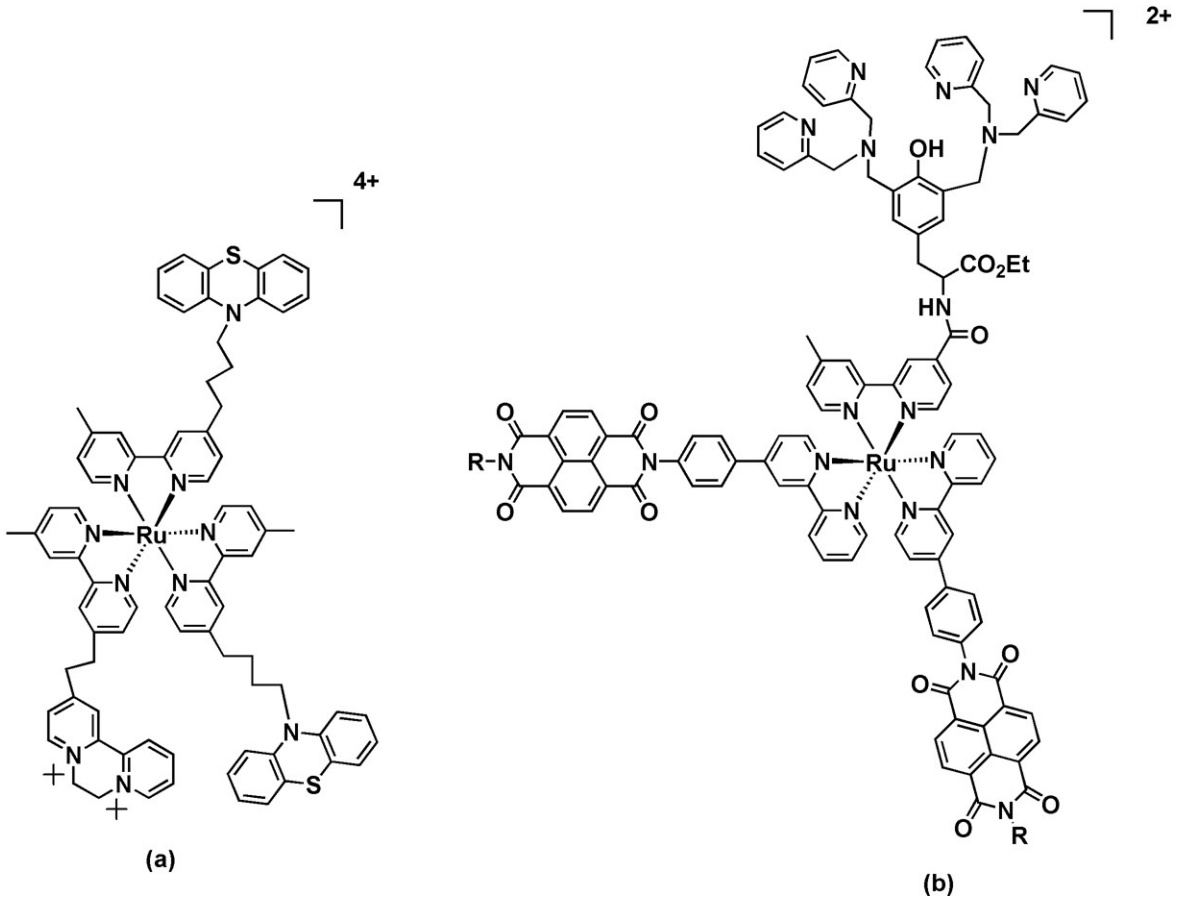

Figure 10: Triads based on $[Ru(bpy)_3]^{2+}$

a $[Ru(bpy)_3]^{2+}$ unit linked to two phenothiazine (PTZ) moieties which serve as electron donors and N,N'-diquaternary-2,2'-bipyridinium (DQ^{2+}) which acts as an acceptor. Ethyl and butyl bridges are used in order to link the different compartments, and the lifetime of the CSS state is estimated to be 150 ns **figure 10.(a)**. Likewise, **figure 10.(b)** shows a donor-chromophore-acceptor triad based on tris(bipyridine) ruthenium(II) as photosensitizer, two naphthalene di-

imide groups as acceptors, and a dpaTyr "bis-2,6-(dipicolylaminomethyl)tyrosine ethyl ester" as electron donor. The acceptors are linked *via* phenyl spacers whereas the donor is linked with amide bonds. In this system a CSS is obtained only in 10% yield.

Since linearity is essential in order to fix the distance between the donor and the acceptor and therefore minimize the charge recombination, two approaches were developed in order to achieve more linear triads:

Approach 1: The first approach was developed by the group of Hammarström by which the $[Ru(bpy)_3]^{2+}$ core bears three unsymmetrical bipyridines **figure 11**.[27] The triad (PTZ - Ru^{2+} - BQ) where PTZ acts as an electron donor, and BQ for benzoquinone which serves as electron acceptor was reported. Different compartments are held together *via* (methyl and ethyl) chains respectively. Upon light irradiation a CSS $PTZ^{\cdot+}$ - Ru^{2+} - $BQ^{\cdot-}$ (τ = 80 ns) with a high yield of (> 90%) is obtained. This value was unprecedented for triads based on $[Ru(bpy)_3]^{2+}$.

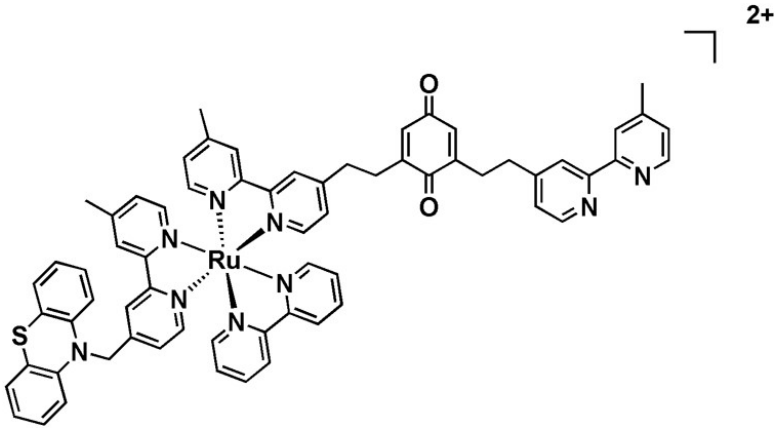

Figure 11: Triad developed by the group of Hammarström based on $[Ru(bpy)_3]^{2+}$.

Approach 2: A more elegant approach was reported by the group of Wenger, through which both the donor and the acceptor are attached on the central bipyridine at the 5 and 5' positions **figure 12**.[28]

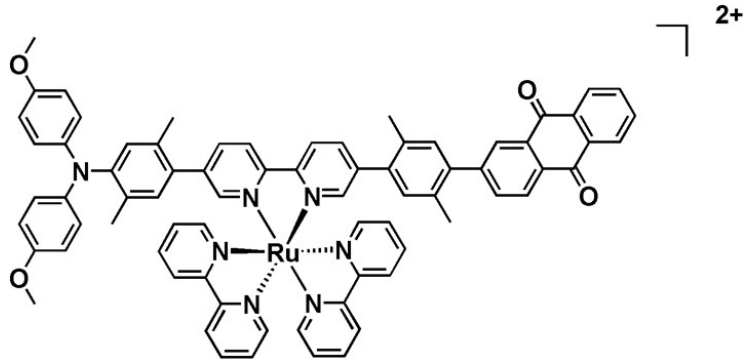

Figure 12: A rigid and linear triad developed by the group of Wenger based on $[Ru(bpy)_3]^{2+}$.

This triad consists of a TAA- Ru^{2+} - AQ where TAA corresponds to triarylamine and is the electron donor and AQ is to 9,10-anthraquinone which serves as an acceptor. These different compartments are held together by phenylene bridges, by which the rigidity and linearity of these spacers will ensure linear assemblies, and will govern a fixed and maximal distance between D and A. Moreover, the tilt angles imposed by the methyls on the phenylene bridge will minimize the conjugation between the different compartments and consequently delay charge recombination along with the previous parameter. Another noteworthy feature of this triad is the absence of statistical isomers which is an inherent asset of linking both the D and A on the same bipyridine moiety. Consequently, upon Ru excitation a vectorial photoinduced transfer takes place leading to the formation of $TAA^{\cdot+}$- Ru^{2+} - $AQ^{\cdot-}$ with a long lifetime of 1.3 μs in acetonitrile and an efficiency estimated to be > 64%. These values are superior to others reported in the literature, which sheds light on the significance of this approach.

0.4 Integrating $[Ru(bpy)_3]^{2+}$ based assemblies onto Electrodes

After this short overview, it is important to stress the utility of electron transfer to and from the $[Ru(bpy)_3]^{2+*}$ core and the important advances which were listed in this field. Most of the breakthroughs accompanied integrating these assemblies onto electrodes especially with the increasing need of incorporating molecular materials in nano-scale devices.[29–32] To our knowledge none of the triads based on $[Ru(bpy)_3]^{2+}$ were grafted onto surfaces, however both monomeric species and dyads were previously reported.

0.4.1 $[Ru(bpy)_3]^{2+}$ monomers

$[Ru(bpy)_3]^{2+}$ complex could be easily functionalized due the large library of commercially available modified bipyridines. This allows introducing different functionalities that could either polymerize or adsorb onto surfaces.[29–34] The electrode then acts as an electron reservoir *via* a bias, meaning that it can either donate or accept an electron. This will allow the generation of a current upon light irradiation in the presence of a sacrificial reagent. The nature of the photocurrent (anodic/cathodic) will be dictated by the applied bias and the nature of the sacrificial reagent.

For instance, the group of Laberty-Robert demonstrated the capability of covalently grafting this photosensitizer on nanostructured ITO surfaces **figure 13**.[35] The covalent attachement is ensured by phosphonate groups. The nanostructured feature of the ITO increases the area which can host molecules, which was translated by the increase of the surface coverage to a value of 3.5×10^{-9} mol.cm^{-2}. These values are approximately 100 times higher than values reported

for planar ITO. In this work, the authors have shown that in the presence of an electron mediator $[Co(NH_3)_5Cl]Cl_2$ a cathodic photocurrent with a value of 50 $\mu A.cm^{-2}$ is produced, and that the value of the photocurrent is significantly related to the surface coverage. In other words, the more molecules grafted on the surface, the higher the response is.

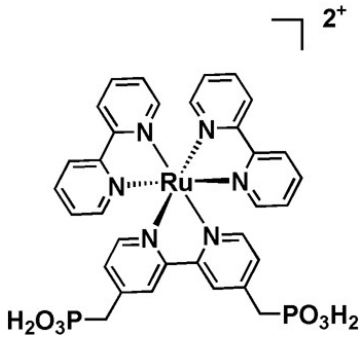

Figure 13: Functionalized $[Ru(bpy)_3]^{2+}$ precursor used to graft onto nanostructured ITO.

0.4.2 $[Ru(bpy)_3]^{2+}$ based bimetallic complexes

Numerous dyads based on $[Ru(bpy)_3]^{2+}$ were reported displaying either current or catalytic applications.[36–38] Among several others, one stimulating example is based on a combination of $[Ru(bpy)_3]^{2+}$ - viologen (V^{2+}) linked to thiol derivatives with different spacer-chain lengths **figure 14**.[37] In these examples, the authors show evidence of anodic current from the Ru^{2+}

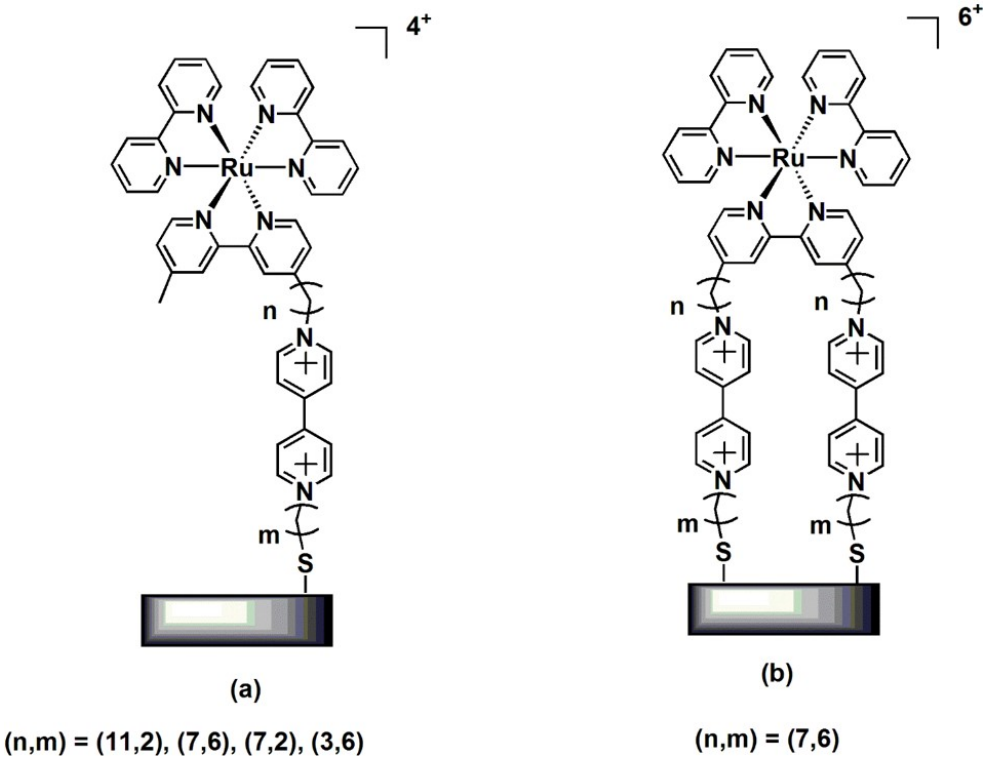

Figure 14: Immobilized $[Ru(bpy)_3]^{2+}$ - Viologen dyad on gold surface.

core to the acceptor (V^{2+}) upon light irradiation and in the presence of triethanolamine as a sacrificial electron donor. Most importantly, they proved that the presence of two (V^{2+}) groups increase the efficiency of electron transfer, and they also demonstrated the importance of optimizing the spatial distance between P, A and gold electrode. As a matter of fact, the distance between the (V^{2+}) final acceptor and the electrode impacted the most the output of the current, where more efficient injection of the electron to the electrode is ensured with shorter distances. However, these authors detected a photocurrent magnitude of only 5 nA.cm^{-2}.

It has always been a challenge to replace arbitrary electron donors or acceptors with others that realize catalytic conversion in order to mimic the photosynthetic machinery. In this context, one example is an immobilized $[Ru(bpy)_3]^{2+}$ -$[Ru(tpy)(bpy)(H_2O)]^{2+}$ dyad linked by a synthetically flexible saturated bridge designed to enable long-lived charge-separated states whereby the second Ru complex is a water oxidation catalyst **figure 15**.[38] Upon excitation of the chromophore an electron is injected to the electrode followed by a rapid intramolecular electron transfer to generate the remote oxidized state. The CSS is estimated to 35 μs at pH = 4.5.

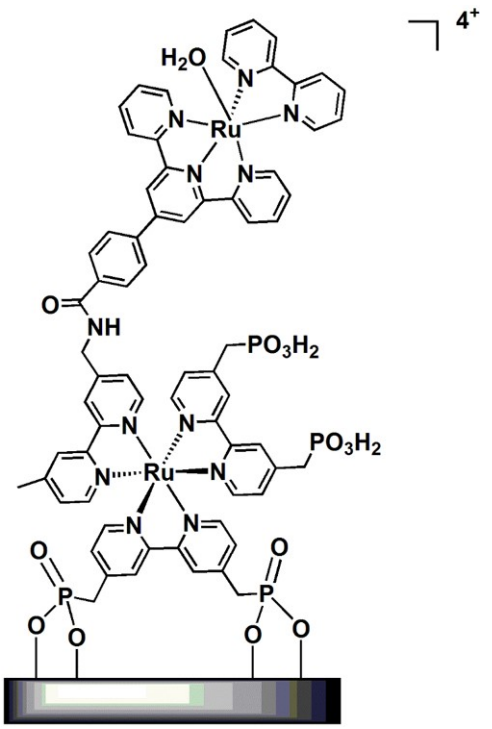

Figure 15: Immobilized $[Ru(bpy)_3]^{2+}$ -$[Ru(tpy)(bpy)(H_2O)]^{2+}$ dyad on TiO_2.

Another system reported by the group of Mallouk showed evidence of the photocatalytic oxidation of water upon visible light irradiation using an immobilized dyad on TiO_2 consisting of $[Ru(bpy)_3]^{2+}$ as a light harvesting entity and $IrO_2.H_2O$ nanoparticles as a water oxidation catalyst **figure 16**.[33] Upon applying a bias of -0.325 mV *vs.* Ag/AgCl, the current efficiency for photoanodic oxygen generation was roughly estimated to 20%. These low values of produc-

tion of oxygen were also associated with a low quantum yield $\approx 0.9\%$. The authors attribute this to the slow electron transfer from the $IrO_2.H_2O$ nanoparticle to the oxidized chromophore, which apparently doesn't compete effectively with the back electron transfer (BET) from the TiO_2 semiconductor to the dye.

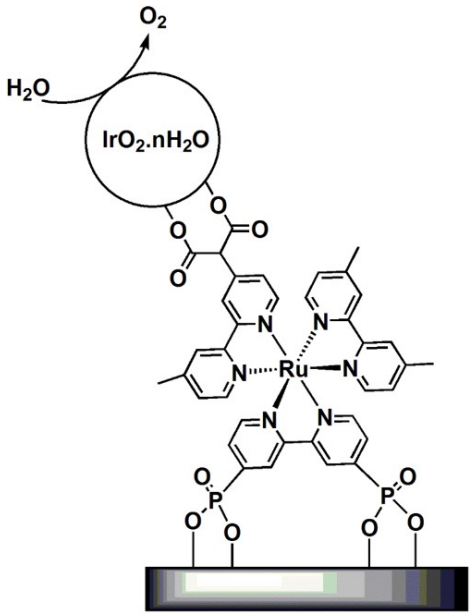

Figure 16: Immobilized $[Ru(bpy)_3]^{2+}$ -$IrO_2.nH_2O$ dyad on TiO_2

Another interesting architecture was described by the group of Wu **figure 17**.[34] In this example a $[Ru(bpy)_3]^{2+}$ photosensitizer is connected *via* an axial pyridine to a cobaloxime catalyst for the proton reduction, and immobilized on NiO surface by the aid of carboxylic acid. This system demonstrated a remarkable stability in water at pH = 7 upon light irradiation and successfully reduced protons to hydrogen with a 68% faradaic efficiency upon applying a bias at 0.1 V. This system functions through multiple electron transfer process, by which the $[Ru(bpy)_3]^{2+*}$ excited state first injects a hole into the NiO, followed by an electron transfer from the reduced dye to the cobaloxime catalyst.

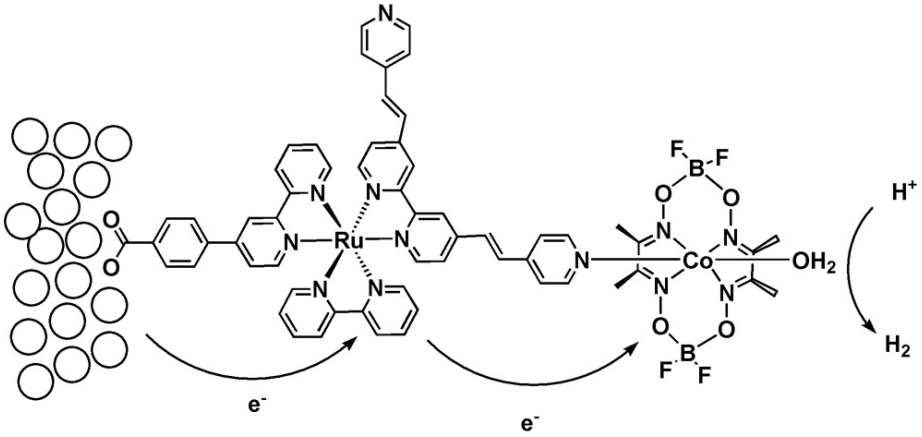

Figure 17: Immobilized $[Ru(bpy)_3]^{2+}$ -cobaloxime dyad on NiO

0.5 Scope of this Thesis

In this thesis, we aim to investigate the factors that influence the quenching of the excited state of $[Ru(bpy)_3]^{2+}$ with different metallic centers, and to subsequently study the effect of these modifications on photo-to-electric conversion and catalysis. The interest in metallic complexes is due to the high stability of the oxidized or reduced system which is attractive for application in molecular electronic devices and catalysis. In this context, we functionalized a $[Ru(bpy)_3]^{2+}$ with one/two free terpyridine coordination site(s). These modified ruthenium complexes are then used to build different systems (trinuclear assemblies or polymers) where the electron donor (D) and acceptor (A) are covalently linked to the photosensitizer (P) **figure 18**.

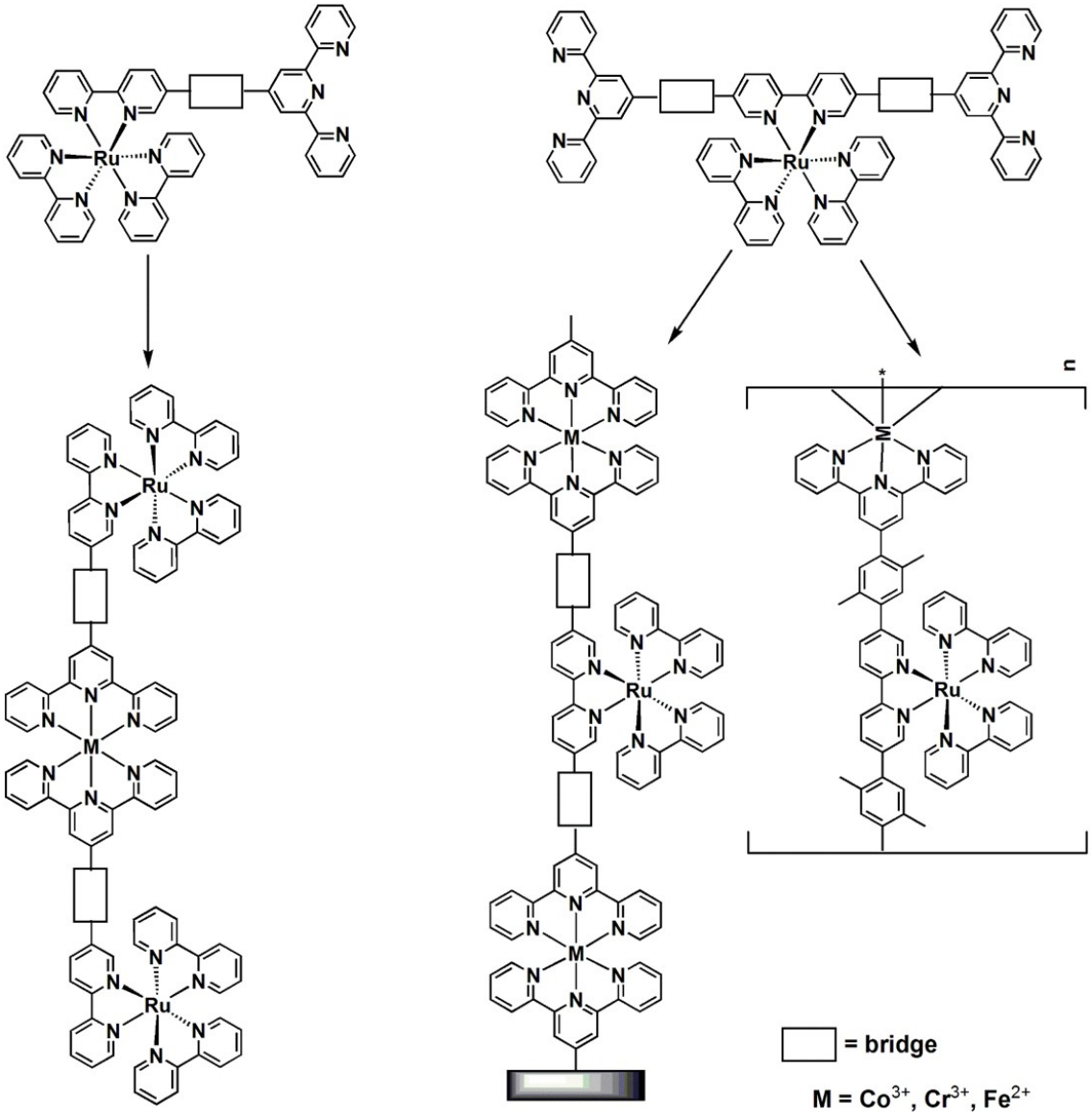

Figure 18: Different assemblies of photosensitizer and quencher.

As for the quenchers (Q), we have grown particular interest in terpyridyl complexes of first row transition metals (Co, Fe and Cr), which offer several advantages; some of which are the abundance, low prices... However, these metals are known for the chemical lability of their coordination sphere, thus making it tricky to form heteroleptic terpyridyl complexes of the latter metals. After figuring out a way to manipulate these complexes in order to block desired assemblies, we studied the possibility of introducing three different types of bridges (amides, ethers and phenylene) modulating the distance, the electronic coupling between the different compartments as well as the photophysical properties of the ruthenium core.

Chapter 1 will present a summary of the work carried out on the synthesis and characterization of different functionalized $[Ru(bpy)_3]^{2+}$ moieties bearing one/two terpyridine(s) unit(s). The latter complexes present a platform to access trimetallic complexes of the general formula P-Q-P. Indeed, the detailed synthesis and characterization of trinuclear complexes of either iron or cobalt will be presented. These assemblies will be used as tools in order to examine the nature of the quenching between the different metallic centers (Fe^{2+}/Co^{3+}) and $[Ru(bpy)_3]^{2+*}$.

In **chapter 2** we will discuss the immobilization of different assemblies of $[Ru(bpy)_3]^{2+}$, $[Co(tpy)_2]^{3+}$, $[Fe(tpy)_2]^{3+}$ and $[Zn(tpy)_2]^{2+}$ with the formula (D-P, A-D, D-P-A) onto electrodes. The isolation of these assemblies is only feasible by the employment of a stepwise methodology which will help to block the heteroleptic form of the terpyridyl complexes. Furthermore, we will also present the possibility of generating an electric current under visible light irradiation and in the presence of a sacrificial reagent in these systems. This will enable us to study the factors that impact the output of the current generation.

Chapter 3 will focus on the study of the nature of quenching between $[Ru(bpy)_3]^{2+*}$ and $[Cr(ttpy)_2]^{3+}$ in a bimolecular system and in trinuclear assemblies of Ru-Cr-Ru. Moreover, preliminary results dealing with the potential catalytic behavior of chromium terpyridyl complexes toward the reduction of protons will be presented.

In **Chapter 4** we will demonstrate the possibility of using the ruthenium bis terpyridine metallo ligand in order to access alternating coordination polymers of $[Ru(bpy)_3]^{2+}$/$[M(tpy)_2]^{n+}$ structure (M = Fe(II) and Cr(III)) . These polymers will be synthesized, fully characterized and their electro and photo-activity will be examined carefully. This indeed assists us to better clarify the limitations and preferences for the eventual application of photoelectric conversion.

Bibliography

[1] V. Balzani, A. Credi, M. Venturi, *ChemSusChem* **2008**, *1*, 26–58.

[2] D. W. Stephan, *Energy Technology* **2013**, *1*, 777–777.

[3] N. S. Lewis, D. G. Nocera, *Proc. Natl. Acad. Sci.* **2006**, *103*, 15729–15735.

[4] E. S. Andreiadis, M. Chavarot-Kerlidou, M. Fontecave, V. Artero, *Photochem. Photobiol* **2011**, *87*, 946–964.

[5] S. Campagna, F. Puntoriero, F. Nastasi, G. Bergamini, V. Balzani, *Photochemistry and Photophysics of Coordination Compounds: Ruthenium*, *Vol. 280*, Springer Berlin Heidelberg, **2007**, pp. 117–214.

[6] I. M. Dixon, E. Lebon, P. Sutra, A. Igau, *Chem. Soc. Rev.* **2009**, *38*, 1621–1634.

[7] P. Ceroni, *The Exploration of Supramolecular Systems and Nanostructures by Photochemical Techniques*.

[8] A. Juris, V. Balzani, F. Barigelletti, S. Campagna, P. Belser, A. von Zelewsky, *Coord. Chem. Rev* **1988**, *84*, 85 – 277.

[9] T. Forster, *Discuss. Faraday Soc.* **1959**, *27*, 7–17.

[10] D. L. Dexter, *J. Chem. Phys.* **1953**, *21*, 836–850.

[11] L. D. Cola, P. Belser, *Coord. Chem. Rev.* **1998**, *177*, 301 – 346.

[12] J.-P. Launay, *Chem. Soc. Rev.* **2001**, *30*, 386–397.

[13] B. Schlicke, P. Belser, L. De Cola, E. Sabbioni, V. Balzani, *J. Am. Chem. Soc.* **1999**, *121*, 4207–4214.

[14] S. Welter, N. Salluce, P. Belser, M. Groeneveld, L. D. Cola, *Coord. Chem. Rev.* **2005**, *249*, 1360 – 1371.

[15] F. S. C. Chiorboli, M. T. Indelli, *Photoinduced Electron/Energy Transfer Across Molecular Bridges in Binuclear Metal Complexes*.

[16] J. Lombard, R. Boulaouche, D. A. Jose, J. Chauvin, M.-N. Collomb, A. Deronzier, *Inorg. Chim. Acta* **2010**, *363*, 234 – 242.

[17] J. Lombard, D. A. Jose, C. E. Castillo, R. Pansu, J. Chauvin, A. Deronzier, M.-N. Collomb, *J. Mater. Chem. C* **2014**, *2*, 9824–9835.

[18] S. Welter, F. Lafolet, E. Cecchetto, F. Vergeer, L. De Cola, *ChemPhysChem* **2005**, *6*, 2417–2427.

[19] J. L. Brennan, T. E. Keyes, R. J. Forster, *Langmuir* **2006**, *22*, 10754–10761.

[20] J. Kroon, J. W. Verhoeven, M. N. Paddon-Row, A. M. Oliver, *Angew. Chem. Int. Ed.* **1991**, *30*, 1358–1361.

[21] A. Yoshimura, K. Nozaki, N. Ikeda, T. Ohno, *J. Am. Chem. Soc.* **1993**, *115*, 7521–7522.

[22] M. E. Walther, O. S. Wenger, *Inorg. Chem.* **2011**, *50*, 10901–10907.

[23] J. Hankache, O. S. Wenger, *Phys. Chem. Chem. Phys.* **2012**, *14*, 2685–2692.

[24] K. Murata, M. Araki, A. Inagaki, M. Akita, *Dalton Trans.* **2013**, *42*, 6989–7001.

[25] T. Klumpp, M. Linsenmann, S. L. Larson, B. R. Limoges, D. Bürssner, E. B. Krissinel, C. M. Elliott, U. E. Steiner, *J. Am. Chem. Soc.* **1999**, *121*, 1076–1087.

[26] O. Johansson, H. Wolpher, M. Borgstrom, L. Hammarstrom, J. Bergquist, L. Sun, B. Akermark, *Chem. Commun.* **2004**.

[27] M. Borgström, O. Johansson, R. Lomoth, H. B. Baudin, S. Wallin, L. Sun, B. Åkermark, L. Hammarström, *Inorg. Chem.* **2003**, *42*, 5173–5184.

[28] J. Hankache, O. S. Wenger, *Chem. Commun.* **2011**, *47*, 10145–10147.

[29] K. Yamada, N. Kobayashi, K. Ikeda, R. Hirohashi, M. Kaneko, *Jpn. J. Appl. Phys.* **1994**, *33*, L544.

[30] C. J. Kleverlaan, M. T. Indelli, C. A. Bignozzi, L. Pavanin, F. Scandola, G. M. Hasselman, G. J. Meyer, *J. Am. Chem. Soc.* **2000**, *122*, 2840–2849.

[31] B. V. Bergeron, C. A. Kelly, G. J. Meyer, *Langmuir* **2003**, *19*, 8389–8394.

[32] J. H. M. Ortiz, C. Longo, N. E. Katz, *Inorg. Chem. Commun.* **2015**, *55*, 69 – 72.

[33] W. J. Youngblood, S.-H. A. Lee, Y. Kobayashi, E. A. Hernandez-Pagan, P. G. Hoertz, T. A. Moore, A. L. Moore, D. Gust, T. E. Mallouk, *J. Am. Chem. Soc.* **2009**, *131*, 926–927.

[34] Z. Ji, M. He, Z. Huang, U. Ozkan, Y. Wu, *J. Am. Chem. Soc.* **2013**, *135*, 11696–11699.

[35] W. Hamd, M. Chavarot-Kerlidou, J. Fize, G. Muller, A. Leyris, M. Matheron, E. Courtin, M. Fontecave, C. Sanchez, V. Artero, C. Laberty-Robert, *J. Mater. Chem. A* **2013**, *1*, 8217–8225.

[36] T. Fushimi, A. Oda, H. Ohkita, S. Ito, *Langmuir* **2005**, *21*, 1584–1589.

[37] N. Terasaki, T. Akiyama, S. Yamada, *Langmuir* **2002**, *18*, 8666–8671.

[38] D. L. Ashford, W. Song, J. J. Concepcion, C. R. K. Glasson, M. K. Brennaman, M. R. Norris, Z. Fang, J. L. Templeton, T. J. Meyer, *J. Am. Chem. Soc.* **2012**, *134*, 19189–19198.

Trimetallic Complexes

Résumé:

L'incorporation de complexes de métaux de transition dans des systèmes à séparation de charges photoinduite présente de nombreux avantages. En effet, ces complexes peuvent posséder différents états rédox et magnétiques, mais aussi offrent une plus grande stabilité que des sous-unités purement organiques. Notre choix s'est porté sur des complexes bis-terpyridiniques de fer(II) et de cobalt(II)/(III) associées à un photosensibilisateur de type $[Ru(bpy)_3]^{2+}$.

Dans ce chapitre, nous décrivons la synthèse des briques de base qui seront utilisées dans le reste du manuscrit. Nous avons réalisé la synthèse de différents complexes construits sur un cœur $[Ru(bpy)_3]^{2+}$. Les différents complexes portent une bipyridine qui est mono ou difonctionalisée en position 5 et 5' par un substituant terpyridinyl. Les complexes varient également de par la nature du lien entre la partie photoactive et le tridentate. Ces liens peuvent être des fonctions amide, éther, ou bien un pont phénylène.

Le lien amide provoque une diminution significative de la luminescence du complexe de Ru et le lien éther influence légèrement les propriétés photophysiques du fait des degrés de liberté qu'il apporte. Le pont phénylène quant à lui conserve l'identité spectrale de l'archétype $[Ru(bpy)_3]^{2+}$.

Nous avons construit des complexes trinucléaires contenant du fer(II) ou du cobalt(II)/(III) liés a deux unités Ru(II) par un pont éther. Ces complexes, de type $[Ru\text{-}Fe\text{-}Ru]^{6+}$ et $[Ru\text{-}Co\text{-}Ru]^{6+/7+}$ ont été entièrement caractérisés et leurs propriétés électrochimiques et photophysiques ont été particulièrement étudiées.

Il a été démontré qun transfert d'énergie efficace vers l'unité $[Fe(tpy)_2]^{2+}$ est responsable de la désactivation rapide de l'état excité du Ru. Ce transfert d'énergie peut toutefois être court-circuité en présence d'un accepteur d'électron sacrificiel. Dans ces conditions, le Fe^{2+} s'avère être un bon donneur d'électron envers le Ru^{3+} photogénéré. La sous-unité Co^{3+} s'est révélée être un accepteur d'électron idéal pour $[Ru(bpy)_3]^{2+*}$.

CHAPTER 1

TRIMETALLIC COMPLEXES

1.1 Introduction

As stated in the **General Introduction**, a large number of photo-active di, tri and tetra-nuclear assemblies based on $[Ru(bpy)_3]^{2+}$ were reported in the literature.[1;2] Considerable attention has been paid to study the nature of the quenching processes in these systems (energy and/or electron transfer). In this chapter we will launch a fundamental investigation about the nature and efficiency of the quenching between $[Ru(bpy)_3]^{2+*}$ and the terpyridyl complexes of $Co^{3+/2+}$ and Fe^{2+}. Our original motivation to study terpyridine based systems developed from the ease of accessing differently functionalized derivatives as well as their capacity of attaining linear, symmetrical and achiral complexes (provided that the substitution is the same on the 4' position of both terpyridines) with a large array of transition metals in the periodic table. Nonetheless, the chosen metals belong to the 1^{st} row series which are known for their lability. This means that the terpyridyl complexes of the previously stated metals are in a continuous ligand exchange process in solution. This makes it difficult, or even impossible to isolate the heteroleptic form (a complex which contains at least two different ligands). Although the quenching pathway could be assessed inter-molecularly in a mixture of both entities, it remains more informative and efficient to build covalently linked assemblies holding both the $[Ru(bpy)_3]^{2+}$ and the $[M(tpy)_2]^{2+/3+}$ together. This will thus require introducing two chromophoric units on the two respective terpyridine ligands of the central metal generating an assembly of the formula Ru-M-Ru. Indeed, examples based on terpyridine transition metal complexes with the formula of Ru-M-Ru have grabbed particular interest. In such architectures the nature of the bridge plays an inherent role in the kinetics of the quenching of the excited state of Ru, since the bridge imposes the distance and controls the electronic communication between the different compartments. The bridge in such applications should bear several fundamental characteristics,

some of which are:

1. Redox innocent: Non-oxidizable/reducible by the excited state of the chromophore.
2. Rigid: To ensure a fixed distance between the different compartments and prevent undesired deactivation pathways.
3. Non-conjugated: In order to conserve the electronic properties of each entity.

It is always important to assess the advances made in the literature before introducing new systems. This is why I will briefly describe tri-nuclear complexes bearing heteroditopic ligands based upon $[Ru(bpy)_3]^{2+}$ and $[M(tpy)_2]^{2+/3+}$.

Constable et al. described the first system where the metal binding domains are linked with a C- C single bond which in principle allows free rotation and leads to potentially maximum conjugation of the two components **figure 1.1**.[3] In this article, the authors argue that in hetero-metallic systems examining just the electrochemical data might be misleading in evaluating the communication between the different metallic centers. For instance, they were not able to detect an electronic communication between the metallic centers at the ground state (in cyclic voltammetry), and this was attributed to the interruption of the conjugation by the well-established non-planar conformation observed for adjacent phenyl or pyridine rings. However, they showed evidence of a strong electronic communication between the bipyridine and the terpyridine components of the bridging ligand based on the spectroscopic data, which indicates that this bridge facilitates energy transfer in the excited state between the metal centers.

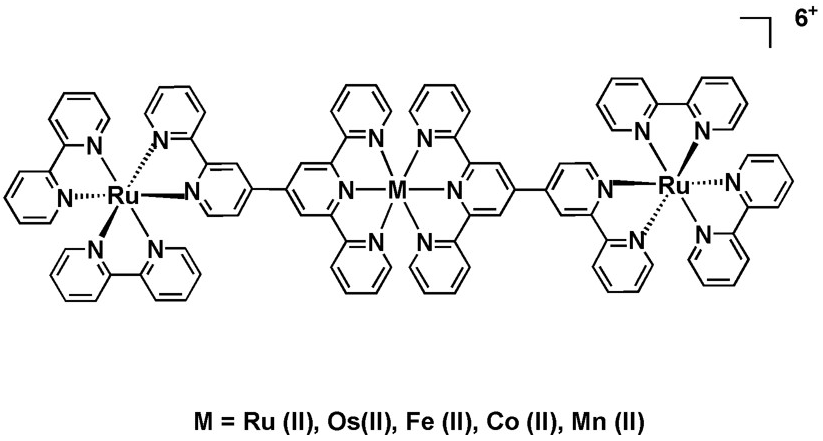

Figure 1.1: Hetero-tri-nuclear complexes with back to back bpy-tpy ligands

The same group reported a different class of trimetallic complexes which is typified by the linkage of the two metal-binding domains by a single oxygen atom, giving a greater degree of conformational freedom at the expense of conjugation of the subunits **figure 1.2**.[4] The authors

briefly described these systems and stated that there is no significant difference when compared to the previous series, with no details about the nature of the quenching between the different metallic centers.

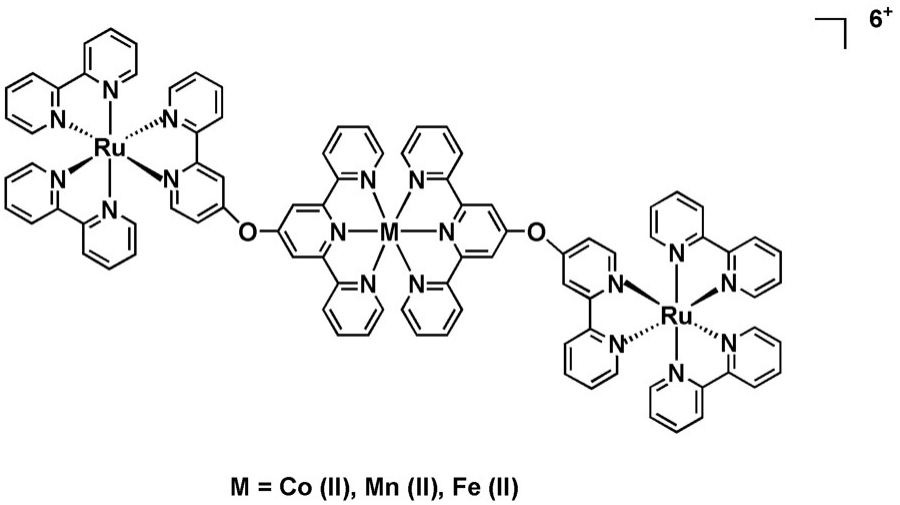

Figure 1.2: Hetero-tri-nuclear complexes with ether linkages

Simultaneously, similar systems were described with the different subunits being held together by the aid of amide bonds **figure 1.3**.[5] The reported hetero-metallic complexes are based on a combination of $[Ru(bpy)_3]^{2+}$ and either $[Fe(tpy)_2]^{2+}$ or $[Mn(tpy)_2]^{2+}$ while the high valent oxidized species of the latter are used to mimic the photosynthetic machinery for the oxidation of water. In these examples, the nature of quenching was attributed to energy or electron transfer without elaboration.

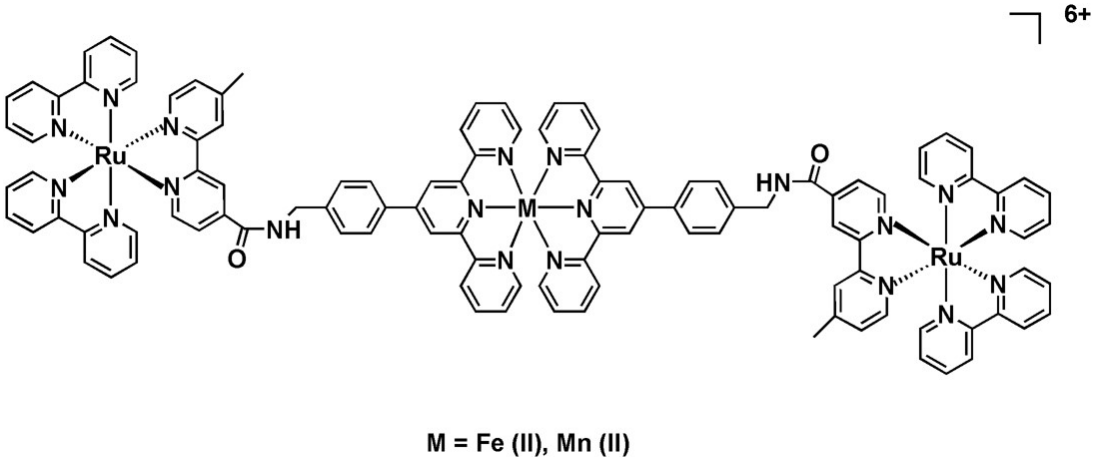

Figure 1.3: Hetero-tri-nuclear complexes based on amide bridges

Our group has done some pioneering work in this field, and the electrochemical, photophysical and photochemical behaviors were thoroughly investigated in systems based on the assembly of a $[Ru(bpy)_3]^{2+}$ photosensitizer to the terpyridyl complexes of $[Fe(tpy)_2]^{2+}$, $[Co(tpy)_2]^{2+}$

and $[Mn(tpy)_2]^{2+}$ **figure 1.4**.[6–8] In these examples, the different subunits are connected *via* ethyl bridges which are introduced at the 4 position of the bipyridine in order to break the conjugation, and hence minimize the electronic communication between the different metallic centers. Although these ethyl bridges give a degree of flexibility to the system, they are short enough in order to ensure a fixed distance to a certain extent. In a series of publications, the quenching pathway of several terpyridyl metallic complexes were assigned as follow: energy transfer in case of $[Fe(tpy)_2]^{2+}$, electron and energy transfer for $[Co(tpy)_2]^{2+}$, electron transfer for $[Co(tpy)_2]^{3+}$ and $[Mn(tpy)_2]^{2+}$.

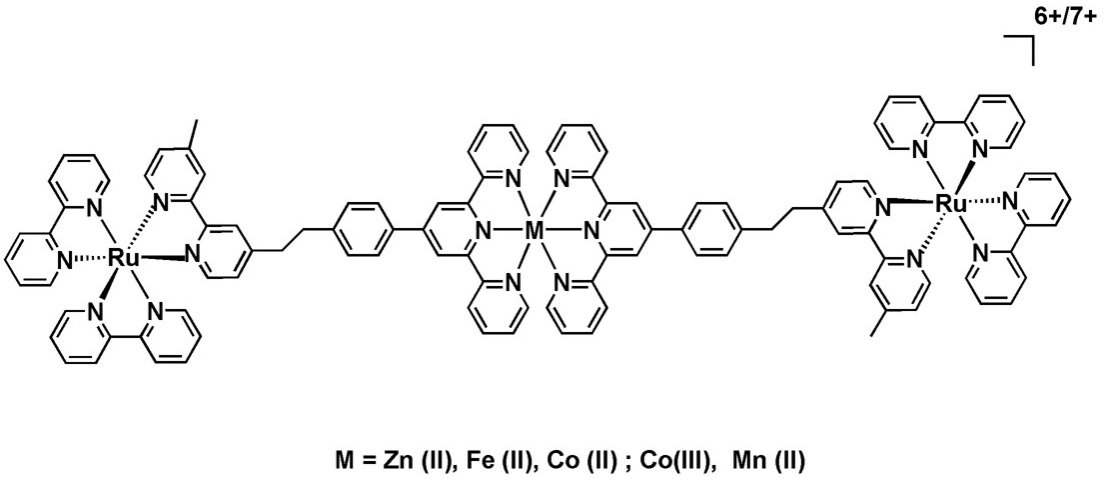

Figure 1.4: Hetero-tri-nuclear complexes with ethyl bridges

Our objectives are to further investigate the influence of the position and nature of the bridge on the communication between the $[Ru(bpy)_3]^{2+*}$ with the different terpyridyl complexes of $Co^{3+/2+}$ and Fe^{2+}. Eventually, this will give insight on the possibility of incorporating the previously mentioned subunits in a D-P-A assembly. This motivated us to functionalize a $[Ru(bpy)_3]^{2+}$, with either one or two terpyridines in order to get access to the different assemblies. In such, three types of linkages (amides, ethers and phenylene) were employed between the photoactive spacer and the pending terpyridine arm affording five ditopic ligands **figure 1.5**. Herein, we will present the synthesis and characterization of all the functionalized Ru moeities which will be used in the rest of the manuscript. Moreover, we will also detail the construction of the trimetallic complexes of the formula Ru-M-Ru using the $[Ru(bpy)_2(bpy\text{-}O\text{-}tpy)]^{2+}$. The latter complexes will be used in order to asses the photochemical quenching of the $[Ru(bpy)_3]^{2+*}$ counterpart by $[Fe(tpy)_3]^{2+}$ and $[Co(tpy)_3]^{3+}$ complexes.

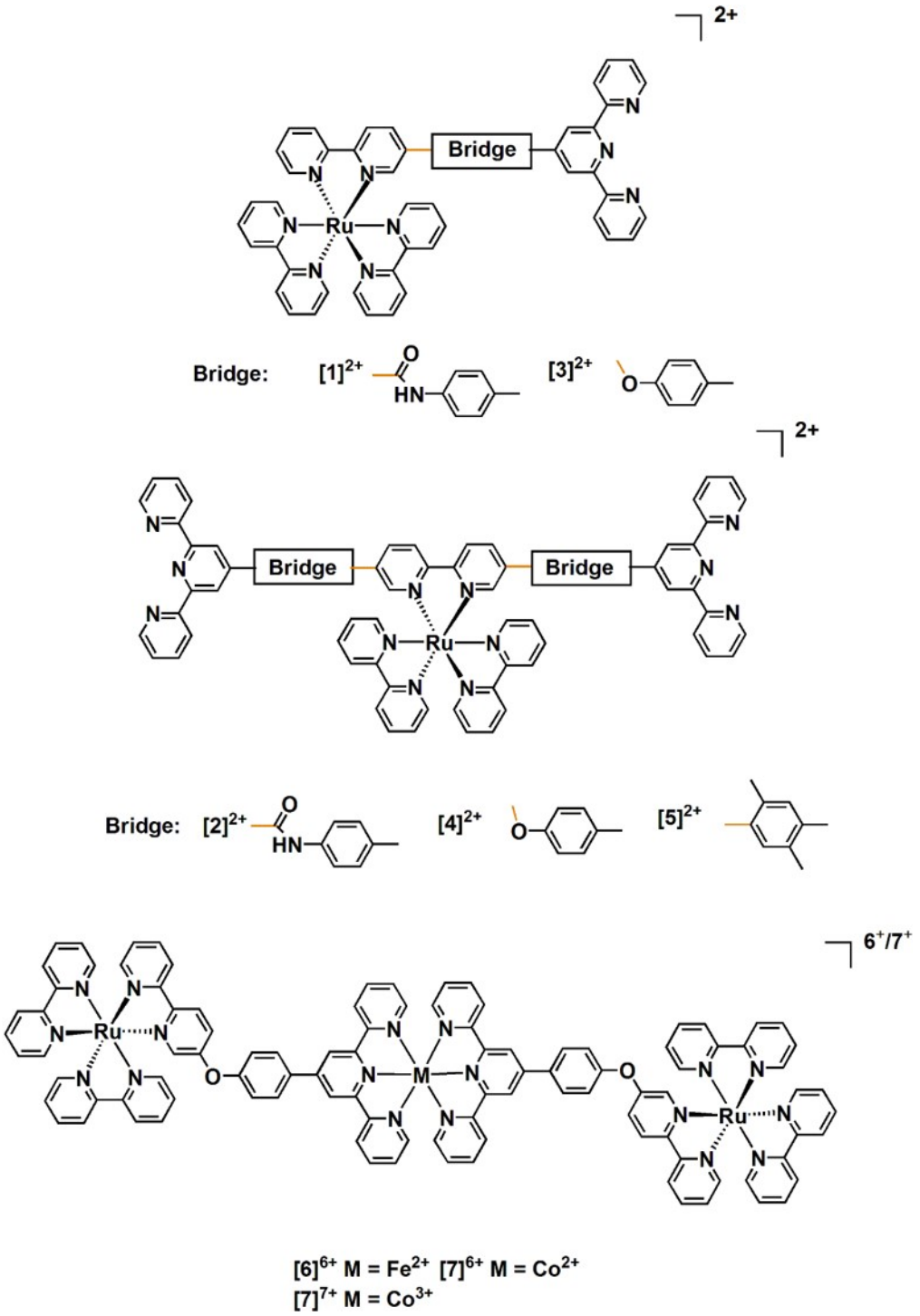

Figure 1.5: Schematic drawing of the target compounds.

1.2 Hetero - Ditopic Ligands Based Upon $[Ru(bpy)_3]^{2+}$

1.2.1 Synthesis

Five ditopic metallo ligands (**[1]**$^{2+}$**, [2]**$^{2+}$**, [3]**$^{2+}$**, [4]**$^{2+}$ and **[5]**$^{2+}$) were synthesized holding bipyridine and terpyridine motifs **figure 1.5**. The metallo ligands are based on a $[Ru(bpy)_3]^{2+}$ core and differ by the number of attached terpyridine and nature of the linker between the bipyridine and terpyridine motifs. Throughout this chapter they will be denoted by Ru-linker-tpy and Ru-(linker-tpy)$_2$ for mono and di-substituted complexes respectively as shown in **table 1.1**.

Table 1.1: Abbreviations of the different metallo ligands

Linker \ Nbr of tpy	One	Two
	Ru-NHCO-tpy **[1]**$^{2+}$	Ru-(NHCO-tpy)$_2$ **[2]**$^{2+}$
	Ru-O-tpy **[3]**$^{2+}$	Ru-(O-tpy)$_2$ **[4]**$^{2+}$
	-	Ru-(ϕ-tpy)$_2$ **[5]**$^{2+}$

All chosen bridges are selected in order to afford a compromise between rigidity, conjugation and linearity. To obtain linear assemblies with a maximal distance attained between respective terpyridines in di-substituted complexes, the bridges are introduced at the 5 and 5' position of the same bipyridine. In all the chemistry reported in this thesis we utilize kinetically inert ruthenium(II) complexes, both as reaction scaffolds and as target molecules due to synthetic necessity. This will thus require introducing suitable functionalities on both the $[Ru(bpy)_3]^{2+}$ and the terpyridine.

The starting compounds of the ruthenium complexes contain two un-substituted bipyridine units and one mono/bis functionalized bipyridine at the 5 or 5 and 5' position with either a carboxylic acid or a bromine. These precursors have the molecular formula of $[Ru(bpy)_2(bpy\text{-}COOH)]^{2+}$, $[Ru(bpy)_2(bpy\text{-}(COOH)_2)]^{2+}$, $[Ru(bpy)_2(bpy\text{-}Br)]^{2+}$ and $[Ru(bpy)_2(bpy\text{-}(Br)_2)]^{2+}$ and are denoted by complexes **[9]**$^{2+}$, **[11]**$^{2+}$, **[13]**$^{2+}$ and **[15]**$^{2+}$ respectively **figure 1.6**. These targets were prepared according to previously reported methods,[9;10] where the carboxylic acid is obtained by the oxidation of the 5-methyl-2,2'-bipyridine or the 5,5'-dimethyl-2,2'bipyridine, while the bromines are introduced *via* a Stille coupling reaction. The desired compounds where then obtained with almost quantitative yields by complexing the latter bipyridines with the precursor $[Ru(bpy)_2(Cl)_2].2H_2O$ in ethylene glycol while heating at 120 °C.

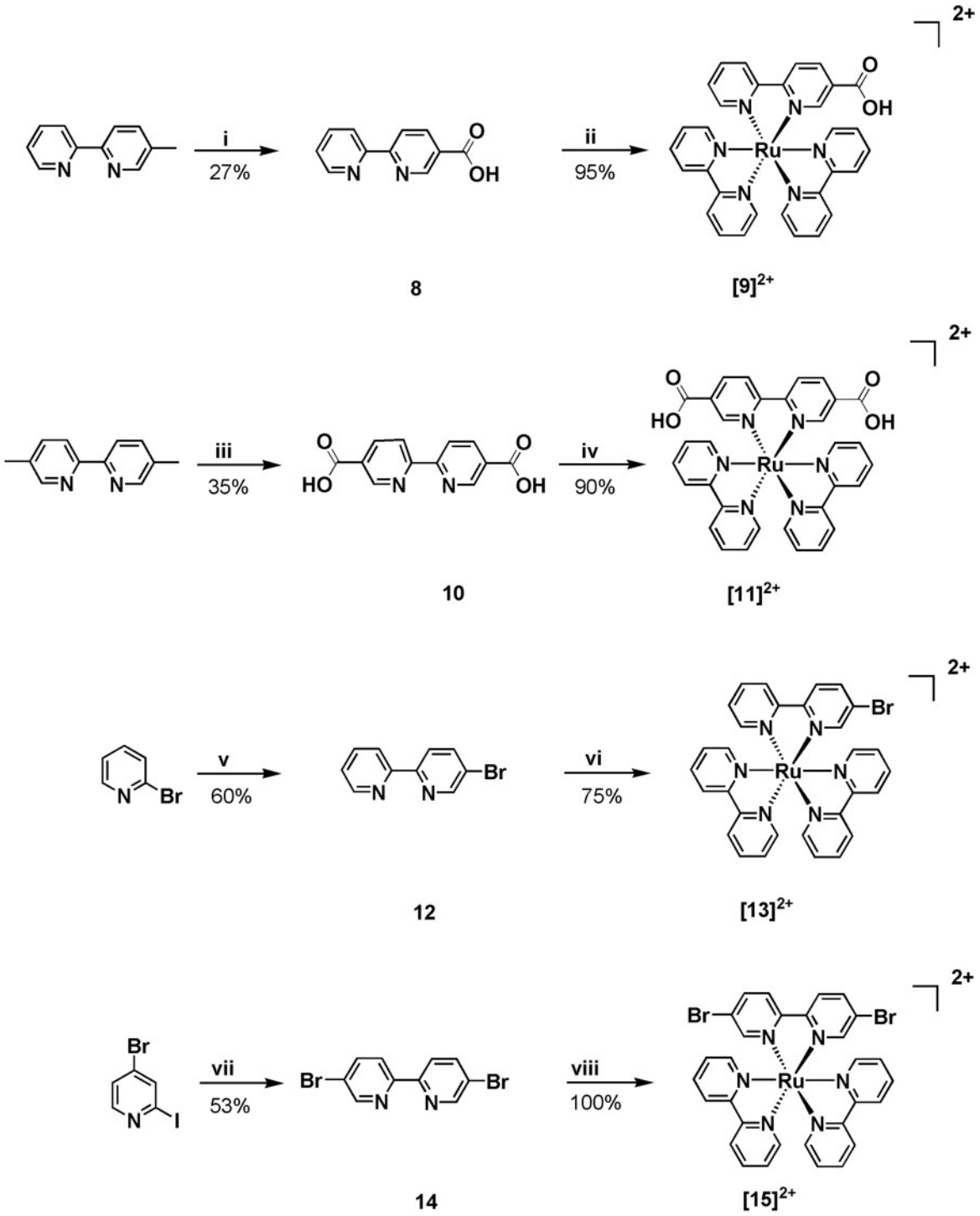

Figure 1.6: Functionalization of the $[Ru(bpy)_3]^{2+}$, (i) $KMnO_4$, H_2O, 48 h, 100 °C, HCl; (ii) $[Ru(bpy)_2(Cl)_2]$, ethylene glycol, 2 h, 120 °C, NH_4PF_6; (iii) $KMnO_4$, H_2O, 48 h, 100 °C, HCl; (iv) $[Ru(bpy)_2(Cl)_2]$, ethylene glycol, 2 h, 120 °C, NH_4PF_6; (v) *n*BuLi, diethylether, 2 h , -78 °C/Me_3SnCl, 10 h, 25 °C/ 4-bromo-2-iodopyridine, $[Pd(PP_3)_4]$, toluene, 24 h, 120 °C; (vi) $[Ru(bpy)_2(Cl)_2]$, ethylene glycol, 2 h, 120 °C, KPF_6; (vii) $(Sn(Bu)_3)_2$, $[Pd(PPh_3)_4]$, toluene, 24 h, 120 °C; (viii) $[Ru(bpy)_2(Cl)_2]$, ethylene glycol, 2 h, 120 °C, KPF_6

Three different classes of terpyridines were prepared containing aniline, bromophenyl and phenol groups namely ligand **17, 19** and **20** respectively **figure 1.7**. The synthesis was achieved

by a conventional Hantsch condensation reaction between two equivalents of 2-acetylpyridine and one equivalent of a functionalized aldehyde in the presence of NH_4OH.[11] For compound **17** the synthesis was not straightforward and passed by the acetylated intermediate which was then hydrolyzed to the desired amine for synthetic ease. Compound **19** also required two steps, by which a phenylene spacer bearing a bromine is firstly introduced on the terpyridine, followed by a Suzuki coupling reaction to afford the boronic ester.

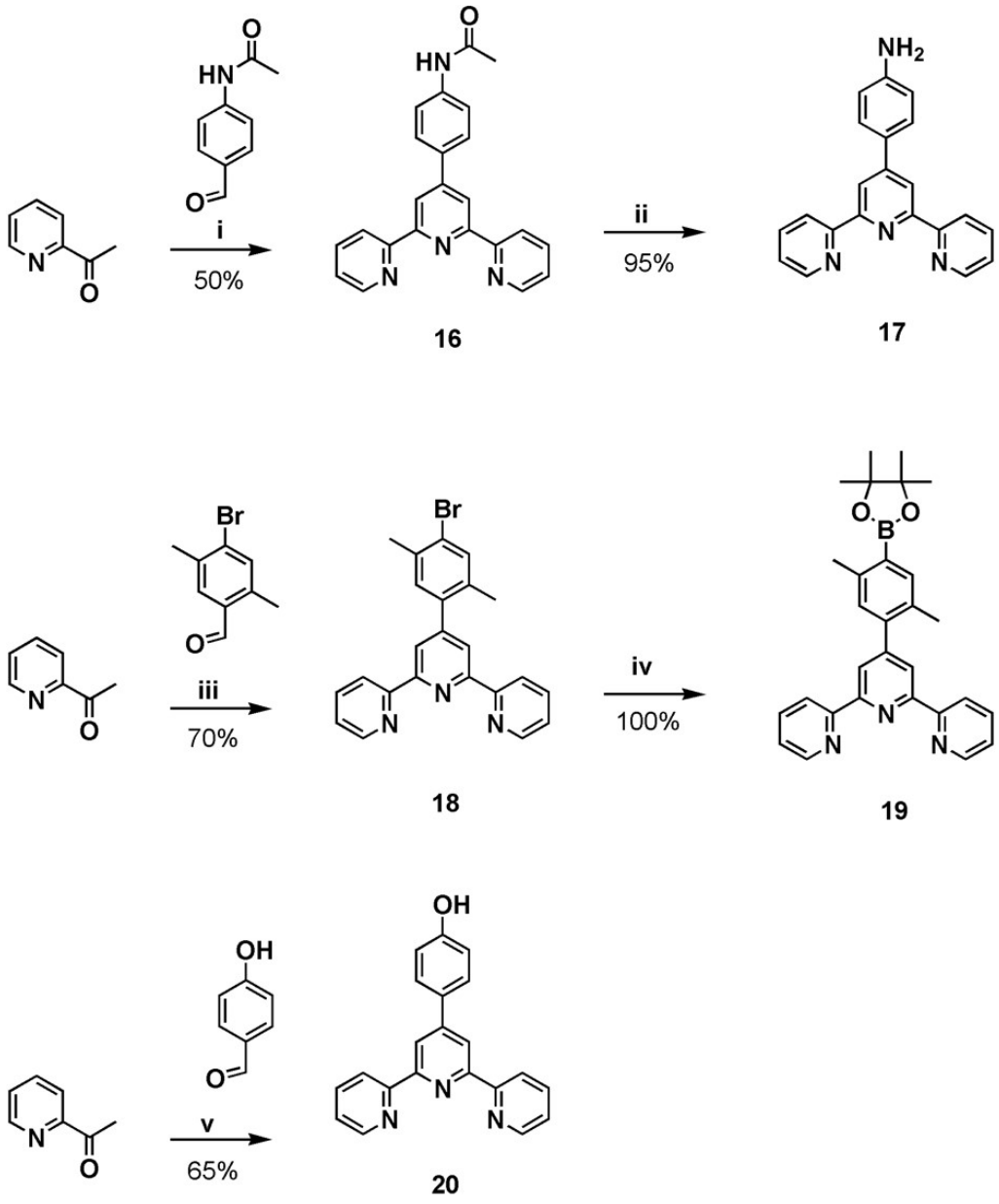

Figure 1.7: Functionalization of terpyridine, (i) NH_4OH, KOH, MeOH, 24 h, 65 °C; (ii) HCl:H_2O (1:1), 84 h, 100 °C, NaOH; (iii) NH_4OH, KOH, MeOH, 24 h, 65 °C; (iv) Bis(pinacolato)diboron, KOAc, [Pd(dppf)$(Cl)_2$], DMSO, 24 h, 80 °C; (v) NH_4OH, KOH, MeOH, 24 h, 65 °C

Final ditopic complexes are isolated by reacting the appropriate Ru and terpyridine precursors as demonstrated in **figure 1.8**.

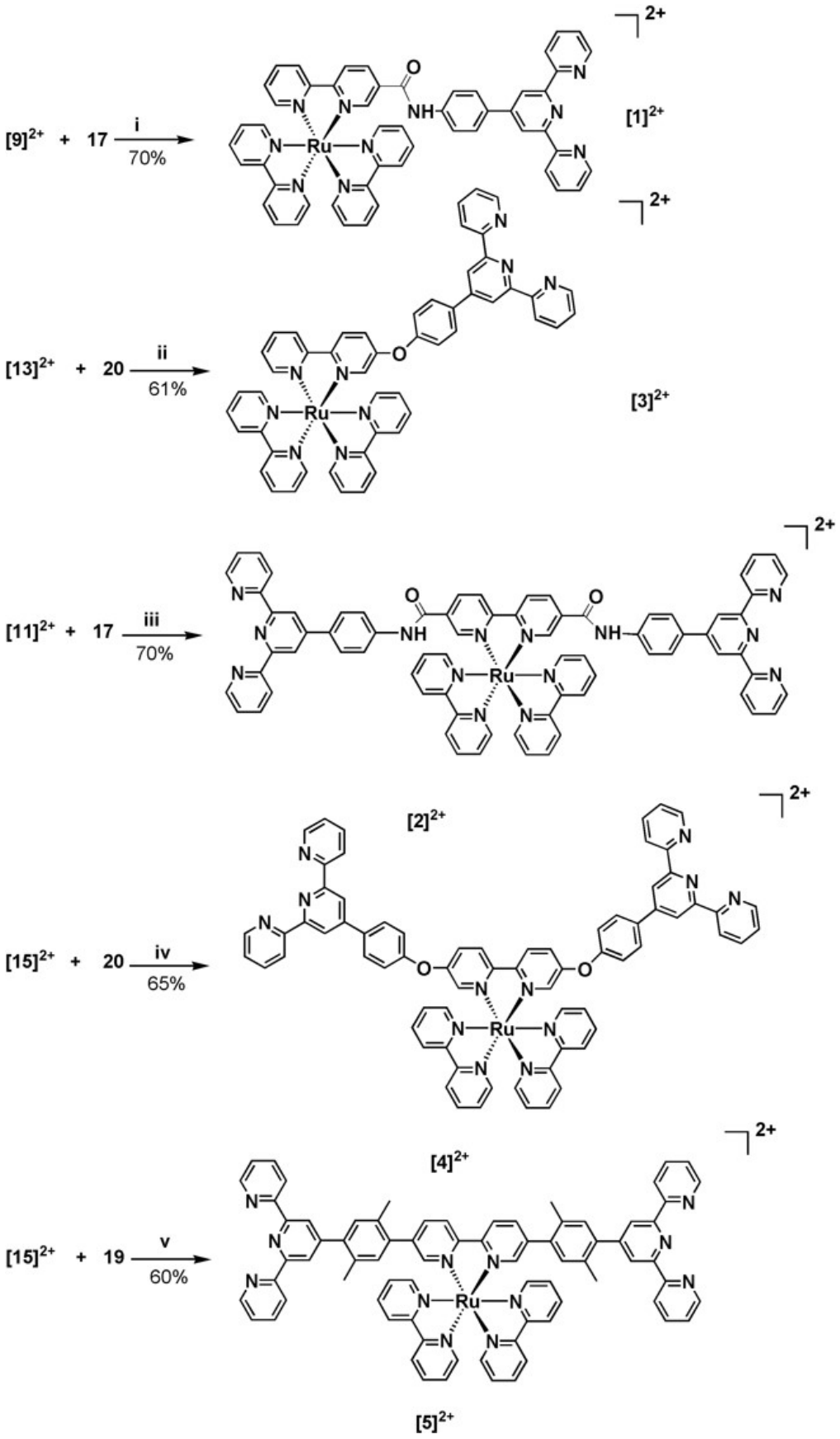

Figure 1.8: Synthesis of the ditopic ligands, (i) (iii) $SOCl_2$, 5 h, 75 °C, Ar /CH_3CN, 24 h, 80 °C, Ar; (ii) (iv) K_2CO_3, CH_3CN, 24 h, 80 °C; (v) K_2CO_3, $[Pd(PPh_3)_4]$, DMF, 24 h, 100 °C

It is noteworthy to state that the monosubstituted Ru precursor is used in order to introduce one terpyridine unit, whereas the di-substitued is used to introduce two terpyridines. Compounds **[1]**$^{2+}$ and **[2]**$^{2+}$ were obtained by generating the acyl chloride in situ from **[9]**$^{2+}$ and **[11]**$^{2+}$ followed by nucleophillic attack from the terpyridine-aniline **17**. No additional base is required because the latter terpyridine is basic enough in order to neutralize the generated HCl. As for compounds [**3**]$^{2+}$ and **[4]**$^{2+}$, they are afforded by a clean Williamson substitution between the phenol-terpyridine **20** and the brominated ruthenium precursors **[13]**$^{2+}$ and **[15]**$^{2+}$. In these reactions, the presence of the $[Ru(bpy)_3]^{2+}$ decreases the electronic density of the Br-bpy, and makes it more electrophilic, which facilitates the displacement of the bromine by the terpyridine phenol.[4] Final compound **[5]**$^{2+}$ is the result of a Suzuki coupling between the bromo-terpyridine **19** and the ruthenium precursor **[15]**$^{2+}$. All the isolated compounds are in the form of PF_6 salt and were purified by column chromatography and fully characterized by ^{1}H NMR and mass spectroscopy MS.

1.2.2 Electrochemistry

The potentials of the different redox processes of complexes (**[1]**$^{2+}$; **[2]**$^{2+}$; **[3]**$^{2+}$; **[4]**$^{2+}$ and **[5]**$^{2+}$) are collected in **table 1.2**. In the cyclic voltammogram (CV) several peaks are recorded and are attributed to the oxidation of the metal center Ru^{3+}/Ru^{2+} in the positive region and the respective reduction of the bipyridine and terpyridine ligands in the negative region. The difference in potentials recorded among the different complexes are the result of the modifications introduced on the bipyridine motif, and hence the electronic adjustments employed by the different functional groups.

Table 1.2: Redox potentials of complexes (**[1]**$^{2+}$; **[2]**$^{2+}$; **[3]**$^{2+}$; **[4]**$^{2+}$ and **[5]**$^{2+}$) in a 10^{-3} M solution of deoxygenated CH_3CN + 0.1 M $[Bu_4N]PF_6$ at a scan rate 100 mV.s^{-1} using carbon vitreous disk (5 mm diameter). $E_{1/2}$ (V) = (E_{pa} + E_{pc})/2; ΔEp (mV) = E_{pc} - E_{pa} *vs.* $Ag/AgNO_3$ 0.01 M in CH_3CN, and L.C corresponds to ligand centered reduction process.

Complex	$E_{1/2}^{oxidation}$, V (ΔEp, mV)	$E_{1/2}$ *reductions*, V (ΔEp, mV)			
	Ru^{3+}/Ru^{2+}	L.C 1	L.C 2	L.C 3	L.C 4
$[Ru(bpy)_3]^{2+(a)}$	0.97 (60)	–1.60 (60)	–1.80 (60)	–2.07 (60)	-
$[1]^{2+}$	1.03 (100) $^{(b)}$	–1.31 (60)	–1.75 (80)	–1.98 (80)	–2.25 (240)$^{(c)}$
$[3]^{2+}$	1.01 (60)	–1.63 (60)	–1.85 (100)	–2.07 (60)	–2.36 (80)
$[2]^{2+}$	1.07 (100)$^{(b)}$	–1.18 (80)	–1.47 (140)	–1.83$^{(c)}$	-
$[4]^{2+}$	1.01 (60)	–1.63(60)	–1.77(60)	–2.09$^{(c)}$	-
$[5]^{2+}$	1.03 (60)	–1.51 (60)	–1.74 (80)	–2.03 (100)$^{(c)}$	-

^{a} These values were reported in the literature,[12] ^{b} This peak is irreversible. ^{c} This value cannot be accurately measured since the wave is strongly distorted by adsorption of the reduction product on the electrode surface.

The parent molecule $[Ru(bpy)_3]^{2+}$ has already been reported in the literature and exhibits a reversible oxidation wave at 0.97 V assigned to Ru^{3+}/Ru^{2+} oxidation process, and three successive reversible reductions at –1.6 , –1.8 and –2.07 V centered on the ligand.[12] It is assumed that the LUMOs in the polypyridine complexes mainly have a ligand character, which enables us to assign the reduction to a specific ligand (bipyridine in this case) rather than to the entire complex.[13].

Regarding complexes Ru-NHCO-tpy and Ru-$(NHCO\text{-}tpy)_2$ namely $\mathbf{[1]}^{2+}$ and $\mathbf{[2]}^{2+}$, the CVs are quite tricky to understand **figure 1.9**.

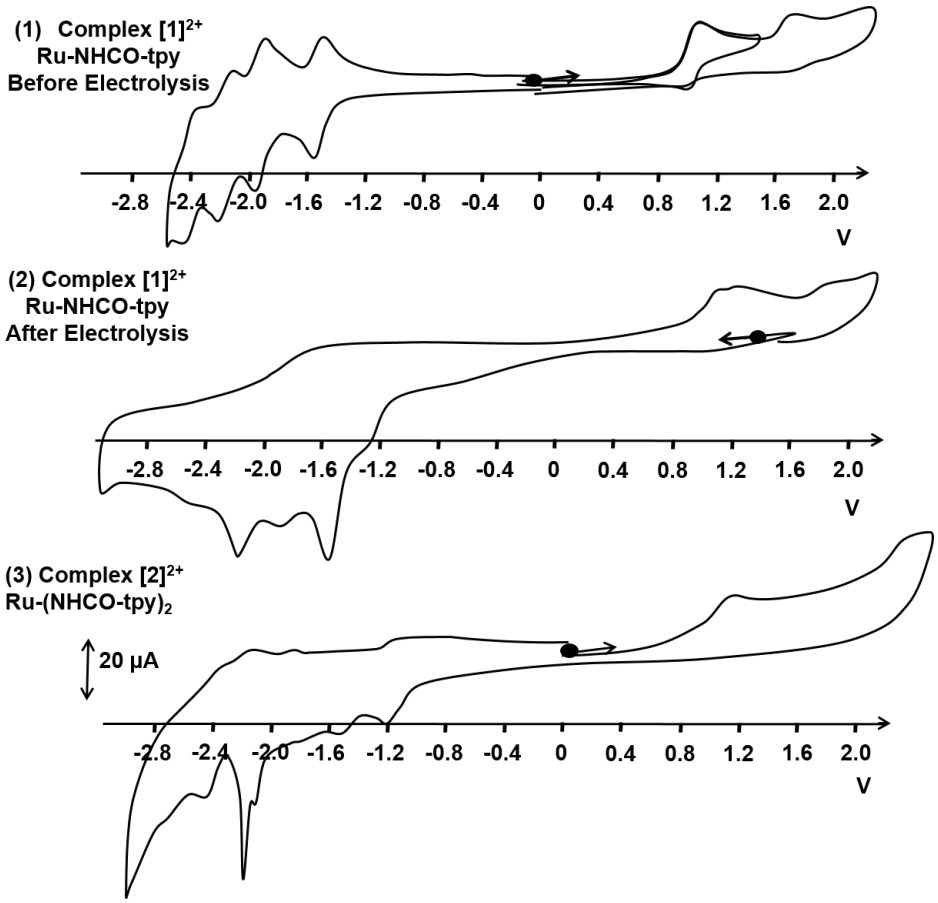

Figure 1.9: CV of modified ruthenium complexes in a 10^{-3} M solution CH_3CN + 0.1 M $[N(Bu)_4]PF_6$ using a glassy carbon electrode(5mm) at a scan rate 100 mV/s recorded *vs.* $Ag/AgNO_3$ (10^{-2} M); (1) Ru-NHCO-tpy before electrolysis; (2) Ru-NHCO-tpy after electrolysis carried out at 1.4 V; (3) Ru-$(NHCO\text{-}tpy)_2$

The electrochemical behavior in the positive region should be the result of the Ru^{3+}/Ru^{2+} oxidation process, which in principle should imply small variation of the value of the potentials with respect to the parent molecule $[Ru(bpy)_3]^{2+}$. Indeed, irreversible oxidations are recorded around 1.03 and 1.07 V for complexes Ru-NHCO-tpy and Ru-$(NHCO\text{-}tpy)_2$ respectively. These potentials lie in the same region as the metal centered oxidation of the unsubstituted parent molecule ($E_{1/2}$ = 0.97 V) with a 6 mV delay for complex $\mathbf{[1]}^{2+}$ due to the electron withdrawing

effect of the amide group, and a more significant delay (10 mV) in the presence of two amide groups in complex Ru-(NHCO-tpy)$_2$. Although the Ru centered oxidation process takes place in the correct region, the irreversibility of this process is puzzling. Thorough investigation of the oxidative region, shows the presence of a second irreversible oxidation (1.76 V) for complex Ru-NHCO-tpy **figure 1.9.1**. Exhaustive electrolysis at 1.4 V after the 1st oxidation peak, lead to the appearance of two peaks with potentials 1.08 and another around 1.3 V **figure 1.9.2**. This lead us to the suggestion, that initially two simultaneous oxidation processes were taking place around the same potential, and are most probably the superimposition of the Ru oxidation, and the oxidation of the nitrogen of the amide to generate the radical cation species. Considering that the metal centered oxidation should be reversible in nature, this will drive us to assume that the nitrogen oxidation is in fact responsible for this irreversible feature. It is also believed, that the second oxidation peak at 1.76 V, is also associated with the second oxidation of the nitrogen to generate the dication.

In the reductive part four quasi reversible reductive peaks appear for compound Ru-NHCO-tpy while that of Ru-(NHCO-tpy)$_2$ is highly deformed. The peak corresponding to **L.C.4**, present at a low potential, is a typical signature of the reduction process of a free terpyridine ligand. The three remaining peaks correspond to the reduction of the three bipyridine ligands on the complex. The presence of the amide functionality should affect the bipyridine domain by which it is directly connected to, more than the other two bipyridines. This should signify that two bipyridine reduction potentials should be slightly modified from those of [Ru(bpy)$_3$]$^{2+}$, and the potential of the bipyridine bearing the amide group should be modified majorly. As a matter of fact, the potentials of **L.C.2** and **L.C.3** are almost unaltered wheareas a significant shift of 29 mV and 42 mV is recorded for complexes Ru-NHCO-tpy and Ru-(NHCO-tpy)$_2$ respectively for **L.C.1**. This suggests that the modified bipyridine is reduced first and that the amide functionality lowers the potential of the LUMO due to its withdrawing effect, which prompts the complex easier to reduction.

Regarding complexes Ru-O-tpy, Ru-(O-tpy)$_2$ and Ru-(ϕ-tpy)$_2$ namely **[3]**$^{2+}$, **[4]**$^{2+}$ and **[5]**$^{2+}$ with ether and phenylene bridges, a nearly ideal behavior is observed in both the positive and the negative region **figure 1.10**. All complexes exhibit a reversible oxidation peak around 1 V which is similar to Ru oxidation in the parent molecule [Ru(bpy)$_3$]$^{2+}$. For the mono-substituted complex Ru-O-tpy, four monoelectronic processes are recorded in reduction. The peak at the negative potential –2.36 V can be easily attributed to the reduction of the free terpyridine. The remaining peaks can be assigned to the monoelectronic reduction of the different bipyridines. Since all the reductions are very similar to those of the unsubstituted complex, it is difficult to differentiate between the substituted and unsubstituted bipyridines. Complex Ru-(O-tpy)$_2$ exhibits a deformation of the third reduction peak and loss of the signal around –2.3 V. This could be probably caused by adsorption and protonation of the free terpyridine ligand. In the metallo ligand Ru-(ϕ-tpy)$_2$, **[5]**$^{2+}$, the Ru oxidation is almost unaltered, and the pattern

in the negative region is similar to that of Ru-(O-tpy)$_2$, **[4]**$^{2+}$. One important difference lies in the first reduction of the bipyridine which is shifted to higher potentials (90 mV) with respect to the parent molecules. This could be assigned to the bridging bipyridine-terpyridine domain, and could be explained by lowering the LUMO of the complex due to extended conjugation.

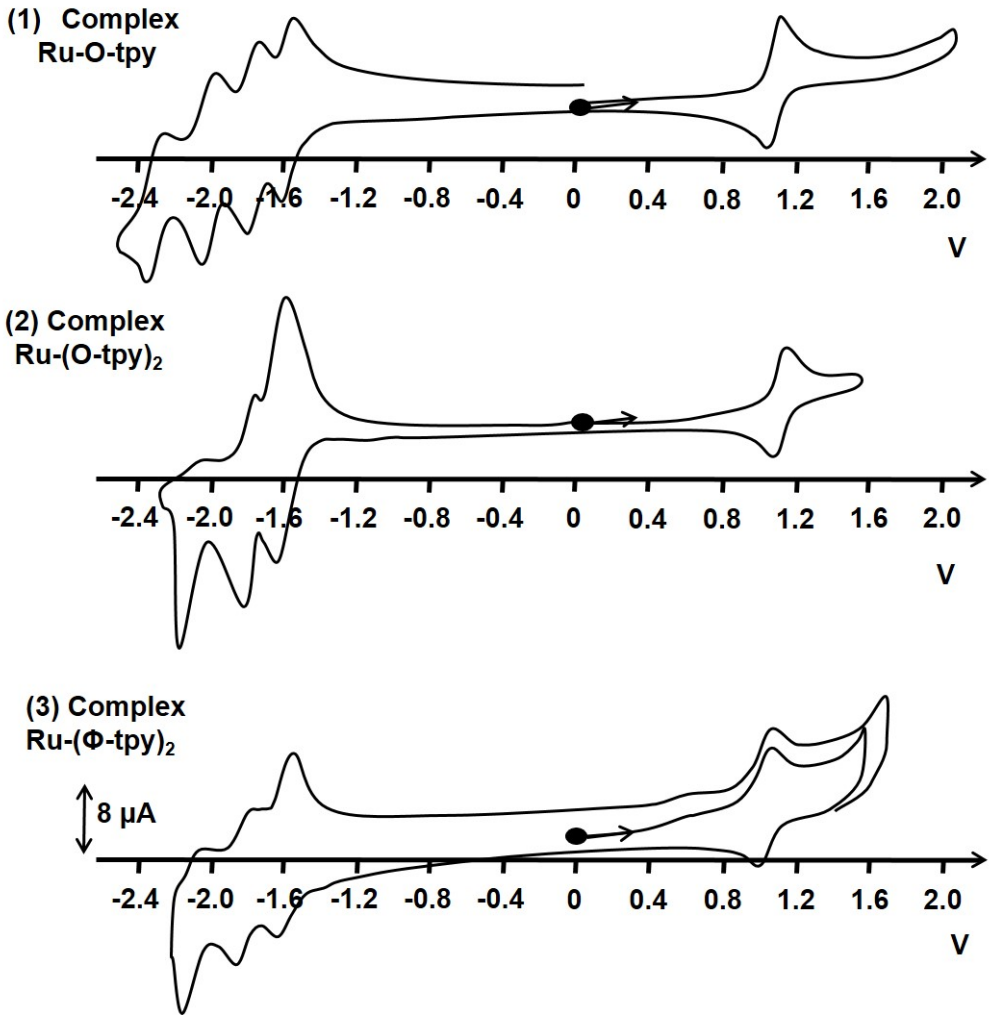

Figure 1.10: CV of modified ruthenium complexes in a 10^{-3} M solution CH_3CN + 0.1 M $[N(Bu)_4]PF_6$ using a glassy carbon electrode(5mm) at a scan rate 100 mV/s recorded *vs.* $Ag/AgNO_3$ (10^{-2} M); (1) Ru-O-tpy; (2) Ru-(O-tpy)$_2$; (3) Ru-(ϕ-tpy)$_2$

1.2.3 Photophysics

The absorption spectra of the synthesized complexes display the typical signatures of the unsubstituted parent molecule $[Ru(bpy)_3]^{2+}$ in the UV region at 280 nm (L.C transition π - π^*), 320 nm (M.C transition d - d) as well as in the visible region at 454 nm (MLCT transition d - π^*). However, there are slight detectable differences that distinguish the different complexes regarding the extinction coefficient and the maximum wavelength of absorbance (λ_{max}^{abs}) as shown in **figure 1.11** .

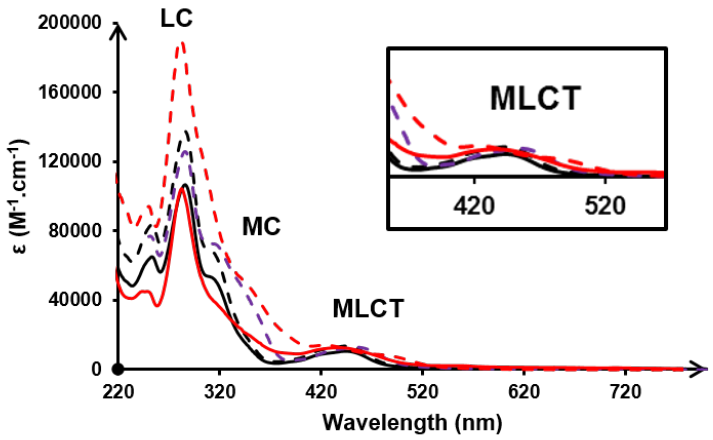

Figure 1.11: UV-vis spectra in CH_3CN of complexes Ru-NHCO-tpy full line red, Ru-(NHCO-tpy)$_2$ dashed red; Ru-O-tpy full line black; Ru-(NHCO-tpy)$_2$ dashed line black, Ru-(NHCO-tpy)$_2$ dashed line purple

These differences arise from the diverse electronic properties, and thus different distribution of energy levels, for every complex as dictated by the number of terpyridine ligands and the nature of bridge. Bis-substituted complexes Ru-(NHCO-tpy)$_2$, Ru-(O-tpy)$_2$ and Ru-(ϕ-tpy)$_2$ presented by dashed lines exhibit higher extinction coefficient at the level of the L.C transition with respect to the mono substituted complexes Ru-NHCO-tpy and Ru-O-tpy presented by full lines in **figure 1.11**. More importantly, there are interesting differences at the level of the MC and MLCT transitions. The MLCT band is slightly red shifted on going from complexes (Ru-O-tpy and Ru-(O-tpy)$_2$) with ether linkage, to (Ru-(ϕ-tpy)$_2$) with substituted phenylene spacer reaching complexes (Ru-NHCO-tpy and Ru-(NHCO-tpy)$_2$) with amide groups as shown in **table 1.3**. This move to lower energies is in a quantitative agreement with the electrochemically observed shift for the first reduction wave (L.C.1) representing the LUMO, accompanied with an unchanged HOMO as evidenced by the oxidation potentials which remain similar for the respective complexes. The LUMO which is centered on the ligand π^* orbitals is stabilized by the electron withdrawing effect of the amide groups in complexes (Ru-NHCO-tpy and Ru-(NHCO-tpy)$_2$), and a less important effect was observed for complex (Ru-(ϕ-tpy)$_2$) due to the extended conjugation of the phenylene ligands, while the presence of ether in (Ru-O-tpy and Ru-(O-tpy)$_2$) has little or no modification. This assumes that the redox potentials are equivalent to the spectroscopic orbitals.

The luminescence data are also collected in **table 1.3**. These values were recorded in CH_3CN solution at 25 °C by the excitation in the MLCT band around 450 $\mp$ 10 nm relative to the absorption spectrum of every complex. This excitation was followed by an emission close to that of $[Ru(bpy)_3]^{2+}$ around 611 nm. A red shift of this value is observed by going from complexes (Ru-O-tpy and Ru-(O-tpy)$_2$) to (Ru-(ϕ-tpy)$_2$) reaching Ru-NHCO-tpy and Ru-(NHCO-tpy)$_2$). Assuming that the ^{3}MLCT is the emitting state, the observed shift in emis-

sion is consistent with both the shift in the first reduction waves in the CV (representing the LUMO), and the shift in the ($\lambda_{absMLCT}$) evidenced in the absorption spectra. Both the quantum yield of emission ϕ_{em} and lifetime τ vary among different complexes. Complexes Ru-NHCO-tpy (τ = 308 ns; ϕ_{em} = 0.010) and Ru-(NHCO-tpy)$_2$ (τ = 68 ns; ϕ_{em} = 0.001) exhibit relatively low values when compared to those of [Ru(bpy)$_3$]$^{2+}$. This could be explained by an extra deactivation pathway of the excited state. The latter is most probably facilitated by the presence of the terpyridine ligands and amide bridges. As evidenced in the CV of these complexes, the oxidation of the amine in the bridge takes place at potentials which are close to that of the oxidation of the ruthenium. This could be one plausible hypothesis for the drop in both the lifetime and quantum efficiency. The magnitude of luminescence in complex Ru-O-tpy is higher than the previously stated complexes as depicted by both the lifetime values and quantum yield (τ = 527 ns; ϕ_{em} = 0.048). Yet, they are still inferior to that of the parent molecule. This could be attributed to the flexibility around the ether bond, which might represent an extra deactivation pathway of the excited state. This is confirmed by analyzing the photophysical data of complexes (Ru-(O-tpy)$_2$ and Ru-(ϕ-tpy)$_2$), by which the former Ru-(O-tpy)$_2$ shows a decrease in both lifetime and quantum yield (τ = 274 ns; ϕ_{em} = 0.037) due to higher flexibility in the system as imposed by the extra terpyridine and hence extra ether bond, while the latter (Ru-(ϕ-tpy)$_2$) demonstrates superior properties (τ = 1000 ns; ϕ_{em} = 0.058) similar to those of the unmodified ligand as governed by the more rigid structure.

Table 1.3: Collected photo-physical data for complexes Ru-NHCO-tpy, Ru-O-tpy, Ru-(NHCO-tpy)$_2$, Ru-(O-tpy)$_2$ and Ru-(ϕ-tpy)$_2$ in deoxygenated CH_3CN solution at 25 °C

Complexes	$\lambda_{absMLCT}$ (nm) ($M^{-1}.cm^{-1}$)	λ_{em} (nm)	Quantum yield ϕ_{em}	Lifetime τ (ns)
[Ru(bpy)$_3$]$^{2+(a)}$	452 (13 000)	611	0.058	890
Ru-NHCO-tpy	457 (13 000)	654	0.010	308
Ru-O-tpy	445 (11 000)	610	0.048	527
Ru-(NHCO-tpy)$_2$	460 (13 100)	695	0.001	68
Ru-(O-tpy)$_2$	445 (13 100)	610	0.037	264
Ru-(ϕ-tpy)$_2$	453 (12 900)	616	0.058	1000

[a] These valued are reported in the literature.[14]

1.3 Trimetallic Complexes [Ru(bpy)$_3$]-[Fe(tpy)$_2$]-[Ru(bpy)$_3$]

1.3.1 Synthesis

The described complex Ru-O-tpy is used for the construction of the different trinuclear assemblies. The $\{Ru(bpy)_2(bpy\text{-}O\text{-}tpy)_2Fe\}^{6+}$ **[6]**$^{6+}$ was synthesized by refluxing one molar equivalent of a $[Fe(H_2O)_6].2BF_4$ salt and two molar equivalents of the building block Ru-O-tpy in acetonitrile **figure 1.12**. The complex was then isolated as a hexafluorophosphate salt and purified by recrystallization from a mixture of CH_3CN : Et_2O. The purity of the complex was verified by NMR and electrochemistry.

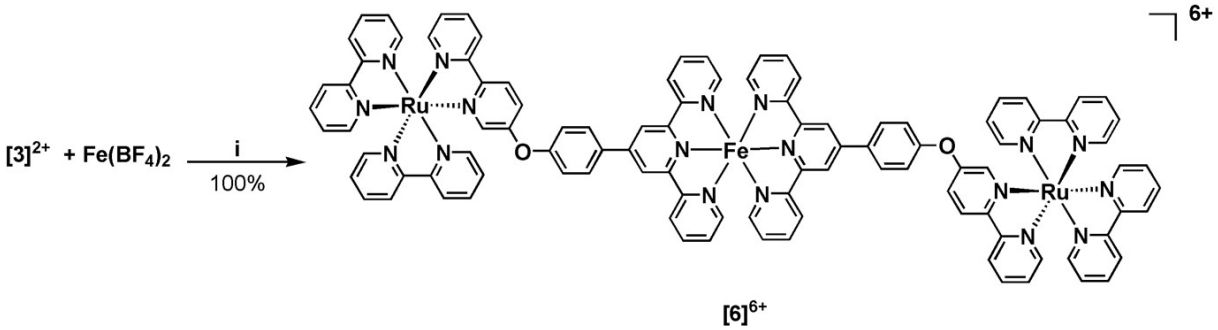

Figure 1.12: Synthesis of the trinuclear complex **[6]**$^{6+}$, (i) $[Fe(H_2O)_6].2BF_4$, CH_3CN, 1 h, 80 °C, KPF_6.

1.3.2 Spectro-electrochemistry

In this section we will discuss the electrochemical and spectroscopic (UV-Visible) behavior of the trimetallic complex **[6]**$^{6+}$. The signatures of Ru-O-tpy **[3]**$^{2+}$ are already discussed previously, and those of $[Fe(ttpy)_2]^{2+}$ have already been published.[7]

Table 1.4: UV-Visible absorption data in CH_3CN for complexes Ru-O-tpy, $[Fe(ttpy)_2]^{2+}$ and **[6]**$^{6+}$.

Complex	λ_{abs} (nm) ($M^{-1}.cm^{-1}$)	
	Ru^{II} MLCT	Fe^{II} MLCT
Ru-O-tpy	446 (13 250)	-
$[Fe(ttpy)_2]^{2+a}$	-	567 (25 900)
$[6]^{6+}$	449 (28 000)	569 (23 700)

[a] These values are reported in the literature in CH_3CN.[7]

The UV-Visible spectrum of **[6]**$^{6+}$ is essentially a superposition of the absorption spectra of

the individual molecular components Ru-O-tpy and $[Fe(ttpy)_2]^{2+}$ in proportion with stoichiometry, and as such are indicative of electronically weakly coupled systems, thanks to the ether linkage **table 1.4** and **figure 1.13**. This weak electronic coupling is also asserted in the CV.

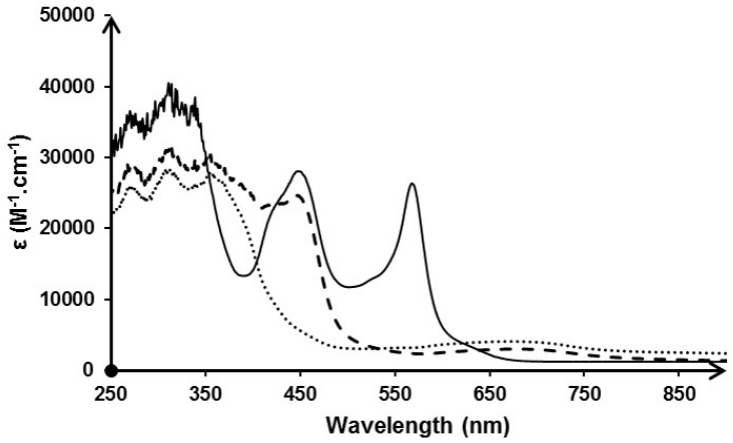

Figure 1.13: UV-Visible absorption of **[6]**$^{6+}$ in a solution of CH_3CN + 0.1 M $[Bu_4N]PF_6$ (l = 1 mm); Full line: Before electrolysis; Dashed line: after electrolysis at 0.9 V; Dotted Line: After electrolysis at 1.2 V.

Regarding the CV of **[6]**$^{6+}$ it is actually the superposition of the electroactivity of both parent subunits: Ru-O-tpy and $[Fe(ttpy)_2]^{2+}$ in their respective (2:1 Ru^{2+}/Fe^{2+}) ratio **table 1.5** and **figure 1.14**.

Table 1.5: Redox potentials of Ru-O-tpy, $[Fe(ttpy)_2]^{2+}$ and **[6]**$^{6+}$ in a 10^{-3} M solutions of CH_3CN + 0.1 M $[Bu_4N]PF_6$, the potentials ($E_{1/2}$, ΔE_p) values are reported *vs.* $Ag/AgNO_3$ (10^{-2} M) at scan rate = 100 mV/s using carbon vitreous disk (5 mm in diameter) as a working electrode.

Complex	$E_{1/2}^{oxidation}$, V (ΔEp, mV)		$E_{1/2}^{reductions}$, V (ΔEp, mV)		
	Ru^{3+}/Ru^{2+}	Fe^{3+}/Fe^{2+}	L.C 1	L.C 2	L.C 3
Ru-O-tpy	1.01 (60)	-	–1.58 (80)	–1.85 (100)	–2.07 (60)
$[Fe(ttpy)_2]^{2+b}$	-	0.76 (60)	–1.54 (60)	–1.65 (60)	–2.30 (90)
($[6]^{6+}$)	1.01 (60)	0.84 (80)	–1.47 (80)	–1.62 (80)	–1.8 (240)^a

^{a}This value cannot be accurately measured since the wave is strongly distorted by adsorption of the reduction product on the electrode surface. ^{b}These values are reported in the literature in CH_3CN + 0.05 M $[Bu_4N]PF_6$.[7]

In the positive region, two well separated reversible redox systems are observed $E_{1/2}$ = 0.84 and 1.01 V *vs.* $Ag/AgNO_3$ 10^{-2} M **figure 1.14**. The potentials of these systems are similar to

the mononuclear parents, allowing the unambiguous assignment of the first oxidative process to the Fe^{3+}/Fe^{2+} redox couple with a (80 mV) shift in the oxidation potential with respect to $[Fe(ttpy)_2]^{2+}]$ due to different electronic properties imposed by the ether bridge, and the more positive one to the Ru^{3+}/Ru^{2+} redox couple.

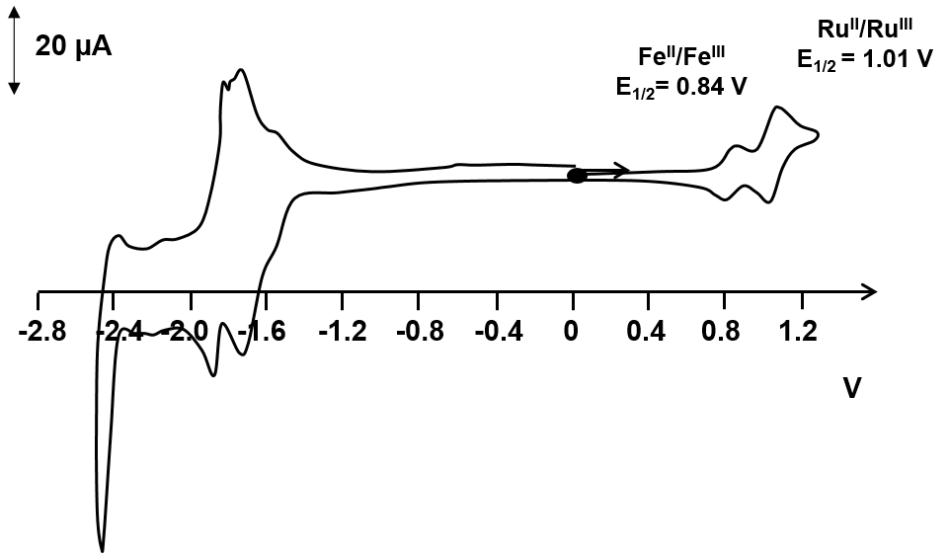

Figure 1.14: CV of **[6]**$^{6+}$ (10^{-3} M) in a solution of CH_3CN + 0.1 M $[Bu_4N]PF_6$, and the $E_{1/2}$ values are reported *vs* $Ag/AgNO_3$ (10^{-2} M) at scan rate = 100 mV/s using carbon vitreous disk (5 mm in diameter) as a working electrode

Moreover, the Rotating Disc Electrode (RDE) experiment confirms that the trinuclear complex is obtained in pure form and that no dissociation occurs in CH_3CN, since the height of the Ru^{3+}/Ru^{2+} wave is twice that of Fe^{3+}/Fe^{2+} , in accordance with the 2:1 Ru:Fe stoichiometry **figure 1.15**. In the negative region, the reduction process located at $E_{1/2} = -1.47$ V corresponds to the reductions of the terpyridine ligand of the Fe(II) subunit, and at lower potentials lies the successive reduction of the second terpyridine as well as the bipyridine ligands. However, the latter reduction processes are strongly distorted by some electroprecipitation-redissolution phenomena, and couldn't be assigned. The stability of this complex under different oxidation states have been evaluated by successive anodic electrolysis at E = 0.9 and 1.2 V, consuming a total of three electrons and leading to the formation of $\{[Ru(bpy)_2(bpy\text{-}tpy)]_2Fe\}^{7+}$ and $\{[Ru(bpy)_2(bpy\text{-}tpy)]_2Fe\}^{9+}$ respectively.

The first electrolysis at 0.9 V lead to the quantitative formation of $\{[Ru(bpy)_2(bpy\text{-}tpy)]_2Fe\}^{7+}$ complex consuming one electron. In the RDE the proportion of the height of both redox waves is maintained 2:1 for the Ru^{2+} and Fe^{3+} respectively emphasizing the stability of the $\{[Ru(bpy)_2(bpy\text{-}tpy)]_2Fe\}^{7+}$ complex **figure 1.15**. This stability arises from the large difference in potential between both redox couples Ru^{3+}/Ru^{2+} and Fe^{3+}/Fe^{2+}. Further electrolysis at 1.2 V lead to the formation of $\{[Ru(bpy)_2(bpy\text{-}tpy)]_2Fe\}^{9+}$ with a 90% yield as estimated

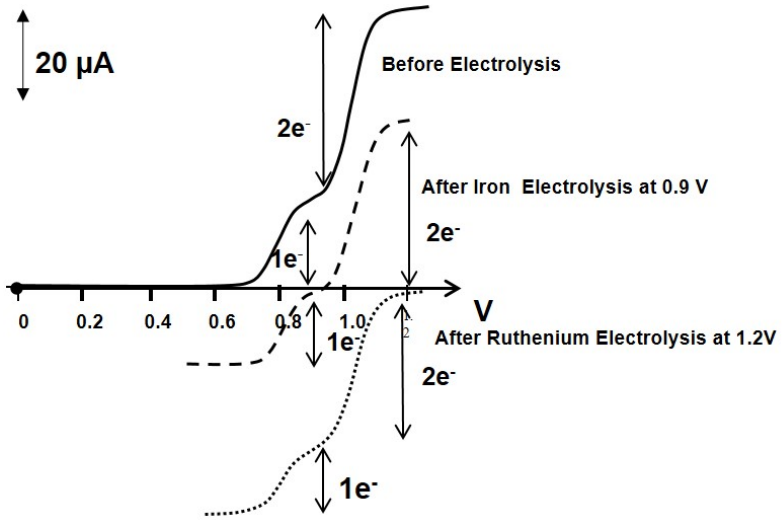

Figure 1.15: RDE voltammogram of **[6]**$^{6+}$ in 10^{-3} M solutions of CH_3CN + 0.1 M $[Bu_4N]PF_6$, and the $E_{1/2}$ values are reported *vs* $Ag/AgNO_3$ (10^{-2} M) at scan rate = 5 mV/s using carbon vitreous disk (5 mm in diameter) as a working electrode; Full line: Before electrolysis; Dashed line: after electrolysis at 0.9 V; Dotted Line: After electrolysis at 1.2 V.

from the RDE. The formation of both oxidized species is evident in the absorption spectrum **figure 1.13**. Initially the absorption spectrum consists of two bands in the visible region at 455 and 568 nm corresponding respectively to the Ru^{II}-bpy-tpy and Fe^{II}-phenol-tpy MLCT. The electrolysis at 0.9 V was accompanied by the disappearance of the Fe^{II} MLCT, with a slight loss of the intensity of the peak beneath the Ru MLCT , as well as the appearance of a low intensity band centered at 670 nm accounting for the presence of the Fe^{3+} species. The exchange of two additional electrons, lead to the total disappearance of the Ru^{2+} MLCT band, and increase in the absorbance around 670 nm validating the formation of the Ru^{3+} species.

1.3.3 Photophysics

The emission spectrum of **[6]**$^{6+}$ is typical of the ^{3}MLCT excited state of the $[Ru(bpy)_3]^{2+}$, nevertheless it is accompanied by a drastic decrease of ϕ_{em} from 0.048 to 0.009 as shown in **figure 1.16** and **table 1.6**. Only 18% of the initial emission of Ru-O-tpy is detected indicating a dominant deactivation pathway. This could be attributed to energy transfer from the excited state of the ruthenium complex to the corresponding $[Fe(tpy)_2]^{2+}$ center. This energy transfer phenomenon has been previously certified in the literature, and is explained by the strong overlap between the emission spectrum of the Ru^{II*} core and the absorption spectrum of the Fe^{2+} one.[7] The hypothesis of an electron transfer is precluded since it is endergonic by 0.48 eV. This value is evaluated from the difference of potential of the Fe^{3+}/Fe^{2+} redox couple and that of Ru^{2+*}/Ru^{+} calculated at room temperature using the Rehm-Weller equation.

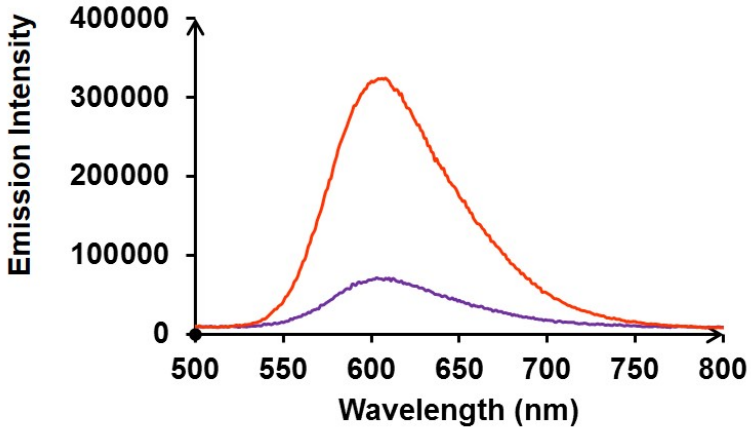

Figure 1.16: Emission of Ru-O-tpy (orange line) and **[6]**$^{6+}$ (purple line) in deoxygenated CH_3CN at 25°*C* upon excitation at 465 nm.

Table 1.6: Emission behavior of the ruthenium centers recorded in deoxygenated CH_3CN + 0.1 M $[Bu_4N]PF_6$ solution at 25 °C. ϕ_{em} represents the emission quantum yield of the complexes

Complex	λ_{em} (nm)	Lifetime	τ (ns)	K_{EnT} (s^{-1})	ϕ_{em}	$\phi_{em}/\ \phi_0$ (%)
		τ_1 ns (%)	τ_2 ns (%)			
Ru-O-tpy	610		527		0.048	-
$[6]^{6+}$	605	5 (72%)	560 (28%)	1.98×10^8	0.009	18%

[a] $\phi_{em}/\ \phi_0$ represents the ratio of the emission of the **[6]**$^{6+}$ *vs.* the emission of Ru-O-tpy.

After analyzing all possible deactivation pathways, it is evident that upon irradiation, the $[Ru(bpy)_3]^{2+}$ gets excited and transfers energy to the Fe counterpart promoting a Fe(II) excited state, which in turn decays to the ground state with non radiative relaxation **equation 1.1**.

$$Ru^{II*}\text{-}Fe^{II}\text{-}Ru^{II} \rightarrow Ru^{II}\text{-}Fe^{II*}\text{-}Ru^{II} \qquad \text{Intramolecular Energy Transfer} \tag{1.1}$$

The luminescence lifetime of **[6]**$^{6+}$ is described by a bi-exponential fit as shown in **equation 1.2**, reflecting the contribution of both the quenched and unquenched ruthenium cores.

$$I(t) = A\ e^{-t/\tau_1} + (1\text{-}A)e^{-t/\tau_2} \tag{1.2}$$

where τ_1 and τ_2 are the short and long lifetime components of the decay and A is the fraction of the emitted intensity associated with τ_1. The fractional amplitude of the decay (A) are listed in %. The shorter component τ_1 is thus attributed to the intramolecular quenching. The longer component τ_2 is slightly higher than the parent molecule Ru-O-tpy, yet close enough to be attributed to the unquenched Ru center by the intramolecular process.

The intramolecular quenching rate constant by energy transfer can be calculated following **equation 1.3**, where τ_1 represents the shorter lifetime of the decay and τ_0 represents the lifetime of Ru-O-tpy complex. .

$$k_{\mathrm{EnT}} = \frac{1}{\tau_1} - \frac{1}{\tau_0} \tag{1.3}$$

A quenching rate constant k_{EnT} of 1.98×10^8 s^{-1} has been estimated, in accordance to reported trinuclear complexes comprising ethyls as bridges.[7] Interestingly, this energy transfer can be short-circuited in the presence of a sacrificial electron acceptor. In this strategy we have added 4-bromophenyldiazonium BF_4 salt (ArN_2^+) which exhibits an irreversible reduction peak E_{red} = –0.4 V *vs.* $Ag/AgNO_3$ 10^{-2} M. When the ^{3}MLCT state of the Ru moiety is generated, an electron transfer process is expected to take place between the Ru^{2+*} center and the diazonium salt following **equation 1.4**.

$$Ru^{II*}\text{-}Fe^{II}\text{-}Ru^{II} + ArN_2^+ \rightarrow Ru^{III}\text{-}Fe^{II}\text{-}Ru^{II} + ArH + N_2 \tag{1.4}$$

The back electron transfer between the photogenrated Ru^{III} center and the transient $ArN_2^{\bullet}$ species is avoided by the rapid evolution of $ArN_2^{\bullet}$ into ArH and N_2.[15] This photoinduced electron transfer is exergonic with (ΔG = –0.62 eV). Thus, with this new component added to solution, the Ru centered ^{3}MLCT state has two routes of deactivation:

1. Intramolecular pathway: Energy transfer to the Fe part
2. Intermolecular pathway: Electron transfer to the ArN_2^+ salt

If the intramolecular pathway takes place, it will be followed directly by non-radiative decay. If the second pathway dominates, this electron transfer will lead to the decomposition of the ArN_2^+ forming N_2 and ArH in CH_3CN and generation of the Ru^{3+} species. The latter species is capable to accept an electron from the Fe^{2+} part with a (ΔG = –0.17 eV).

In order to test the feasibility of this reaction with our system, a solution containing a mixture of **[6]**$^{6+}$ (0.5 mM) and ArN_2^+ (15 mM) was continuously irradiated by a Xenon lamp using a 400-800 nm featbuster filter and the process is followed by UV-Vis spectroscopy **figure 1.17.a**.

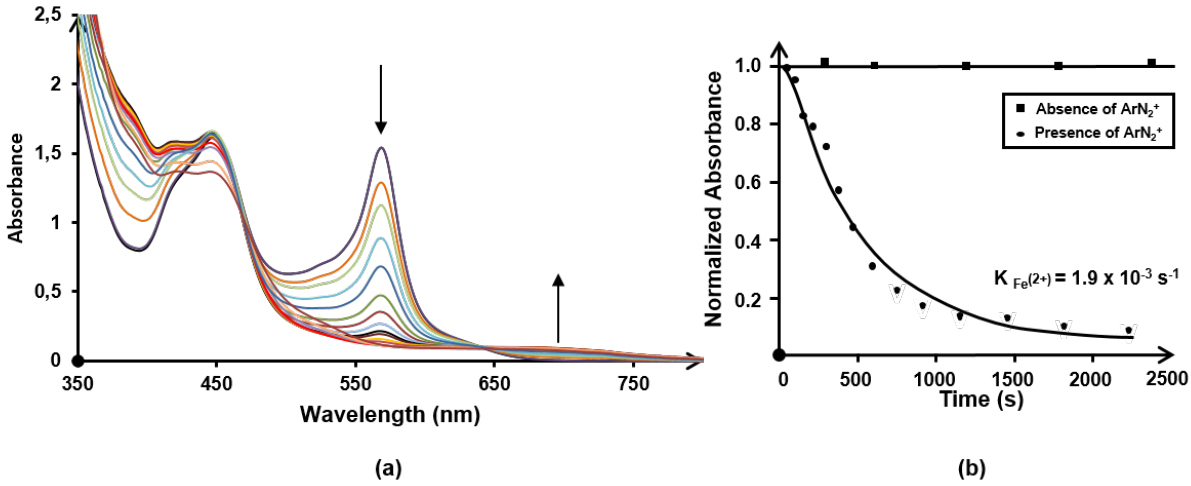

Figure 1.17: (a)Spectroscopic probing of the photoinduced oxidation of **[6]**$^{6+}$ (b) Evolution of absorbance at 560 nm induced by continuous irradiation.

Initially in the visible region we observe the spectroscopic signature of **[6]**$^{6+}$ without any perturbation coming from the ArN_2^+ salt that absorbs only in the UV part. This photolysis experiment shows a similar pattern as that evidenced in the electrolysis experiment which allows the easy identification of the different intermediates. Irradiation is accompanied by a gradual decrease in the Fe MLCT band around 569 nm, accompanied by the evolution of a broad band centered around 700 nm, consistent with the formation of Fe^{3+}. This proves that the intermolecular pathway was ruled out, and that the energy transfer was short circuited by electron transfer.

A proposed pathway that explains the generation of Fe^{3+} is depicted in **figure 1.18**. Initially the Ru^{2+}-Fe^{2+}-Ru^{2+} is irradiated with a wavelength of 450 nm in order to selectively excite the Ru in its MLCT band **step 1**.

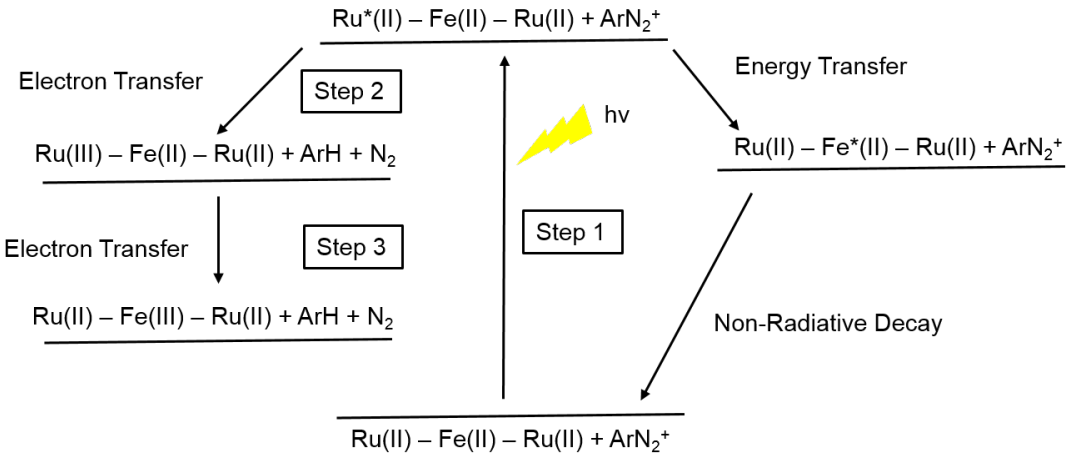

Figure 1.18: Proposed mechanism for the electron transfer process in Ru-Fe-Ru

Then the Ru^{2+*}-Fe^{2+}-Ru^{2+} undergoes oxidative quenching thanks to the diazonium salt in order to form the Ru^{3+}-Fe^{2+}-Ru^{2+} **step 2**. The generated Ru^{3+} can now accept an electron from the Fe^{2+} with a ΔG estimated as –0.17 eV forming Ru^{2+}-Fe^{3+}-Ru^{2+} **step 3**. The kinetics of electron transfer between $\mathbf{[6]}^{6+}$ and ArN_2^+ was estimated following a Stern-Vollmer plot according to **equation 1.5**:

$$\frac{\tau_0}{\tau} = 1 + k_q\ \tau_0[ArN_2^+] \tag{1.5}$$

where τ and τ_0 are the lifetime with an without ArN_2^+ and k_q the quenching rate constant.

Upon adding increasing concentrations of ArN_2^+ varying from 0 to 1.4×10^{-3} mol.L^{-1}, τ_1 remains unaltered, while τ_2 decreases from 560 to 304 ns as shown in **figure 1.19.a**.

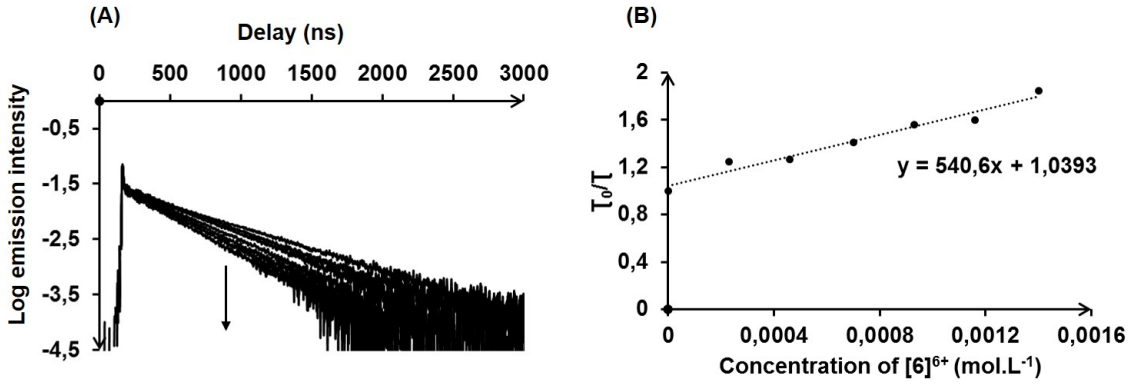

Figure 1.19: (a) Variation of the lifetime of $\mathbf{[6]}^{6+}$ upon addition of increasing amounts of ArN_2^+, (b) Stern volmer plot of the quenching of $\mathbf{[6]}^{6+}$ by ArN_2^+

The intramolecular quenching rate constant k_q of $\mathbf{[6]}^{6+}$ with ArN_2^+ is estimated to 9.1×10^8 $M^{-1}.s^{-1}$ and is slightly slower than the diffusion limit and proves the high efficiency of the photoinduced electron transfer process **figure 1.19.b**.

This overall transformation can be followed by the evolution of the UV-vis absorption at 569 nm in course of irradiation **figure 1.17.b**. The decrease of the Fe(II) MLCT band follows a pseudo first order kinetics with a kinetic rate constant of the global photoinduced transformation of 1.9×10^{-3} s^{-1}.

1.4 [Ru(bpy)$_3$]-[Co(tpy)$_2$]-[Ru(bpy)$_3$]

1.4.1 Synthesis

The {[Ru(bpy)$_2$(bpy-tpy)]$_2$Co}$^{6+}$ complex **[7]**$^{6+}$ was synthesized from the [Co(OAc)$_2$] .6H$_2$O salt by refluxing in methanol **figure 1.20**. Since the latter complex is paramagnetic, it was difficult to perform ^{1}HNMR experiments. Due to the inertness of Co^{3+}, it is difficult to have direct access to the [Co(tpy)$_2$]$^{3+}$ core, thus complex **[7]**$^{7+}$ was obtained by the electrochemical oxidation of **[7]**$^{6+}$.

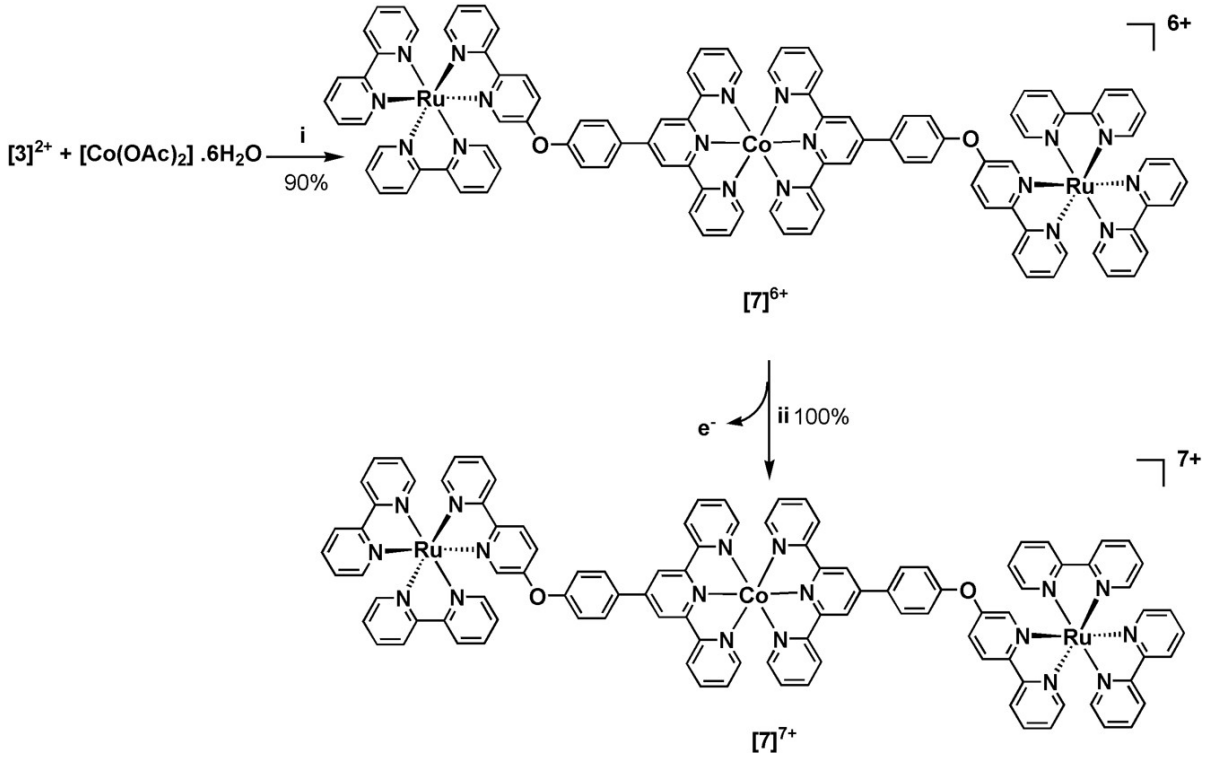

Figure 1.20: Synthesis of the trinuclear complex **[7]**$^{6+}$, (i) [Co(OAc)$_2$] .6H$_2$O, MeOH, 1 h, 65 °C, KPF$_6$; (ii) electrochemical oxidation : Applied potential = 0.9 V *vs.* Ag/AgNO$_3$ (10^{-2} M), CH$_3$CN, 0.1 M TBAPF$_6$

1.4.2 Spectro-electrochemistry

The UV Visible spectrum of **[7]**$^{6+}$ is essentially a superposition of the absorption spectra of the individual molecular components Ru-O-tpy and [Co(ttpy)$_2$]$^{2+}$ with the suitable 2:1 proportion **table 1.7** and **figure 1.23**. While the UV spectrum of **[7]**$^{6+}$ confirms the formation of the trimetallic complex, the CV remains tricky to comprehend. All the electrochemical data are collected in **table 1.8**. In the presence of [Bu$_4$N]PF$_6$ as a supporting electrolyte, the CV in the positive region shows only one oxidative process at $E_{1/2}$ = 1.01 V which lies in the same region

of Ru^{3+}/Ru^{2+} redox couple, with no evident wave corresponding to the Co^{3+}/Co^{2+} oxidation process **figure 1.21.c**. However, on the reverse scan two reductive peaks are observed with E = 1 V corresponding to the Ru^{III} reduction process and E = –0.2 V which may correspond to the Co^{III} reduction.

Table 1.7: UV-Visible absorption data in CH_3CN for complexes Ru-O-tpy, $[Co(ttpy)_2]^{2+}$ and **[7]**$^{6+}$

Complex	λ_{abs} (nm) ($M^{-1}.cm^{-1}$)	
	Ru^{II} MLCT	Co^{II}
Ru-O-tpy	446 (13 250)	-
$[Co(ttpy)_2]^{2+a}$	-	513 (2700)
$[7]^{6+}$	449 (26 500)	513 (270)

[a] These values are reported in the literature in CH_3CN[8]

Table 1.8: Redox potentials of Ru-O-tpy, $[Co(ttpy)_2]^{2+}$ and **[7]**$^{6+}$ studied in a 10^{-3} M solutions of CH_3CN + 0.1 M $[Bu_4N]PF_6$, the potentials ($E_{1/2}$, ΔE_p) values are reported *vs* $Ag/AgNO_3$ (10^{-2} M) at scan rate = 100 mV/s using carbon vitreous disk (5 mm in diameter) as a working electrode.

Complex	$E_{1/2}^{oxidation}$, V (ΔEp, mV)		$E_{1/2}^{reductions}$, V (ΔEp, mV)		
	Ru^{3+}/Ru^{2+}	Co^{3+}/Co^{2+}	Co^{2+}/Co^{+}	L.C 1	L.C2
$(Ru-O-tpy)$	1.01 (60)	-	-	–1.58 (80)	–1.85 (100)
$[Co(ttpy)_2]^{2+b}$	-	–0.06 (70)	–1.06 (70)	–1.90 (60)	–2.26 (50)[a]
$[7]^{6+}$	1.01 (60)	–0.06 [c]	–1.03 (60)	–1.63 (100)	–1.76 (70) [a]

[a] This value cannot be accurately measured since the wave is strongly distorted by adsorption of the reduction product on the electrode surface. [b] These values are reported in the literature in CH_3CN + 0.05 M $[Bu_4N]PF_6$.[8] [c] The electrochemical properties of the different complexes have been studied in 10^{-5} M solutions of CH_3CN + 0.1 M $[Bu_4N]ClO_4$, and the $E_{1/2}$ values are reported *vs* $Ag/AgNO_3$ (10^{-2} M) at scan rate = 100 mV/s using carbon vitreous disk (5 mm in diameter) as a working electrode.

The study of this unique oxidation wave at 1.01 V at slower scan rates showed evidence of two processes occurring at this potential, which was later verified by the RDE experiments **figure 1.21.b** and **1.22**. In the negative region, there are three successive reduction processes. The first reversible one-electron process, located at $E_{1/2}$ = –1.0 V is attributed to the Co^{2+}/Co^{+} system. The following ones are ligand centered reductions. Distortion of the waves is observed at more negative potentials which could be associated to the electroprecipitation-redissolution phenomena.

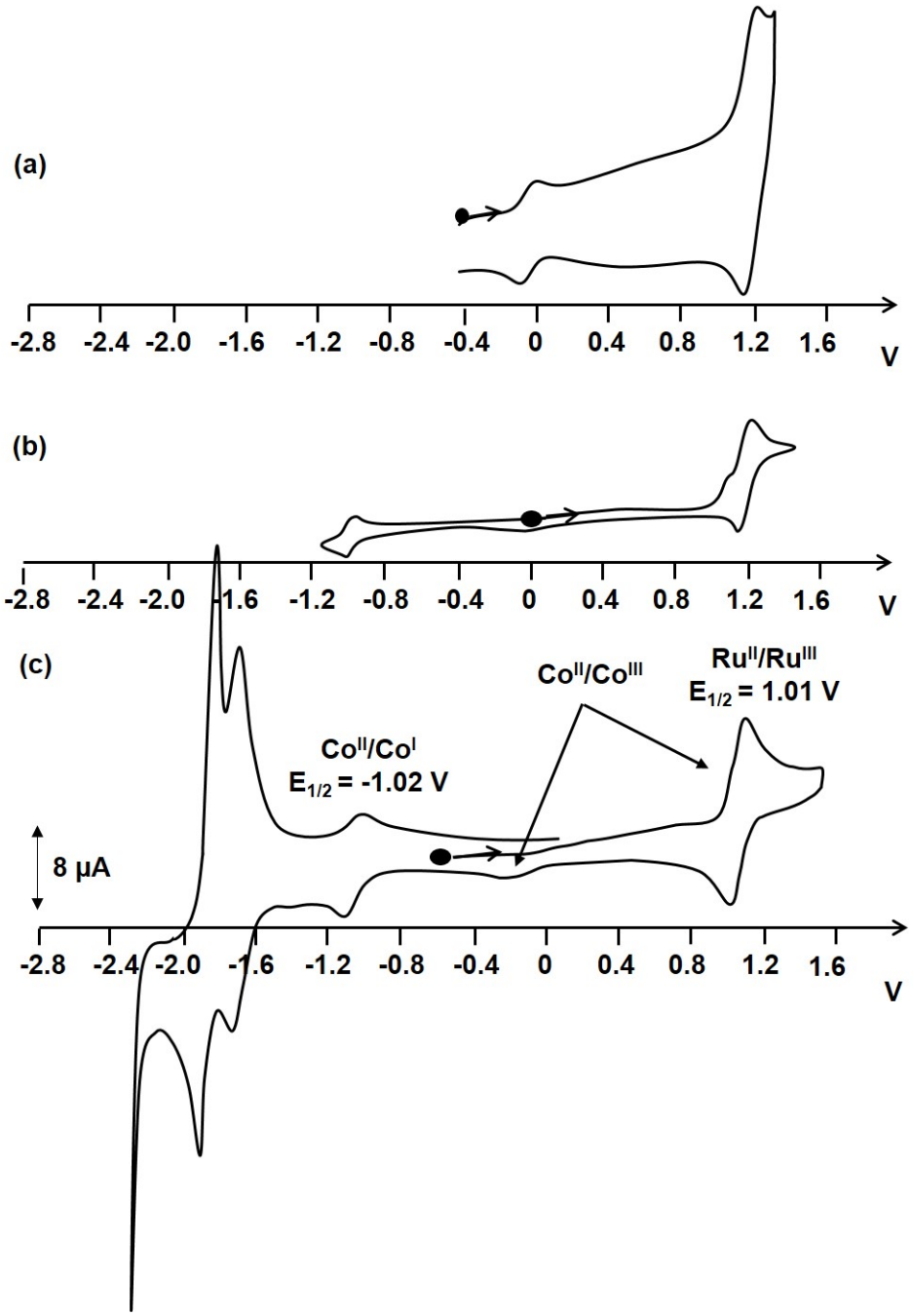

Figure 1.21: CV of **[7]**$^{6+}$ using carbon vitreous disk (5 mm in diameter) as a working electrode and $E_{1/2}$ values are reported *vs* $Ag/AgNO_3$ (10^{-2} M) (a) 10^{-5} M solution of CH_3CN + 0.1 M $[Bu_4N]ClO_4$, at scan rate = 100 mV/s, (b) 10^{-3} M solution of CH_3CN + 0.1 M $[Bu_4N]PF_6$, at scan rate = 5 mV/s, (c) 10^{-3} M solution of CH_3CN + 0.1 M $[Bu_4N]PF_6$, at scan rate = 100 mV/s

Assuming a 1 e^- redox process for Co^{2+}/Co^+ at –1.03 V, the RDE experiment **figure 1.22** proved the exchange of 2 e^- for both reduction waves at –1.63 and –1.76 V. These reductions are located on the bipyridine of each ruthenium subunit of the complex. In the anodic part, the

RDE shows the exchange of 3 e^- per complex at 1.01 V following **equation 1.6**:

$$Ru^{II}\text{-}Co^{II}\text{-}Ru^{II} \rightarrow Ru^{III}\text{-}Co^{III}\text{-}Ru^{III} + 3\ e^- \tag{1.6}$$

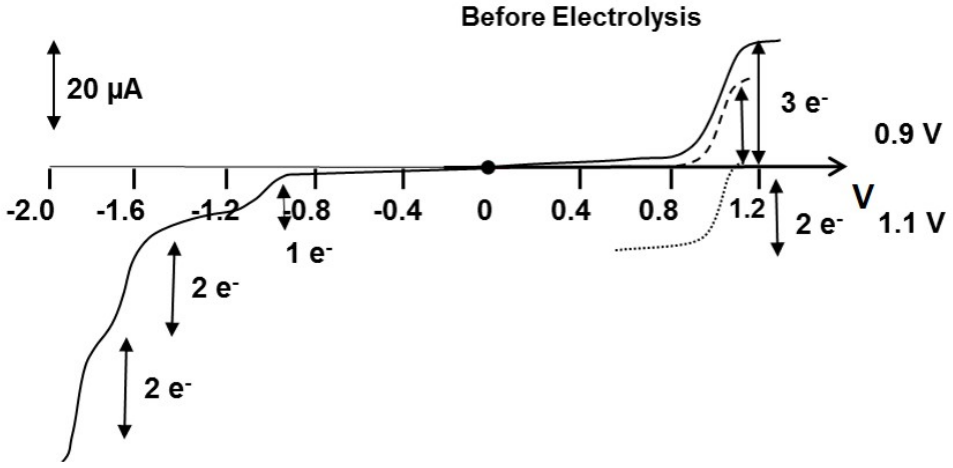

Figure 1.22: RDE of $[7]^{6+}$ in 10^{-3} M solutions of CH_3CN + 0.1 M $[Bu_4N]PF_6$, and the $E_{1/2}$ values are reported *vs* $Ag/AgNO_3$ (10^{-2} M) at scan rate = 5 mV/s using carbon vitreous disk (5 mm in diameter) as a working electrode; Full line: Before electrolysis; Dashed line: after electrolysis at 0.9 V; Dotted Line: After electrolysis at 1.2 V

This lead to the suggestion that the oxidation process of the Co(III) core is delayed in **[7]**$^{6+}$ compared to $[Co(ttpy)_2]^{2+}$ complex where it appears around 0 V *vs* $Ag/AgNO_3$ 10^{-2} M **table 1.8**. Thus, the oxidation of the Ru^{II} center catalyses the oxidation of the Co(II) core. A recent report by Elliott showed that the presence of large, bulky alkyl substituents, such as t-butyl, located in the pseudo-para-position of bipyridine and terpyridine ligands significantly diminishes the ability of a metal complex to couple electronically with electrode surfaces during the electrochemical electron transfer event.[16;17] When the reorganization energy associated with that electron transfer process is large, as is the case of Co^{3+}/Co^{2+} the CV response can become quite non-Nernstian and electrode/electrolyte dependent. In contrast, when the reorganization energy is small, as is the case of Fe^{3+}/Fe^{2+} or Ru^{3+}/Ru^{2+}, with the same ligands, the CV behavior appears nearly diffusion controlled and is fairly independent of electrolyte and electrode material. To relate to our case, we assume that the geometric and steric constraints due to the presence of both ruthenium complexes *via* the relatively rigid ether linkage in para positions on the terpyridines disturb the ability of the cobalt complex to couple electronically with the electrode surface (platinum or glassy carbon), which was translated by a delay of the Co^{3+}/Co^{2+} oxidation process without any significant disturbing of the Co^{2+}/Co^{+} and Ru^{3+}/Ru^{2+} processes.

The CV reported under dilute conditions and in the presence of $[Bu_4N]ClO_4$ as a supporting electrolyte **figure 1.21.a** shows clearly the oxidation peak of Co^{2+} at its regular potential (–0.06 V*vs.* $Ag/AgNO_3$) and in such validating our hypothesis.

Exhaustive electrolysis of a solution of $\mathbf{[7]}^{6+}$ in CH_3CN + 0.1 M $[Bu_4N]PF_6$ was carried out at 0.9 and 1.1 V consuming a total of three electrons and leading to the formation of $\{Ru(bpy)_2(bpy\text{-}tpy)]_2Co\}^{7+}$ and $\{[Ru(bpy)_2(bpy\text{-}tpy)]_2Co\}^{9+}$ respectively. The first electron consumption at 0.9 V lead to the decrease of the height under the Ru^{3+}/Ru^{2+} wave by one third, while the second lead to the quantitative formation of $\{[Ru(bpy)_2(bpy\text{-}tpy)]_2Co\}^{9+}$ **figure 1.22**. The oxidation products of the sequential electrolysis were characterized by UV-Vis spectroscopy **figure 1.23**.

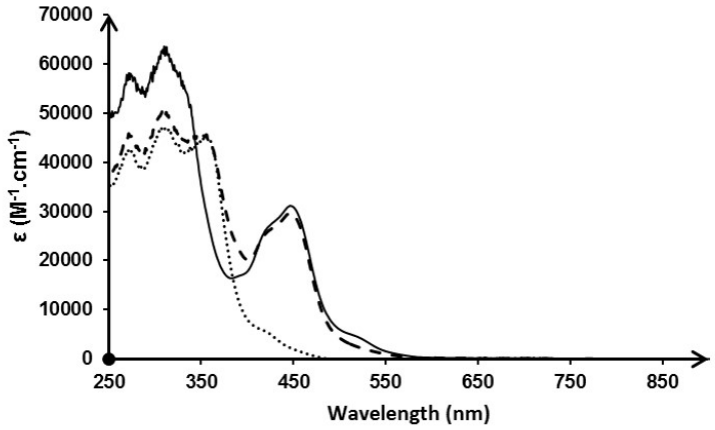

Figure 1.23: UV-Visible absorption spectra of $\mathbf{[7]}^{6+}$ in 10^{-3} M solutions of CH_3CN + 0.1 M $[Bu_4N]PF_6$; Full line: Before electrolysis; Dashed line: After electrolysis at 0.9 V; Dotted Line: After electrolysis at 1.2 V

The initial solution showed in the visible region a band at 454 nm corresponding to the Ru^{II} MLCT as stated previously, with an extending shoulder around 513 nm which is a typical signature of the d-d transition of $[Co(ttpy)_2]^{2+}$. After one electron has passed at 0.9 V, the shoulder at 513 nm disappears leaving the Ru^{II} MLCT unaltered, accompanied by an intense band at 350 nm (transition π - π^*), which all comes in agreement with the oxidation of the cobalt complex and formation of the respective $\{[Ru(bpy)_2(bpy\text{-}tpy)]_2Co\}^{7+}$. Further electron consumption lead to the complete disappearance of the Ru^{II} MLCT band and its replacement by the Ru^{3+} ones at 434 and 670 nm.

1.4.3 Photophysics

The photophysical data of compounds $\mathbf{[7]}^{6+}$ and $\mathbf{[7]}^{7+}$ are collected in **table 1.9**.

Table 1.9: Photophysical data of ruthenium complexes recorded in deoxygenated CH_3CN + 0.1 M $[Bu_4N]PF_6$ solution at 25 °C. ϕ_{em} represents the emission quantum yield of the complexes

Complex	λ_{em} (nm)	Lifetime	τ (ns)	K_q (s^{-1})	ϕ_{em}	ϕ_{em}/ϕ_0 (%)
		τ_1 ns (%)	τ_2 ns (%)			
Ru-O-tpy	610		527	-	0.048	-
$[7]^{6+}$	610	89 (65)	636 (35)	9.4×10^6	0.008	17
$[7]^{7+}$	610	96 (50)	768 (50)	8.5×10^6	0.005	10

The emission spectra are similar in shape and energy to that of **[6]**$^{6+}$ displaying a poor emission at λ = 610 nm. This is a typical signature for the ^{3}MLCT excited state of the $[Ru(bpy)_3]^{2+}$. However, the poor quantum yields 0.008 and 0.005 for compounds **[7]**$^{6+}$ and **[7]**$^{7+}$ respectively suggest that there is a significant quenching taking place. Undoubtedly, the Co metallic centers are responsible for these quenching processes. Thorough investigation of both UV and emission spectra as well as the redox potentials of all involved couples allows the determination of the possible quenching pathways.

The luminescence decay of both **[7]**$^{6+}$ and **[7]**$^{7+}$ are fitted by a bi-exponential function as described earlier. The bi-exponential decay proves that the quenching is not total and only part of the species undergo an intermolecular interaction process. Emission quantum yield of **[7]**$^{7+}$ constitutes only 10% of that of the parent molecule Ru-O-tpy. The $[Co(tpy)_2]^{3+}$ species is poorly absorbing in the visible region, this will thus exclude any possibility of overlapping with the emission spectrum of the Ru moiety which in turn eliminates the energy transfer pathway. Examining the ΔG of the different redox couples reveals a largely negative free enthalpy reaction with a ΔG = –0.97 eV (assuming E^0 $Ru^{3+/2*}$ to –1.03 V by the Rehm Weller relation and the Co^{3+}/Co^{2+} to –0.06 V). This will unambiguously assign the nature of the quenching to an electron transfer process generating Co(II) and Ru(III) species **equation 1.7**. The photoinduced electron transfer between the Co(III) polypyridine complex and Ru(II)* center was already evidenced by Rillema et al[18] and Ohno et al.[19]

$$Ru^{II*}\text{-}Co^{III}\text{-}Ru^{II} \rightarrow Ru^{III}\text{-}Co^{II}\text{-}Ru^{II} \qquad \text{Intramolecular Electron Transfer} \tag{1.7}$$

In the case of **[7]**$^{6+}$, the attribution of the quenching mechanism becomes more complicated. As stated previously, the Co^{2+} center absorbs in the visible region (untill 600 nm). Hence, despite the small extinction coefficient of this absorption, there is still an overlap between the absorption of the Co center and the emission of Ru which favors the energy transfer pathway

equation 1.8.

Ru^{II*}-Co^{II}-Ru^{II} $\rightarrow$ Ru^{II}-Co^{II*}-Ru^{II} Intramolecular Energy Transfer

(1.8)

Analyzing the thermodynamics of all possible redox reaction involving the Co^{III}/Co^{II}, Co^{II}/Co^{I}, Ru^{III}/Ru^{II*} and Ru^{II*}/Ru^{I} gives the following ΔG values: For an oxidative quenching following **equation 1.9** ΔG = –0.05 eV, whereas for a reductive quenching according to **equation 1.9** ΔG = –0.33 eV

Ru^{II*}-Co^{II}-Ru^{II} $\rightarrow$ Ru^{III}-Co^{I}-Ru^{II} Oxidative quenching

Ru^{II*}-Co^{II}-Ru^{II} $\rightarrow$ Ru^{I}-Co^{III}-Ru^{II} Reductive quenching

(1.9)

Despite the multiple quenching pathways for **[7]**$^{6+}$, the quenching in **[7]**$^{7+}$ seems to be more efficient as described by the remaining intensities 17 and 10% respectively. This could be explained by the more negative ΔG values for the quenching reaction in **[7]**$^{7+}$.

The kinetics of the quenching of the latter compounds is determined by luminescence lifetime measurements. The luminescence lifetimes are described by a bi-exponential fit, reflecting the contribution of both the quenched and unquenched ruthenium cores. The shorter component τ_1 represents 65% for **[7]**$^{6+}$ and 50% for **[7]**$^{7+}$ and is attributed to the intramolecular quenching. This quenching occurs slightly faster for complex **[7]**$^{7+}$ with a value of 96 ns. The longer component τ_2 are slightly higher than the one of the parent molecule Ru-O-tpy, yet close enough to be attributed to the unquenched Ru center by the intramolecular process.

The intramolecular quenching rate constant k_q values are 3 to 5 times smaller than the value reported for similar trinuclear complexes based on ethyl groups as bridging entities **figure 1.4**.[8] Since the dominant deactivation pathway is electron transfer, this means that employing ether as a bridge at the 5 position of the bipyridine slows down the rate of electron transfer. This is coherent with the difference in the redox couple potentials of the excited state for complexes Ru-O-tpy and $[Ru(bpy)_2(CH_2CH_2tpy)]^{2+}$ **table 1.10**. When ethers are used as bridges, the ground state potential of the Ru^{3+}/Ru^{2+} is slightly higher than that with ethyls due to the more donating effect of the oxygen atoms, which means that $E_{1/2}$ Ru^{3+}/Ru^{2+*} is higher. This thus will increase the ΔG values which in turn increases the quenching reactions rate .

Table 1.10: Redox potentials (V) of the excited state of complex Ru-O-tpy and $[Ru(bpy)_2(CH_2CH_2tpy)]^{2+}$

Complexes	Ru^{III}/Ru^{II*}	Ru^{II*}/Ru^{I}
Ru-O-tpy	-1.027	0.43
$[Ru(bpy)_2(CH_2CH_2tpy)]^{2+}$	-1.117	0.36

A photolysis experiment was performed on compound **[7]**$^{7+}$ in the presence of a triethanol amine (TEOA) as a sacrificial electron donor in order to induce a net photoreduction of the $[Co(tpy)_2]^{3+}$ subunit. Thus, a mixture of **[7]**$^{7+}$ and TEOA were subject to continuous irradiation, and several UV-Vis spectra were recorded to monitor the evolution of the species **figure 1.24.a**. The changes detected are in accordance with those obtained during electrolysis and confirm the formation of the $[Co(tpy)_2]^{2+}$ center.

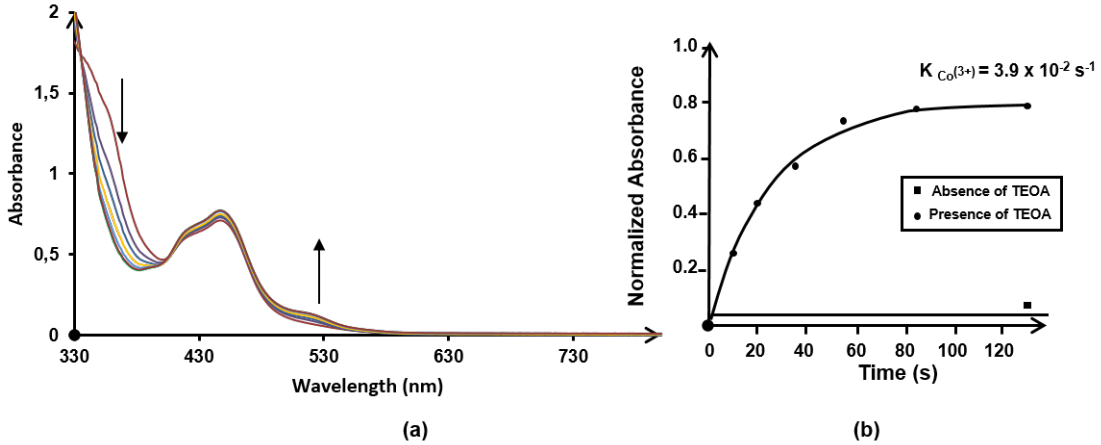

Figure 1.24: (a) Spectroscopic probing of the photoinduced reduction of **[7]**$^{7+}$ (b) Evolution of the absorbance of **[7]**$^{7+}$ at 513 nm upon continuous irradiation

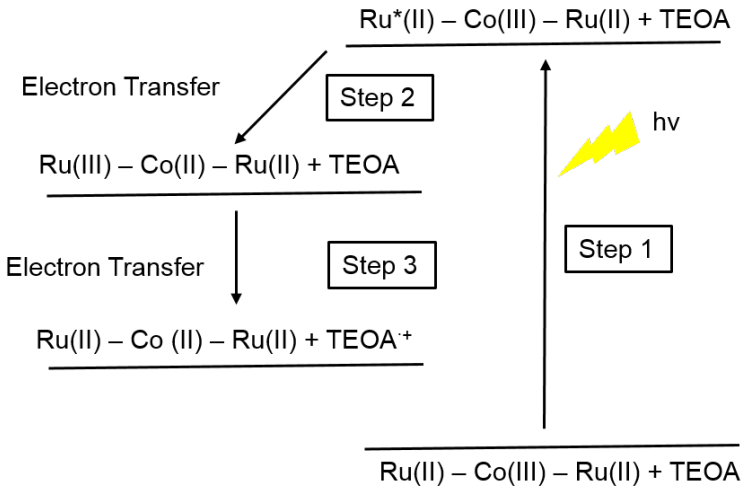

Figure 1.25: Proposed mechanism for the electron transfer in **[7]**$^{7+}$

The mechanism is depicted in **figure 1.25**. Briefly, **step 1** requires the selective excitation of the Ru center in order to generate Ru^{2+*}-Co^{3+}-Ru^{2+}. Assuming that intramolecular electron transfer is faster than intermolecular electron transfer, we can safely say that the generated state then undergoes oxidative quenching by the Co part in order to form the Ru^{3+}-Co^{2+}-Ru^{2+} species (ΔG = –0.97 eV). Final step includes the regeneration of the Ru^{2+} from the sacrificial electron donor TEOA. For the calculation of the kinetic rate of electron transfer in **step 2**, the band of Co^{2+} at 513 nm was used because Co^{2+} band may be disturbed by UV absorption of organic groups. By fitting the curve with a first-order exponential decay function, a global kinetic rate constant of the photoquenching reaction $k_q = 3.9 \times 10^{-2}$ s^{-1} is found **figure 1.24.b**.

1.5 Conclusion

In this chapter we have reported the synthesis, electrochemical and photophysical characterization of five modified $[Ru(bpy)_3]^{2+}$ complexes, where one or two terpyridine motifs are introduced on the same bipyridine *via* amide, ether and phenylene spacers. We have shown that the amide is not the ideal bridge in such assemblies, for it exhibits oxidation potentials close to that of the Ru core, whereas ethers and phenylenes are good candidates. Moreover, we selected the mono-substituted complex bearing ether as a bridge in order to construct assemblies of the formula Ru-M-Ru. It was proven that in such architectures the energy transfer can take place from the Ru core to the Fe metallic center. Nonetheless, this energy transfer was short circuited in the presence of an electron acceptor. In this case, the $[Fe(tpy)_2]^{2+}$ can act as electron donor towards the photogenerated $[Ru(bpy)_3]^{3+}$ core. We have also shown that $[Co(tpy)_2]^{3+}$ represents a good electron acceptor to the $[Ru(bpy)_3]^{2+*}$. An extension of this work is presented in **chapter 2** where both $[Co(tpy)_2]^{3+}$ and $[Fe(tpy)_2]^{2+}$ are connected to a $[Ru(bpy)_3]^{2+}$ to generate a (D-P-A) assembly.

Bibliography

[1] S. Campagna, F. Puntoriero, F. Nastasi, G. Bergamini, V. Balzani, *Photochemistry and Photophysics of Coordination Compounds: Ruthenium*, *Vol. 280*, Springer Berlin Heidelberg, **2007**, pp. 117–214.

[2] F. Puntoriero, S. Campagna, A.-M. Stadler, J.-M. Lehn, *Coord. Chem. Rev.* **2008**, *252*, 2480 – 2492.

[3] E. C. Constable, E. Figgemeier, C. E. Housecroft, J. Olsson, Y. C. Zimmermann, *Dalton Trans.* **2004**, 1918–1927.

[4] E. C. Constable, P. Harverson, C. E. Housecroft, E. Nordlander, J. Olsson, *Polyhedron* **2006**, *25*, 437 – 458.

[5] H. Wolpher, P. Huang, M. Borgström, J. Bergquist, S. Styring, L. Sun, B. Åkermark, *Catal. Today* **2004**, *98*, 529 – 536.

[6] C. E. Castillo, S. Romain, M. Retegan, J.-C. Leprêtre, J. Chauvin, C. Duboc, J. Fortage, A. Deronzier, M.-N. Collomb, *Eur. J. Inorg. Chem.* **2012**, *2012*, 5485–5499.

[7] J. Lombard, J.-C. Leprêtre, J. Chauvin, M.-N. Collomb, A. Deronzier, *Dalton Trans.* **2008**, *5*, 658–666.

[8] J. Lombard, R. Boulaouche, D. A. Jose, J. Chauvin, M.-N. Collomb, A. Deronzier, *Inorg. Chim. Acta* **2010**, *363*, 234 – 242.

[9] F. Venema, H. F. M. Nelissen, P. Berthault, N. Birlirakis, A. E. Rowan, M. C. Feiters, R. J. M. Nolte, *Chem. Eur. J* **1998**, *4*, 2237–2250.

[10] J.-F. Ayme, B. J. E., D. A. Leigh, R. T. McBurney, K. Rissanen, D. Schultz, *Nature Chemistry* **2012**, *4*, 15–20.

[11] J. Wang, G. S. Hanan, *SynLett* **2005**, *8*, 1251–1254.

[12] H. B. Ross, M. Boldaji, D. P. Rillema, C. B. Blanton, R. P. White, *Inorg. Chem.* **1989**, *28*, 1013–1021.

[13] V. Balzani, A. Juris, M. Venturi, S. Campagna, S. Serroni, *Chem. Rev.* **1996**, *96*, 759–834.

[14] A. Juris, V. Balzani, F. Barigelletti, S. Campagna, P. Belser, A. von Zelewsky, *Coord. Chem. Rev.* **1988**, *84*, 85 – 277.

[15] H. Cano-Yelo, A. Deronzier, *J. Chem. Soc. Faraday Trans. 1* **1984**, *80*, 3011–3019.

[16] R. S. Gaddie, C. B. Moss, C. M. Elliott, *Langmuir* **2013**, *29*, 825–831.

[17] R. S. G. Di Xue, Lance N. Ashbrook, C. M. Elliott, *J. Electrochem. Soc.* **2013**, *160*, H355–H359.

[18] X. Song, Y. Lei, S. Van Wallendal, M. W. Perkovic, D. C. Jackman, J. F. Endicott, D. P. Rillema, *J. Phys. Chem. A* **1993**, *97*, 3225–3236.

[19] A. Yoshimura, K. Nozaki, N. Ikeda, T. Ohno, *J. Am. Chem. Soc.* **1993**, *115*, 7521–7522.

Self-Assembled Dyads and Triads

Résumé:

Les études préliminaires sur les complexes trinucléaires en solution du Chapitre 1 ont conforté la synthèse de triades trimétalliques. Afin de convertir l'énergie solaire en courant électrique, ces systèmes à séparation de charge ont été greffés à la surface d' électrode.

Ce chapitre décrit la première synthèse de la première triade trimétallique construite autour d'un fragment $[Ru(bpy)_3]^{2+}$. La triade a été construite en suivant une approche pas à pas. Ceci permet un contrôle de l'assemblage sur la surface. La synthèse de la triade pas à pas sur la surface est indispensable, car du fait de la labilité des ligands terpyridine sur le fer et le cobalt, une synthèse en solution est inenvisageable.

Ces triades sont donc du type ITO/$[Co^{III}(tpy)_2]$-$[Ru^{II}(bpy)_3]$-$[Fe^{II}(tpy)_2]$, le Co^{III} joue le rôle d'accepteur, et le Fe^{II} celui de donneur d'électron. En appliquant un potentiel à l'électrode, celle-ci devient l'accepteur final d'électron. Ainsi, en présence d'un donneur d'électrons en solution, il a été possible de générer un courant électrique sous irradiation lumineuse. Les paramètres gouvernant le photocourant ont étés étudiés.

Une augmentation de 40% de la densité de courant est observée en passant d'une diade à une triade démontrant l'importance de disposer d'un relais d'électron. Des paramètres tels que la densité de surface ou la puissance d'irradiation ont été également étudiés. Pour étudier l'influence de la linéarité du système deux triades ont été construites avec des liens différents entre les différentes parties. Les liens phénylène, plus rigides et linéaires ont démontré une plus grande efficacité que les liens éther, offrant plus de degrés de liberté.

Afin de pouvoir proposer un mécanisme de transfert d'électron, une étude détaillée de la cinétique de transfert d'électron a été réalisée. Dans ce but, les dyades ont été construites sur des électrodes d'or.

CHAPTER 2

SELF-ASSEMBLED DYADS AND TRIADS

2.1 Introduction

The ordered and controlled position of functional molecules such as a triad composed of a photosensitizer, donor and acceptor onto surfaces is of great significance for the design of electrochemical interfaces in view of electron transfer studies and photo-responsive devices.[1] Some of the most common surface preparation techniques are Langmuir-Blodgett (LB) films, electro-polymerization, chemical vapor deposition and self-assembled-monolayers (SAMs). As a matter of fact, SAMs provide an effective method to obtain target functions simply by the spontaneous adsorption and organization of adsorbate molecules on a solid surface upon exposure to dilute solutions. Furthermore, stepwise layer by layer assembly of molecules on preorganized SAMs affords an easy and fast pathway in order to access highly organized molecular structures with mixed properties. During this process, a stepwise coordination bond is formed on the surface by alternating dipping in different solutions containing desired molecules. In particular, coordination reactions were employed in order to construct different assemblies with the desired number and nature of hetero-layered structures **figure 2.1**.

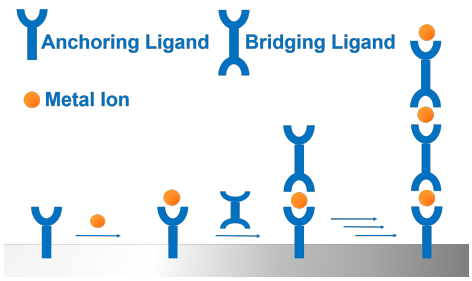

Figure 2.1: A schematic representation of the stepwise (layer by layer) preparation of surfaces

Popular systems in this context are transition metal-based polypyridyl complexes, which became a focal point in diverse research areas due to their tunable photophysical and electrochemical properties. Recently, this field has been extensively developed.[2–5] We don't intend to review the field, instead we are going to highlight several examples which serve for the better understanding of the work developed in this chapter.

The group of Nishihara has done some pioneering work in this context. They have implemented this stepwise method in order to build several molecular wires as well as dyads. In 2006 they reported the possibility of assembling a $[Ru(tpy)_2]^{2+}$ -$[Co(tpy)_2]^{2+}$ dyad layer by layer on a gold electrode **figure 2.2**.[6] They have proven through electrochemical studies, that the electroactivity of the ruthenium center is not perturbated by the presence of the cobalt relay, which indicates that the complex wire is electronically conducting.

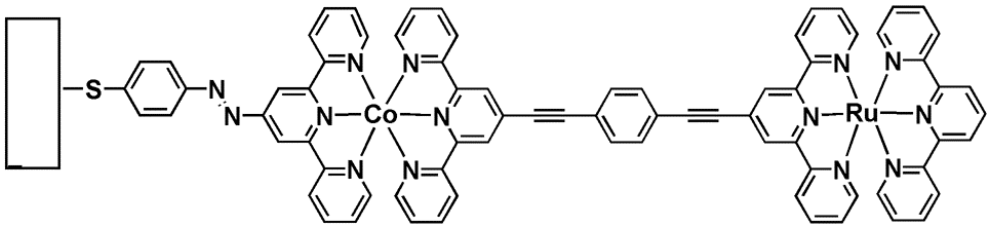

Figure 2.2: $[Ru(tpy)_2]^{2+}$ -$[Co(tpy)_2]^{2+}$ dyad immobilized on gold

In a similar manner, the same group fabricated a series of modified ITO electrodes containing a zinc porphyrin as a light harvesting unit and either $[Co(tpy)_2]^{2+}$, $[Fe(tpy)_2]^{2+}$ or $[Zn(tpy)_2]^{2+}$ as a relay **figure 2.3**.[7]

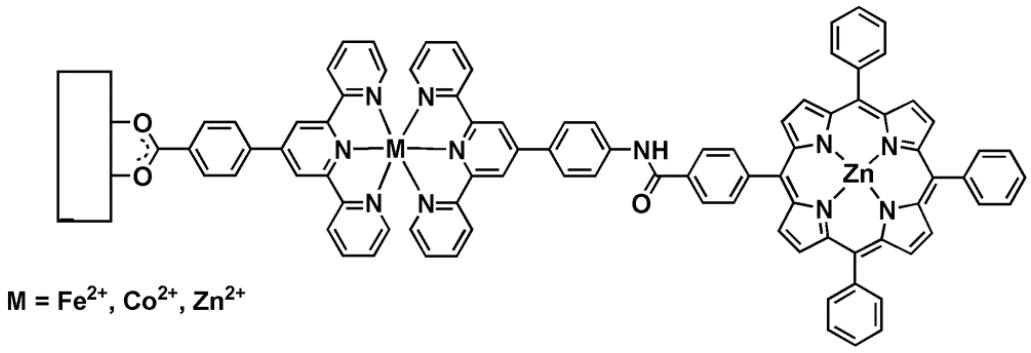

Figure 2.3: Porphyrin- $[M(tpy)_2]^{2+}$ dyad immobilized on ITO

All the electrodes efficiently produced photocurrent upon irradiation in the presence of triethanolamine as a sacrificial electron donor. The authors showed that the quantum efficiency varied upon changing the nature of the metal which serves as an electron relay; i.e: 0.57% for ITO/Co-porphyrin; 0.2% ITO/Zn-porphyrin and 0.15% ITO/Fe-porphyrin. This was explained in terms of the electronic nature of the molecular wire. The ITO containing the Co as an electron mediator showed superior photo-to-electron conversion since it serves as a good electron

acceptor to the excited state of the porphyrin and hence transports the electron from the terminal porphyrin to the electrode through the d orbitals of the cobalt center. Whereas Fe and Zn complexes displayed similar performance, since they can transport electrons through the π^* orbitals of the terpyridine solely since the d orbitals of Fe are higher than the ground state of porphyrin, while those of Zn are fully occupied.

In 2012, they also reported the construction of ferrocene-terminated heterometallic complex wires, containing both $[Co(tpy)_2]^{2+}$ and $[Fe(tpy)_2]^{2+}$ complexes as electron relays between the ferrocene and the gold surface **figure 2.4**.[8] In this work, the authors argued that the electron transfer properties can be modulated by the alignment of metal ions. For instance, they proved that the electron transfer rate constants from the ferrocene to the gold electrode were twice faster in **(a)** when the cobalt is directly connected to the gold electrode with respect to **(b)**, which has an inverse order of metallic centers. It is assumed that the first step involves an electron transfer from the ferrocene to the Co center followed by injection of an electron to the electrode. Thus, by changing the order of metals, the distance between the cobalt center and the electrode is modulated which undoubtedly influences the electron transfer rate.

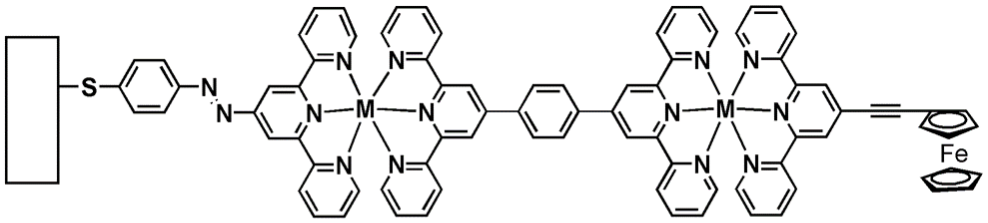

(a) M = Co^{2+} M' = Fe^{2+}
(b) M = Fe^{2+} M' = Co^{2+}

Figure 2.4: Ferrocene-$[Co(tpy)_2]^{2+}$ -$[Fe(tpy)_2]^{2+}$ wire immobilized on gold

One of the few examples that contain three different metallo-ligands assembled together was reported recently based on terpyridyl complexes of osmium, ruthenium and iron connected together with Cu^{2+} ions as a linker **figure 2.5**.[9] This system exhibited a variety of redox peaks corresponding to the individual complexes, which evidences the interaction among the three different metallic centers. Moreover, the addition of external stimuli like NO^+, H_2O and Et_3N lead to the consecutive oxidation of the osmium and iron forming systems of (Os^{2+}-Ru^{2+}-Fe^{2+}; Os^{3+}-Ru^{2+}-Fe^{2+} and Os^{3+}-Ru^{2+}-Fe^{3+}). In other words, this hetero triad can function as a Boolean logic gate at the molecular level. More importantly, this report is one of the rare demonstrations of the robustness of the stepwise technique, by which the construction of the layers was monitored by several techniques (contact angle, Atomic force spectroscopy AFM, Ellipsometry, X-ray photon-electron spectroscopy and Near-Edge X-Ray absorption fine structure spectroscopy) and suggests the formation of uniform films.

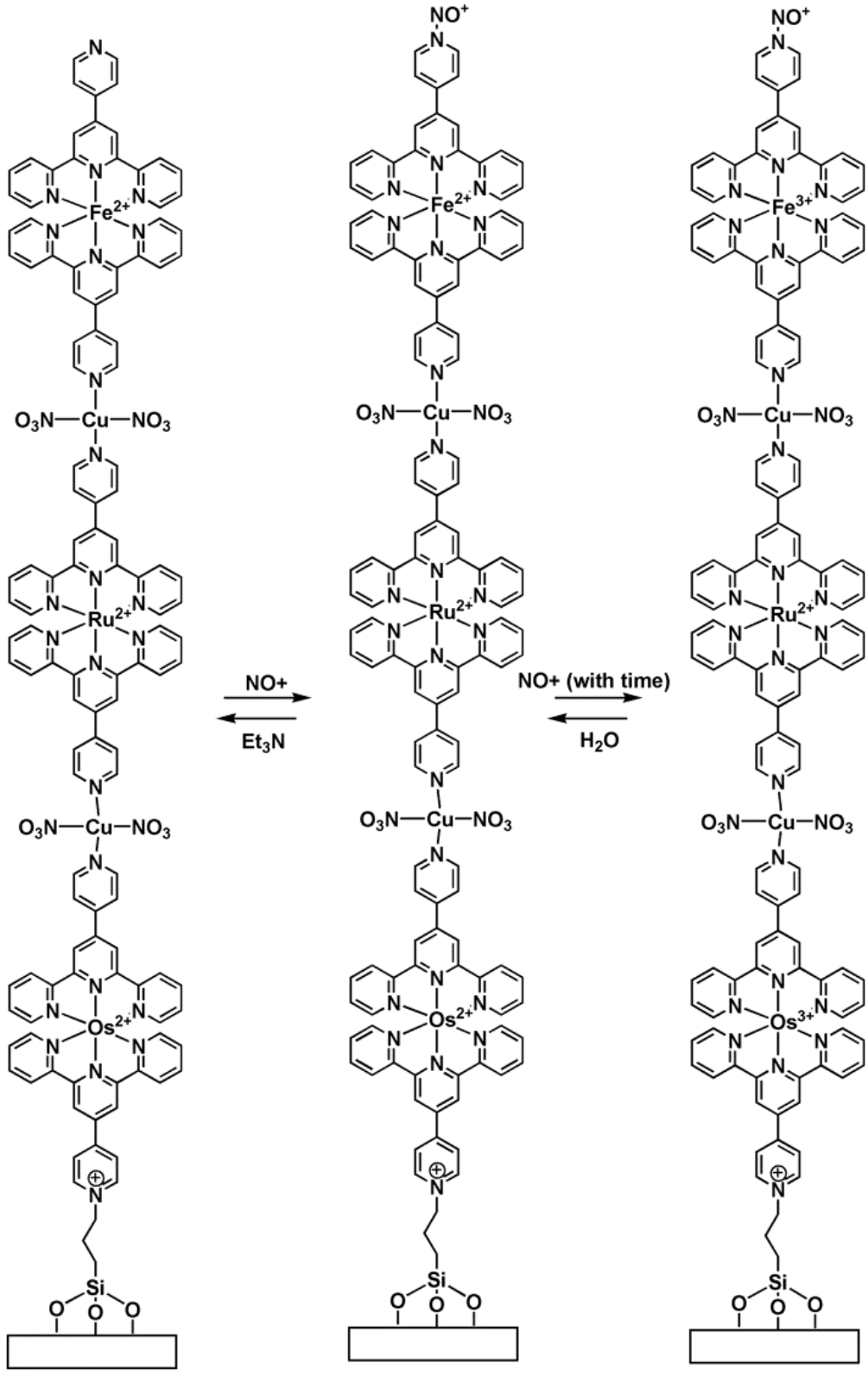

Figure 2.5: Immobilized $[Os(tpy)_2]^{2+}$ - $[Ru(tpy)_2]^{2+}$ -$[Fe(tpy)_2]^{2+}$ triad

Nowadays, it remains a challenge to immobilize triads containing donor-photosensitizer-acceptor moieties onto surfaces, for it is expected that the order and presence of electron relays to have an important influence on the photo-to-electric conversion. For instance, Imahori et

al. showed an elegant illustration of the importance of both electron and energy transfer on the output of the light to current conversion.[10] In this work, three different systems were immobilized onto gold electrodes containing (a) porphyrin as a photosensitizer; (b) ferrocene -porphyrin-fullerene triad; (c) combination of a ferrocene -porphyrin-fullerene triad reaction center with a BODIPY **figure 2.6**.

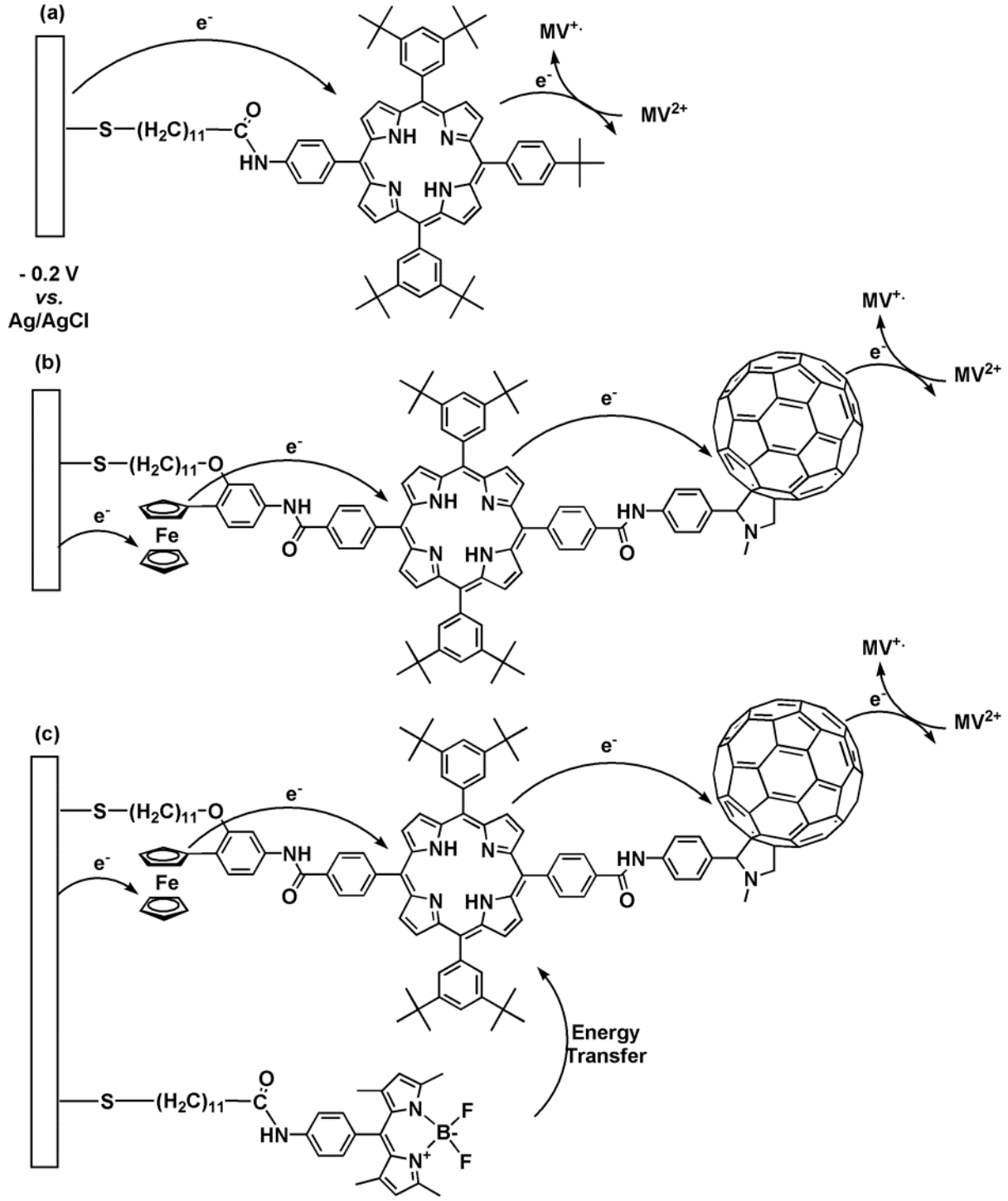

Figure 2.6: (a) Immobilized porphyrin on a a gold electrode; (b) Immobilized ferrocene-porphyrin-fullerene triad on a gold electrode; (c) Mixed layers containg a ferrocene-porphyrin-fullerene triad and a BODIPY immoblized on gold

The authors tested the efficiency of these systems to produce current upon irradiation, with an applied bias of –200 mV *vs.* Ag/AgCl and in the presence of a sacrificial electron acceptor. All of these systems were successful in producing current, yet with tremendous differences in their performance efficiency. While with system **(a)** the authors reported an efficiency of 1.8 $\pm$ 0.3% at 430 nm, **(b)** generated a cathodic current with an efficiency that ranges between 20-25%, and more interestingly **(c)** lead to superior values reaching 50%. This enhancement in the output of photocurrent can be easily rationalized in terms of cascade electron transfer and energy transfer. Photocurrent generation in complex **(a)** involves a simple electron transfer from the gold electrode to the excited porphyrin moiety, which is then regenerated from the methyl viologen present in solution. However, the process in **(b)** is more complex and requires multiple electron transfers. The process can be summarized as follow: A photoinduced electron transfer takes place from the excited porphyrin to the fullerene C_{60} followed by an efficient charge-shift from the ferrocene to the resulting porphyrin radical cation, to yield the final charge separated state, Fc^{+}-P-$C_{60}^{\cdot-}$. The $C_{60}^{\cdot-}$ moiety in the charge-separated state gives an electron to a charge carrier such as MV^{2+} , whereas an electron is donated from the gold electrode to the Fc^{+} moiety. It is suggested by the authors, that this cascade of electrons is indeed responsible for the improvement of the photocurrent. Furthermore, system **(c)** incorporated BODIPY which acts as an extra antenna molecule. Luckily, it can readily undergo an energy transfer to the porphyrin moiety. Thus, the introduction of this unit enables more efficient utilization of larger range of wavelengths which reflects in a better behavior.

Triads based on platinum pyridyl complexes as photosensitizers grabbed particular attention. Recently Suzuki et al. reported the synthesis and immobilization of a naphthalenediimide-bipyridine diacetylide platinum (II) - dimethoxytriphenylamine triad on gold and introduced in a solar cell **figure 2.7**.[11] The gold immobilized triad **(a)** generated a photocurrent upon irradiation in an aqueous solution containing sodium ascorbate as a sacrificial electron donor, yet with low photon-to-current conversion efficiency (ICPE) estimated to be 0.011% at 403 nm. This system was also incorporated in a dye sensitized solar cell FTO/TiO_2/electrolyte (LiI-I_2)/Pt by which an analogous triad bearing a carboxylate was adsorbed on the tin oxide. Indeed, poor energy conversion efficiency was recorded with a value of 0.20%. The authors attributed that to the bent shape of the triad which most probably leads to an electrical short circuit between the donor and the TiO_2. This is indeed another demonstration of the importance of the arrangement of the assemblies in such photo-electric applications.

Surprisingly, none of the latest work was based on the prototype $[Ru(bpy)_3]^{2+}$, regardless of its outstanding photophysical properties as discussed in earlier chapters. This could be mainly attributed to the increased challenge in obtaining linear assemblies, and thus controlling the orientation of molecules on surfaces which has proven to be a crucial factor in photo-electric devices.[12] Furthermore, few of the reported triads are purely metallic in nature, despite the importance of incorporation of transition metals as electron donors or acceptors since they can

offer oxidized and reduced systems with better stability and with multiple redox or spin state.

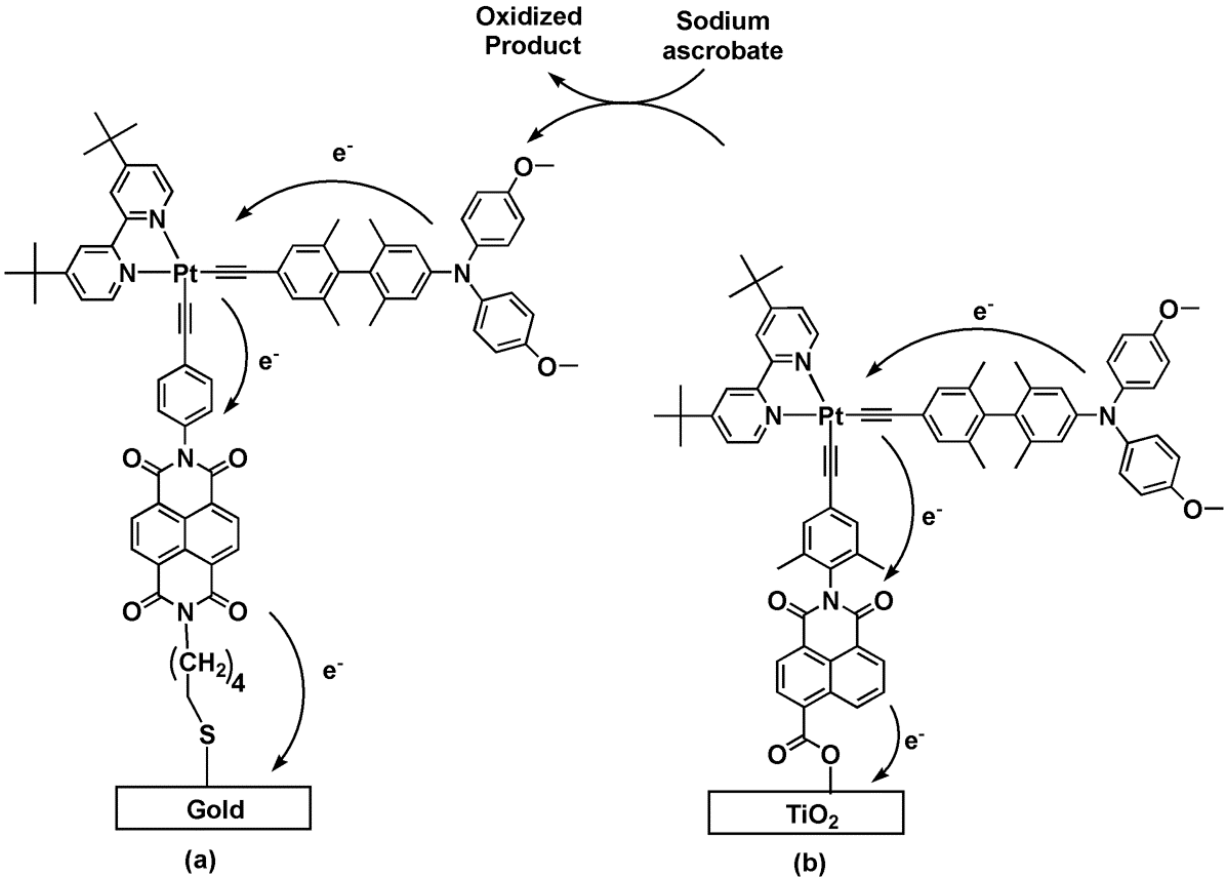

Figure 2.7: (a) Naphthalenediimide- bipyridine diacetylide platinum (II) - dimethoxytriphenylamine triad on gold; (b) naphthalenediimide- bipyridine diacetylide platinum (II) - dimethoxytriphenylamine triad on tin oxide

Herein, we will discuss our efforts to construct $[Ru(bpy)_3]^{2+}$ based trimetallic dyads and triads on different surfaces (ITO, gold and silicon oxide) adopting a stepwise methodology **figure 2.8**. Moreover, we will study the factors that tune the photo-electric conversion power of the system. Terpyridyl complexes of cobalt and iron were selected to act as electron acceptors and donors following the results obtained in **Chapter 1**. Moreover, it has been evidenced that molecular wires containing bis terpyridyl complexes exhibit one dimensional ordered structures and display redox conduction through the molecular wire using their redox-active d orbital electrons.[13] Thus, this type of electron transfer is expected to contribute to enhanced photo-electron transport as well, along with the linear structures which are awaited to help control the orientation of the assemblies.

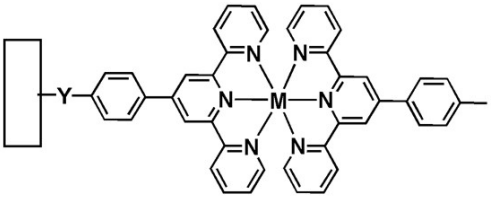

ITO/[Fe(tpy)$_2$] M = Fe; Y = $CH_2PO_3^{2-}$

ITO/[Co(tpy)$_2$] M = Co; Y = $CH_2PO_3^{2-}$
Au/[Co(tpy)$_2$] M = Co; Y = S^-

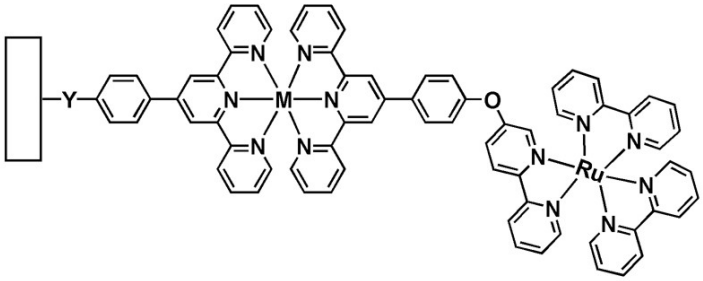

ITO/[Zn(tpy)$_2$]O[Ru(bpy)$_3$] M = Zn; Y = $CH_2PO_3^{2-}$
Au/[Zn(tpy)$_2$]O[Ru(bpy)$_3$] M = Zn; Y = S^-

ITO/[Fe(tpy)$_2$]O[Ru(bpy)$_2$] M = Fe; Y = $CH_2PO_3^{2-}$

ITO/[Co(tpy)$_2$]O[Ru(bpy)$_3$] M = Co; Y = $CH_2PO_3^{2-}$
Au/[Co(tpy)$_2$]O[Ru(bpy)$_3$] M = Co; Y = S^-

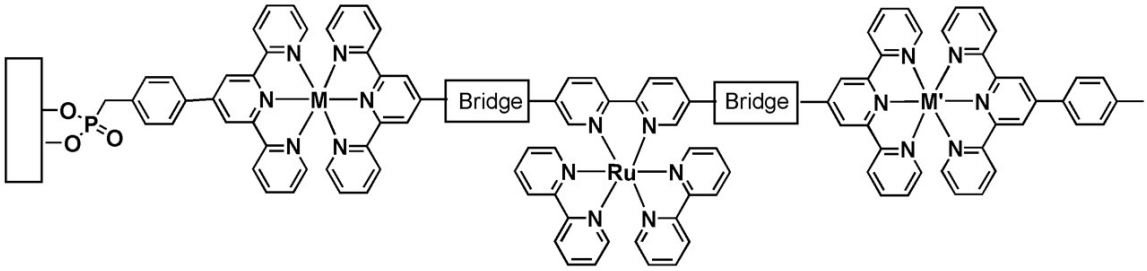

ITO/[Co(tpy)$_2$]O[Ru(bpy)$_3$]O[Fe(tpy)$_2$] M = Co; M' = Fe; bridge = ether
ITO/[Zn(tpy)$_2$]O[Ru(bpy)$_3$]O[Fe(tpy)$_2$] M = Zn; M' = Fe; bridge = ether

ITO/[Co(tpy)$_2$]Φ[Ru(bpy)$_3$]Φ[Fe(tpy)$_2$] M = Co; M' = Fe; bridge = phenylene
SiO_2/[Co(tpy)$_2$]Φ[Ru(bpy)$_3$]Φ[Fe(tpy)$_2$] M = Co; M' = Fe; bridge = phenylene

Figure 2.8: Schematic drawing of the fabricated dyads and triads

2.2 Immobilized Dyads [M(tpy)$_2$]-[Ru(bpy)$_3$]

2.2.1 Preparation of Surfaces

Several dyads consisting of a $[Ru(bpy)_3]^{2+}$ as a light harvesting entity and terpyridyl complexes of iron, cobalt and zinc are immobilized on electrodes (Au or ITO) and are denoted by Electrode/[Fe(tpy)$_2$]O[Ru(bpy)$_3$], Electrode/[Co(tpy)$_2$]O[Ru(bpy)$_3$] and Electrode/[Zn(tpy)$_2$]O [Ru(bpy)$_3$] respectively. Gold electrodes were selected because they have excellent thermal and electric conductivity, and these functionalized surfaces are used in order to study electron transfer rates. On the other hand, the dyads immobilized on ITO are used for photo-electric conversion taking advantage of the transparency of the electrode which allows maximum light absorption. As previously stated, first row transition metals are known for the kinetic lability of their coordination sphere, which means that they are in a constant ligand exchange process in solution. This makes it challenging to isolate the heteroleleptic form of their corresponding terpyridyl complexes. To lessen the ligand exchange rate, the dyads are fabricated directly on gold or ITO electrodes by a combination of the SAM formation with a suitable terpyridine derivative, followed by a stepwise metal-terpyridine coordination reaction.

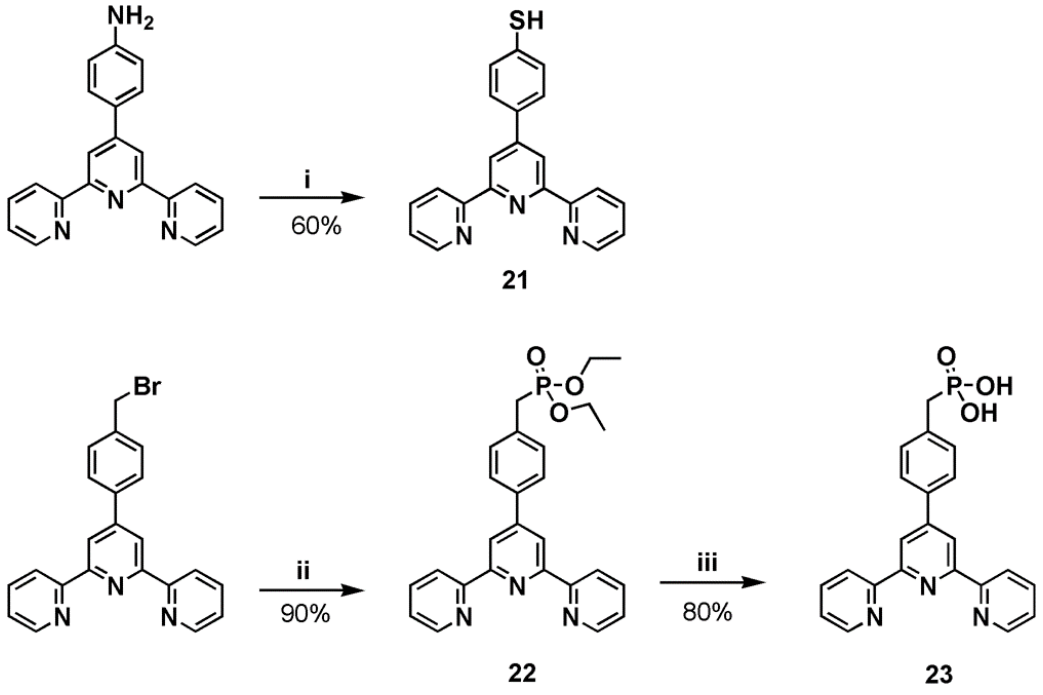

Figure 2.9: Functionalization of terpyridine, (i) HCl, $NaNO_2$, H_2O, 0 °C; AcONa, 0 °C, pH = 4; KSAc, H_2O, 10 min, 80 °C, 1 h; KOH , EtOH, 80 min, 80 °C, NH_4Cl, H_2O, 80 °C; (ii) $P(OCH_2CH_3)_3$, 24 h; 160 °C; (iii) TMSBr, CH_2Cl_2, 24 h, 25 °C; CH_3OH , 2 h, 25 °C

In this context, we synthesized **21** according to previously reported literature, by which it is well known that the thiol instantaneously adsorbs onto gold surfaces forming covalent and

stable bonds **figure 2.9**.[14] We also developed a methodology to introduce phosphonates on a terpyridine ligand **23** to aid the attachment with the hydroxylated ITO surfaces **figure 2.9**. The preparation of **23**, is a straightforward two step synthesis with almost quantitative yields. Initially 4',4-[(bromomethyl)phenyl]-2,2':6',2"-terpyridine undergoes a substitution reaction to form intermediate **22**, followed by deprotection of the phosphonic ester to yield compound **23**.

It is not easy to connect ruthenium ions at the surface using the stepwise chemistry, because the rate constant of complexation of a ruthenium ion with polypyridine ligand is very slow. Accordingly, we synthesized a metallo ligand consisting of a $[Ru(bpy)_3]^{2+}$ bearing a free terpyridine coordination site **Ru-O-tpy**. The synthesis, electrochemical and photophysical characterization of this complex were detailed previously. This photoactive subunit **Ru-O-tpy** is hence used for the stepwise construction of the dyads on the surface. The preparation of surfaces is summarized in **figure 2.3**.

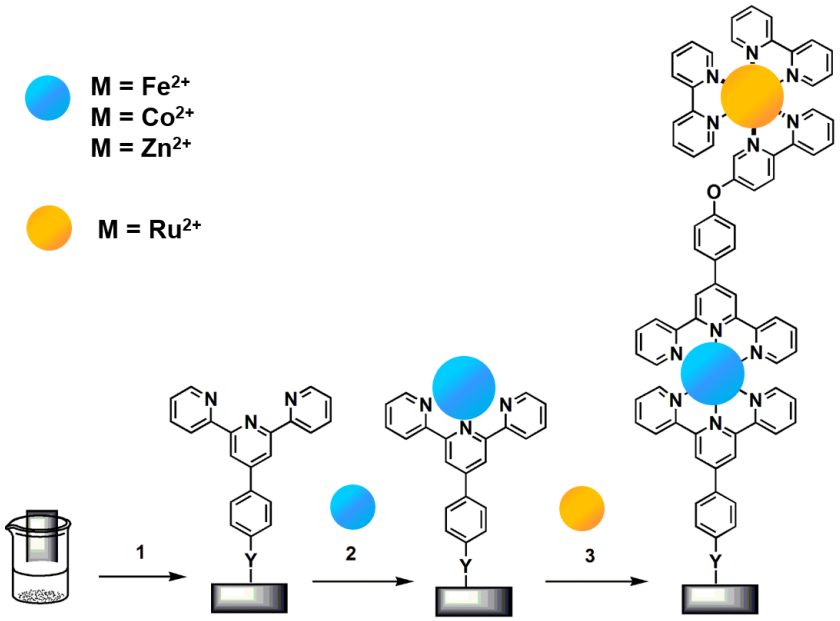

Figure 2.10: Stepwise assembly of the dyads $[Fe(tpy)_2]O[Ru(bpy)_3]$, $[Co(tpy)_2]O[Ru(bpy)_3]$ and $[Zn(tpy)_2]O[Ru(bpy)_3]$ on gold/ITO surfaces, for clarity charges have been omitted

Both gold and ITO electrodes are prepared similarly. Nonetheless, herein we will just detail the preparation of the ITO surfaces. ITO electrodes were purchased from Solems, and cleaned by consecutive sonication in acetone and ethanol. Then they were dried by a stream of argon and used for the preparation of dyads. Then the cleaned electrodes are immersed in a 10^{-3} M solution of the desired terpyridine over a period of 24 hours (**21** is used for grafting on gold surfaces and **23** is used to immobilize on ITO electrodes). The modified surface is cleaned and dipped in an ethanolic solution of the desired metal source $[M(BF_4)_2]^{2+}$ for 2-3 hours for metal-terpyridine reaction. After thorough rinsing, the surface is dipped again in a 10^{-3} M ethanolic solution of the photoactive **Ru-O-tpy** unit for 24 h to afford the desired target dyads. Mono-

layers of the terpyridyl complexes of iron and cobalt namely ITO/[Fe(tpy)$_2$], ITO/[Co(tpy)$_2$] respectively were also prepared in a similar manner. The only difference is in step 3 by which the system is capped with a 4',4-[(methyl)phenyl]-2,2':6',2"-terpyridine instead of the photoactive unit.

2.2.2 *Electrochemistry*

The SAMs are mainly characterized by cyclic voltammetry (CV). The CVs are recorded on the functionalized substrates as working electrodes in acetonitrile in the presence of 0.1 M of [Bu$_4$N]ClO$_4$ **figure 2.11**. All the redox potentials are collected in **table 2.1**.

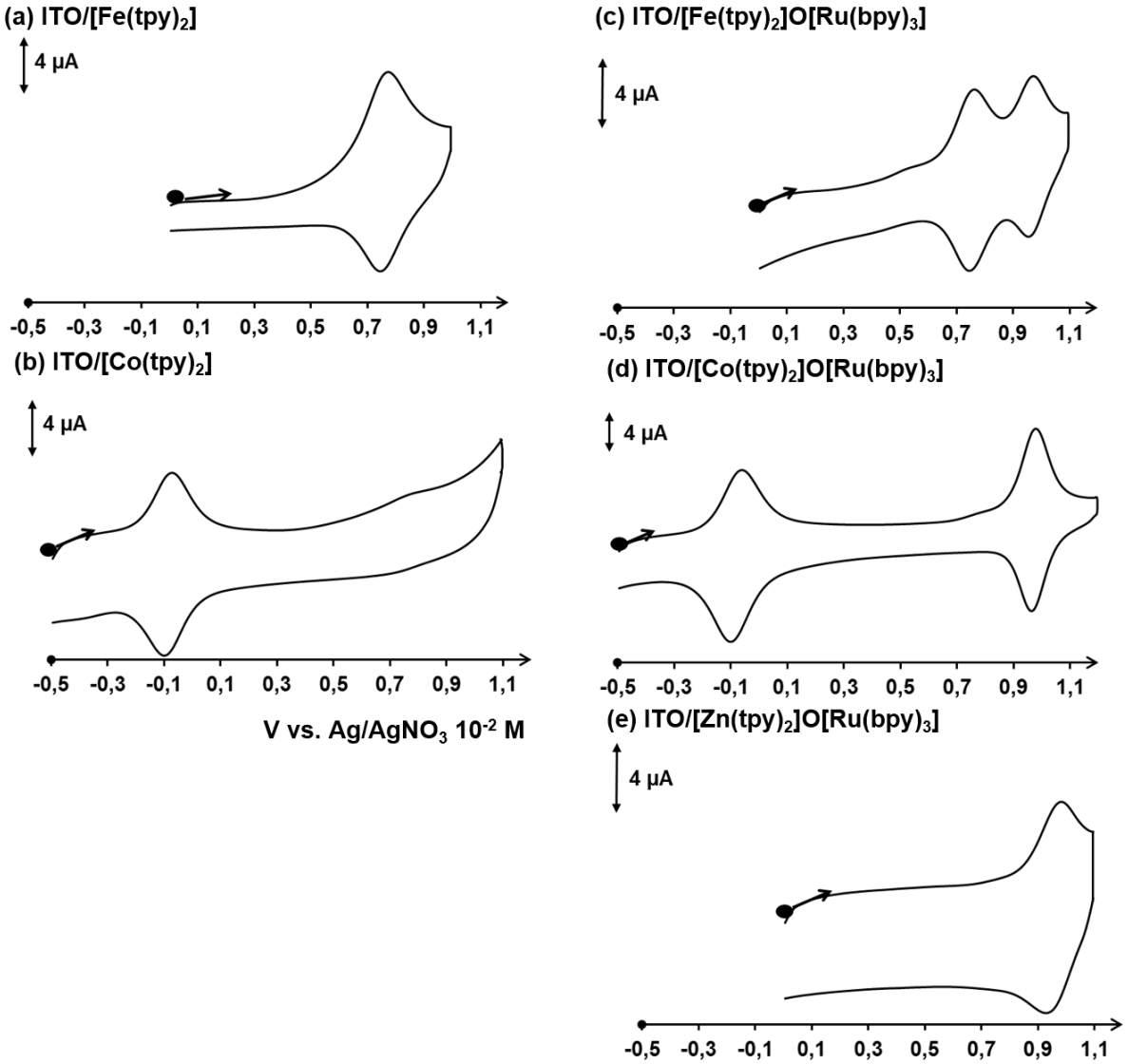

Figure 2.11: Cyclic voltammetry (CV) of the SAMs in CH_3CN + 0.1 M [Bu$_4$N]ClO$_4$ *vs* Ag/AgNO$_3$ (10^{-2} M) at a scan rate = 100 mV.s^{-1} (a) ITO/[Fe(tpy)$_2$]; (b) ITO/[Co(tpy)$_2$]; (c) ITO/[Fe(tpy)$_2$]O[Ru(bpy)$_3$]; (d) ITO/[Co(tpy)$_2$]O[Ru(bpy)$_3$]; (e) ITO/[Fe(tpy)$_2$]O[Ru(bpy)$_3$]

The immobilized ITO/[Fe(tpy)$_2$] exhibits an oxidation peak around 0.75 V which is similar to the oxidation of [Fe(tpy)$_2$]$^{2+}$ in solution with a 10 mV shift and can be attributed to the mono-electronic oxidation of the Fe center (Fe^{3+}/Fe^{2+}). This slight modification of oxidation potential between solution and the modified surface could be the result of the different electron transfer modes between the surface and solution, by which it is diffusion dependent in the former. Similarly, the CV of ITO/[Co(tpy)$_2$] shows an oxidation at –0.07 V which is identical to the Co^{3+}/Co^{2+} oxidation of the [Co(ttpy)$_2$]$^{2+}$ in solution.

Table 2.1: Redox potentials of modified surfaces ITO/[Fe(tpy)$_2$], ITO/[Co(tpy)$_2$], ITO/[Fe(tpy)$_2$]O[Ru(bpy)$_3$], ITO/[Co(tpy)$_2$]O[Ru(bpy)$_3$] and ITO/[Zn(tpy)$_2$]O[Ru(bpy)$_3$] in a solution of CH_3CN + 0.1 M [Bu_4N]ClO_4 *vs* $Ag/AgNO_3$ (10^{-2} M) at a scan rate 100 mV.s^{-1}

$E^{ox}_{1/2}$ (V) (ΔE_p, mV)	Fe^{3+}/Fe^{2+}	Co^{3+}/Co^{2+}	Ru^{3+}/Ru^{2+}
ITO/[Fe(tpy)$_2$]	0.75 (15)	-	-
ITO/[Co(tpy)$_2$]	-	–0.07 (15)	-
ITO/[Fe(tpy)$_2$]O[Ru(bpy)$_3$]	0.76 (10)	-	0.96 (15)
ITO/[Co(tpy)$_2$]O[Ru(bpy)$_3$]	-	–0.07 (10)	0.96 (10)
ITO/[Zn(tpy)$_2$]O[Ru(bpy)$_3$]	-	-	0.96 (15)

In the dyad ITO/[Zn(tpy)$_2$]O[Ru(bpy)$_3$], only one oxidation peak is recorded in the positive region around 0.96 V. This process is attributed to the oxidation of the ruthenium center ($E_{1/2}$ = 1.03 V in solution), whereas the zinc metal is redox inactive, and thus is not associated with an oxidation/reduction signal. In multinuclear complexes, the electronic interactions between the metal centers are of major importance in determining the physical, photophysical and chemical behavior of the compounds. In terms of electrochemistry, the coupling of adjacent metal centers generally results in a shift of the redox potential relative to the mononuclear fragments. The electrochemical responses of the metal centers in dyads ITO/[Fe(tpy)$_2$]O[Ru(bpy)$_3$] and ITO/[Co(tpy)$_2$]O[Ru(bpy)$_3$] are identical to those of the immobilized subunits. This certifies that there is no electronic coupling between the different metallic centers as ensured by the ether linkage. This conclusion is supported by earlier results of the electrochemical behavior of the respective trimetallic complexes Ru-Co-Ru and Ru-Fe-Ru in solution. In addition, this also allows the unambiguous assignment of the signals to their corresponding metal centers. For ITO/[Fe(tpy)$_2$]O[Ru(bpy)$_3$] the peak at 0.76 V is the result of the Fe^{3+}/Fe^{2+} oxidation, while the more positive peak at 0.96 V is due to the Ru^{3+}/Ru^{2+} process. Likewise the oxidation at –0.07 V is associated to the Co^{3+}/Co^{2+} and that at 0.96 V to the Ru^{3+}/Ru^{2+} couple in dyad ITO/[Co(tpy)$_2$]O[Ru(bpy)$_3$].

Thorough analysis of the cyclic voltammograms can allow the extraction of two important parameters. To begin with, the linear dependence of the peak current to the scan rate for the different redox couples in the respective dyads **figure 2.12** indicates that they are surface confined

species.

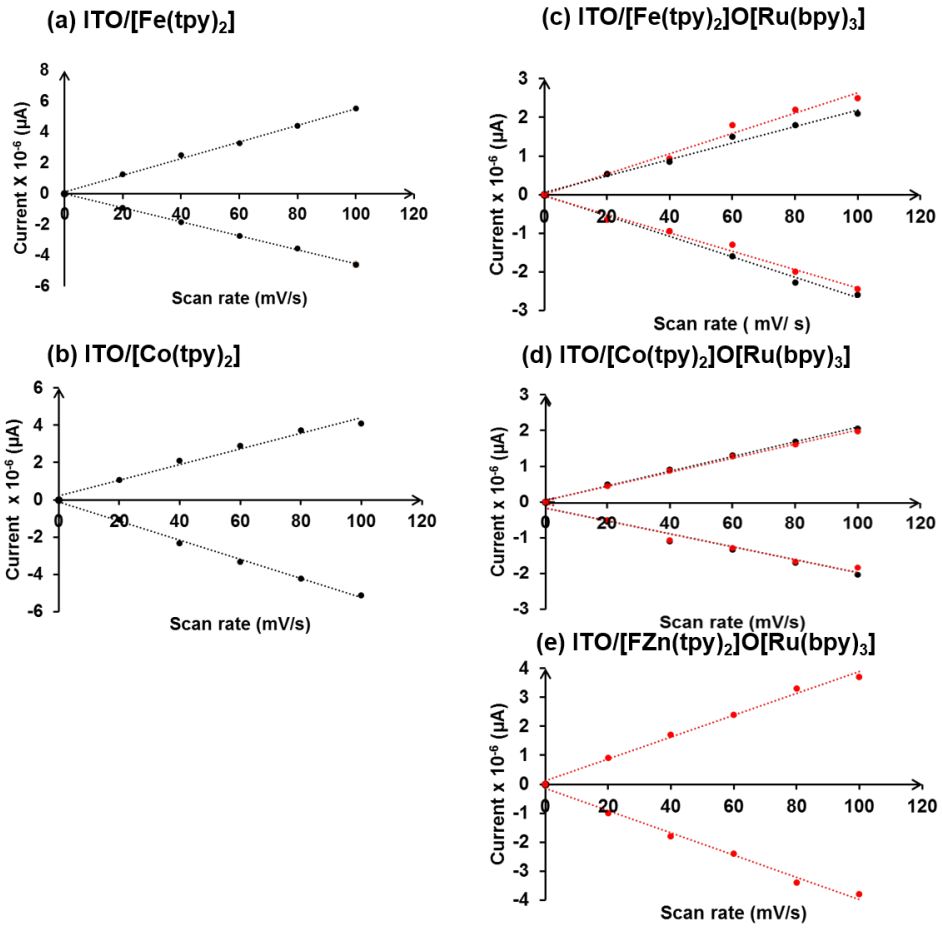

Figure 2.12: Plotting of current *vs.* scan rate for the SAMs (a) ITO/[Fe(tpy)$_2$]; (b) ITO/[Co(tpy)$_2$]; (c) ITO/[Fe(tpy)$_2$]O[Ru(bpy)$_3$]; (d) ITO/[Co(tpy)$_2$]O[Ru(bpy)$_3$]; (e) ITO/[Fe(tpy)$_2$]O[Ru(bpy)$_3$]

Moreover, the surface coverage Γ of the electroactive centers in the film were estimated from the electric charge of the redox reactions using **equation 2.1**:

$$\Gamma = \frac{Q}{nFA} \tag{2.1}$$

where Q (C) is the charge required to oxidize the metallic center determined from the area under the oxidation peak of M^{2+}/M^{3+}, n the number of electrons transferred (n = 1), F the Faraday's constant (96485 C.mol^{-1}) and A (cm^2) the area of the electrode.

The results are summarized in **table 2.2**. The values obtained are in the order of 10^{-11} mol.cm^{-2} and are consistent with literature for similar stepwise assembled layers on gold and ITO surfaces.[7;15] By the help of the theoretical chemistry group in our department, we calculated the size of the molecular dyads on gold surfaces and the results are presented in **figure 2.13**.

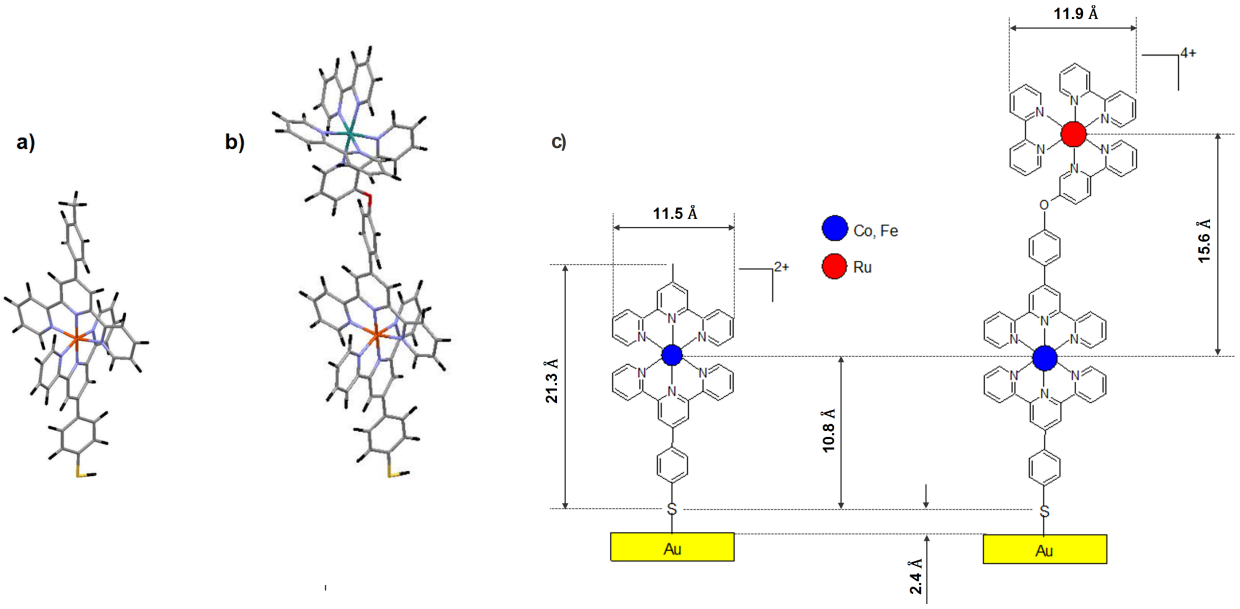

Figure 2.13: Modelling of the complexes (a) Au/[Fe(tpy)$_2$] (b) Au/[Fe(tpy)$_2$]O[Ru(bpy)$_3$]

The dimensions of the dyad is assumed to be similar on gold and ITO. From this modelling a maximum surface coverage of the SAM should be about 1.7×10^{-10} mol.cm^{-2}, suggesting a 27-37% coverage of the theoretical value. Regarding the molecular dyads on Au surface **figure 2.13.(b)**, although the [Ru(bpy)$_3$]$^{2+}$ unit has a projected area of 1.1 nm^2, its area does not overlap with the terpyridine groups, making the overall area slightly larger.

Indeed, comparable surface coverage's were estimated for dyads ITO/[Fe(tpy)$_2$]O[Ru(bpy)$_3$] $\Gamma_{Ru} = 2.5 \times 10^{-11}$ and $\Gamma_{Fe} = 3.0 \times 10^{-11}$ mol.cm^{-2}, ITO/[Co(tpy)$_2$]O[Ru(bpy)$_3$] are $\Gamma_{Ru} = 3.1 \times 10^{-11}$ and $\Gamma_{Co} = 3.2 \times 10^{-11}$ mol.cm^{-2} and the respective monolayers. Moreover, the similar values indicate the reproducibility of the preparation of the films and verifies that almost all the cobalt and iron units are connected to ruthenium photoactive subunits.

Table 2.2: Surface coverage of modified surfaces ITO/[Fe(tpy)$_2$], ITO/[Co(tpy)$_2$], ITO/[Fe(tpy)$_2$]O[Ru(bpy)$_3$], ITO/[Co(tpy)$_2$]O[Ru(bpy)$_3$] and ITO/[Fe(tpy)$_2$]O[Ru(bpy)$_3$]

Surface coverage Γ ($mol.cm^{-2}$)	Fe peak	Co peak	Ru peak
ITO/[Fe(tpy)$_2$]	3.1×10^{-11}	-	-
ITO/[Co(tpy)$_2$]	2.5×10^{-11}	-	-
ITO/[Fe(tpy)$_2$]O[Ru(bpy)$_3$]	3.0×10^{-11}	-	2.5×10^{-11}
ITO/[Co(tpy)$_2$]O[Ru(bpy)$_3$]	-	3.2×10^{-11}	3.1×10^{-11}
ITO/[Zn(tpy)$_2$]O[Ru(bpy)$_3$]	-	-	4.8×10^{-11}

In the frame of a master 2 internship, these dyads were also grafted onto gold surfaces in order to study the rate of electron transfer using the Laviron method with potential sweep

voltammetry.[16] Considering a half reaction Ox + $ne^- \rightarrow$ Re where Ox and Re are the oxidized and reduced form of the same species respectively, Laviron showed a relation between the change in its redox potential upon altering scan rate. Thus, the kinetic rate of electron transfer between the electrode and the metal center k_{ET} can be extracted from the plot of the variation of potential with different scan rates.[16] We therefore anchored the complexes on gold microelectrodes to minimize resistance and capacitive current and kinetic rate was only taken into account at high scan rates (ν > 20 V/s). The values obtained for Au/[Co(tpy)$_2$], Au/[Zn(tpy)$_2$]O[Ru(bpy)$_3$] and Au/[Co(tpy)$_2$]O[Ru(bpy)$_3$] are summarized in **table 2.3**. Although it is not accurate to compare k_{ET} values obtained with different methods, it still provides us with general information on the overall process. The rate of electron transfer k_{ET} reported for our systems are smaller than those calculated for analogous [Co(benzylmercaptotpy)$_2$]$^{3+}$ using chronoamperometry.[15] The absence of the methylene spacer between the thiol and the phenyl in our system will most probably slow down the electron transfer rate from the cobalt to the electrode due to increased geometrical constraints. Regarding the dyad consisting of two electroactive units Au/[Co(tpy)$_2$]O [Ru(bpy)$_3$] the k_{ET} is estimated to 3900 $\pm$ 1000 and 4200 $\pm$ 1600 s^{-1} for the Co^{3+} and Ru^{2+} centers respectively. In these systems, the electron transfer from the Ru^{2+} to the electrode can take place either by super exchange current with the electrode or through a hopping mechanism from the Ru^{2+} to the Co^{3+} core which in turn injects an electron to the surface. Comparing the k_{ET} of the Ru^{2+} centers in dyads Au/[Zn(tpy)$_2$]O[Ru(bpy)$_3$] and Au/[Co(tpy)$_2$]O[Ru(bpy)$_3$] suggests that the hopping mechanism is the dominant pathway in the latter. This also shows that the rate of intramolecular electron transfer is faster than the direct electron injection from the Co^{3+} to the electrode rendering the latter the rate limiting step in such systems. Furthermore, the difference of k_{ET} values of electron injection from the Co^{3+} to the electrode between Au/[Co(tpy)$_2$] and Au/[Co(tpy)$_2$]O[Ru(bpy)$_3$] are justified with different reorganization energy due to the different substitution on the para position of the terpyridine ligand as detailed in **Chapter 1**. The presence of the rigid and bulky groups Ru-O-tpy in Au/[Co(tpy)$_2$]O[Ru(bpy)$_3$] will most probably increase the reorganization energy which slows down the electron transfer rate. This is reflected by the decrease of k_{ET} from 7900 $\pm$ 1500 to 4200 $\pm$ 1600 s^{-1} as going from the more flexible system Au/[Co(tpy)$_2$] to the more strained one Au/[Co(tpy)$_2$]O[Ru(bpy)$_3$]. Unfortunately, the Laviron method doesn't give access to the reorganization energy value.

Table 2.3: Electron transfer rate k_{ET} in the immobilized Au/[Co(tpy)$_2$]; Au/[Zn(tpy)$_2$]O[Ru(bpy)$_3$] and Au/[Co(tpy)$_2$]O[Ru(bpy)$_3$]

Immobized Surface	Au/[Co(tpy)$_2$]	Au/[Zn(tpy)$_2$]O[Ru(bpy)$_3$]	Au/[Co(tpy)$_2$]O[Ru(bpy)$_3$]	
	Co^{3+}	Ru^{2+}	Co^{3+}	Ru^{2+}
k_{ET} (s^{-1})	7900 $\pm$ 1500	1600 $\pm$ 300	3900 $\pm$ 1000	4200 $\pm$ 1600

2.2.3 *Photophysics*

The absorption spectra of the dyads ITO/[Fe(tpy)$_2$]O[Ru(bpy)$_3$] , ITO/[Co(tpy)$_2$]O[Ru(bpy)$_3$] and ITO/[Zn(tpy)$_2$]O[Ru(bpy)$_3$] are measured and the values are collected in **table 2.4**. These films have poor absorption due to small surface coverages, yet, we were still able to detect signals which were correlated to the individual building blocks **figure 2.14**. To begin with, ITO/[Fe(tpy)$_2$]O[Ru(bpy)$_3$] exhibits two λ_{max}^{abs} with values = 461 and 566 nm . The first absorption is a common feature for all dyads and is believed to be the characteristic metal-to-ligand-charge-transfer band (MLCT) of the ruthenium center. This value is shifted to the red with a value of (12 nm) as compared to the solution (acetonitrile) spectrum, such a shift has also been evidenced in the literature with similar systems.[9;10] The peak at higher wavelength is comparable with the MLCT band of [Fe(tpy)$_2$]$^{2+}$ in solution. In ITO/[Co(tpy)$_2$]O[Ru(bpy)$_3$], the signature of [Co(tpy)$_2$]$^{2+}$ was not detected due to the small extinction coefficient and low surface coverage.

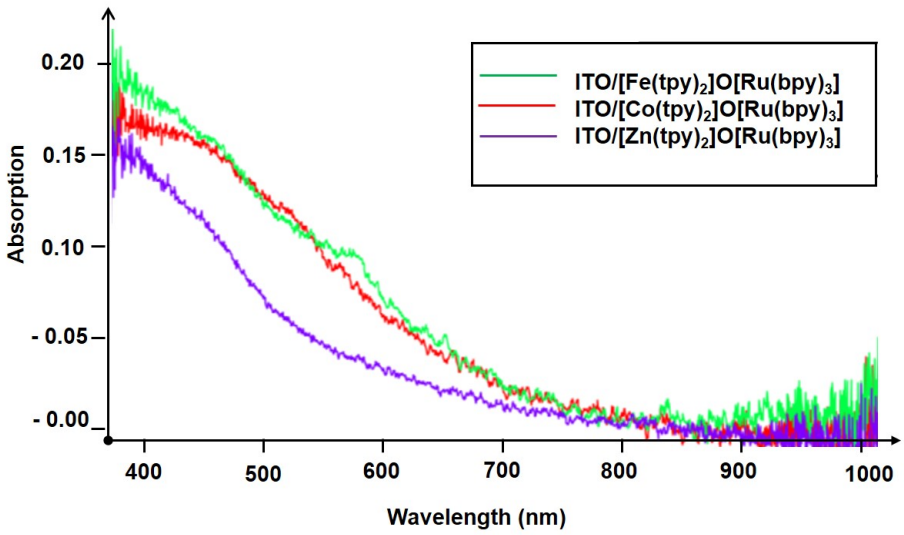

Figure 2.14: The UV-vis absorption spectra of the functionalized surfaces (a) green line corresponds ITO/[Fe(tpy)$_2$]O[Ru(bpy)$_3$]; (b) red line corresponds to ITO/[Co(tpy)$_2$]O[Ru(bpy)$_3$]; (c) purple line corresponds to ITO/[Zn(tpy)$_2$]O[Ru(bpy)$_3$]

Table 2.4: UV-vis and emission properties of functionalized surfaces ITO/[Fe(tpy)$_2$]O[Ru(bpy)$_3$]; ITO/[Co(tpy)$_2$]O[Ru(bpy)$_3$] and ITO/[Zn(tpy)$_2$]O[Ru(bpy)$_3$]

Functionalized surface	λ_{abs} (nm)	λ_{em} (nm)	Luminescence lifetime τ (s)	
			τ_1	τ_2
ITO/[Fe(tpy)$_2$]O[Ru(bpy)$_3$]	461, 566	608	-	-
ITO/[Co(tpy)$_2$]O[Ru(bpy)$_3$]	461	610	8.5×10^{-10}	9.6×10^{-9}
ITO/[Zn(tpy)$_2$]O[Ru(bpy)$_3$]	461	600	-	8.9×10^{-9}

The luminescence properties of the modified electrodes were detected under microscope at the "Laboratoire de Photophysique et Photochimie Supra et Macromoleculaire, PPSM ENS de Chachan". Time-resolved luminescence lifetime experiments on films were performed using a space- and time-correlated photon-counting photomultiplier (QA) from EuroPhoton GmbH mounted onto a microscope. These films are poorly luminescent, and their emission properties remain difficult to analyze with this experimental setup. Nonetheless, we were able to detect emission signals, in areas of high concentration of molecules, with λ_{em}^{max} around 605 $\pm$ 5 nm of experimental error upon excitation at 512 nm **figure 2.15**. This value is indeed similar to the emission of the photoactive subunit **[3]**$^{2+}$ in acetonitrile, and thus is attributed to the deactivation of the ruthenium core. This weak signal could be the result of the quenching with the ITO electrode or different metallic centers.

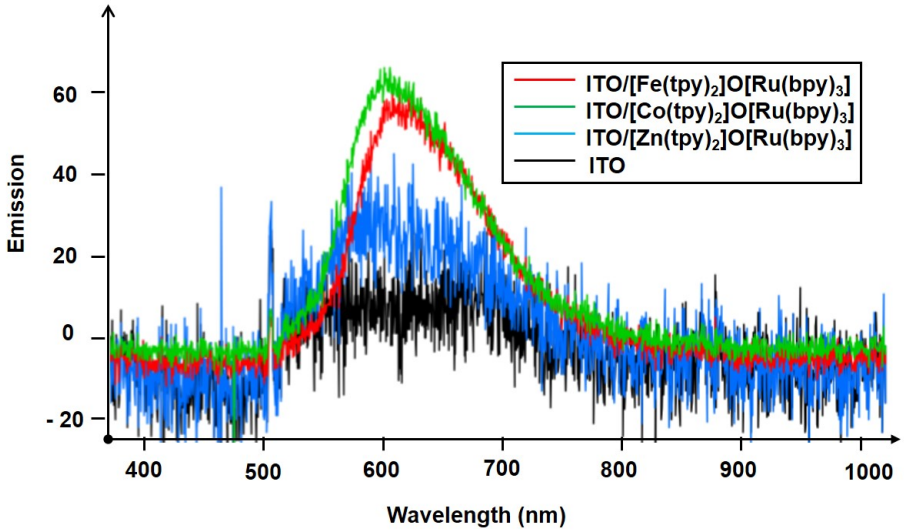

Figure 2.15: Emission spectra of the functionalized ITO surfaces recorded at room temperature upon excitation at 512 nm (a) red line corresponds to ITO/[Fe(tpy)$_2$]O[Ru(bpy)$_3$]; (b) green line corresponds to ITO/[Co(tpy)$_2$]O[Ru(bpy)$_3$]; (c) blue line correspond to ITO/[Zn(tpy)$_2$]O[Ru(bpy)$_3$]; (d) nacked ITO

The luminescent decays of the films were recorded upon excitation at 512 nm **figure 2.16**. The decay in ITO/[Zn(tpy)$_2$]O[Ru(bpy)$_3$] was fitted with a mono-exponential decay wit τ = 8.9 ns. Regarding ITO/[Fe(tpy)$_2$]O[Ru(bpy)$_3$] , the detected luminescence is very weak, and it was difficult to treat the spectrum **figure 2.16**. However, this is a good reflection of the strong quenching of the ruthenium phosphorescence by the iron center through energy transfer as discussed earlier. The decay of ITO/[Co(tpy)$_2$]O[Ru(bpy)$_3$] is bi-exponential and is best fitted to two components τ_1 = 0.85 ns and τ_2 = 9.6 ns. Close examination of these values shows that τ_2 is analogous to that detected for the ITO/[Zn(tpy)$_2$]O[Ru(bpy)$_3$], and is thought to be the luminescence of the ruthenium center without an intervention from the cobalt. Moreover, the first and shorter component is believed to correspond to the quenched emission of ruthenium by the by the Co^{3+} center. As a matter of fact, a similar behavior was detectable for Ru-Co-

Ru **[7]**$^{7+}$ complex in acetonitrile. This shows, that the metal centers are not innocent, and are indeed interacting with the excited state of ruthenium in a manner similar to that reported in solution.

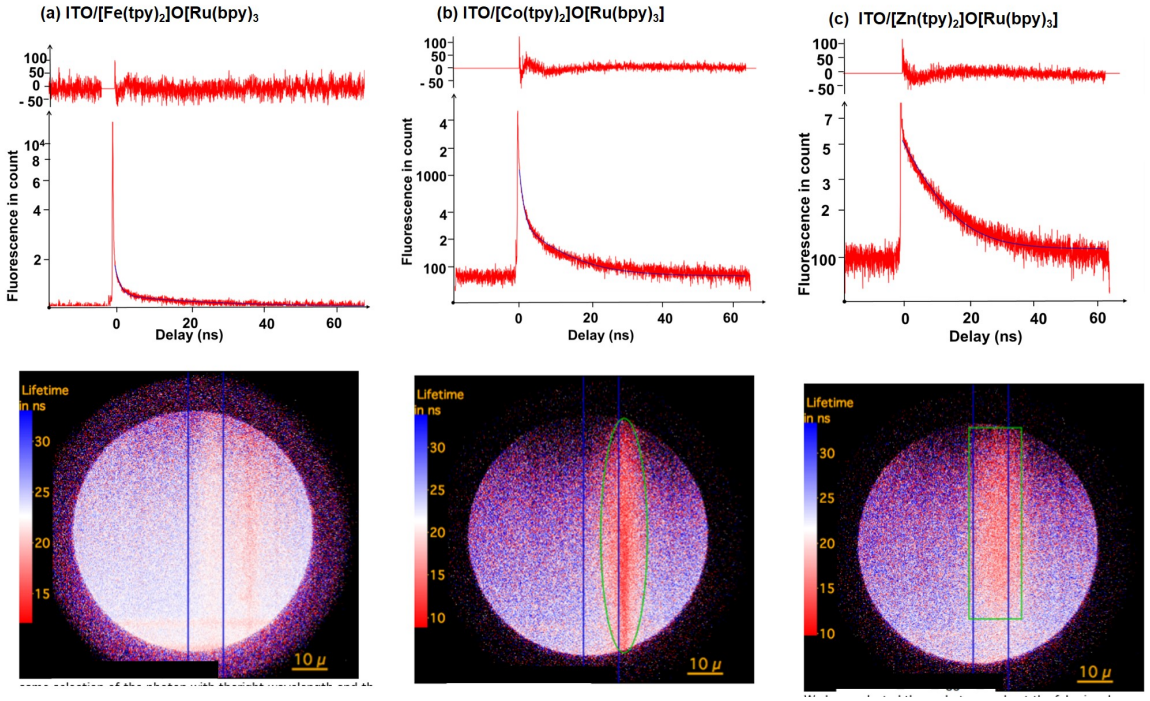

Figure 2.16: Emission properties of the modified surfaces on ITO upon excitation with at 512 nm, emission decay and emission map (a) ITO/[Fe(tpy)$_2$]O[Ru(bpy)$_3$] (b) ITO/[Co(tpy)$_2$]O[Ru(bpy)$_3$] (c) ITO/[Zn(tpy)$_2$]O[Ru(bpy)$_3$]

2.2.4 Anodic Photocurrent with [Co(tpy)$_2$]-[Ru(bpy)$_3$] in the Presence of TEOA

We also investigated the photoelectrochemical properties of the dyads ITO/[Co(tpy)$_2$]O-[Ru(bpy)$_3$] and ITO/[Zn(tpy)$_2$]O[Ru(bpy)$_3$] in the presence of an external electron mediator namely triethanolamine (TEOA) in CH_3CN + 0.1 M $[Bu_4N]ClO_4$. Under these conditions, the bare ITO produced a rather insignificant amount of anodic current upon irradiation. Likewise, ITO/[Co(tpy)$_2$] displayed a minor light gate response upon applying a potential of 0.12 V, and this is most probably due to the bare ITO **figure 2.17.a** . Both dyads comprise the same photoactive center $[Ru(bpy)_3]^{2+}$, yet with different relays between the latter and the ITO. In the case of ITO/[Zn(tpy)$_2$]O-[Ru(bpy)$_3$] the $[Zn(tpy)_2]^{2+}$ has full occupied d orbitals, and serves as a spacer between the ruthenium center and the electrode. Thus we can safely assume that in both dyads, the ruthenium is maintained at the same distance from the electrode. With applying a bias of 0.12 V to ITO/[Co(tpy)$_2$]O[Ru(bpy)$_3$] and ITO/[Zn(tpy)$_2$]O[Ru(bpy)$_3$] *vs.* $Ag/AgNO_3$ 10^{-2} M in a 0.1 M $[Bu_4N]ClO_4$ CH_3CN solution with TEOA (15 mM), visible light irradiation lead to the generation of a stable anodic current with a density of 12.2 and 10 $\mu A/cm^2$

respectively **figure 2.17**. This applied potential was particularly chosen in order to ensure the complete oxidation of all cobalt species to $[Co(tpy)_2]^{3+}$.

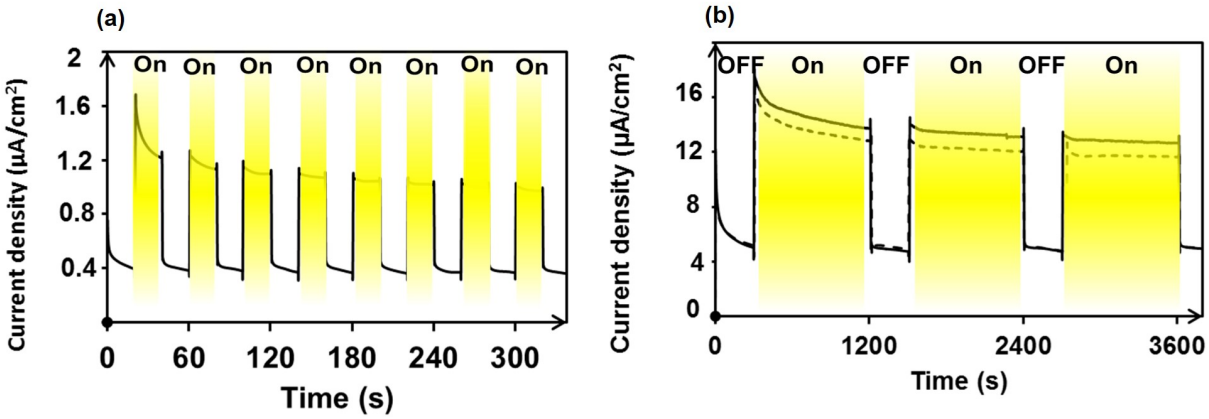

Figure 2.17: Photocurrent density ($\mu A.cm^{-2}$) *vs.* time. Irradiation periods are highlighted in yellow (a) ITO/$[Co(tpy)_2]$; (b) Full line ITO/$[Co(tpy)_2]O[Ru(bpy)_3]$; dashed line ITO/$[Zn(tpy)_2]O[Ru(bpy)_3]$

The magnitude of the anodic current showed a linear dependence on the power of irradiation in both dyads as shown in **figure 2.18** with the values of ITO/$[Co(tpy)_2]O[Ru(bpy)_3]$ being slightly higher than that of ITO/$[Zn(tpy)_2]O[Ru(bpy)_3]$. This is indeed a proof of the stability of the prepared films.

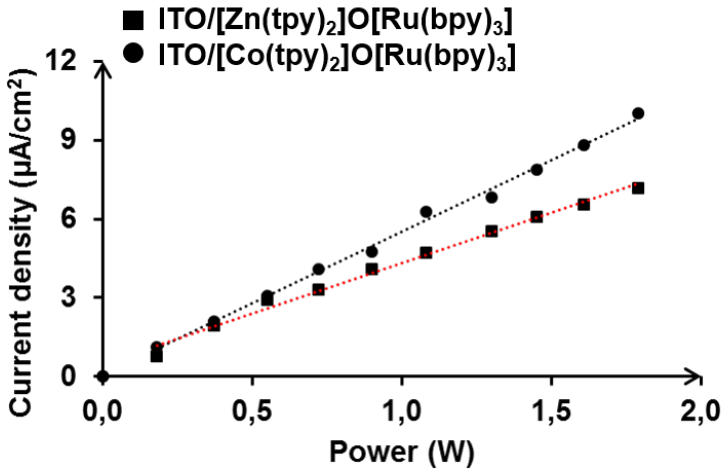

Figure 2.18: The variation of the magnitude of the photocurrent for ITO/$[Zn(tpy)_2]O[Ru(bpy)_3]$ and ITO/$[Co(tpy)_2]O[Ru(bpy)_3]$ with changing the power of irradiation

The incident-photon-to-electron conversion efficiency (IPCE) was also calculated for both

systems by irradiation at 455 nm according to **equation 2.2**:

$$\text{IPCEE} = 1240 \times \frac{j}{W_{in}\lambda_{exc}} \tag{2.2}$$

where j is the photocurrent intensity ($A.cm^{-2}$), W_{in} the incident intensity in ($W.cm^{-2}$) and λ_{exc} stands for the excitation wavelength (nm). The IPCE values were found 0.013 and 0.011 for ITO/$[Co(tpy)_2]O[Ru(bpy)_3]$ and ITO/$[Zn(tpy)_2]O[Ru(bpy)_3]$ respectively. These values are in agreement with the slight higher photoresponse in ITO/$[Co(tpy)_2]O[Ru(bpy)_3]$ with respect to ITO/$[Zn(tpy)_2]O[Ru(bpy)_3]$.

In order to understand the origin of this difference, we propose the following mechanism **figure 2.19**.

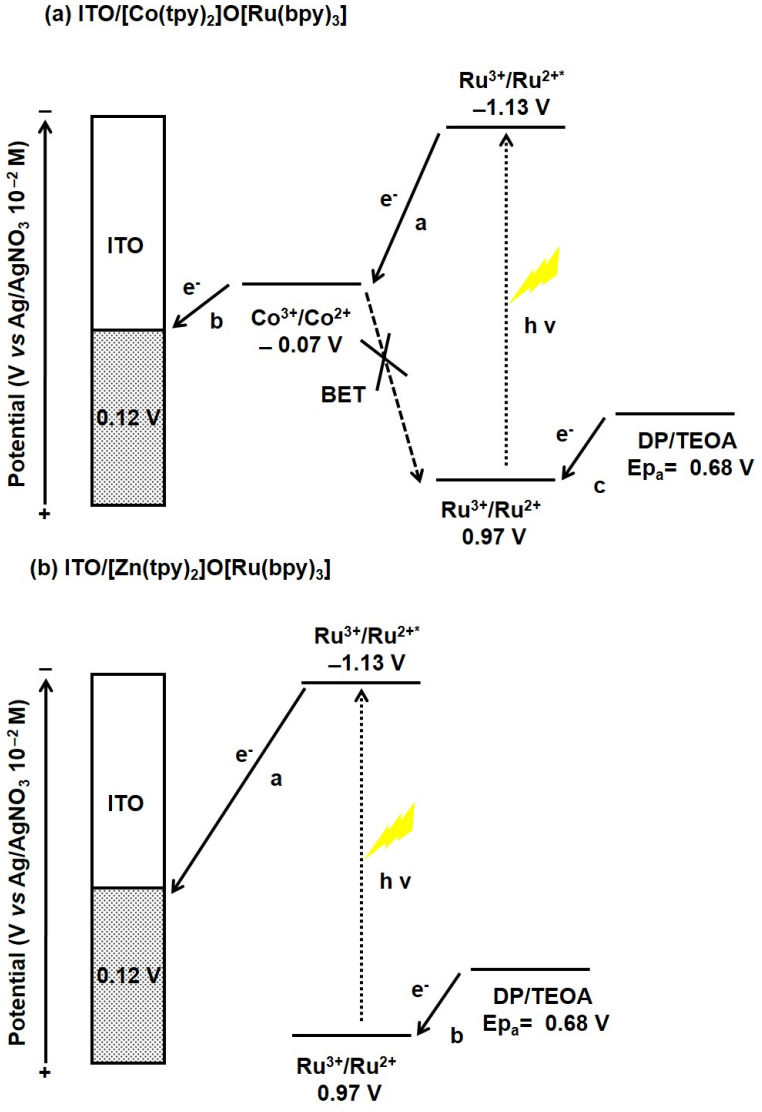

Figure 2.19: Proposed mechanism for the electron transfer in (a) ITO/$[Co(tpy)_2]O[Ru(bpy)_3]$; (b) ITO/$[Zn(tpy)_2]O[Ru(bpy)_3]$

As a start, the origin of the anodic photo-response is due to the vectorial electron transfer from the TEOA found in solution to the electrode. Nonetheless, different roots are expected to take place upon changing the electron relays in the two respective dyads. The proposed mechanism is based on the assumption that intramolecular electron transfer as well as electron injection to the electrode are faster than intermolecular electron transfer. This hypothesis is also strengthened with the k_{ET} values obtained for similar systems on gold as discussed earlier. After absorption of light by the ruthenium entity (as proved by the photoaction spectrum in the triads section), the ruthenium transfers an electron to the cobalt center followed by an injection of the electron to the electrode for ITO/[Co(tpy)$_2$]O[Ru(bpy)$_3$], whereas in ITO/[Zn(tpy)$_2$]O[Ru(bpy)$_3$] the electron is directly injected from the ruthenium center to the electrode. Since the electron transfer is in strong relation with both distance[8] and pathway[7] as elucidated in the introduction of this chapter, it is expected that the electron transfer is more efficient in ITO/[Co(tpy)$_2$]O[Ru(bpy)$_3$]. Then in both cases, the Ru^{2+} center is regenerated from TEOA present in the solution. This undoubtedly explains the differences arising between both dyads.

We have also studied the dependence of the magnitude of photocurrent upon variation of the surface coverage for dyad ITO/[Co(tpy)$_2$]O[Ru(bpy)$_3$] as shown in **figure 2.20**. Several ITO/[Co(tpy)$_2$]O[Ru(bpy)$_3$] electrodes were prepared with different surface coverage. This was achieved by introducing an increasing percentages of benzyl-phosphonic acid as a spacer in addition to compound **23**. Noticeably, the current density increases from 1.6 to 4.8 μA.cm^{-2} with an increasing Γ from 0.63 $\times$ 10^{-11} to 2.2 $\times$ 10^{-11} mol.cm^{-2}. However, there is no linear relationship between the number of the immobilized photoactive molecules and the photorespones of the electrode.

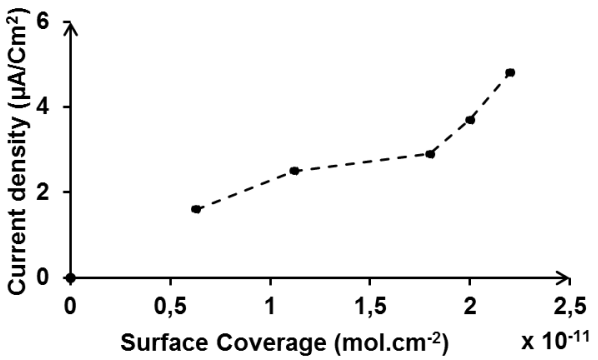

Figure 2.20: Variation of current density as function of Γ for dyad ITO/[Co(tpy)$_2$]O[Ru(bpy)$_3$]

Last but not least, the value of the current in **ITO/[Co(tpy)$_2$]O[Ru(bpy)$_3$]** is also related to the applied voltage **figure 2.21**. This could be rationalized in terms of changing the electron transfer rate from the cobalt center to the electrode upon changing the value of the applied potential and hence the oxidation state of cobalt. When a potential lower 0 V is applied, the

cobalt center is in the form of Co^{2+}. In this case cobalt can no longer serve as an electron acceptor to the excited state of the ruthenium, and thus low currents of 0.6 $\mu A.cm^{-2}$ is recorded. At higher potentials, the cobalt is in the Co^{3+} oxidation state, meaning that it can act as an electron relay. Thus the mechanism discussed earlier is valid. This shows, the importance of the implication of the d orbitals of the cobalt center in the generation of the photocurrent.

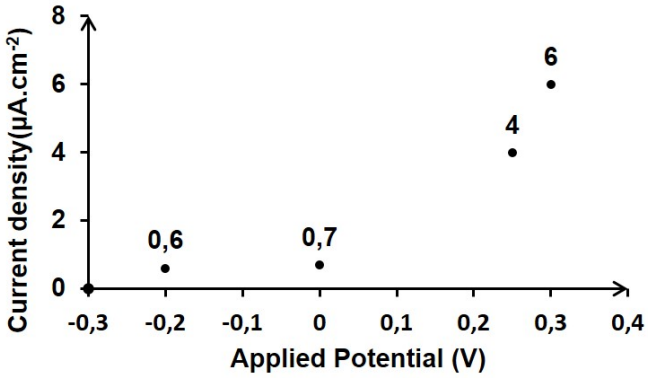

Figure 2.21: Variation of current density as a function of applied bias for dyad ITO/[Co(tpy)$_2$]O[Ru(bpy)$_3$]

2.2.5 *Cathodic Photocurrent with [Fe(tpy)$_2$]-[Ru(bpy)$_3$] in the Presence of ArN_2^+*

For dyads ITO/[Fe(tpy)$_2$]O[Ru(bpy)$_3$] and ITO/[Zn(tpy)$_2$]O[Ru(bpy)$_3$], aryl diazonium (ArN_2^+) is used as external electron acceptor by which it exhibits an irreversible reduction peak at E_{pc}= –0.4 V *vs.* Ag/$AgNO_3$ 10^{-2} M, and has proved to be an efficient oxidative quencher of the excited state of pyridyl ruthenium complexes.[17]

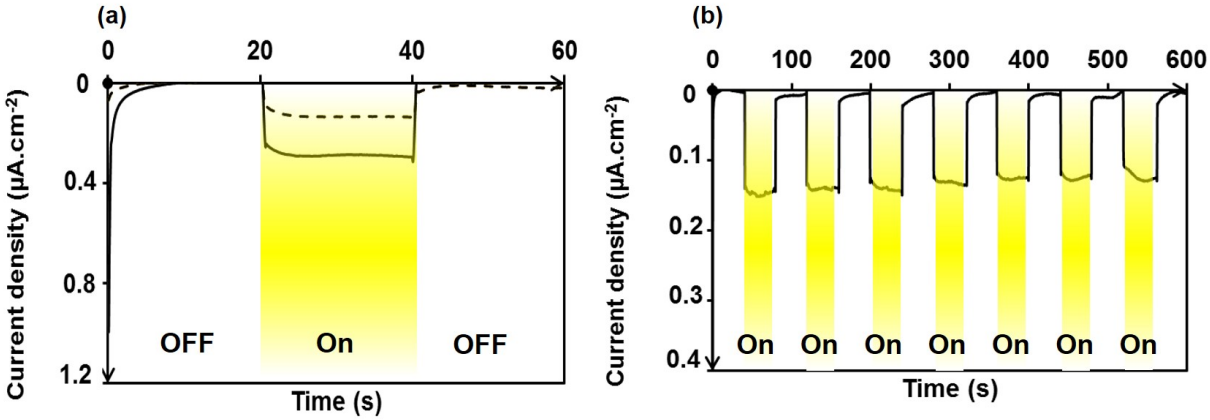

Figure 2.22: Photocurrent density (μ A.cm^{-2}) *vs.* time. Irradiation periods are highlighted in yellow (a) ITO/[Fe(tpy)$_2$]O[Ru(bpy)$_3$] full line and ITO/[Zn(tpy)$_2$]O[Ru(bpy)$_3$] dotted line; (b) Several on off cycles for ITO/[Fe(tpy)$_2$]O[Ru(bpy)$_3$]

Moreover, our group has recently reported that complex $[Fe(tpy)_2]^{2+}$ can act as an efficient electron relay between $[Ru(tpy)_2]^{2+}$ and gold electrodes.[18]

With a 0.4 V applied bias *vs.* $Ag/AgNO_3$ (10^{-2}) in the presence of ArN_2^+ (15 mM), visible light irradiation leads to the generation of a stable cathodic current with a density of 0.12 and 0.07 μ A/cm^2 for ITO/$[Fe(tpy)_2]O[Ru(bpy)_3]$ and ITO/$[Zn(tpy)_2]O[Ru(bpy)_3]$ respectively as shown in **figure 2.22**. The photocurrent drops immediately with the illumination switched off.

The mechanism of current generation is depicted in **figure 2.23**. The photoaction spectrum certifies that the $[Ru(bpy)_3]^{2+}$ is indeed responsible for the photocurrent (see in section triads).

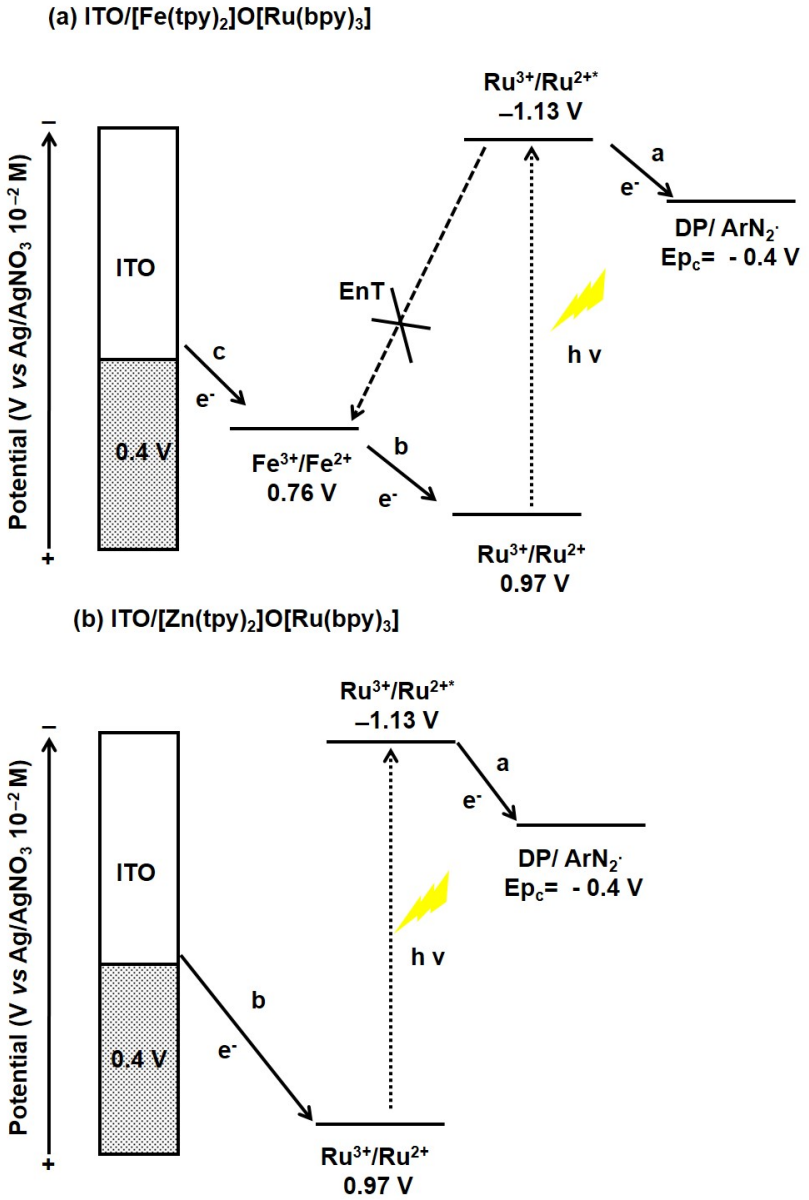

Figure 2.23: Proposed mechanism for the electron transfer in (a) ITO/$[Fe(tpy)_2]O[Ru(bpy)_3]$; (b) ITO/$[Zn(tpy)_2]O[Ru(bpy)_3]$

Undoubtedly, the first step which takes place is the formation of the excited state $[Ru(bpy)_3]^{2+*}$ for both dyads. In the case of ITO/$[Zn(tpy)_2]$O$[Ru(bpy)_3]$, a plausible mechanism that can explain the generation of the photocurrent is that $[Ru(bpy)_3]^{2+*}$ first undergoes an oxidative quenching by the diazonium found in solution, in order to form Ru^{3+}, and then the initial state is recovered by accepting an electron from the electrode. Taking into account the fully occupied metal orbitals of the Zn complex, it will just act as a spacer between the Ru and the electrode. However, in the case of ITO/$[Fe(tpy)_2]$O$[Ru(bpy)_3]$, the first two steps are assumed to be identical to the earlier case, nonetheless the recovery of the ground state of ruthenium takes place differently. Due to the presence of the Fe^{2+} which serves as a good electron donor to the Ru^{3+} as demonstrated in **Chapter 1**, the ruthenium will most preferably accept an electron from the iron instead of the ITO surface due to closer distances and lower potential, which in turn is regenerated by the bias applied to the ITO. It is expected that the rate of electron transfer in ITO/$[Fe(tpy)_2]$O$[Ru(bpy)_3]$ to be faster and more effective than ITO/$[Zn(tpy)_2]$O$[Ru(bpy)_3]$ as the iron can serve as an electron relay. Overall, in both dyads an electron is moved from the ITO surface to the counter electrode *via* the electron carriers in the electrolyte solution which generates a cathodic current. The low values of photocurrent can be due to the high value of applied bias, which is necessary in order to prevent the direct generation of the $Ar^{\cdot+}$ at the electrode, and thus the modification of the surface. The lower values can also be due to the strong quenching of the $[Ru(bpy)_3]^{2+*}$ state by the $[Fe(ttpy)_2]^{2+}$ subunit by energy transfer. Moreover, the first step which governs the production of the current, is diffusion dependent and thus slow, which could represent another limitation to our system.

The photo-to-electrical conversion for ITO/$[Fe(tpy)_2]$O$[Ru(bpy)_3]$ is linear for light power used in this study demonstrating the stability of the dyad under different light intensities, as well as long time irradiation **figure 2.24**.

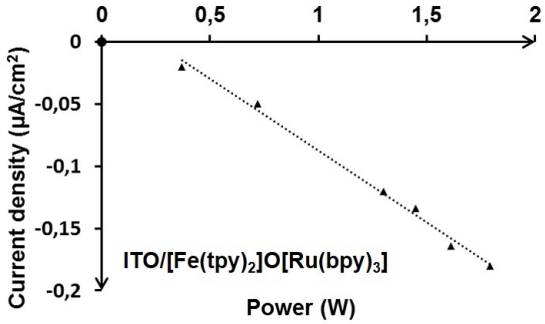

Figure 2.24: Dependence of the magnitude of the current density on the power of irradiation

2.3 Immobilized Triads

2.3.1 Preparation of Surfaces

The assembly of the triads on electrodes has been carried out stepwise similarily to the dyads, taking advantage of the strong self-assembling interaction between oxygen-containing functional groups such as phosphonates with ITO and between terpyridine ligands with first row transition metals **figure 2.25**.

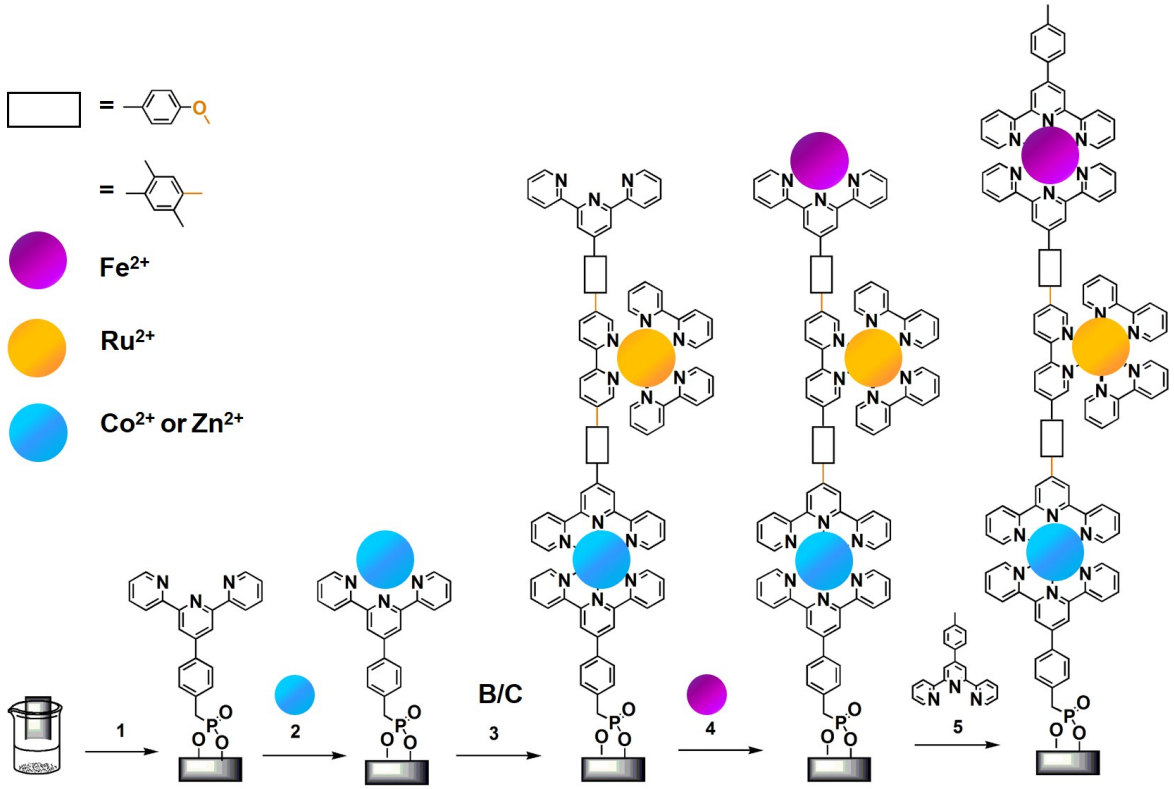

Figure 2.25: Stepwise assembly of the triads ITO/[Co(tpy)$_2$]O[Ru(bpy)$_3$]O[Fe(tpy)$_2$], ITO/[Zn(tpy)$_2$]O[Ru(bpy)$_3$]O[Fe(tpy)$_2$] and ITO/[Co(tpy)$_2$]ϕ[Ru(bpy)$_3$]ϕ[Fe(tpy)$_2$] on ITO surfaces, for clarity charges have been omitted

In a first step, the surface is grafted with a phosphonate-substituted terpyridine. This modified surface is then dipped in an ethanolic solution of $Co(BF_4)_2$ or $Zn(BF_4)_2$ at room temperature. After thorough rinsing, the surface is again dipped in a solution containing the photosensitizing moiety [Ru-(O-tpy)$_2$] or [Ru-(ϕ-tpy)$_2$] that self-assembles on the pending metallic center leaving a free terpyridine exposed to the outer solution. This free tridentate ligand can then be involved in a coordination process with a metallic center, namely Fe^{2+}. After rinsing, the system is capped with a final 4'-*p*-tolyl-2,2':6',"-terpyridine. It is noteworthy that the terpyridines are introduced on the 5 and 5' position of the same bipyridine on the photosensitizing unit. This indeed increases the distance between the donor and the acceptor relative to the more common

substitution at the 4 and 4' position.[19] This will also enable us to gain more control over the orientation of molecules on the surfaces. In this context, we prepared two sets of trimetallic triads with different nature of linkages and combination of metals. In the first set the different subunits are held together with the help of an ether linkage to ensure a minimum electronic communication between the different centers, and to gain relative rigidity. The triads are denoted by ITO/[Co(tpy)$_2$]O[Ru(bpy)$_3$]O[Fe(tpy)$_2$] and ITO/[Zn(tpy)$_2$]O[Ru(bpy)$_3$]O[Fe(tpy)$_2$]. The first comprises cobalt, ruthenium and iron whereas the latter consists of zinc, ruthenium and iron metals. Regarding the second type of triads namely ITO/[Co(tpy)$_2$]ϕ[Ru(bpy)$_3$]ϕ[Fe(tpy)$_2$], the different metallic centers are connected *via* methyl substituted phenylene, in order to attain more rigid structures and a higher degree of linearity.

2.3.2 *Electrochemistry*

All these triads are characterized by cyclic voltammetry in CH_3CN and 0.1 M $[Bu_4N]ClO_4$ **figure 2.26**. The redox potentials are collected in **table 2.5**.

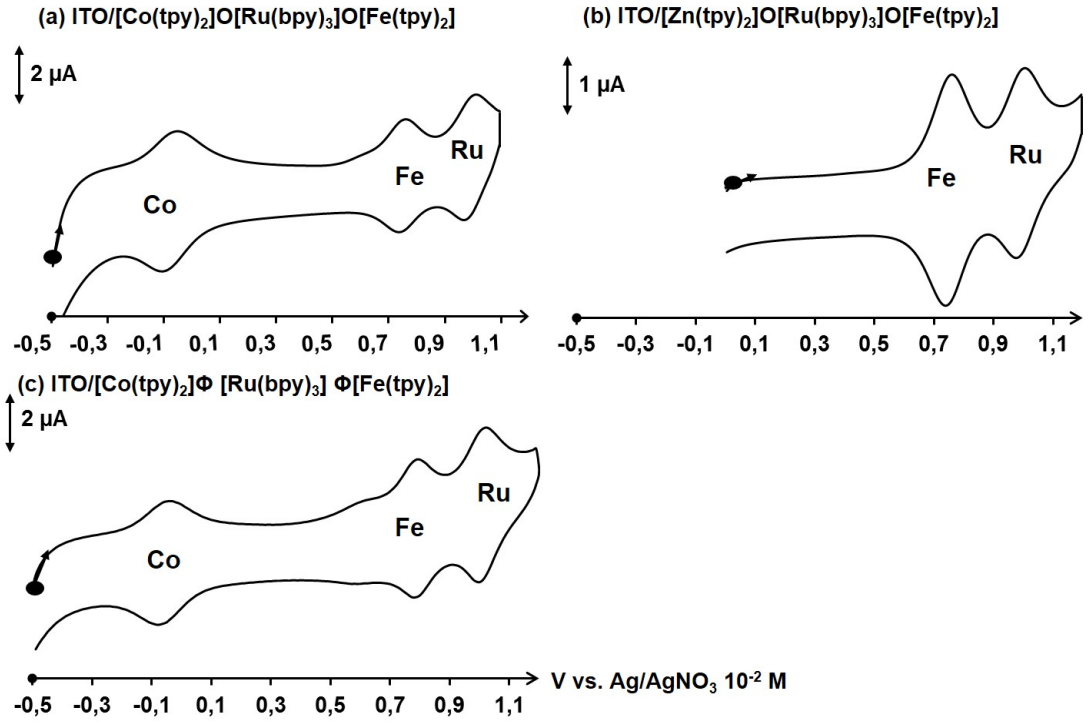

Figure 2.26: CV of the SAMs used as the working electrode in a solution of CH_3CN and 0.1 M $[Bu_4N]ClO_4$ at a scan rate = 20 mV/s *vs.* $Ag/AgNO_3$ (10^{-2} M) (a) ITO/[Co(tpy)$_2$]O[Ru(bpy)$_3$]O[Fe(tpy)$_2$]; (b) ITO/[Zn(tpy)$_2$]O[Ru(bpy)$_3$]O[Fe(tpy)$_2$]; (c) ITO/[Co(tpy)$_2$]ϕ[Ru(bpy)$_3$]ϕ[Fe(tpy)$_2$]

In all triads, we are able to detect the signals of the different redox-active metallic centers with a slight modification of potentials which most probably lies in the experimental error

marge. This implies that there is a weak electronic coupling between the different subunits as ensured by the introduced spacers. This is consistent with both the results obtained in solution and with the respective dyads. Regarding ITO/[Zn(tpy)$_2$]O[Ru(bpy)$_3$]O[Fe(tpy)$_2$] two redox peaks are registered, the first at 0.76 V and is attributed to the monoelectronic oxidation of Fe^{2+}, and in the more positive region the second reversible oxidation with a potential = 0.98 V is associated to the ruthenium center. The extra wave in ITO/[Co(tpy)$_2$]O[Ru(bpy)$_3$]O[Fe(tpy)$_2$] and ITO/[Co(tpy)$_2$]ϕ[Ru(bpy)$_3$]ϕ[Fe(tpy)$_2$] is the result of the one electron oxidation of the cobalt center Co^{3+}/Co^{2+}.

Table 2.5: Redox potentials of modified surfaces ITO/[Co(tpy)$_2$]O[Ru(bpy)$_3$]O[Fe(tpy)$_2$]; ITO/[Zn(tpy)$_2$]O[Ru(bpy)$_3$]O[Fe(tpy)$_2$]; and ITO/[Co(tpy)$_2$]ϕ[Ru(bpy)$_3$]ϕ[Fe(tpy)$_2$] in a solution of CH_3CN + 0.1 M $[Bu_4N]ClO_4$ at a scan rate 100 mV.s^{-1}

$E^{ox}_{1/2}$ (V) (ΔE_p,mV)	Fe^{3+}/Fe^{2+}	Co^{3+}/Co^{2+}	Ru^{3+}/Ru^{2+}
ITO/[Co(tpy)$_2$]O[Ru(bpy)$_3$]O[Fe(tpy)$_2$]	0.77 (15)	–0.09 (15)	0.98 (10)
ITO/[Zn(tpy)$_2$]O[Ru(bpy)$_3$]O[Fe(tpy)$_2$]	0.76 (10)	-	0.98 (10)
ITO/[Co(tpy)$_2$]ϕ[Ru(bpy)$_3$]ϕ[Fe(tpy)$_2$]	0.78 (10)	–0.06 (10)	0.98 (15)

For every triad the CV was registered at different scan rates ranging between 20 and 100 mV.s^{-1}. The linear relationship between the intensity of the peaks and the scan rate clearly indicates that the processes observed occur on a grafted surface **figure 2.27**. The same cyclic voltammograms were also obtained after a period of two weeks, showing the stability of the assemblies.

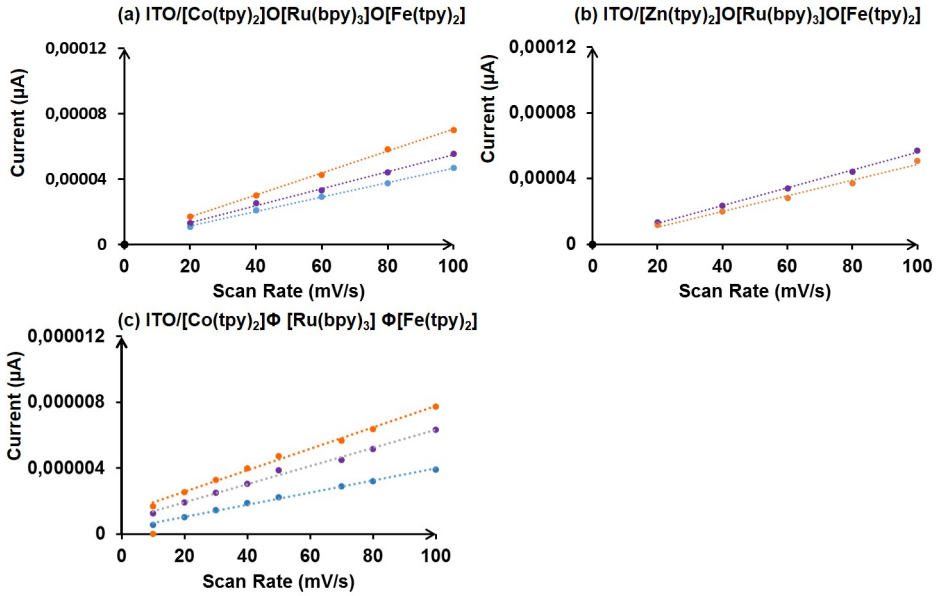

Figure 2.27: Plotting of current *vs.* scan rate for the SAMs (a) ITO/[Co(tpy)$_2$]O[Ru(bpy)$_3$]O[Fe(tpy)$_2$]; (b) ITO/[Zn(tpy)$_2$]O[Ru(bpy)$_3$]O[Fe(tpy)$_2$]; (c) ITO/[Co(tpy)$_2$]ϕ[Ru(bpy)$_3$]ϕ[Fe(tpy)$_2$]

The surface coverage values (Γ) were also estimated by integrating the area under every peak in oxidation and the values are summarized in **table 2.6**. There are two interesting observations to be made upon examining the obtained value. To begin with, all the calculated Γ values are similar among the different complexes with an average $\approx 0.5 \times 10^{-11}$ mol.cm^{-2}, which validates the integrity of this method, and at the same time certifies the 1:1:1 ratio of metallic centers in the different triads. Yet all the recorded values are inferior to those obtained with the dyads (with a factor 6). This dilution of the surfaces could be the result of de-coordination associated with every extra dipping steps. This hypothesis was validated by QCM studies which were done with the dyads on the gold surface during a M2 internship.

Table 2.6: Surface coverage of modified surfaces ; ITO/[Zn(tpy)$_2$]O[Ru(bpy)$_3$]O[Fe(tpy)$_2$]; and ITO/[Co(tpy)$_2$]ϕ[Ru(bpy)$_3$]ϕ[Fe(tpy)$_2$]

Surface coverage Γ ($mol.cm^{-2}$)	Fe peak	Co peak	Ru peak
ITO/[Co(tpy)$_2$]O[Ru(bpy)$_3$]O[Fe(tpy)$_2$]	0.4×10^{-11}	0.5×10^{-11}	0.4×10^{-11}
ITO/[Zn(tpy)$_2$]O[Ru(bpy)$_3$]O[Fe(tpy)$_2$]	0.8×10^{-11}	-	0.7×10^{-11}
ITO/[Co(tpy)$_2$]ϕ[Ru(bpy)$_3$]ϕ[Fe(tpy)$_2$]	0.5×10^{-11}	0.5×10^{-11}	0.5×10^{-11}

2.3.3 *Surface Characterization*

In order to investigate the orientation of the immobilized triads with the rigid phenylene spacers on surfaces, we conducted AFM experiments.

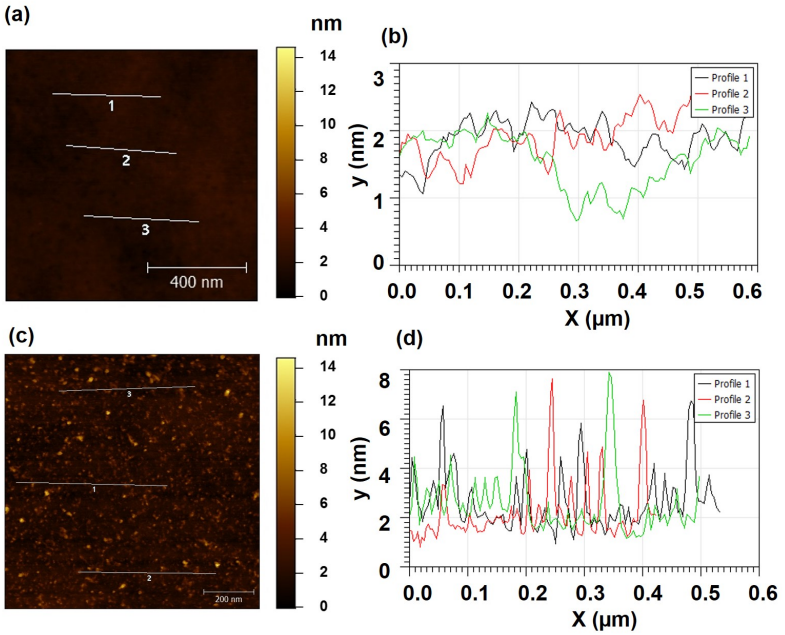

Figure 2.28: (a) AFM topography of a 1 μm^2 nacked silicon oxide, (b) Profile of nacked ITO, (c) AFM of a of a 1 μm^2 SiO$_2$/[Co(tpy)$_2$]ϕ[Ru(bpy)$_3$]ϕ[Fe(tpy)$_2$], (d) Profile of SiO$_2$/[Co(tpy)$_2$]ϕ[Ru(bpy)$_3$]ϕ[Fe(tpy)$_2$]

Generally, the ITO surface is very rough and thus it is tricky to get AFM images with monolayers. SiO_2, are generally adapted for such measurements. This is why we immobilized the triad $[Co(tpy)_2]\phi[Ru(bpy)_3]\phi[Fe(tpy)_2]$ on SiO_2. The bare surfaces were subject to ozone irradiation for 10 minutes, and rinsed thoroughly with ethanol prior to grafting. Then the triads are constructed as previously detailed for ITOs. The morphology of a nacked SiO_2 is presented in **figure 2.28.a**, and shows that the surface is flat and homogeneous. The AFM image of $SiO_2/[Co(tpy)_2]\phi[Ru(bpy)_3]\phi[Fe(tpy)_2]$ shows an increase in the roughness compared to the nacked surface, nonetheless the distribution is nonhomogeneous, with islands of aggregates **figure 2.28.b**. Due to the small height of the monolayers, it is difficult to perform a scratching in order to deduce the height of the assembly. Nonetheless, extracting the profile from the AFM image will allow an estimation of the height of the immobilized dyads. As a matter of fact, the profile shows a distribution of different heights with values between 3 and 5 nm. This is consistent with the formation of both dyads and triads on the surface, which are most probably maintaining a linear upward orientation **figure 2.28.c**.

2.3.4 Photocurrent Generation

Upon visible light irradiation, the modified electrodes $ITO/[Co(tpy)_2]O[Ru(bpy)_3]O[Fe(tpy)_2]$ and $ITO/[Zn(tpy)_2]O[Ru(bpy)_3]O[Fe(tpy)_2]$ to which we apply a bias of 0.12 V are able to generate current in the presence of triethanolamine (TEOA) as a sacrificial electron donor.

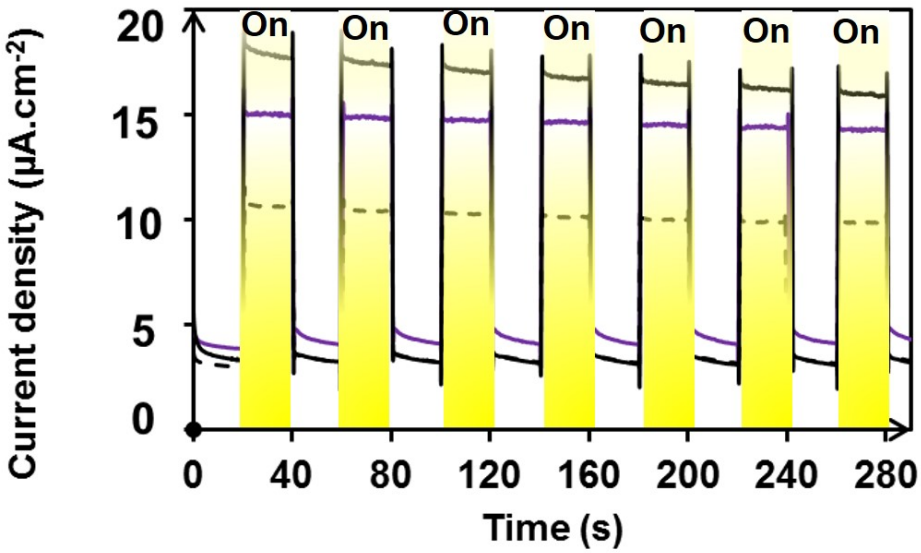

Figure 2.29: Photocurrent density ($\mu A.cm^{-2}$) *vs.* time. Irradiation periods are highlighted in yellow $ITO/[Co(tpy)_2]O[Ru(bpy)_3]$ dashed line; $ITO/[Co(tpy)_2]O[Ru(bpy)_3]O[Fe(tpy)_2]$ full black line; $ITO/[Zn(tpy)_2]O[Ru(bpy)_3]O[Fe(tpy)_2]$ full purple line

To recall, the bias has been selected since at that potential the cobalt subunit is under its Co^{3+} form which is a good electron acceptor towards the $[Ru(bpy)_3]^{2+*}$ species, without directly oxidizing TEOA. **Figure 2.29** shows the typical response as the excitation light was turned on and off. These value are also compared to those of the dyad ITO/$[Co(tpy)_2]$O$[Ru(bpy)_3]$. An anodic photocurrent magnitude of 12, 15 and 19 μ A.cm^{-2} is quickly reached for ITO/$[Co(tpy)_2]$O$[Ru(bpy)_3]$, ITO/$[Zn(tpy)_2]$O$[Ru(bpy)_3]$O$[Fe(tpy)_2]$ and ITO/$[Co(tpy)_2]$O$[Ru(bpy)_3]$O$[Fe(tpy)_2]$ respectively.

It should be noted that the irradiation of a nacked ITO in the absence or presence of TEOA causes only negligeable photocurrent. At the chosen bias, the photocurrent originating from irradiation of the respective triads ITO/$[Co(tpy)_2]$O$[Ru(bpy)_3]$O$[Fe(tpy)_2]$ and ITO/$[Zn(tpy)_2]$O $[Ru(bpy)_3]$O$[Fe(tpy)_2]$ is 30-40% higher than from the dyad ITO/$[Co(tpy)_2]$O$[Ru(bpy)_3]$ (12μ A.cm^{-2}) despite the remarkably lower surface coverage values. In all systems, this photocurrent is due to the ruthenium center as evidenced in the photoaction spectrum **figure 2.30**.

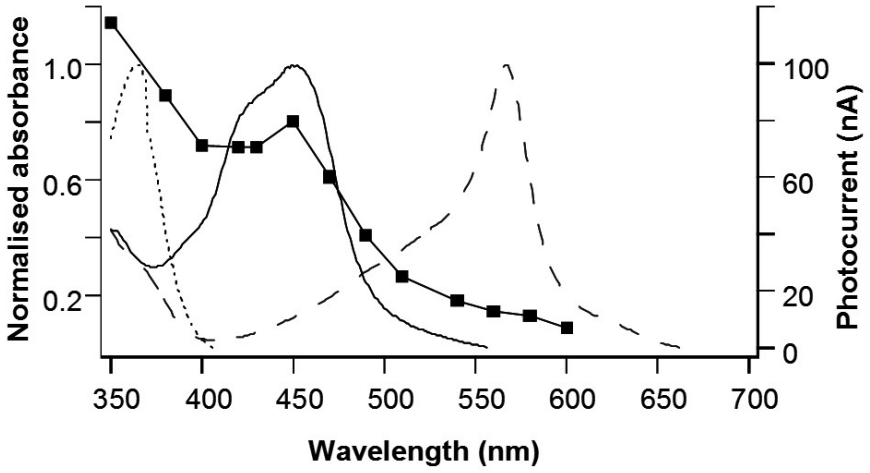

Figure 2.30: Photoaction spectrum (■) of ITO/$[Co(tpy)_2]$O$[Ru(bpy)_3]$O$[Fe(tpy)_2]$ along with UV-vis absorption spectra of the building blocks: $[Ru(bpy)_3]^{2+}$ full line, $[Co(tpy)_2]^{3+}$ dotted line and $[Fe(tpy)_2]^{2+}$ dashed line

Despite the energy transfer (En.T.) process between Ru^{2+*} and Fe^{2+} subunits which reduce the excited state lifetime of Ru^{2+*}, both triads ITO/$[Co(tpy)_2]$O$[Ru(bpy)_3]$O$[Fe(tpy)_2]$ and ITO/$[Zn(tpy)_2]$O$[Ru(bpy)_3]$O$[Fe(tpy)_2]$ are still able to generate a large amount of current. As a matter of fact, the En. T is short-circuited by an electron transfer process from Ru^{2+*} to the Co^{3+} subunit in the case of ITO/$[Co(tpy)_2]$O$[Ru(bpy)_3]$O$[Fe(tpy)_2]$, and by the electrode in the case of ITO/$[Zn(tpy)_2]$O$[Ru(bpy)_3]$O$[Fe(tpy)_2]$. As we proved in the section of dyads, the electron transfer from the $[Ru(bpy)_3]^{2+*}$ center to the electrode is more efficient in the presence of the cobalt which acts as an electron shuttle between the ruthenium and the surface **figure 2.31**. This rationalizes the differences in the magnitude of current among ITO/$[Co(tpy)_2]$O$[Ru(bpy)_3]$O$[Fe(tpy)_2]$ and ITO/$[Zn(tpy)_2]$O$[Ru(bpy)_3]$O$[Fe(tpy)_2]$. Moreover, the Fe^{2+} subunit reacts efficiently with the photogenerated Ru^{3+} species to compete with the

back electron transfer (BET) reaction between the Co^{2+} and Ru^{3+}. This indeed shows the importance of having triad architectures in order to increase the lifetime of the CSS to achieve higher efficiencies in photo-electric conversion. The $[Ru(bpy)_3]^{2+}$ ground state is then regenerated from TEOA in the solution. The incident photon-to-electron conversion efficiency (IPCE) at 455 nm is estimated to 0.031% for ITO/$[Co(tpy)_2]O[Ru(bpy)_3]O[Fe(tpy)_2]$ relative to 0.013% for ITO/$[Co(tpy)_2]O[Ru(bpy)_3]$, which is in agreement with the increase of current.

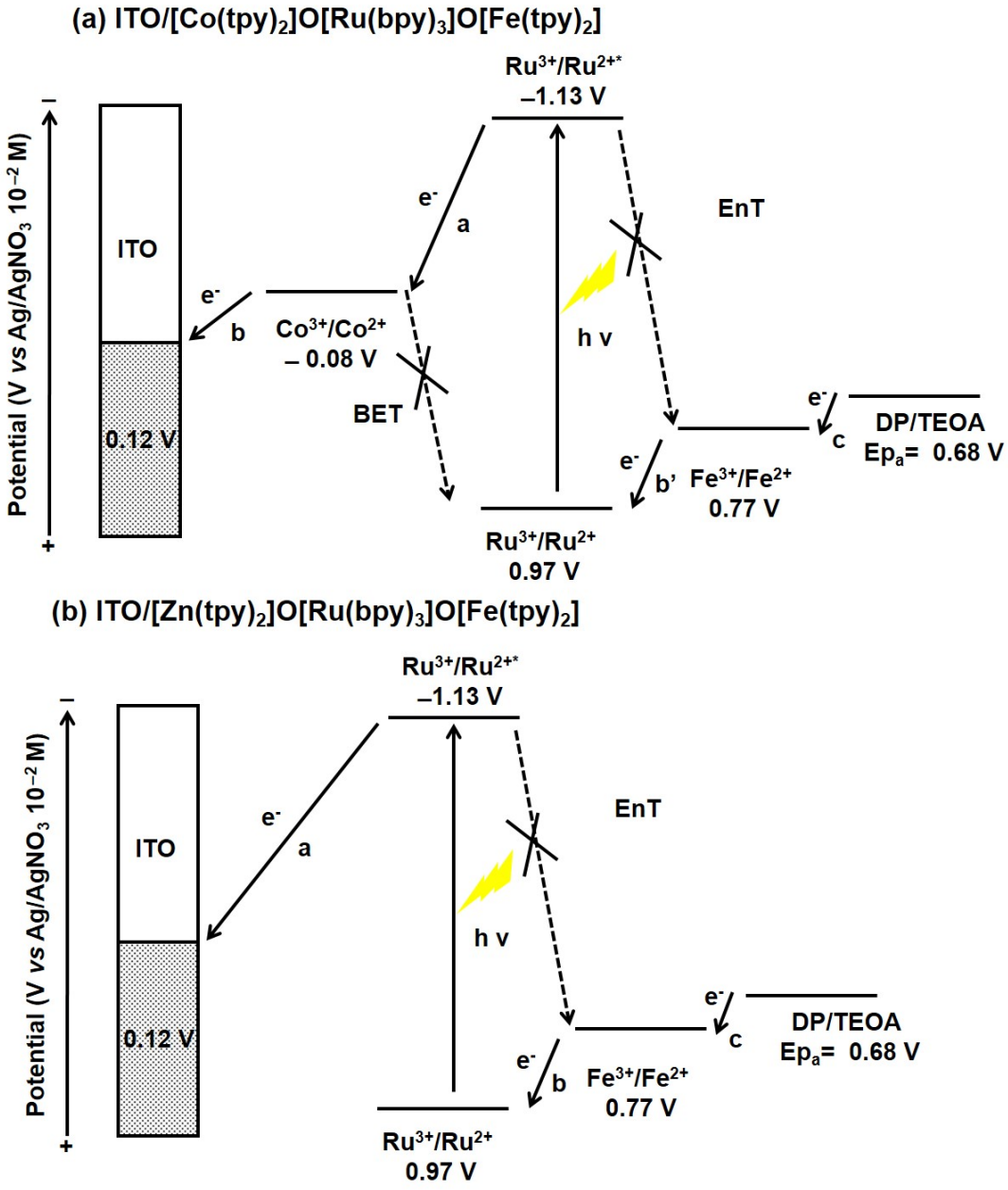

Figure 2.31: Proposed mechanism for the electron transfer in (a) ITO/$[Co(tpy)_2]O[Ru(bpy)_3]O[Fe(tpy)_2]$; (b) ITO/$[Zn(tpy)_2]O[Ru(bpy)_3]O[Fe(tpy)_2]$

The irradiation process for ITO/$[Co(tpy)_2]O[Ru(bpy)_3]O[Fe(tpy)_2]$ was repeated over 2 h providing reproducible photocurrent response and hence showing the mechanical and photo-

physical stability of the film **figure 2.32**.

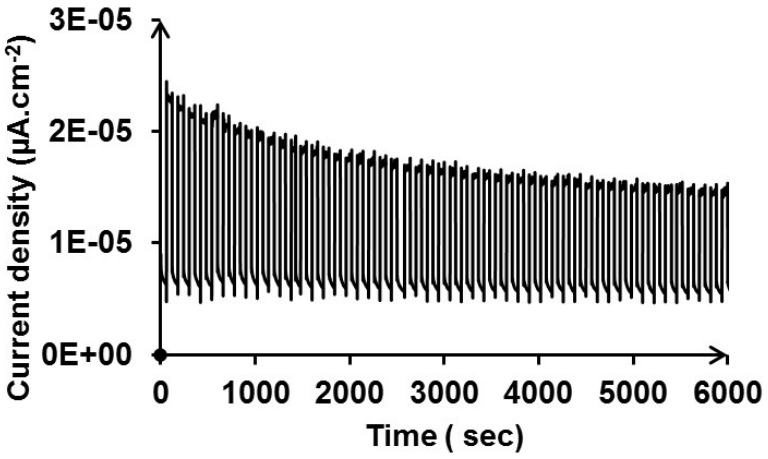

Figure 2.32: Photocurrent density (μA.cm^{-2}) *vs.* time over a period of 2 h for the immoblized triad ITO/[Co(tpy)$_2$]O[Ru(bpy)$_3$]O[Fe(tpy)$_2$]

On the contrary to dyads, the magnitude of the photocurrent doesn't change linearly with increasing light excitation power as shown in **figure 2.33**. This can be due to a lower fatigue resistant structure. We also prepared ITO/[Co(tpy)$_2$]ϕ[Ru(bpy)$_3$]ϕ[Fe(tpy)$_2$] with the same metallic composition yet with a more rigid linker (phenylene).

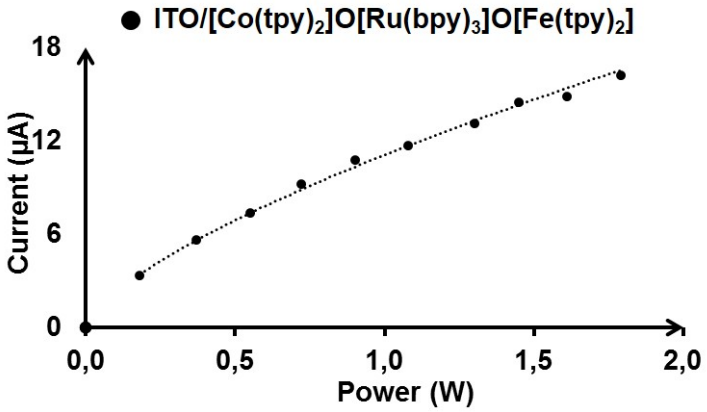

Figure 2.33: Dependence of the magnitude of the current density on the power of irradiation

Under the same experimental condition that were detailed earlier, the triad containing a phenylene as a bridge denoted by ITO/[Co(tpy)$_2$]ϕ[Ru(bpy)$_3$]ϕ[Fe(tpy)$_2$] can efficiently produce an anodic current with a 30% enhancement relative to ITO/[Co(tpy)$_2$]O[Ru(bpy)$_3$]O[Fe(tpy)$_2$] **figure 2.34**. This increase is quite valuable considering the little modification introduced. It is expected, that in ITO/[Co(tpy)$_2$]ϕ[Ru(bpy)$_3$]ϕ[Fe(tpy)$_2$], the more rigid backbone allows attaining more linear assemblies, which most probably decreases the deactivation of the Ru* by the electrode, or by neighboring molecules.

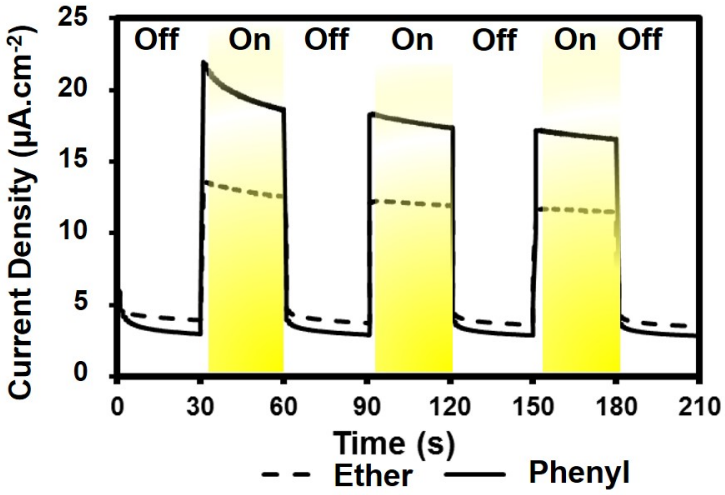

Figure 2.34: Photocurrent density (μA.cm^{-2}) *vs.* time. Irradiation periods are highlighted in yellow ITO/[Co(tpy)$_2$]O[Ru(bpy)$_3$]O[Fe(tpy)$_2$] dashed line, ITO/[Co(tpy)$_2$]ϕ[Ru(bpy)$_3$]ϕ[Fe(tpy)$_2$] full line

2.4 Conclusion

During this chapter we reported the possibility of assembling several metallic dyads and triads on gold, ITO and SiO_2 surfaces in a stepwise manner. These layers consist of a different combination of $[Ru(bpy)_3]^{2+}$ as a photoactive spacer, $[Co(tpy)_2]^{3+}$ as an electron acceptor and $[Fe(tpy)_2]^{2+}$ as an electron donor. In some cases $[Zn(tpy)_2]^{2+}$ is used as an innocent spacer. All of these assemblies were efficient to produce a current in the presence of a sacrificial reagent. The magnitude of the photocurrent was found to linearly increase with power, monitoring the thermal stability of the assemblies. Moreover, it showed a strong dependence on the surface coverage, however no specific trend could be concluded. More importantly, we have shown that the magnitude of the photocurrent is enhanced by the addition of extra relays and guarding higher orientation of the assemblies. One attractive modification would be to change the electron acceptors, donors with others of different potentials or catalytic activity. Indeed this will be discussed in **chapters 3**. These triads also allow accessing photoactive molecular electronic devices. For instance, these triad can be incorporated between two electrodes in order to form a photo-activable molecular junction. Recent experiments carried out on a porphyrin/C_{60} dyad linked between an ITO electrode and a gold STM needle proved the modulation of the conductance by photoinduced electron transfer process. In such, the stepwise approach in terpyridine sites will be beneficial for such an application.[20].

Bibliography

[1] T. Kondo, K. Uosaki, *J. Photochem. Photobiol.* **2007**, *8*, 1 – 17.

[2] M. aki Haga, K. Kobayashi, K. Terada, *Coord. Chem. Rev.* **2007**, *251*, 2688 – 2701.

[3] H. Maeda, R. Sakamoto, H. Nishihara, *Polymer* **2013**, *54*, 4383 – 4403.

[4] H. Nishihara, K. Kanaizuka, Y. Nishimori, Y. Yamanoi, *Coord. Chem. Rev.* **2007**, *251*, 2674 – 2687.

[5] A. Winter, S. Hoeppener, G. R. Newkome, U. S. Schubert, *Adv. Mater.* **2011**, *23*, 3484–3498.

[6] Y. Ohba, K. Kanaizuka, M. Murata, H. Nishihara, *Macromol. Symp.* **2006**, *235*, 31–38.

[7] M. Miyachi, M. Ohta, M. Nakai, Y. Kubota, Y. Yamanoi, T. Yonezawa, H. Nishihara, *Chem. Lett.* **2008**, *37*, 404–405.

[8] Y. Nishimori, H. Maeda, S. Katagiri, J. Sendo, M. Miyachi, R. Sakamoto, Y. Yamanoi, H. Nishihara, *Macromol. Symp.* **2012**, *317-318*, 276–285.

[9] P. C. Mondal, V. Singh, Y. L. Jeyachandran, M. Zharnikov, *ACS Appl. Mater. Interfaces* **2015**, *7*, 8677–8686.

[10] H. Imahori, H. Norieda, H. Yamada, Y. Nishimura, I. Yamazaki, Y. Sakata, S. Fukuzumi, *J. Am. Chem. Soc.* **2001**, *123*, 100–110.

[11] S. Suzuki, Y. Matsumoto, M. Tsubamoto, R. Sugimura, M. Kozaki, K. Kimoto, M. Iwamura, K. Nozaki, N. Senju, C. Uragami, H. Hashimoto, Y. Muramatsu, A. Konno, K. Okada, *Phys. Chem. Chem. Phys.* **2013**, *15*, 8088–8094.

[12] P. Bonhôte, J.-E. Moser, R. Humphry-Baker, N. Vlachopoulos, S. M. Zakeeruddin, L. Walder, M. Grätzel, *J. Am. Chem. Soc.* **1999**, *121*, 1324–1336.

[13] K. Kanaizuka, M. Murata, Y. Nishimori, I. Mori, K. Nishio, H. Masuda, H. Nishihara, *Chem. Lett.* **2005**, *34*, 534–535.

[14] T. Kurita, Y. Nishimori, F. Toshimitsu, S. Muratsugu, S. Kume, H. Nishihara, *J. Am. Chem. Soc.* **2010**, *132*, 4524–4525.

[15] E. Campagnoli, J. Hjelm, C. J. Milios, M. Sjodin, Z. Pikramenou, R. J. Forster, *Electrochim. Acta* **2007**, *52*, 6692 – 6699.

[16] E. Laviron, *J. Electroanal. Chem.* **1979**, *101*, 19 – 28.

[17] J. Lombard, J.-C. Leprêtre, J. Chauvin, M.-N. Collomb, A. Deronzier, *Dalton Trans.* **2008**, *5*, pp. 658–666.

[18] S. Liatard, J. Chauvin, D. Jouvenot, F. Loiseau, A. Deronzier, *J. Phys. Chem. C* **2013**, *117*, 20431–20439.

[19] B. Galland, D. Limosin, H. Laguitton-Pasquier, A. Deronzier, *Inorg. Chem. Commun.* **2002**, *5*, 5 – 8.

[20] S. Battacharyya, A. Kibel, G. Kodis, P. A. Liddell, M. Gervaldo, D. Gust, S. Lindsay, *Nano Lett.* **2011**, *11*, 2709–2714.

Chromium Terpyridyl Complexes

Résumé:

Nous nous sommes intéressé ici à l'utilisation de complexes bisterpyridine de Cr(III) pour remplacer la sous unité $[Co(tpy)_2]^{3+}$ comme accepteur d'électron au sein de diade ou triade construite autour du $[Ru(bpy)_3]^{2+}$. Le comportement électrochimique et les propriétés photophysiques du $[Cr(tpy)_2]^{3+}$ ont été étudiés en détail. Nos résultats montrent notamment que $[Cr(tpy)_2]^{3+*}$ peut être réduit par la triphénylphosphine (PPh_3) sous irradiation UV. La réaction de quenching permet la photogénération du complexe $[Cr(tpy)_2]^{+}$ après le transfert de deux électrons avec un rendement de 30%. Ce taux de conversion peut-être amélioré en ajoutant dans le milieu le $[Ru(bpy)_3]^{2+}$ comme photosensibilisateur complémentaire. La réduction s'oppère alors par des cycles de quenching oxidant du $[Ru(bpy)_3]^{2+*}$ par le $[Cr(tpy)_2]^{3+}$, le $[Ru(bpy)_3]^{3+}$ photogénéré est ensuite réduit par PPh_3.

Nous avons également élaboré le complexe $[Ru\text{-}Cr\text{-}Ru]^{7+}$ à l'exemple des complexes trinucléaire du chapitre 1. Le transfert d'électron qui s'opère sous irradiation au sein de l'édifice permet la formation de l'intermédiaire $[Ru(III)\text{-}Cr(II)\text{-}Ru(II)]^{7+}$ pour lequel l'état à charge séparé a une durée de vie suffisamment longue pour être inhibé par PPh3. Les réactions de transferts d'électron photoinduites permettent le stockage de deux électrons sur la sous unité $[Cr(tpy)_2]^{3+}$. Nos premiers essais pour élaborés une triade D-P-A en utilisant le $[Cr(tpy)_2]^{3+}$ n'ont pas été concluants.

En marge de ce travail nous présentons aussi dans ce chapitre des études préliminaires sur l'utilisation de complexes monoterpyridine et bis terpyridine comme catalyseur de réduction des protons en dihydrogène.

CHAPTER 3

CHROMIUM TERPYRIDYL COMPLEXES

3.1 Introduction

As stated in **Chapter 2**, it is interesting to replace the electron acceptor $[Co(tpy)_2]^{3+}$ with other metals with lower E_{red} in order to increase the storage energy in architectures based on D-P-A. In this context, we explored the possibility of using chromium polypyridyl complexes as an electron acceptor to the $[Ru(bpy)_3]^{2+*}$ state. Moreover, the chromium polypyridyl complexes have distinct photochemical properties that render them interesting. The photochemistry of Cr(III) polypyridyl complexes has grasped a particular attention, especially due to its high value of the excited state reduction potential.[1] In the octahedral Cr(III) pyridyl complexes, Cr^{3+} is a d^3 metal and thus in the ground state configuration the three valence electrons occupy the t_{2g} metal orbitals affording a quartet spin state as shown in **figure 3.1**.[2] Upon absorption of light, spin allowed excitation gives access to quartet excited states (^{4}MC) by which one electron is promoted to the metal-ligand antibonding orbital. This is followed by a rapid internal conversion (IC) to the low energy quartet state namely $^4T_{2g}$. From the lowest quartet state, there are possibilities of non radiative decay back to the ground state, or intersystem crossing giving access to the doublet excited states ^2E and $^2T_{1g}$. These doublets can either undergo back intersystem crossing (BISC), non radiative decay (NR) or phosphorescence (in the case of ^2E). In the presence of suitable quenchers, the doublet excited states can take part either in electron or energy transfer processes.

The metal excited state ^2E of $[Cr(bpy)_3]^{3+}$ was found to take part in bimolecular energy and electron transfer processes.[1;3] This is mainly possible due to the long lifetimes of these complexes reaching 48 μs in aqueous solutions.[4] For instance, Balzani et al. showed that quenching of ^{2}MC of $[Cr(bpy)_3]^{3+}$ by $[Ru(bpy)_3]^{2+}$ and of ^{3}MLCT of $[Ru(bpy)_3]^{2+}$ by $[Cr(bpy)_3]^{3+}$

takes place by an electron transfer mechanism leading in both cases to the transient formation of the $[Cr(bpy)_3]^{2+}$ and $[Ru(bpy)_3]^{3+}$ redox pairs.[5].

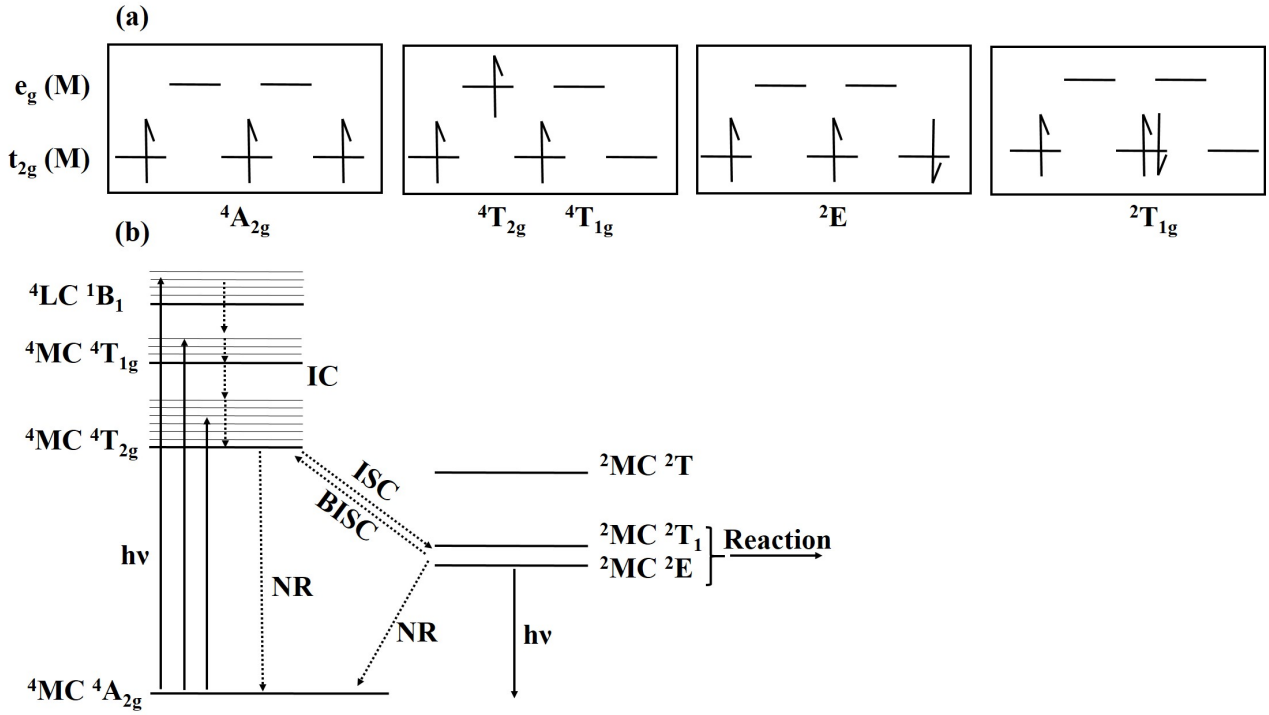

Figure 3.1: (a) A simplified molecular orbital diagram of the ground and excited state (b) A simplified Perrin-Jablonski diagram indicating radiative and non radiative transition for octahedral Cr(III) polypyridine complexes.

The same group showed the possibility of photo-generating H_2 in an aqueous solution containing $[Cr(dmp)_3]^{3+}$ where (dmp = 4,7-Me_2phen), platinum catalyst and ethylenediaminetetraacetic acid (EDTA) with a turnover number (TON) of 4.[6] The catalytic cycle is depicted in **figure 3.2**.

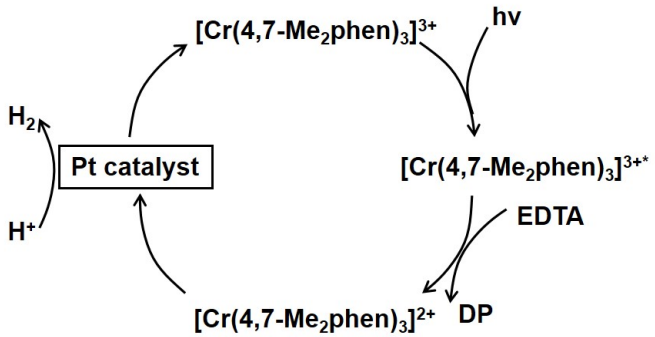

Figure 3.2: Suggested catalytic cycle for the photo-generation of H_2

After absorption of light, the $[Cr(dmp)_3]^{3+*}$ efficiently undergoes reductive quenching by EDTA in order to photogenerate the $[Cr(dmp)_3]^{2+}$ species. The latter transfers an electron

to the platinum catalyst in order to reduce protons, as well as recovering the initial ground state $[Cr(dmp)_3]^{3+}$. The low TON is attributed to the instability of the chromium complex under these conditions, by which the formation of $[Cr(dmp)_3]^{2+}$ catalyzes the aquation of the $[Cr(dmp)_3]^{3+}$ leading to partial ligand loss.

Although the bisterpyridyl complex $[Cr(tpy)_2]^{3+}$ can afford more linear and symmetrical structures, both, lifetime and quantum yield of emission drop drastically when compared to those of $[Cr(bpy)_3]^{3+}$, ie: τ = 66 μs for $[Cr(bpy)_3]^{3+}$ and 50 ns for $[Cr(tpy)_2]^{3+}$ in 1 M HCl at 25 °C.[7] This behavior is also evidenced in $[Ru(tpy)_2]^{2+}$ complexes with respect to $[Ru(bpy)_3]^{2+}$. The reasons behind this decrease are explained from a structural point of view. As a matter of fact, $[Cr(tpy)_2]^{3+}$ has a highly distorted structure. The Cr(III) core would now be more exposed to solvent perturbation so that direct vibrational coupling between the excited state metal core and the solvent could occur causing the non-radiative decay to increase dramatically.[1]

In addition to the rich photochemical properties, chromium complexes exhibit a series of one electron reversible redox couples between a number of formal oxidation states (+3, +2, +1 and 0). For complexes $[Cr(ttpy)_2]^{3+}$, these reductions were at first assigned to metal centered reductions until recently it was proven that they involve the sequential filling of the π^* orbital of the terpyridine ligands, while the metal is always in the +3 oxidation state although the $[Cr(ttpy)_2]^{2+}$ contains a small degree of Cr^{2+} character.[8] The relatively high reduction potentials of the terpyridine ligand in $[Cr(tpy)_2]^{3+}$ (–0.45 V *vs.* $Ag/AgNO_3$ for the first reduction) with respect to that in $[Fe(tpy)_2]^{2+}$ and $[Co(tpy)_2]^{3+}$ (–1.53 and –1.9 V *vs.* $Ag/AgNO_3$ respectively) is the result of the different electronic properties of the complex. Generally, the stable configuration of complexes is 18 e^-, however, $[Cr(ttpy)_2]^{3+}$ complex has a total of 15 e^- and hence requires three more electrons in order to satisfy the 18 e^- rule. This justifies the relatively high potentials of the reduction and the presence of several redox states formally denoted by $[Cr(tpy)_2]^{2+}$, $[Cr(tpy)_2]^{+}$ and $[Cr(tpy)_2]^{0}$. This is a significant feature, which is useful in catalytic cycles involving multi-electron redox properties.

For instance, Abruña et al. reported the catalytic activity of the polymerized vinyl terpyridyl complexes of Co, Cr, Ni, Fe, Ru and Os on glassy carbon electrodes towards the reduction of CO_2 yielding formaldehyde in an aqueous medium **figure 3.3**.[9] In the presented work, the authors demonstrate that superior electrocalytic activity is obtained with first row transition metals. This is explained by the necessity of generating an open coordination site that can bind CO_2 which is more feasible with labile first row transition metals. Moreover, the authors argue that the highest faradaic yield for the CO_2 reduction is obtained for the $[Cr(v\text{-}tpy)_2]^{3+}$ (87%) with respect to $[Fe(v\text{-}tpy)_2]^{2+}$ (28%) and $[Co(v\text{-}tpy)_2]^{3+}$ (39%) due to the ability of $[Cr(tpy)_2]^{3+}$ to exchange several electrons facilitating the reduction of CO_2 to formaldehyde which consumes a total of four electrons.

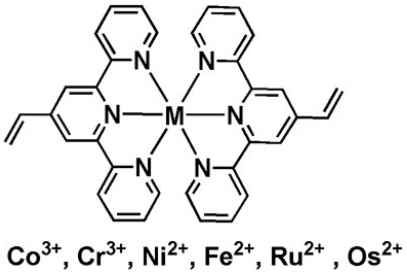

Figure 3.3: Molecular structure of [M(vinyl-tpy)$_2$]

Herein, we report the synthesis and characterization of mono and bisterpyridyl complexes of chromium. We will present a detailed study of the quenching of $[Cr(ttpy)_2]^{3+*}$ with PPh_3 used as a sacrificial electron donor. In a second step, the $[Cr(ttpy)_2]^{3+}$ is connected to a $[Ru(bpy)_3]^{2+}$ unit generating trinuclear assemblies of Ru-Cr-Ru. The nature of quenching between the different compartments will be studied in details in both bimolecular systems and trinuclear complexes. Moreover, we will discuss some preliminary results on the electrocatalytic activity of the mono and bisterpyridine chromium complexes towards the reduction of protons to dihydrogen.

3.2 $[Cr(ttpy)_2]^{3+}$ as a Potential Electron Acceptor:

3.2.1 Synthesis

The synthesis of $[Cr(ttpy)_2]^{3+}$ complex which is denoted by **[24]**$^{3+}$ is presented in **figure 3.4**. The Cr^{3+} metal center is known to be inert which means that it exchanges ligands very slowly in contrast to Cr^{2+} center which is very labile. Therefore, $CrCl_2$ is used in order to prepare complex **[24]**$^{2+}$ in a mixture of H_2O and EtOH, which is then oxidized by oxygen in order to give the desired complex **[24]**$^{3+}$. A key step is the precipitation of the complex by the addition of the desired salt prior to oxidation. As a matter of fact, it was evidenced in analogous $[Cr(bpy)_3]^{3+}$ that the oxidation of a solution of $[Cr(bpy)_3]^{2+}$ in water leads to the formation of a mixture of $[Cr(bpy)_3]^{3+}$ and $[Cr(bpy)_3]^{2+}$ during which the latter leads to the catalytic dissociation of $[Cr(bpy)_3]^{3+}$ generating $[Cr(bpy)_2(H_2O)_2]^{3+}$.[10] This undesired dissociation is prevented by oxidizing the suspension.

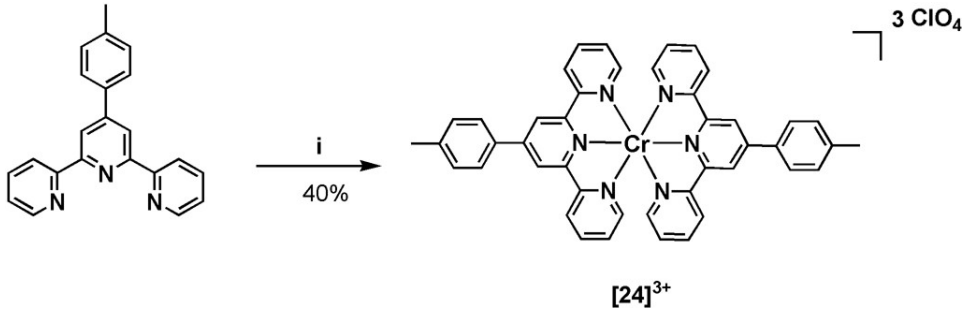

Figure 3.4: Synthesis of complex **[24]**$^{3+}$ (i) $CrCl_2$, H_2O:EtOH, 25 °C, 1 h, Ar; $NaClO_4$, O_2

3.2.2 Electrochemistry

The potentials of the different reduction processes of **[24]**$^{3+}$ are summarized in **table 3.1**.

Table 3.1: Redox potentials of complexes (**[24]**$^{3+}$ in a 10^{-3} M solution of deoxygenated CH_3CN + 0.1 M $[Bu_4N]BF_4$ at a scan rate 100 mV.s^{-1} using carbon vitreous disk (5 mm diameter). $E_{1/2}$ (V) ΔEp (mV) *vs.* $Ag/AgNO_3$ 0.01 M in CH_3CN, and L.C corresponds to ligand centered reduction process.

Complex	$E_{1/2}^{reduction}$, V (ΔEp, mV)		
	L.C 1	L.C 2	L.C 3
$[24]^{3+}$	–0.41 (60)	–0.77 (60)	–1.27 (60)

$[Cr(ttpy)_2]^{3+}$ complex is known to exhibit a series of one electron reversible reductions

between a number of oxidation states varying from +3 to +2, +1 and 0.[11] Nonetheless, the literature lacks a detailed spectro-electrochemical study that demonstrates both the spectroscopic and electrochemical signatures of the distinct oxidation states. Herein, we generated in situ the different $[Cr(ttpy)_2]^{2+}$, $[Cr(ttpy)_2]^{+}$ and $[Cr(ttpy)_2]^{0}$ species by exhaustive electrolysis of the solution. It is notable to mention that different solubility profiles are detected for $[Cr(ttpy)_2]^{n+}$ in acetonitrile depending on both the counter anion and the degree of oxidation. For instance $[Cr(ttpy)_2]^{3+}$ is only soluble in the form of BF_4^-, while $[Cr(ttpy)_2]^{2+}$ and $[Cr(ttpy)_2]^{+}$ are soluble in the form of BF_4^-, ClO_4^- and PF_6^-. Finally $[Cr(ttpy)_2]^{0}$ is only soluble as a ClO_4 salt. Thus we have studied the electrochemical and spectroscopic properties of $[Cr(ttpy)_2]^{n+}$ in the presence of two different supporting electrolytes $[Bu_4N]BF_4$ and $[Bu_4N]ClO_4$. To begin with, the CV of $[Cr(ttpy)_2]^{3+}$ shows three successive reversible one- electron reduction waves at –0.41, –0.77 and –1.27 V which is consistent with the electrochemical signatures of polypyridyl chromium complexes presented in the literature **figure 3.5.A**.[11]

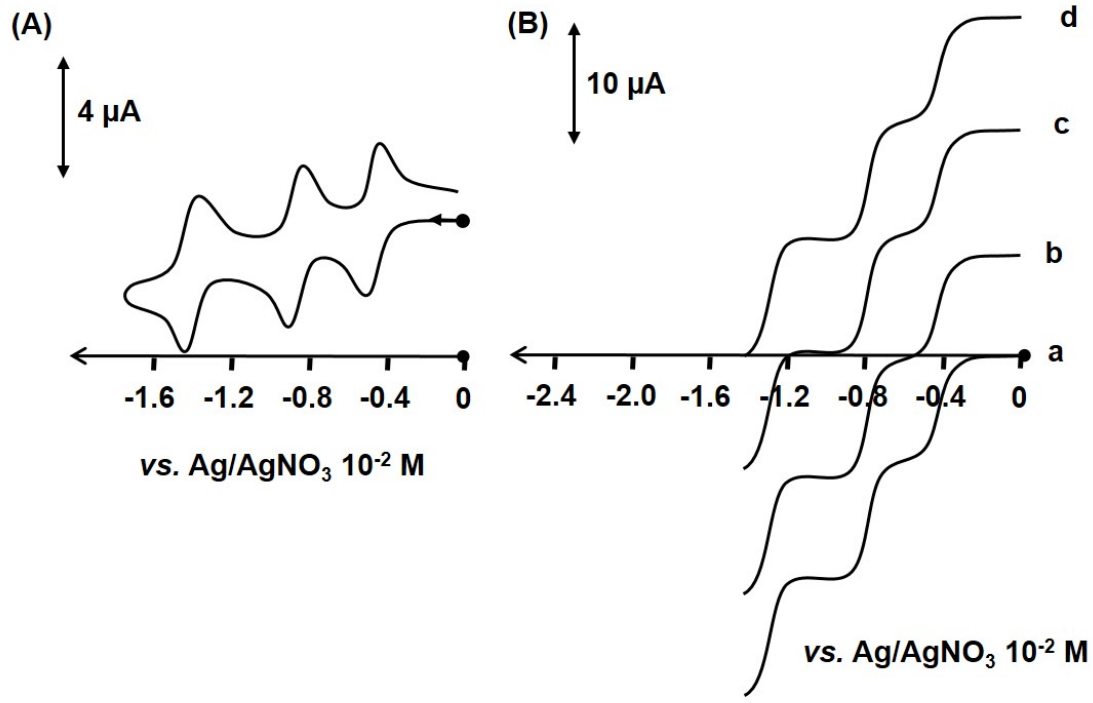

Figure 3.5: (A) CV of **[24]**$^{3+}$ (10^{-3} M) in CH_3CN + 0.1 M $[Bu_4N]BF_4$ at a carbon electrode (5 mm diameter); scan rate: 100 mV.s^{-1} *vs.* $Ag/AgNO_3$ (10^{-2} M); (B) Voltammogram at a carbon RDE of the same solution, ω = 600 rpm, scan rate: 5 mV.s^{-1}: (a) **[24]**$^{3+}$, (b) **[24]**$^{2+}$, (c) **[24]**$^{+}$, (d) **[24]**^{0}

The spectroscopic signatures of **[24]**$^{n+}$ are presented in **figure 3.6** and summarized in **table 3.2**. Initially the yellow-orange solution of $[Cr(ttpy)_2]^{3+}$ in CH_3CN displays intense absorption in the UV which is due to ligand-centered $\pi \rightarrow \pi^*$ transitions and a small absorption in the visible region around 470 nm and is attributed to a MC d $\rightarrow$ d transition **figure 3.6**.[1] Exhaustive electrolysis at –0.65 V lead to the generation of the $[Cr(ttpy)_2]^{2+}$ as validated by the RDE (line

b) **figure 3.5.B**. The formation of the latter species is accompanied by the emergence of two prominent bands in the visible region (500, 584 nm) and low energy transition around 800 nm which are assigned to $\pi^* \rightarrow \pi^*$ of the terpyridine radical anion by comparison with published results for analogous $[Cr(tpy)_2]^{2+}$.[8] Further reduction at –1 V consumes a total of one electron and leads to the generation of the purple $[Cr(ttpy)_2]^{+}$ species (line c) **figure 3.5.B** with the evolution of three intense bands in the visible region at 524, 560 and 723 nm. The exchange of an extra electron upon exhaustive electrolysis around –1.7 V lead to the isolation of $[Cr(ttpy)_2]^{0}$ species in the perchlorate form due to solubility problems (line d) **figure 3.5.B**. This is escorted by a significant increase of absorption in the whole visible spectrum ($\varepsilon \approx 37 \times 10^3$) reaching maxima at 520, 571, 670, 776 nm.

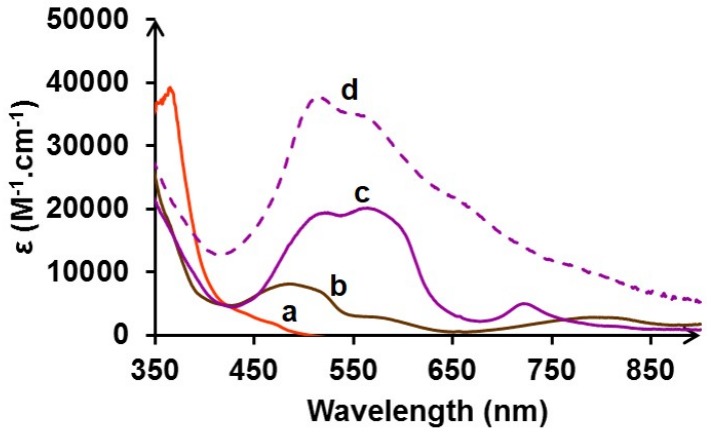

Figure 3.6: Absorption spectra of the different oxidation states of complex **[24]**$^{n+}$, orange line represents **[24]**$^{3+}$ in CH_3CN + 0.1 M $[Bu_4N]BF_4$; brown represents **[24]**$^{2+}$ CH_3CN + 0.1 M $[Bu_4N]BF_4$; purple full line represents **[24]**$^{+}$ CH_3CN + 0.1 M $[Bu_4N]BF_4$; dashed purple line represents **[24]**^{0} CH_3CN + 0.1 M $[Bu_4N]ClO_4$

Table 3.2: Spectroscopic signatures of **[24]**$^{3+}$, **[24]**$^{2+}$, **[24]**$^{+}$ in deoxygenated CH_3CN + 0.1 M $[Bu_4N]BF_4$ and of **[24]**^{0} in deoxygenated CH_3CN + 0.1 M $[Bu_4N]ClO_4$

Complex	λ_{abs}, nm (ε, $M^{-1}.cm^{-1}$)
$[24]^{3+}$	370 (36 500), 441 (3 500), 475 (1 500)
$[24]^{2+}$	500 (7 700), 584 (2 600), 800 (2 800)
$[24]^{+}$	524 (20 200), 560 (19 500) and 723 (5 000)
$[24]^{0}$	520 (37 500), 571 (33 600), 670 (19 900), 776 (10 500)

3.2.3 Photophysics

$[Cr(ttpy)_2]^{3+}$ displays a weak emission around 770 nm upon excitation at 370 nm. This emission arises from the population of the ^2E excited state through intersystem crossing.[1]

Low quantum yield of emission ($< 5 \times 10^{-4}$) and short lifetime (15 ns) has been obtained in deoxygenated CH_3CN solution at room temperature **table 3.5** which is consistent with results obtained for $[Cr(tpy)_2]^{3+}$ in the literature.[7]

In order to gain insight into the spectroscopic signatures of the excited states, we have studied the transient absorption profile of the complex with time, in a range of wavelengths varying from 340 - 800 nm using a nanosecond laser at λ = 355 nm for excitation **figure 3.7**. Upon excitation of the chromium complex, a negative peak is observed around 370 nm which reflects the photo-bleaching of the ground state of the chromium complex. Using this technique, we were able to detect a specific spectral signature with a large variation of absorbance around 550 nm. The signal decreases back to zero with a mono-exponential decay fitted with a lifetime of 415 ns. Without further investigation, we presume that this transient absorption would be due to the population of the $^2T_{1g}$ metal centered excited state.

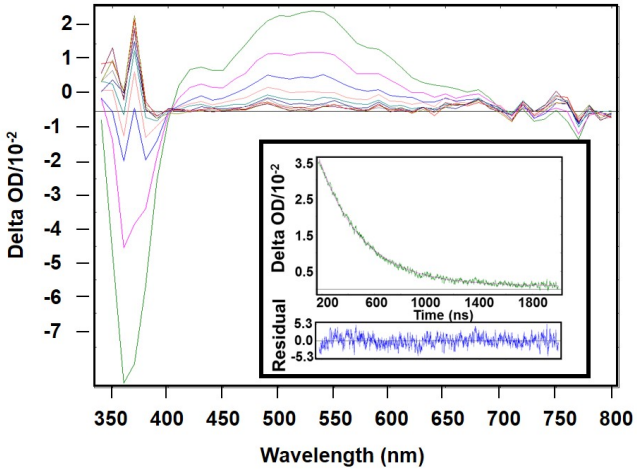

Figure 3.7: Transient absorption profile of a solution of $[Cr(ttpy)_2]^{3+}$ in CH_3CN at 25°C in a range of wavelengths varying from 340 to 800 nm upon excitation at 355 nm. Inset represent the decay of the signal at 550 nm as function of time.

3.2.4 Photoreduction of $[Cr(tpy)_2]^{3+}$ in the presence of PPh_3

As evidenced earlier, excitation of the $[Cr(ttpy)_2]^{3+}$ in the UV will lead to the formation of two distinctive excited states with two lifetimes. One emissive state with a lifetime of 15 ns and non emissive one with a lifetime of 415 ns. It is believed, that the second excited state can take part in bimolecular reactions in the presence of suitable reagents. In this work we are interested in the reductive quenching of the $[Cr(ttpy)_2]^{3+}$ complex. In this context, we studied the effect of addition of different irreversible electron donors such as triethanolamine, triethylamine, diethyldithiocarbamate and oxalate. All of these sacrificial electron donors react directly with the $[Cr(ttpy)_2]^{3+}$ in the absence of light. Triphenylphosphine (PPh_3) was finally

selected. A blank experiment was conducted by following the stability of our complex in the presence of the PPh_3 and in the absence of light. Indeed, the $[Cr(ttpy)_2]^{3+}$ showed a significant stability, showing that no direct thermal reduction takes place with triphenyl phosphine. PPh_3 is characterized by an irreversible oxidation (0.91 V *vs.* $Ag/AgNO_3$) and is known to produce $PPh_3^{+\bullet}$ which later reacts with traces of water found in the solution to produce HO-PPh_3. The latter can donate an extra electron to produce the O=PPh_3.[12]

In order to follow the behavior of the non-emitting excited state $^2T_{1g}$ of $[Cr(ttpy)_2]^{3+*}$ with PPh_3, we have conducted a Stern-Volmer experiment **figure 3.8**. The lifetime of $^2T_{1g}$ was recorded with variable concentrations of PPh_3 (0 to 2×10^{-3} mol.L^{-1}). Indeed, the lifetime decreased from 415 to 311 ns upon addition of PPh_3 showing the quenching of the $^2T_{1g}$. The reaction rate constant was calculated to 3×10^8 M^{-1}.s^{-1} using the Stern-Volmer equation described earlier.

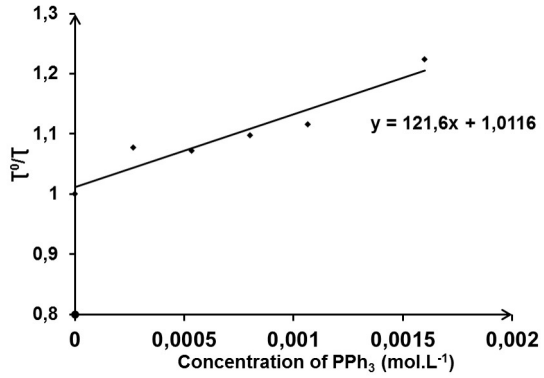

Figure 3.8: Stern-Volmer plot for the quenching of the $[Cr(ttpy)_2]^{3+*}$ ($^2T_{1g}$) with PPh_3

Then a mixture of $[Cr(ttpy)_2]^{3+}$ and PPh_3 (15 mM) in CH_3CN was irradiated with a Xenon Lamp and a UV-visible spectrum of the solution is registered in the course of irradiation **figure 3.9**.

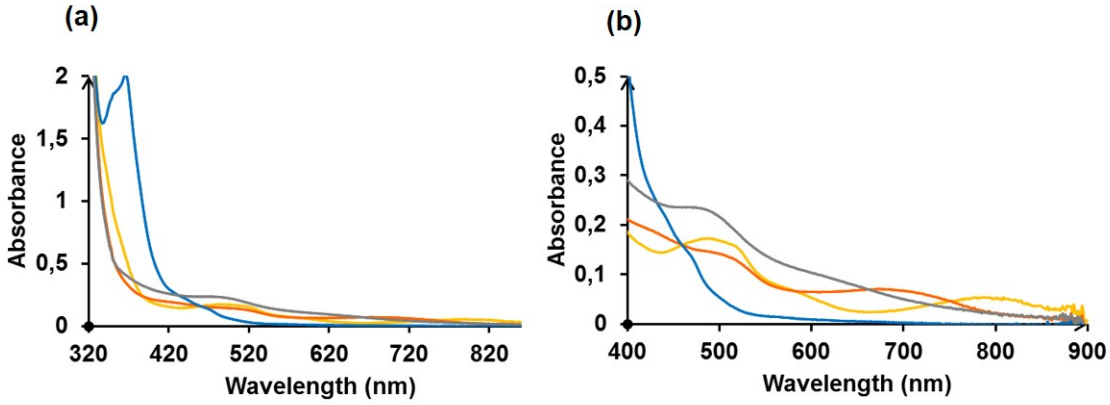

Figure 3.9: (a) Absorption spectra of a mixture of PPh_3 and $[Cr(ttpy)_2]^{3+}$ in CH_3CN; Blue: before irradiation; Yellow: After 18 minutes of irradiation, Orange: After 50 minutes; Grey after 90 minutes; (b) Zoom on the visible near-infrared region

Meanwhile, the absorption in UV decreases drastically, with a significant increase in the absorbance in the visible-near infrared spectrum. The evolution of several pseudo isosbestic points is observed during irradiation, which is consistent with the transformation between several species. In particular, four different spectroscopic signatures were distinguished. The absorption spectrum of the initial solution is presented in blue and is described by a strong absorption around 370 nm which is due to $\pi \rightarrow \pi^*$ transition in the $[Cr(ttpy)_2]^{3+}$, and a week absorption in the visible region.

After 18 minutes of continuous irradiation in the presence of triphenyl phosphine as a sacrificial electron donor, the absorption in the UV significantly drops accompanied by an increase in the bands at 500, 584 and 800 nm with the formation of an isosbestic point at 477 nm as shown in **figure 3.10**. This is consistent with the consumption of $[Cr(ttpy)_2]^{3+}$ and accumulation of the $[Cr(ttpy)_2]^{2+}$ species in solution. The reaction yield is estimated to 40% based on the absorption band at 800 nm.

The kinetic rate of electron transfer was calculated by plotting the variation of the absorbance of the bands at 370 and 801 nm with time. By fitting the curves with a first-order exponential decay function, a kinetic rate constant k = 1.7 $\times$ 10^{-3} s^{-1} and k = 4.7 $\times$ 10^{-3} s^{-1} are found for the bands under 370 and 801 nm respectively. The slight difference in the constants could be due to a perturbation of the band at 370 nm due to the absorbance of the degradation product of PPh_3.

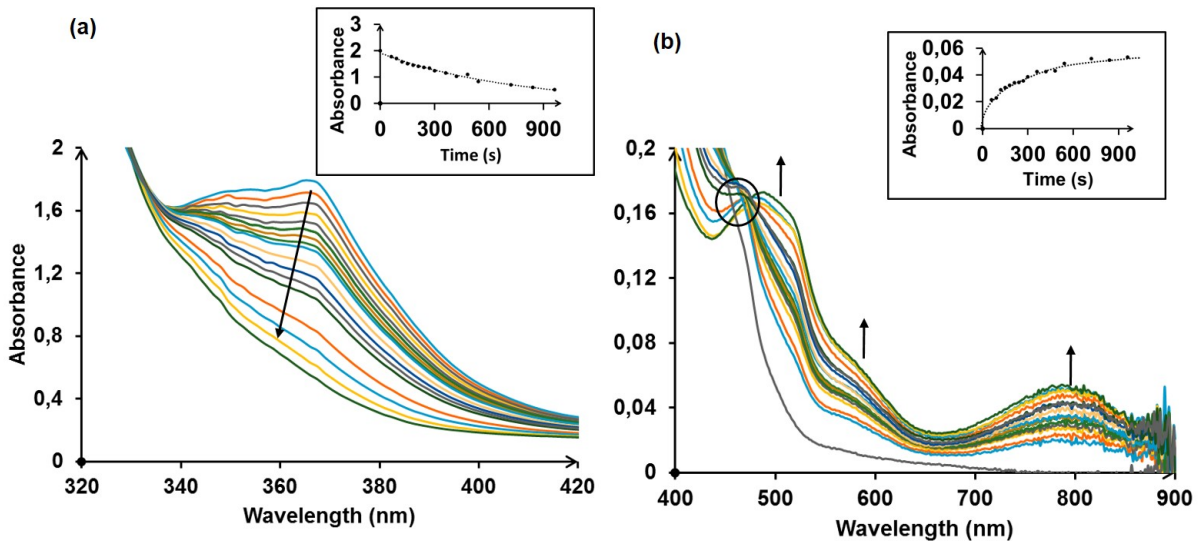

Figure 3.10: Evolution of the absorption spectrum with a 30 second time interval during the first 18 minutes of irradiation of a mixture of PPh_3 and $[Cr(ttpy)_2]^{3+}$ in deoxygenated CH_3CN. (a) wavelength range between 320 and 420 nm, inset: plot of the variation of the absorbance at 370 nm as a function of time (b) wavelength range 400 to 900 nm, inset: plot of the variation of the absorbance at 801 nm as a function of time.

Continuous irradiation for up to 50 minutes lead to the disappearance of the band at 800 nm and the appearance of another one with a maximum around 720 nm accompanied with the formation of a pseudo isosbestic point at 770 as shown in **figure 3.11**. This was also associated with increase of absorbance at 440 nm, which is coherent with the formation of the $[Cr(ttpy)_2]^+$ species. This suggests that the generated $[Cr(ttpy)_2]^{2+}$ species can be engaged in a photoreduction process with PPh_3 This unique behavior allows the storage of two electrons on the $[Cr(ttpy)_2]^{3+}$. The reaction yield is estimated to 30% based on the absorption band at 720 nm.

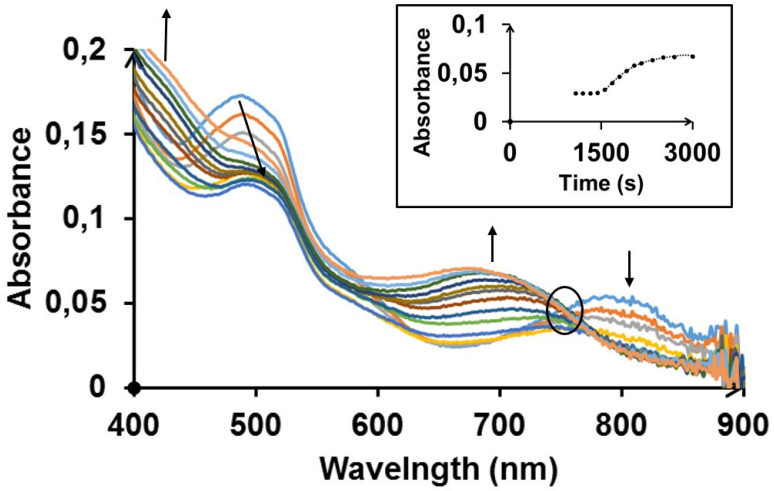

Figure 3.11: Evolution of the absorption spectrum with a 60 second time interval between 18 and 50 minutes of irradiation of a mixture of PPh_3 and $[Cr(ttpy)_2]^{3+}$ in deoxygenated CH_3CN; Inset: plot of the variation of the absorbance at 700 nm with time.

Prolonged irradiation for more than 50 minutes lead to the disappearance of the signature of $[Cr(ttpy)_2]^+$ and the appearance of new and intense peaks in the visible with maxima at 480 and 610 nm. These absorptions are not identical to that of the $[Cr(ttpy)_2]^0$ profile and may correspond to the degradation product. This shows that two electron transfers takes place between $[Cr(ttpy)_2]^{3+}$ and PPh_3 generating $[Cr(ttpy)_2]^{2+}$ and $[Cr(ttpy)_2]^+$ consecutively with a respective yield of 40 and 30%. In order to increase the transformation rate and yield, we studied the influence of the addition of $[Ru(bpy)_3]^{2+}$ as an external photosensitizer on the reaction.

3.2.5 Photoreduction of $[Cr(tpy)_2]^{3+}$ in the presence of $[Ru(bpy)_3]^{2+}$ and PPh_3

A photolysis experiment was performed on a bimolecular mixture of $[Ru(bpy)_3]^{2+}$ and $[Cr(ttpy)_2]^{3+}$ (1:1) in CH_3CN in the presence of a sacrificial electron donor PPh_3. Continuous irradiation with the Xenon lamp under the same experimental conditions lead to the formation of three species with different spectroscopic signatures as monitored in **figure 3.12**.

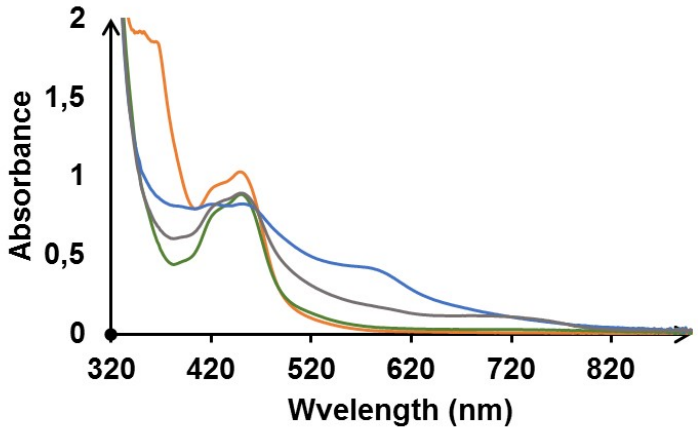

Figure 3.12: Evolution of the absorption spectra in a (1:1) mixture of $[Ru(bpy)_3]^{2+}$ and $[Cr(ttpy)_2]^{3+}$, in the presence of PPh_3 (15 mM) in deoxygenated CH_3CN; Orange: Before irradiation; Green: After 4 minutes of irradiation, Grey: After 23 minutes of irradiation; Blue: After 50 minutes of irradiation.

Initially the absorption spectra in the visible region is dominated by the MLCT of $[Ru(bpy)_3]$ with a maximum around 450 nm. In addition to that an intense band in the UV (370 nm) is also evident and is the superimposition of the $\pi \rightarrow \pi^*$ transitions of both complexes. During the first 4 minutes of irradiation, the band at 370 nm significantly drops in intensity with only a slight increase in the absorbance near the red part of the spectrum **figure 3.13**.

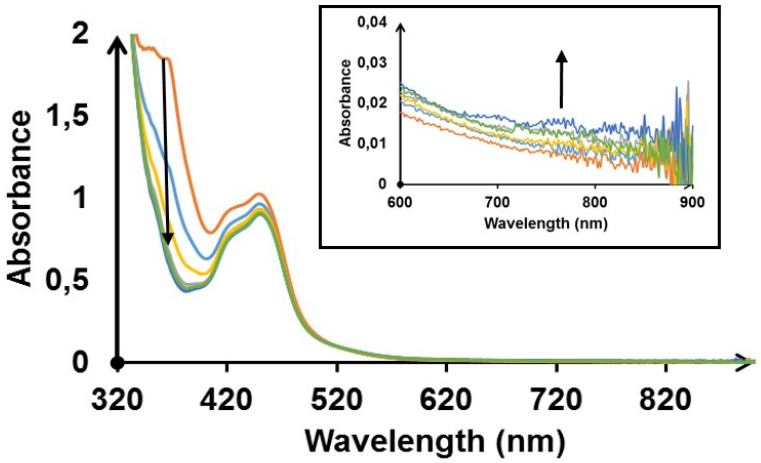

Figure 3.13: The absorption spectra with a 30 s time interval in a (1:1) mixture of $[Ru(bpy)_3]^{2+}$ and $[Cr(ttpy)_2]^{3+}$, in the presence of PPh_3 (15 mM) in deoxygenated CH_3CN during the first 4 minutes of irradiation; Inset: zoom on the red part of the spectrum

This is an indication of the consumption of $[Cr(ttpy)_2]^{3+}$ species present in the medium, with a small accumulation of $[Cr(ttpy)_2]^{2+}$. Thus, the first transformation is accelerated in the presence of $[Ru(bpy)_3]^{2+}$ with respect to the mixture of $[Cr(ttpy)_2]^{3+}$/ PPh_3 (18 minutes) **figure 3.14**. This suggests that the consumption of $[Cr(ttpy)_3]^{3+}$ is most probably mediated by the

$[Ru(bpy)_3]^{2+}$ photosensitizer. However the quantification of the photogenerated $[Cr(ttpy)_3]^{2+}$ remains difficult to determine. After 4 minutes, the absorption bands at 590 and 720 nm start to increase significantly **figure 3.15**.

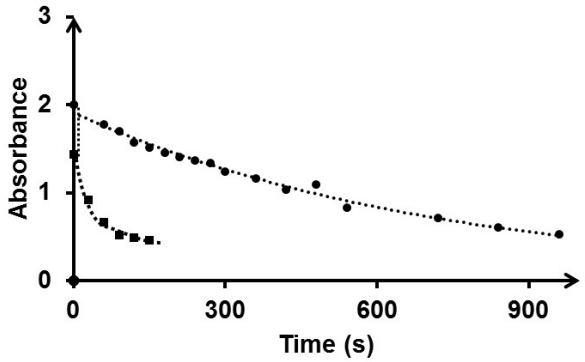

Figure 3.14: The evolution of the absorption at 370 nm under similar experimental conditions for a mixture of $[Cr(tpy)_2]^{3+}/PPh_3$ (●) and a mixture of $[Ru(bpy)_3]^{2+}/[Cr(ttpy)_2]^{3+}$ /PPh_3 (■).

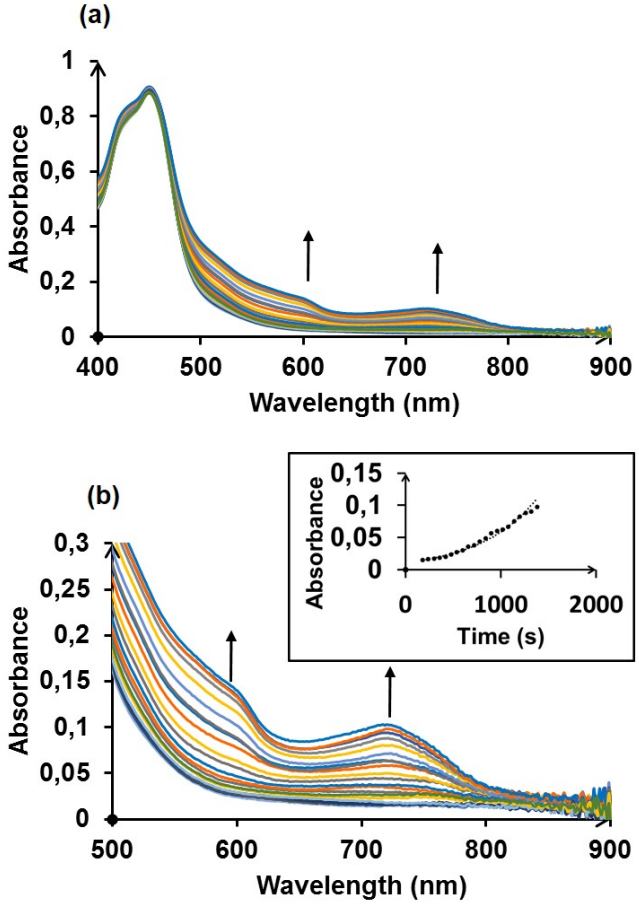

Figure 3.15: The absorption spectra with a 30 s time interval in a (1:1) mixture of $[Ru(bpy)_3]^{2+}$ and $[Cr(ttpy)_2]^{3+}$, in the presence of PPh_3 (15 mM) in deoxygenated CH_3CN from 4 to 23 minutes of irradiation; Inset: Variation of the absorbance at 720 nm during irradiation.

This is in accordance with the formation of $[Cr(ttpy)_2]^+$ species. The enhancement of the kinetic rate is also accompanied by an increase of the reaction yield to 55% of photogenerated $[Cr(ttpy)_2]^+$. Prolonged irradiation, (more than 23 minutes) lead to the replacement of the $[Cr(ttpy)_2]^+$ signatures with bands around 580 nm as presented by the blue line in **figure 3.12**. The nature of the formed species is not clear at this point, but might include some amounts of $[Cr(ttpy)_2]^0$. Here again, these results show that $[Cr(ttpy)_2]^{3+}$ can efficiently accept a minimum of two electrons forming $[Cr(ttpy)_2]^+$.

In order to investigate the reactivity of the photoreduction of $[Cr(ttpy)_2]^{3+}$ in the presence of $[Ru(bpy)_3]^{2+}$ we performed a series of experiments. First we confirmed that there is no photoinduced electron transfer process between the $[Ru(bpy)_3]^{2+}$ and PPh_3. Under irradiation, the mixture is stable and shows degradation of the $[Ru(bpy)_3]^{2+}$ without the formation of $[Ru(bpy)_3]^+$ only after prolonged irradiation (more than one hour). Thus, the only possible interaction for the $[Ru(bpy)_3]^{2+*}$ will be with $[Cr(ttpy)_2]^{3+}$ species.

In order to confirm this hypothesis a Stern-Volmer experiment was conducted between the two species. The lifetime of the ^{3}MLCT of the $[Ru(bpy)_3]^{2+*}$ core was recorded upon addition of variable concentrations of $[Cr(ttpy)_2]^{3+}$ reaching 10 equivalents with respect to the ruthenium. As a matter of fact, the lifetime of $[Ru(bpy)_3]^{2+*}$ gradually decreases from 914 to 805 ns upon gradual addition of the $[Cr(ttpy)_2]^{3+}$ **figure 3.16**. The reaction rate constant is estimated to 3.02×10^9 s^{-1} using the Stern-Volmer equation described earlier.

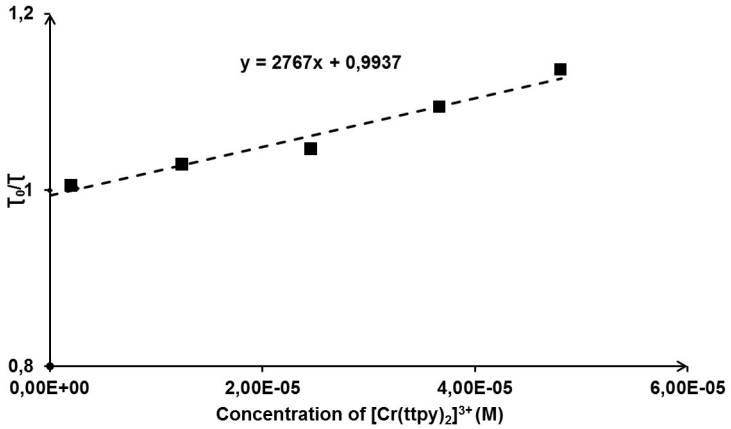

Figure 3.16: A Stern-Volmer plot of the quenching of $[Ru(bpy)_3]^{2+}$ upon addition of increasing concentration of $[Cr(ttpy)_2]^{3+}$ in deoxygenated CH_3CN

The nature of this interaction is most probably due to an electron transfer process, since there is no overlap between the emission of $[Ru(bpy)_3]^{2+*}$ and the absorption of $[Cr(ttpy)_2]^{3+}$. Careful examination of the ΔG value shows that the reaction is highly exergonic with a ΔG = –0.66 eV following **equation 3.1**:

$$[Ru(bpy)_3]^{2+*} + [Cr(ttpy)_2]^{3+} \rightarrow [Ru(bpy)_3]^{3+} + [Cr(ttpy)_2]^{2+} \tag{3.1}$$

In this experiment, the photogenerated $[Ru(bpy)_3]^{3+}$ species obtained after the oxidative quenching with $[Cr(ttpy)_2]^{3+}$ can react with PPh_3 to regenerate $[Ru(bpy)_3]^{2+}$. The formed $[Cr(ttpy)_2]^{2+}$ absorbs in the visible region and can also interact by energy transfer with the $[Ru(bpy)_3]^{2+*}$ state, or by reductive or oxidative quenching **equation 3.2**:

$$[Ru(bpy)_3]^{2+*} + [Cr(ttpy)_2]^{2+} \rightarrow [Ru(bpy)_3]^{2+} + [Cr(ttpy)_2]^{2+*} \text{ Energy Transfer}$$

$$[Ru(bpy)_3]^{2+*} + [Cr(ttpy)_2]^{2+} \rightarrow [Ru(bpy)_3]^{+} + [Cr(ttpy)_2]^{3+} \quad \text{Reductive Quenching } (\Delta G = -0.79 \text{ eV})$$

$$[Ru(bpy)_3]^{2+*} + [Cr(ttpy)_2]^{2+} \rightarrow [Ru(bpy)_3]^{3+} + [Cr(ttpy)_2]^{+} \quad \text{Oxidative Quenching } (\Delta G = -0.3 \text{ eV}) \tag{3.2}$$

Despite the more negative ΔG value for reductive quenching, the formation of $[Cr(ttpy)_2]^{+}$ in our photolysis experiment suggests that the oxidative quenching is kinetically faster.

Thus, upon irradiation in the UV and in the visible region, two pathways are possible for the photogeneration of $[Cr(ttpy)_2]^{+}$ either by the direct reductive quenching of $[Cr(ttpy)_2]^{3+*}$ by PPh_3, or mediated by the $[Ru(bpy)_3]^{2+*}$ state *via* electron transfer. Undoubtedly, the presence of both photosensitizers will allow the utilization of a larger range of wavelengths which is most probably responsible for the enhancement of the kinetics and the yield of the photoredox reaction.

3.3 Trimetallic Complex [Ru(bpy)$_3$]-[Cr(tpy)$_2$]-[Ru(bpy)$_3$]

3.3.1 Synthesis

The previously described complex Ru-O-tpy **[3]**$^{2+}$ is used for the construction of the trinuclear assembly {[Ru(bpy)$_2$(bpy-O-tpy)]$_2$Cr}$^{6+}$, **[25]**$^{6+}$, holding both [Cr(ttpy)$_2$]$^{2+}$ and [Ru(bpy)$_3$]$^{2+}$ **figure 3.17**. Complex **[25]**$^{6+}$ is synthesized by refluxing one molar equivalent of a $CrCl_2$ and two molar equivalents of the building block Ru-O-tpy in methanol for 5 hours. The complex was then isolated as a hexafluorophosphate salt and purified by recrystallization from a mixture of CH_3CN : Et_2O. It is noteworthy, that the complexation of the chromium in the trinuclear complex is very slow and requires more heat and time with respect to [Cr(ttpy)$_2$]$^{2+}$. This could be rationalized by the increase of charge present in the trinuclear complex, which most probably makes it more difficult to complex the chromium. Then **[25]**$^{6+}$ is oxidized by exhaustive electrolysis in a glove box to yield **[25]**$^{7+}$. The following study is performed with the air stable **[25]**$^{7+}$ complex.

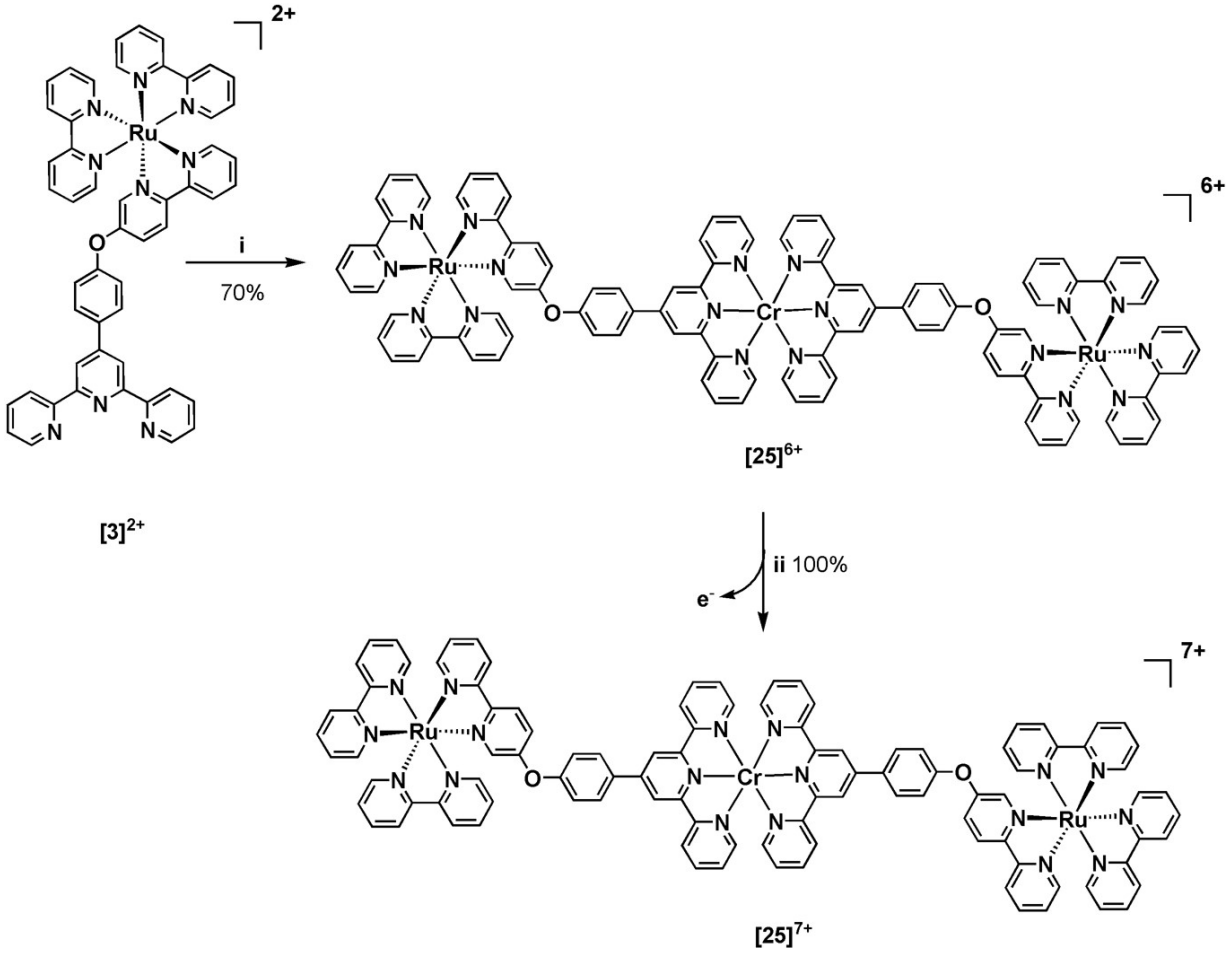

Figure 3.17: Synthesis of the trinuclear complex **[25]**$^{6+}$, (i) $CrCl_2$, MeOH, 65 °C, 4 h, KPF_6; (ii) oxidation by exhaustive electrolysis at 0 V *vs.* Ag/$AgNO_3$ (10^{-2} M) in CH_3CN + 0.1 M $[(Bu)_4N]ClO_4$.

3.3.2 Spectro-electrochemistry

In this section we will examine the electrochemical and spectroscopic (UV-visible) behavior of the trimetallic complex Ru^{II}-Cr^{III}-Ru^{II} denoted by **[25]**$^{7+}$. The signatures of Ru-O-tpy have already been discussed in **Chapter 1** and those of $[Cr(ttpy)_2]^{3+}$ in the previous section and are collected in **tables 3.3** and **3.4**. Both the cyclic voltammogram and the UV-visible spectrum are essentially the superimposition of the signatures of the individual molecular components in their respective (2:1) ratio verifying the net formation of Ru^{II}-Cr^{III}-Ru^{II} in its pure form.

Table 3.3: Redox potentials of complexes (**[3]**$^{2+}$; **[24]**$^{3+}$ and **[25]**$^{7+}$ in a 10^{-3} M solution of deoxygenated CH_3CN + 0.1 M $[Bu_4N]ClO_4$ at a scan rate 100 mV.s^{-1} using carbon vitreous disk (5mm diameter). $E_{1/2}$ (V) ΔEp (mV) *vs.* $Ag/AgNO_3$ 0.01 M in CH_3CN, and L.C corresponds to ligand centered reduction process.

Complex	$E_{1/2}^{oxidation}$, V (ΔEp, mV)	$E_{1/2}^{reductions}$, V (ΔEp, mV)			
	Ru^{3+}/Ru^{2+}	L.C 1	L.C 2	L.C 3	L.C 4
$[3]^{2+}$	1.01 (60)	–1.63 (60)	–1.85 (100)	–2.07 (60)	–2.36 (80)
$[24]^{3+}$		–0.41 (60)	–0.77 (60)	–1.27 (60)	
$[25]^{7+}$	1.01 (60)	–0.37 (60)	–0.73 (60)	–1.23 (60)	–1.54 (80)

Table 3.4: Absorption signatures of **[3]**$^{2+}$, **[24]**$^{3+}$, **[25]**$^{9+}$, **[25]**$^{7+}$, **[25]**$^{6+}$, **[25]**$^{5+}$ and **[25]**$^{4+}$ in deoxygenated CH_3CN + 0.1 M $[Bu_4N]ClO_4$

Complex	λ_{abs}, nm (ε, M^{-1}.cm^{-1})
$[3]^{2+}$	445 (11 000)
$[24]^{3+}$	370 (36 500), 441 (3 500), 475 (1 500)
$[25]^{9+}$	361 (43 500), 656 (2 800)
$[25]^{7+}$	370 (35 500), 445 (25 300)
$[25]^{6+}$	370 (26 200), 449 (28 500), 524 (9 500), 580 (3 800), 782 (3 500)
$[25]^{5+}$	448 (23 500) , 527 (16 800), 572 (19 500), 722 (5 500)
$[25]^{4+}$	449 (30 100), 518 (29 700), 568 (34 500), 727 (13 800)

The CV of **[25]**$^{7+}$ is generally the superimposition of the electroactivity of $[Ru(bpy)_3]^{2+}$ and $[Cr(ttpy)_2]^{3+}$ **figure 3.18.a**. In the positive region of the CV, a reversible redox system is observed with $E_{1/2}$ = 1.01 V. This redox event appears at an identical potential to the oxidation of the parent molecule Ru-O-tpy **[3]**$^{2+}$ and is hence attributed with no doubt to the oxidation of the ruthenium center. The fact, that this process takes place in an identical potential in both **[25]**$^{7+}$ and Ru-O-tpy ascertains the weak electronic coupling between the metallic centers. This has also been evidenced in a series of Ru^{II}-Fe^{II}-Ru^{II} and Ru^{II}-Co^{III}-Ru^{II} trimetallic complexes

discussed earlier in **Chapter 1** and is thought to be governed by the presence of the ether linkage which minimizes the electronic communication between the different entities of the system.

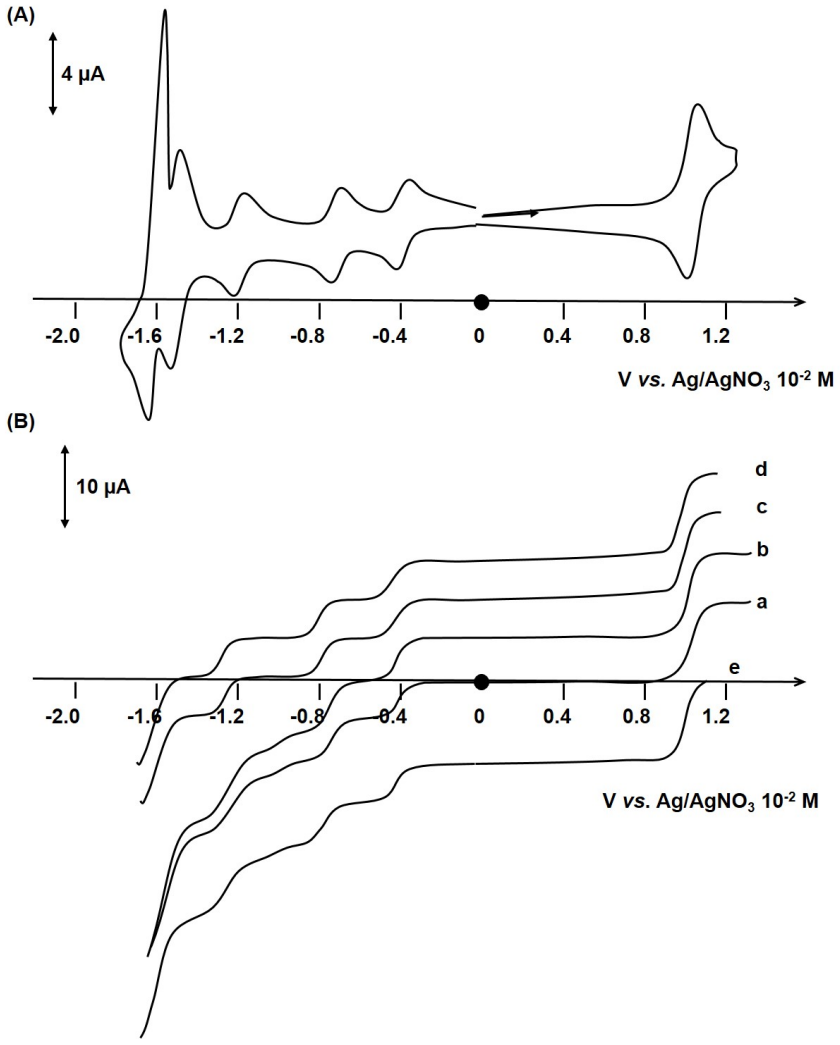

Figure 3.18: (A) CV of **[25]**$^{7+}$ (10^{-3} M) in CH_3CN + 0.1 M $[Bu_4N]ClO_4$ at a carbon electrode; scan rate: 100 mV.s^{-1} ; (B) Voltammogram at a carbon RDE of the same solution, ω = 600 rpm, scan rate: 5 mV.s^{-1}: (a) **[25]**$^{7+}$ initial solution , (b) after electrolysis at –0.7 V forming **[25]**$^{6+}$, (c) after electrolysis at –1.0 V forming **[25]**$^{5+}$, (d) after electrolysis at –1.3 V forming **[25]**$^{4+}$, (e) after electrolysis at 1.2 V forming **[25]**$^{9+}$

Moreover, in the negative region three reversible reduction waves are recorded with potentials varying from –0.37 V, to –0.73 V and –1.23 V in addition to a quasi reversible peak at –1.54 V. The first three reduction peaks have comparable $E_{1/2}$ values to those of $[Cr(ttpy)_2]^{3+}$. Thus, they are assigned to the succesive terpyridine reduction of the $[Cr(tpy)_2]^{3+}$ in the trinuclear complex. The slight shift in potential is due to the different substitution on the para position of the terpyridine within the trinuclear complex (ether) and the proposed model (methyl). As a matter of fact, the presence of the ethers renders the complex easier to reduction. The wave at –1.54 V is closer in potential to the L.C 1 in Ru-O-tpy **[3]**$^{2+}$ with a shift of 90 mV and

is attributed to the reduction of the bipyridine of the $[Ru(bpy)_3]^{2+}$ subunit. At a lower potential lies the reduction of the other bipyridine ligands, however they are distorted by some electroprecipitation-redissolution phenomena and couldn't be assigned.

The stoichiometry of the metallic constitution is also verified by RDE experiment **figure 3.18.b**. By comparison of the height of the peak under the oxidation process and the first three reduction waves, a 2:1 ratio is obtained, which is consistent with the presence of two Ru centers and one Cr unit. Using the values obtained from the RDE, the reduction processes can be summarized by the following **equations 3.3**.

$$\{[Ru^{II}(bpy)_2(bpy\text{-}tpy)_2]_2Cr^{III}\}^{7+} + e^- \rightleftarrows \{Ru^{II}(bpy)_2(bpy\text{-}tpy^{\bullet-})Cr^{III}\ (tpy\text{-}bpy)(bpy)_2Ru^{II}\}^{6+}$$

$$\{Ru^{II}(bpy)_2(bpy\text{-}tpy^{\bullet-})Cr^{III}\ (tpy\text{-}bpy)(bpy)_2Ru^{II}\}^{6+} + e^- \rightleftarrows \{[Ru^{II}(bpy)_2(bpy\text{-}tpy^{\bullet-})]_2Cr^{III}\}^{5+}$$

$$\{[Ru^{II}(bpy)_2(bpy\text{-}tpy^{\bullet-})]_2Cr^{III}\}^{5+} + e^- \rightleftarrows \{Ru^{II}(bpy)_2(bpy\text{-}tpy^{2-})Cr^{III}\ (^{\bullet-}tpy\text{-}bpy)(bpy)_2Ru^{II}\}^{4+}$$

$$\{Ru^{II}(bpy)_2(bpy\text{-}tpy^{2-})Cr^{III}\ (^{\bullet-}tpy\text{-}bpy)(bpy)_2Ru^{II}\}^{4+} + 2e^- \rightleftarrows \{Ru^{II}(bpy^{\bullet-})(bpy)(bpy\text{-}tpy^{2-})Cr^{III}\ (^{\bullet-}tpy\text{-}bpy(bpy^{\bullet-})(bpy)Ru^{II}\}^{2+} \quad (3.3)$$

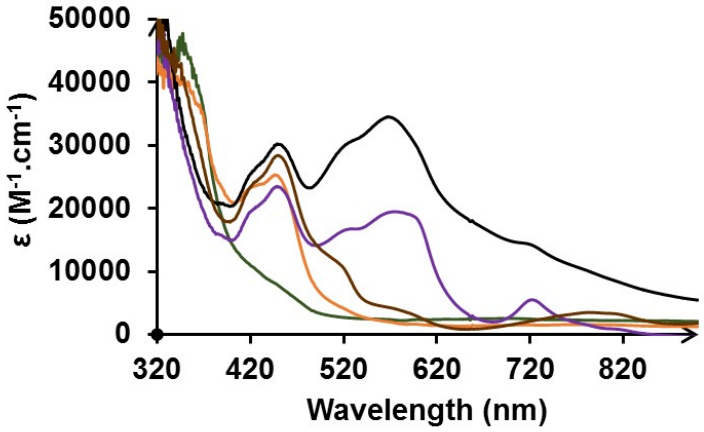

Figure 3.19: Absorption spectra of the different oxidation states of complex **[25]**$^{n+}$ in CH_3CN + 0.1 M $[Bu_4N]ClO_4$, black line represents **[25]**$^{4+}$, purple line represents **[25]**$^{5+}$; brown line represents **[25]**$^{6+}$; red line represents **[25]**$^{7+}$; green line represents **[25]**$^{9+}$

Initially the complex is under the form **[25]**$^{7+}$ as evidenced in the RDE voltammogram and in the absorption spectra which is characterized by a strong $\pi \rightarrow \pi*$ absorption due to the presence of $[Cr(tpy)_2]^{3+}$ and MLCT band at 445 nm which confirms the presence of two $[Ru(bpy)_3]^{2+}$ cores. Exhaustive electrolysis at –0.6 V consumed a total of one electron and lead to the formation of **[25]**$^{6+}$ which is characterized by the low energy $\pi* \rightarrow \pi*$ transitions around 800 nm. Further electrolysis at –1.0 V was accompanied by an exchange of one extra electron generating **[25]**$^{5+}$. This also lead to the disappearance of the band at 800 nm and an increase of the absorption in the visible region and at 527, 570 and 720 nm, with the formation of an isosbestic point at 770 nm. This is all in accordance with the net reduction of $[Cr(tpy)_2]^{2+}$ to $[Cr(tpy)_2]^{+}$. Electrolysis at more negative potential –1.3 V lead to the consumption of an extra electron with a significant increase of the absorption in the visible region with maxima at 520, 571, 670 and 760 nm which are typical transitions for $[Cr(ttpy)_2]^{0}$. Applying a potential of 0 V lead to the consumption of a total of three electron regenerating complex **[25]**$^{7+}$. This is also accompanied by the disappearance of the absorption in the visible region of the spectrum with an increase of absorbance around 370 nm. This is all in agreement with the formation of the $[Cr(ttpy)_2]^{3+}$ species and proves the reversibility of all the redox systems. This was further validated by the RDE curve. The exchange of two additional electrons at 1.2 V lead to the total disappearance of the Ru(II) MLCT band, and an increase in the absorbance around 670 nm in accordance with the formation of the Ru^{3+} species.

Analysis of the RDE voltammogram of the different species lead to two important observations. To begin with, during all transformations the ratio of the peaks is unaltered and as such an indication of the stability of the complex under several oxidation states. Nonetheless, in some cases the signals in the negative region are not well defined, and this could be attributed to different solubility patterns of the differently reduced species. As a matter of fact, such solubility problems are evidenced for the $[Cr(ttpy)_2]^{n+}$ under its different oxidation states as discussed earlier.

3.3.3 Photophysics

The photophysical data of compounds **[25]**$^{7+}$, **[25]**$^{6+}$, **[25]**$^{5+}$ and **[25]**$^{4+}$ along with **[24]**$^{3+}$ and Ru-O-tpy are collected in **table 3.5**. Upon excitation in the visible region (450 nm), emission with a λ_{em} = 610 nm is observed. This is a typical signature of the ^{3}MLCT excited state of $[Ru(bpy)_3]^{2+}$. However, the quantum yield of emission in complexes **[25]**$^{n+}$ are inferior to that of the parent molecule Ru-O-tpy (0.048) suggesting that there is a significant quenching pathway. It is noteworthy that quantum yield of emission is highly dependent on the oxidation state of the chromium showing that different deactivation mechanisms are taking place in the series of complexes.

Table 3.5: Photophysical data of compounds Ru-O-tpy, **[24]**$^{3+}$, **[25]**$^{7+}$, **[25]**$^{6+}$, **[25]**$^{5+}$ and **[25]**$^{4+}$ recorded in deoxygenated CH_3CN + 0.1 M $[Bu_4N]ClO_4$ solution at 25 °C. ϕ_{em} represents the emission quantum yield of the complexes

Complex	λ_{em} (nm)	Lifetime	τ (ns)	k_q (s^{-1})	ϕ_{em}	ϕ_{em}/ϕ_0 (%)
		τ_1 ns (%)	τ_2 ns (%)			
Ru-O-tpy	610	527	-	-	0.048	-
$[24]^{3+}$	770	15	-		$< 5 \times 10^{-4}$	
$[25]^{7+}$	610	5 (62)	628 (38)	2.0×10^8	0.013	27
$[25]^{6+}$	610	6 (40)	678 (60)	1.6×10^8	0.029	60
$[25]^{5+}$	610	9 (47)	650 (53)	1.09×10^8	0.034	70
$[25]^{4+}$	610	9 (58)	628 (42)	1.09×10^8	0.009	19

The luminescence decays of complexes **[25]**$^{n+}$ in all oxidation states are fitted by a biexponential function as demonstrated for earlier trimetallic complexes **[6]**$^{6+}$, **[7]**$^{6+}$ and **[7]**$^{7+}$ with iron and cobalt respectively. This biexponential decay shows that the quenching is not total, and only part of the species undergoes an intra-molecular quenching. Hence the short lifetime τ_1 represents the intramolecular quenching, while the longer one τ_2 is slightly higher than the parent molecule Ru-O-tpy, yet close enough to be assigned to the unquenched Ru center. The fractional amplitude of this biexponential decay (%) are collected in **table 3.5**.

The fastest quenching in the range of $2\times\ 10^8$ s^{-1} occurs within the Ru^{2+}-Cr^{3+}-Ru^{2+} system. As previously discussed, this interaction is due to an intramoleulcar electron transfer process resulting to the formation of the Ru^{3+}-Cr^{2+}-Ru^{2+} transient species.The assignment of the quenching mechanism for complexes **[25]**$^{6+}$, **[25]**$^{5+}$ and **[25]**$^{4+}$ is more complicated. One of the prominent aspects of the absorption spectra of these complexes is the strong absorption in the visible region. This implies an overlap with the emission of the Ru core which significantly increases passing from **[25]**$^{6+}$ to **[25]**$^{5+}$ and **[25]**$^{4+}$. Thus, energy transfer represents an important deactivation pathway for this series of complexes.

As mentioned in the case of $[Ru(bpy)_3]^{2+}$ and $[Cr(ttpy)_2]^{2+}$, oxidative and reductive quenching are thermodynamically feasible for complex **[25]**$^{6+}$.

Concerning **[25]**$^{5+}$, the oxidative quenching pathway is eliminated since it is endergonic with ΔG = 0.2 eV. Yet, reductive quenching is possible due the highly negative ΔG = –1.16 eV leading to the transient formation of Ru^{+}-Cr^{2+}-Ru^{2+}.

Lastly, for **[25]**$^{4+}$, the thermodynamics of a reductive quenching is exergonic by = –1.6 eV forming the transient Ru^{+}-Cr^{+}-Ru^{2+}.

The efficiency of the quenching varies significantly following the trend **[25]**$^{4+}$ > **[25]**$^{7+}$ > **[25]**$^{5+}$ ≈ **[25]**$^{6+}$ as described by the remaining intensities 19, 27, 60 and 70 % respectively. The

more significant quenching for compound **[25]**$^{4+}$ can be the result of more favorable energy and electron transfer as evidenced by both the strong overlap and the highly negative ΔG values.

3.3.4 *Photoredox behavior of [Ru(bpy)$_3$]-[Cr(tpy)$_2$]-[Ru(bpy)$_3$] in the presence of PPh$_3$*

For the photolysis experiment, a mixture of the trinuclear complex Ru-Cr-Ru **[25]**$^{7+}$ (0.05 mM) and PPh_3 (15 mM) in CH_3CN and 0.1 M TBAP as a supporting electrolyte were continuously irradiated with a Xenon Lamp during which the reaction was followed by UV-visible spectroscopy.

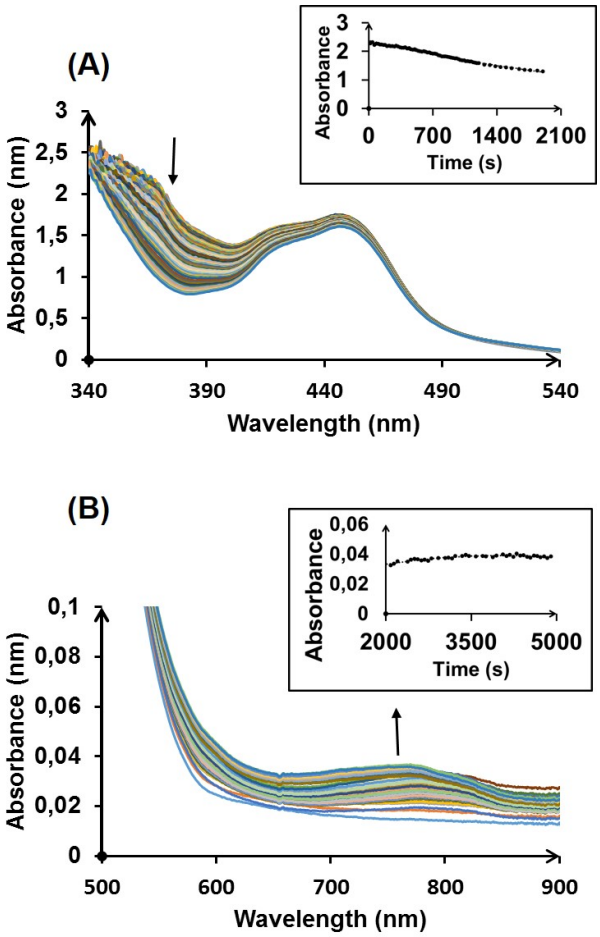

Figure 3.20: (A) Evolution of the absorption spectrum of a mixture of **[25]**$^{7+}$ and PPh_3 (15 mM) in CH_3CN + 0.1 M TBAP during the first 25 minutes of irradiation with a Xenon lamp (20 s time interval); Inset: Plot of the variation of the absorption at 370 nm with time. (b) Zoom on the visible-near infrared region; Inset: Plot of the variation of the absorption at 700 nm with time

Upon irradiation, the band at 360 nm directly drops with an immediate evolution of a band

between 700 nm and 800 nm **figure 3.20**. This band is not defined and appears to be the result of the overlap of the transition at 800 nm of complex $[Cr(ttpy)_2]^{2+}$ and that of 720 nm characteristic of $[Cr(ttpy)_2]^{+}$ **figure 3.20** .

The lack of a clear isosbestic point for the transformation is in accordance with the presence of a mixture of compounds most probably $[Cr(ttpy)_2]^{2+}$ and $[Cr(ttpy)_2]^{+}$. When the sample is subject to prolonged irradiation, the absorption in the visible region continues to increase following a trend similar yet not identical to $[Cr(ttpy)_2]^{0}$. This step has not been clarified yet.

These results tend to indicate that even when both the $[Ru(bpy)_3]^{2+}$ and $[Cr(tpy)_2]^{3+}$ are linked together in a supramolecular system, the photogenerated transient species $[Ru(bpy)_3]^{3+}$-$[Cr(tpy)_2]^{2+}$-$[Ru(bpy)_3]^{2+}$ species can live long enough to be engaged in a bimolecular process with PPh_3 as a sacrificial electron donor. The same trend seems to happen with the transient species $[Ru(bpy)_3]^{3+}$-$[Cr(tpy)_2]^{+}$-$[Ru(bpy)_3]^{2+}$ obtained after irradiation of $[Ru(bpy)_3]^{2+}$-$[Cr(tpy)_2]^{2+}$-$[Ru(bpy)_3]^{2+}$. In order to confirm this hypothesis, transient absorption measurements should be conducted. These preliminary data suggest that this system presents certain advantages for solar-drive bi electronic reduction process.

3.4 Proton Reduction Electrocatalysis

3.4.1 $[Cr(ttpy)_2]^{2+}$ Catalyst

As described earlier, $[Cr(ttpy)_2]^{3+}$ can act as a reservoir of electrons, and in such, we intended to investigate its ability to work as a catalyst for the two electron reduction of protons. Trifluoroacetic acid (TFA) was chosen as the proton source for its relatively low pK_a in organic medium (12.8 in CH_3CN), and its reduction on a bare carbon glassy electrode at a potential sufficient to allow the correct analysis of any catalytic process related to $[Cr(ttpy)_2]^{2+}$.[13]

The electrochemical behavior of complex $[Cr(ttpy)_2]^{3+}$ in CH_3CN was discussed earlier. Briefly, in the absence of acid the CV features three mono-electronic reversible redox waves with potentials = –0.41, –0.77 and –1.27 V and are believed to be ligand reductions.

For synthetic ease we studied the influence of the addition of TFA on $[Cr(ttpy)_2]^{2+}$. The addition of trifluoroacetic acid (TFA) triggers the appearance of new waves, while a large excess leads to the clear identification of two successive irreversible systems **figure 3.21**, the first appears at –1.0 V after the $[Cr(ttpy)_2]^{2+}$/ $[Cr(ttpy)_2]^{+}$ redox couple, which is suspected to be a necessary intermediate for the catalytic process, and a second one with a more pronounced effect at –1.2 V before the $[Cr(ttpy)_2]^{+}$/ $[Cr(ttpy)_2]^{0}$ couple. The response of the latter system is slow as shown by the slow loss of reversibility upon addition of TFA.

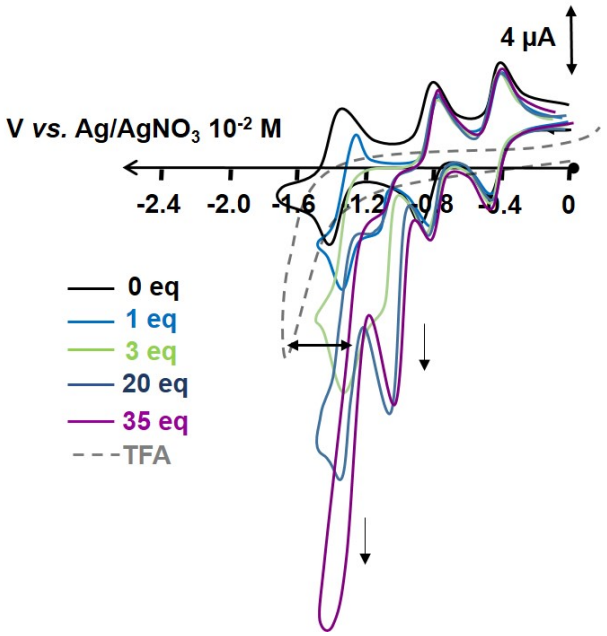

Figure 3.21: CV of **[24]**$^{2+}$ in CH_3CN + 0.1 M $[Bu_4N]BF_4$ at a carbon electrode of 1 mM solution; scan rate: 100 mV.s^{-1} upon addition of 1, 3, 20, 35 equivalent of TFA ; Dashed grey line represents the CV of a solution of 55 equivalence of TFA in CH_3CN + 0.1 M $[Bu_4N]BF_4$.

Some preliminary exhaustive electrolysis in the presence of 50 equivalents of TFA was carried out at –1.20 V *vs.* $Ag/AgNO_3$ during which it allows the production of hydrogen as analyzed by GC with a faradaic yield of 45 % and TON = 10 after 4 hours.

The complex under consideration has a full coordination sphere, which is theoretically unsuitable for substrate binding and activation. For instance it is evidenced that for $[Cr(bpy)_3]^{3+}$, the formation of the hepta-coordinated complex $[Cr(bpy)_3(H_2O)]^{3+}$ lead to the dissociation of one bipyridine ligand.[6] This suggests that the catalytic species generated during bulk electrolysis is different from the starting complex, resulting from either the decoordination of one pyridine ring of the terpyridine or the complete loss of a terpyridine ligand. Indeed, it is shown in the literature that an open coordination site is triggered by ligand reduction in $[Co(tpy)_2]^{2+}$.[14] In our case, the electrolysis at –1.2 V will lead to three consecutive reductions of the terpyridine ligands. The highly reduced species is presumed to decoordinate a full terpyridine in order to initiate the catalytic reduction of protons.

It is difficult to compare our system with analogous $[Co(tpy)_2]^{2+}$ which exhibits a faradaic yield of hydrogen production 80% in DMF due to the presence of a different acid (acetic acid in their case) and more negative applied potential –2.0 V *vs.* $Ag/AgNO_3$.[14] Although both catalytic processes take place at the level of the terpyridine reductions, there is an important difference in the mechanism of production of hydrogen between the two metals. In the case of $[Cr(ttpy)_2]$, the metal center is in the form of Cr(III), while in the case of $[Co(tpy)_2]$, the metal center is in the form of Co(I) which then participates in the formation of the metal-hydride species and eventually hydrogen. Hence, the low faradaic yield could be attributed to the absence of the metal hydride Cr(III) species as well as to the side reactions of the reduced terpyridine ligand such as hydrogenation in the case of $[Zn(tpy)_2]^{2+}$, which makes it compete with the hydrogen formation.[15] Despite of the low faradaic yield, our results look promising since the $[Cr(ttpy)_2]^{2+}$ system offers the advantage of working at higher potentials with a gain around 800 mV.

3.4.2 [Cr(ttpy)(OTf)$_3$] Catalyst

Synthesis

Based on the previous results, we synthesized a monoterpyridine complex denoted by **[27]** in order to investigate the influence of the coordination sphere on the catalytic activity towards the reduction of protons. The procedure for the synthesis of **[27]** was described by Constable et al.[16] using equimolar equivalents of $CrCl_3$ and ttpy in the presence of catalytic amounts of zinc **figure 3.22**. The zinc reduces the chromium complex to favorize the coordination of the terpyridine which is then reoxidized to the Cr^{3+} thanks to the presence of the three chloride ligands

blocking the mono substituted form **[26]**. The chloride ligands form strong coordination bonds with the chromium complex, this is why we exchanged them with less coordinating triflate ions ($CF_3SO_3^-$, OTf) by simple reflux in triflic acid yielding **[27]** with three open coordination sites.

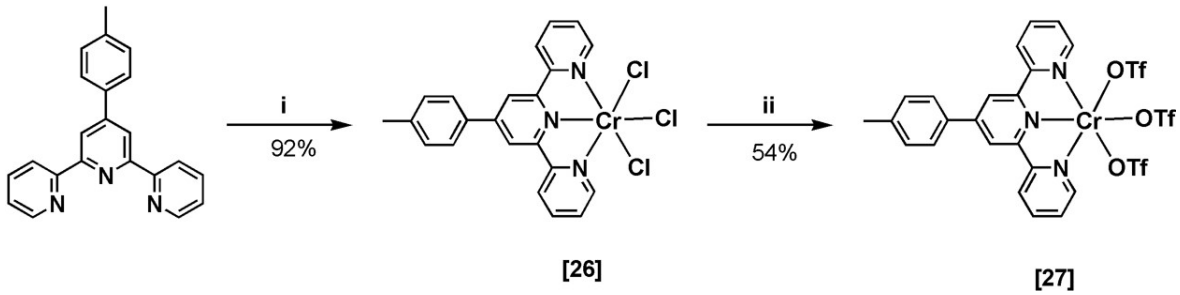

Figure 3.22: Synthesis of **[27]** (i) $CrCl_3$, Zn, EtOH, 78°, 24 h (ii) CF_3SO_3H, 25 °C, 24 h

Electrochemistry

Two reduction processes are observed in the negative potential window of the CV of **[27]** **figure 3.23.A**. Both reductions consume the same number of electrons as evidenced by the equal height of peaks under both processes at the level of the RDE voltammogram **figure 3.23.B**. By comparison with $\mathbf{[24]}^{3+}$, the first reduction wave at –0.44 V is attributed to the first reduction of the terpyridine ligand generating complex $\mathbf{[27]}^{-}$. On the contrary to $\mathbf{[24]}^{3+}$, this peak is irreversible with a ΔE_p = 160 mV. Several cycling at the same peak leads to the appearance of a reversible couple with $E_{1/2}$ = –0.40 V. This implies that the reduction process is followed by a chemical reaction. This could be attributed to the exchange of the labile triflate ligands with the relatively strong binding CH_3CN ligands upon reduction. The process is therefore summarized in **equation 3.4**:

$$[Cr(ttpy)(OTf)_3] + e^- \rightarrow [Cr(ttpy^{\bullet -})(OTf)_3]^- \rightarrow [Cr(ttpy^{\bullet -})(CH_3CN)_3]^{2+} + 3(CF_3SO_3)^- \tag{3.4}$$

A more negative reduction process takes place at –1.17 V and is associated with the second electron reduction of the terpyridine ligand as described by **equation 3.5**. This peak is shifted to the negative potential by a value of 400 mV with respect to complex $\mathbf{[24]}^{+}$ due to the difficulty of accumulating another charge on the same terpyridine ligand.

$$[Cr(ttpy^{\bullet -})(CH_3CN)_3]^{2+} + e^- \rightarrow [Cr(ttpy^{2-})(CH_3CN)_3]^{+} \tag{3.5}$$

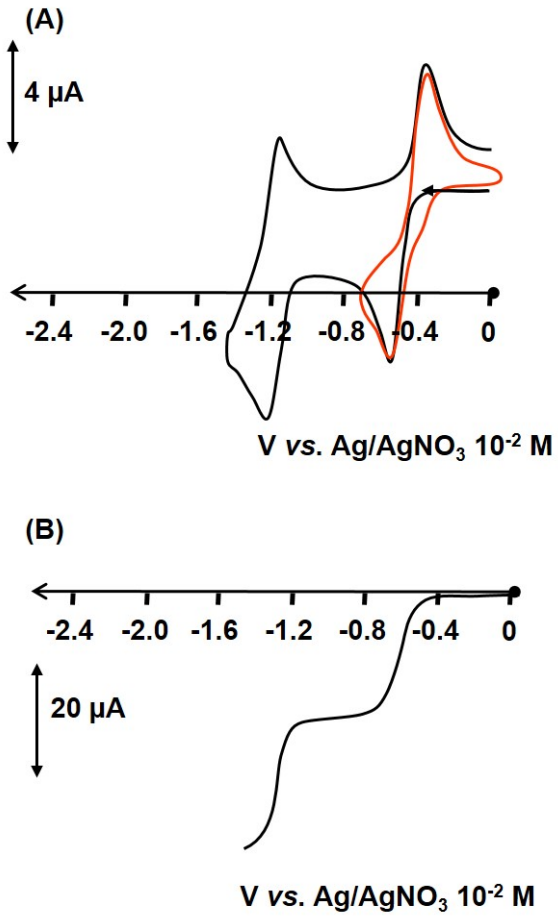

Figure 3.23: (A) black: CV of **[27]** in CH_3CN + 0.1 M $[Bu_4N]ClO_4$ at a carbon electrode of 1 mM solution; scan rate: 100 $mV.s^{-1}$; Red: second scan (B) Voltammogram at a carbon RDE of a solution of **[27]** in CH_3CN + 0.1 M $[Bu_4N]ClO_4$, ω = 600 rpm, scan rate: 5 $mV.s^{-1}$

Regarding complex **[27]**, the addition of increasing amounts of TFA induces the formation of two catalytic waves at –1.0 V and –1.2 V similar to those found for $[Cr(ttpy)_2]^{3+}$ complex. Two major features differentiate $[Cr(ttpy)_2]^{3+}$ and **[27]** systems: (i) Direct loss of reversibility of all signals after the addition of one equivalent of acid in the case of the **[27]**, while at least 3 equivalents are needed for $[Cr(ttpy)_2]^{3+}$; (ii) The second catalytic peak at –1.2 V involves the triple reduced species in the case of $[Cr(ttpy)_2]^{3+}$, while it involves the double reduced one in the case of **[27]**.

Exhaustive electrolysis in the presence of 50 equivalents of TFA was carried out at –1.20 V during which a large current density of 10 $mA.cm^{-1}$ is produced, nonetheless this current is significantly unstable and reaches 0 after four hours of electrolysis accompanied by degradation

of the complex. The obtained product was analyzed by GC, and indeed H_2 was detected with a faradic yield of 40% and a TON of 12 after 4 hours.

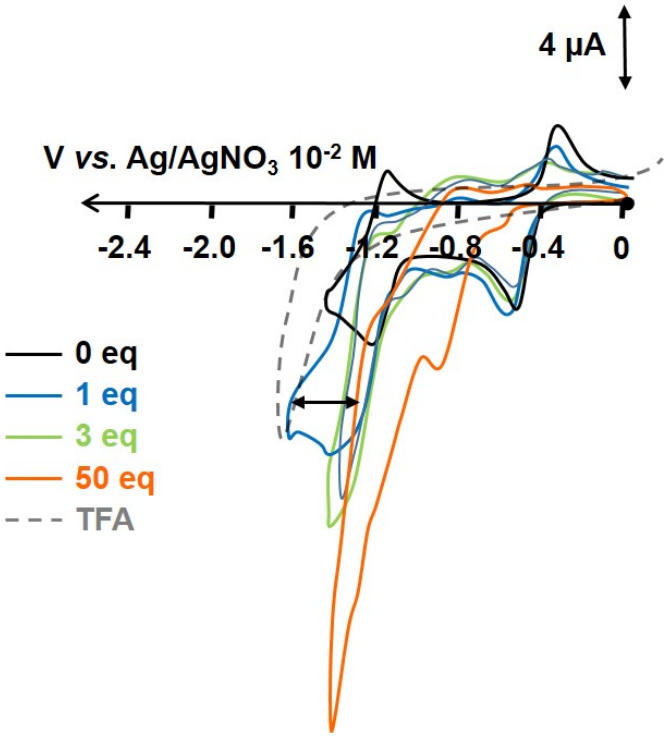

Figure 3.24: CV of **[27]** in CH_3CN + 0.1 M $[Bu_4N]ClO_4$ at a carbon electrode of 1 mM solution; scan rate: 100 $mV.s^{-1}$ upon addition of 1, 3, 50 equivalent of TFA ; Dashed grey line represents the CV of a solution of 55 equivalence of TFA in CH_3CN + 0.1 M $[Bu_4N]ClO_4$

Although **[27]** is equivalently efficient than $[Cr(ttpy)_2]^{3+}$ towards the reduction of protons, the values are still rather low. In order to further understand the nature of interaction between **[27]** and TFA a series of electrolysis were carried out on a mixture of **[27]** in the presence of one equivalent of acid **figure 3.25** during which the absorption spectra were recorded. For comparative reasons, the redox potentials of **[27]** and $[Cr(ttpy)_2]^{3+}$ are collected in **table 3.6**.

Table 3.6: Redox potentials of complexes **[24]**$^{3+}$ and **[27]** in a 10^{-3} M solution of deoxygenated CH_3CN + 0.1 M $[Bu_4N]BF_4$ at a scan rate 100 $mV.s^{-1}$ using carbon vitreous disk (5mm diameter). $E_{1/2}$ (V) ΔEp (mV) *vs.* $Ag/AgNO_3$ 0.01 M in CH_3CN, and L.C corresponds to ligand centered reduction process.

Complex	$E_{1/2}^{reduction}$, V (ΔEp, mV)		
	L.C 1	L.C 2	L.C 3
$[24]^{3+}$	–0.41 (60)	–0.77 (60)	–1.27 (60)
[27]	–0.44 (160)	–1.17 (60)	

Exhaustive electrolysis at –0.80 V lead to the replacement of the electrochemical signatures

of **[27]** with two reversible reductions with $E_{1/2}$ = –0.44 V and –0.78, while the catalytic wave at –1.2 V remained unaltered **figure 3.25**. This was also associated with the evolution of several bands at 500, 584 and 800 nm in the absorption spectra **figure 3.26**. These signatures are indeed associated with those of $[Cr(ttpy)_2]^{2+}$. Further electrolysis at –1.6 V lead to the isolation of $[Cr(ttpy)_2]^{+}$ as evident by the presence of the spectroscopic signatures at 520, 571 and 723 nm **figure 3.26** although this potential is generally sufficient to form the $[Cr(ttpy)_2]^{0}$ complex. At the level of the CV, four reversible redox waves were observed, three of which are associated with the chromium bisterpyridine complex at –0.44, –0.77 and –1.24 V, with an extra reversible system that appears around –1.0 V.

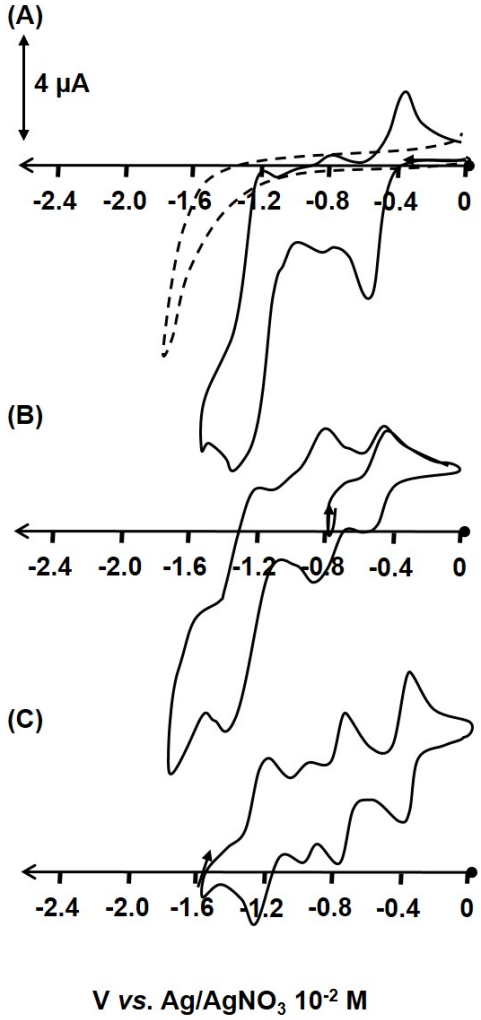

Figure 3.25: (A) Full line: CV of **[27]** in CH_3CN + 0.1 M $[Bu_4N]BF_4$ at a carbon electrode of 1 mM solution; scan rate: 100 $mV.s^{-1}$ in the presence of 1 equivalent of trifluoroacetic acid (TFA), Grey dashed line: CV of 1 equivalent of TFA in CH_3CN + 0.1 M $[Bu_4N]BF_4$; (B)After electrolysis at –0.8 V; (C) After electrolysis at –1.6 V

These results suggest, that although initially the mono terpyridine $[Cr(ttpy)](OTf)_3]$ is prepared, exhaustive electrolysis lead to the generation of the bis-terpyridyl complex in situ upon

applying a potential of –1.2 V. As a matter of fact, this could explain the low faradaic yield and TON numbers obtained for this complex. Future work might imply the immobilization of the $[Cr(ttpy)](OTf)_3$] on a surface during which the formation of the bisterpyridyl form will be prevented. Indeed, recent work regarding immobilized monoterpyridyl complexes of cobalt have shown a significant activity towards the reduction of protons in DMF and H_2O with faradaic yield reaching 95% and TON of 24 000.[17]

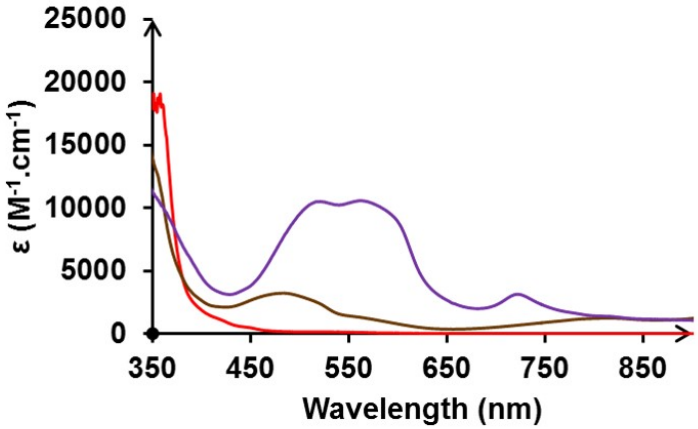

Figure 3.26: Absorption spectra of **[27]** and one equivalent of acid in CH_3CN + $[Bu_4N]BF_4$: Red: UV before electrolysis, Brown: UV After electrolysis at –0.8; Purple: UV After electrolysis at –1.6 V

3.5 Conclusion

In this chapter, we have reported the synthesis of the mono and bis terpyridine complexes of chromium, which were fully characterized by spectro-electrochemistry. Moreover, a detailed study of the photophysics of $[Cr(ttpy)_2]^{3+}$ showed the population of two excited states with different lifetimes under UV irradiation, a short emitting one ^2E, and a longer non luminescent lifetime. It is believed that the latter state is capable of interacting with PPh_3 upon irradiation photogenerating a $[Cr(ttpy)_2]^{+}$ species. The kinetics and yield of the photogeneration of $[Cr(ttpy)_2]^{+}$ were enhanced by the addition of $[Ru(bpy)_3]^{2+}$. In addition to that, trinuclear $[Ru\text{-}Cr\text{-}Ru]^{7+}$ complex was also constructed with the Ru-O-tpy photosensitive unit. Trinuclear complex was fully analyzed and photolysis performed under continuous irradiation in the presence of PPh_3 showed the possible two electron photoreduction of the $[Cr(tpy)_2]^{3+}$ subunit. Preliminary results show that both $[Cr(ttpy)_2]^{2+}$ and $[Cr(ttpy)(OTf)_3]$ can act as a catalyst for the two electron reduction of protons. The nature of the intermediate catalytic species is unknown yet. However, these results are promising, since the catalysis take place at relatively low potentials when compared to analogous $[Co(tpy)_2]^{2+}$. Future work would deal with investigating the catalytic behavior of these complexes in aqueous media.

Bibliography

[1] N. Serpone, M. A. Jamieson, M. S. Henry, M. Z. Hoffman, F. Bolletta, M. Maestri, *J. Am. Chem. Soc.* **1979**, *101*, 2907–2916.

[2] P. S. Wagenknecht, P. C. Ford, *Coord. Chem. Rev.* **2011**, *255*, 591 – 616.

[3] M. Maestri, F. Bolletta, L. Moggi, V. Balzani, M. S. Henry, M. Z. Hoffman, *J. Chem. Soc. Chem. Commun.* **1977**, 491–492.

[4] A. D. Kirk, G. B. Porter, *J. Phys. Chem.* **1980**, *84*, 887–891.

[5] F. Bolletta, M. Maestri, L. Moggi, V. Balzani, *J. Chem. Soc. Chem. Commun.* **1975**, 901–902.

[6] R. Ballardini, A. Juris, G. Varani, V. Balzani, *Nouv. J. Chim.* **1980**, *4*, 563–564.

[7] B. Brunschwig, N. Sutin, *J. Am. Chem.Soc.* **1978**, *100*, 7568–7577.

[8] C. C. Scarborough, K. M. Lancaster, S. DeBeer, T. Weyhermüller, S. Sproules, K. Wieghardt, *Inorg. Chem.* **2012**, *51*, 3718–3732.

[9] J. A. Ramos Sende, C. R. Arana, L. Hernandez, K. T. Potts, M. Keshevarz-K, H. D. Abruna, *Inorganic Chemistry* **1995**, *34*, 3339–3348.

[10] A. M. Zwickel, H. Taube, *Discuss. Faraday Soc.* **1960**, *29*, 42–48.

[11] M. C. Hughes, D. J. Macero, *Inorg. Chem.* **1976**, *15*, 2040–2044.

[12] J. Lombard, R. Boulaouche, D. A. Jose, J. Chauvin, M.-N. Collomb, A. Deronzier, *Inorg. Chim. Acta* **2010**, *363*, 234 – 242.

[13] V. Fourmond, P.-A. Jacques, M. Fontecave, V. Artero, *Inorg. Chem.* **2010**, *49*, 10338–10347.

[14] N. Elgrishi, M. B. Chambers, M. Fontecave, *Chem. Sci.* **2015**, *6*, 2522–2531.

[15] N. Elgrishi, M. B. Chambers, V. Artero, M. Fontecave, *Phys. Chem. Chem. Phys.* **2014**, *16*, 13635–13644.

[16] E. C. Constable, C. E. Housecroft, M. Neuburger, J. Schonle, J. A. Zampese, *Dalton Trans.* **2014**, *43*, 7227–7235.

[17] N. Elgrishi, S. Griveau, M. B. Chambers, F. Bedioui, M. Fontecave, *Chem. Commun.* **2015**, *51*, 2995–2998.

Alternated Bimetallic Coordination Polymers

Résumé:

Les polymères contenant des sous-unités métalliques sont des objets attrayants pour leur incorporation au sein de dispositifs. Les métallo-ligands à base de pont phénylène que nous avons utilisés au chapitre précédent sont idéaux pour obtenir des polymères alternant deux métaux de transition.

Ainsi nous avons construit deux polymères unidimensionnels alternant des unités $[Ru(bpy)_3]2+$ et $[Fe(tpy)_2]^{2+}$ pour l'un et des unités $[Ru(bpy)_3]2+$ et $[Cr(tpy)_2]^{3+}$ pour l'autre. Les études en RMN DOSY ainsi qu'en spectrométrie de masse semblent indiquer la répétition d'une dizaine de monomères. L'étude électrochimique, en plus de démontrer le ratio 1:1 entre centres metalliques a aussi permis de montrer la possibilité d'électrodéposer ces polymères sur électrode par des cycles en réduction.

Les films de polymère possèdent des propriétés d'électrochromisme reliées au changement de couleur des différentes unités redox en fonction de leur degré d'oxydation. Ces électrodes modifiées permettent aussi la production d'un photocourant. L'électrode modifiée par le polymère associant les centres RuII et CrIII se comporte sous irradiation en présence d'un donneur d'électron comme une photoanode, tandis que l'électrode modifiée par le polymère associant les centres RuII et FeII permet la génération d'un photocourant cathodique. L'intensité du photocourant généré est supérieure à celle observée dans le cas des triades. Ceci est attribué à une plus grande couverture de la surface. Cependant, la stabilité du système au cours de l'irradiation est moins grande que pour les systèmes liés de manière covalente à l'électrode.

CHAPTER 4

ALTERNATED BIMETALLIC COORDINATION POLYMERS

4.1 Introduction

Numerous groups have been exploring the use of metal-containing polymers for implementation in devices because these type of species exhibit very interesting optical, electrical, redox, photochemical, magnetic or catalytic activities.[1–3] $[Ru(bpy)_3]^{2+}$, received a particular attention, and was incorporated in several polymeric systems.[4–7] This is mainly due to its unique combination of chemical stability, reversible redox behavior, excited-state reactivity, luminescence emission, and excited-state lifetime. Moreover, it has been evidenced that the presence of the ruthenium complexes in polymers increases the charge carrier mobility which is essential for the construction of advanced devices.[8;9] Despite the outstanding properties of ruthenium complexes, systems based on a single type of molecules will most probably have limited properties and applications. It is expected that through attachment of multiple transition metal complexes on a polymer chain, we will be able to develop advanced materials with tuneable properties. This could be achieved by the preparation of coordination polymers taking advantage of the wide available platform of organic ligands and metallic cation using a simple self assembly process. In particular, a one dimensional metallopolymer can be obtained from the *in situ* formation of a chain of coordination bonds resulting in the incorporation of a metal ion in a ligand containing two coordination sites. In this context, pyridyl complexes, and more specifically 2,2':6';2"-terpyridine aroused a considerable interest due to their rigid backbone, and their high binding affinity toward transition metal ions to form linear octahedral complexes.[10] Two main approaches are employed, the main strategy used consists of the synthesis of a bis-terpyridine ligand on which the two chelating units are covalently connected by a bridging group, while the other relies on unsymmetrical coordination sites to selectively coordinate different metals. Herein, I will shed light on the most recent examples that deal with the assembly of alternating

bimetallic systems in pyridyl based polymers.

For instance, Higushi et al. reported a polymer based on the alternating assembly of Fe^{2+} and Eu^{3+} terpyridyl complexes **figure 4.1**.[11] This was achieved with the help of an unsymmetrical ligand bearing both a terpyridine and a carboxylate substituted terpyridine moiety, taking advantage of the different coordination structures of transition metals and lanthanides. Overall, the lanthanide preferentially bound to carboxylate terpyridine while the Fe bound to the unsubstituted terpyridine. Thanks to the presence of two metallic centers, this polymer exhibited a reversible ON/OFF switching of the emission of the Eu^{3+}. It was demonstrated, that when the iron metal is in its Fe^{2+} form, the emission of the europium is strongly quenched by energy transfer to the Fe part which is non emissive. However, in the Fe^{3+} state, this energy transfer is prohibited, and thus the emission of Eu^{3+} is detected.

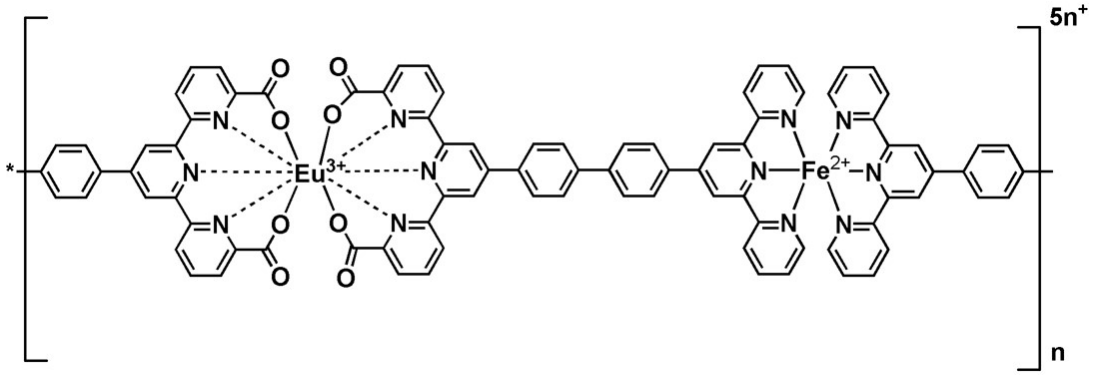

Figure 4.1: Alternating Eu^{3+} and Fe^{2+} terpyridyl polymer

This approach was also extended to selectively bind multiple transition metals depending on different tetrahedral and octahedral coordination structures. For instance, the same group reported the synthesis of a heterometallo-polymer with Cu^{+} and Fe^{2+} introduced alternately using an unsymmetrical ligand bearing a phenanthroline and a terpyridine binding site **figure 4.2**.[12] Incorporation of this polyCuFe film and a gel electrolyte layer showed multi-color electrochromic behavior with color varying from purple to blue to colorless upon successive oxidation of the iron and copper centers.

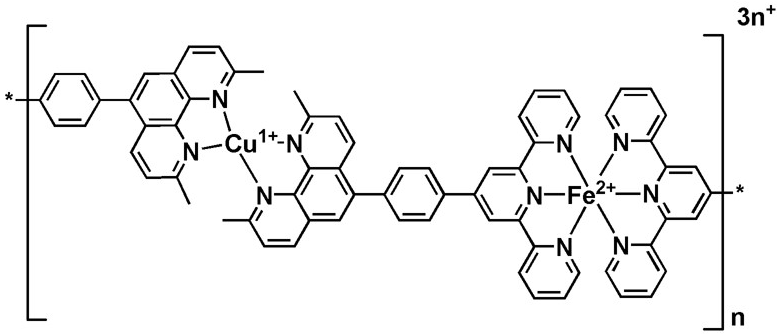

Figure 4.2: Alternating $[Fe(tpy)_2]^{2+}$-$[Cu(phen)_2]^{+}$ polymer

Although these designs are interesting, they will limit us to the combination of different metallic systems with distinctive binding demands. For example, the authors claim that when two d^6 transition metals like Ru and Fe are to be incorporated in the polymer with similar coordination sites, the metal-ion species are randomly introduced to the polymer backbone, loosing control of stoichiometry and hence polymer composition **figure 4.3**.[13] These results are questionable since the ruthenium is known to be inert and the $[Ru(tpy)_2]$ bearing two different terpyridine pending arms can be isolated in a pure form, and can be further used for the construction of a polymer with 1:1 ratio of both iron and ruthenium.

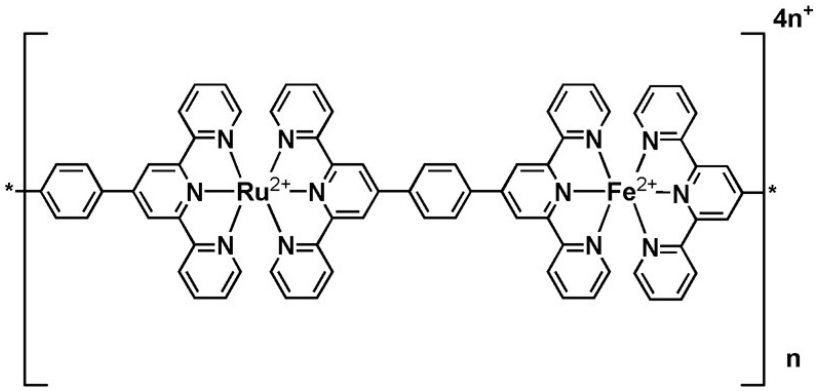

Figure 4.3: Bimetallic polymer based on ruthenium and iron terpyridyl complexes with uncontrolled stoichiometry

Recently our laboratory achieved success in the synthesis of alternating coordination polymers by introducing two terpyridine pending arms to an active building block like cyclam **figure 4.4**.[14] Using the cyclam bis-terpyridine platform a series of homo and heterometallic polymers were synthesized (Cu^{2+}, Fe^{2+}, Co^{2+} and Ni^{2+} ions). This class of materials displays rich properties due to the dual presence of the terpyridine and the cyclam moieties. For example, the homo-metallic copper(II) polymer can undergo an acid controlled breaking into dinuclear complexes. Moreover, in the presence of Fe^{2+}, Co^{2+} and Ni^{2+}, redox-responsible polymeric gels were generated.

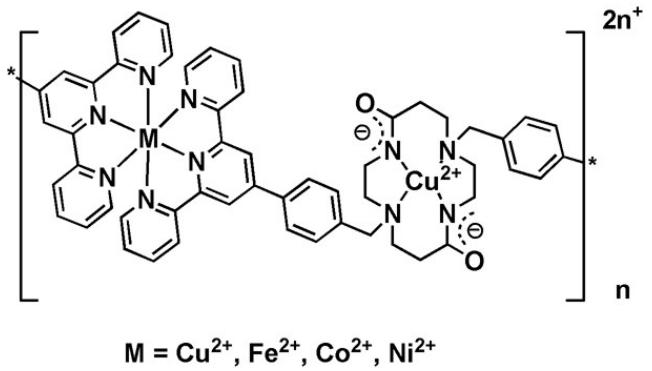

Figure 4.4: Heterometallic coordination polymer based on a bis-terpyridine functionalized dioxocyclam ligand

Our group was also successful in preparing a $[Ru(bpy)_3]^{2+}$ platform bearing two terpyridine pending arms, which was used for accessing alternating coordination polymers containing either $[Fe(ttpy)_2]^{2+}$ or $[Zn(ttpy)_2]^{2+}$ **figure 4.5**.[15] These polymers were deposited onto ITO surfaces by a simple electro-deposition process in reduction. In these films, intramolecular quenching of the emission of ruthenium is more efficient than intermolecular quenching. This means that in this type of assemblies, the excited state of ruthenium can undergo electron or energy transfer to other connected counterparts. Moreover, these films are both electro-and photoactivable, demonstrating a rich electrochromic behavior following the different oxidation states of the Fe and Ru couples. However, the presence of the two terpyridine binding parts on the same bipyridine at the 4 and 4' position can lead to the formation of macrocycles as well as one dimensional polymers.

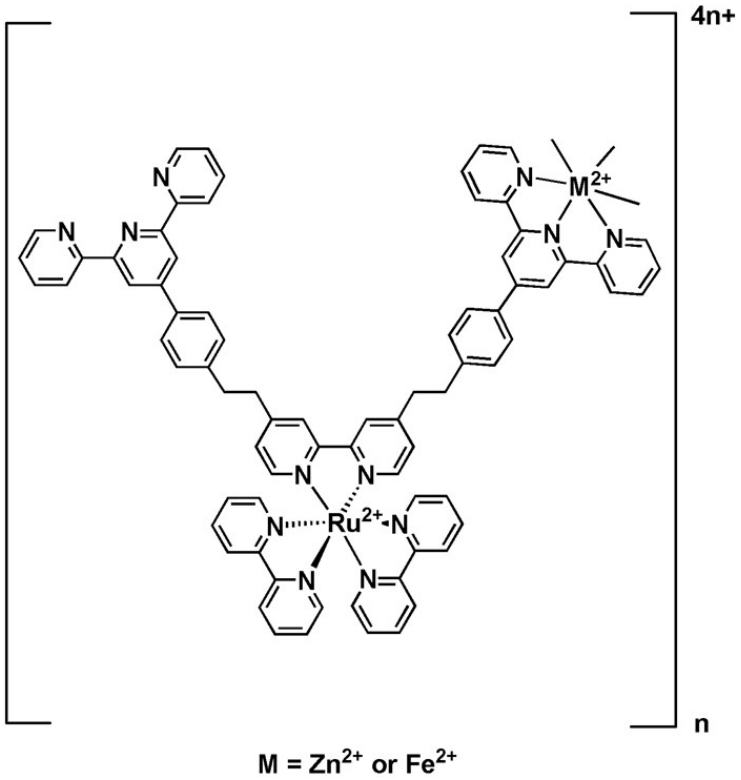

Figure 4.5: Alternating bimetallic polymer based on $[Ru(bpy)_3]^{2+}$ and terpyridyl complexes of zinc and iron

In previous chapters, we discussed the synthesis of a rigid and linear $[Ru(bpy)_3]^{2+}$ complex bearing two free terpyridine coordination sites connected *via* phenylene bridges namely [Ru-(ϕ-tpy)$_2$]. We also showed that it can be used as a photoactive spacer in trimetallic triads containing both $[Fe(tpy)_2]^{2+}$ and $[Co(tpy)_2]^{3+}$. This triad efficiently generated photocurrent in the presence of a sacrificial reagent. Nonetheless, our complex also presents an attractive platform which allows accessing linear alternating polymers using a simple self assembly process.

We report here the synthesis of a one-dimentional linear class of polymers containing al-

ternating ruthenium and either iron or chromium fragments **figure 4.6**. These polymers were characterized in solution and were also deposited onto surfaces in order to study their capability of electrochromism and photo-electric conversion. This study gave us insight on the important parameters that should be modulated in order to obtain better photo-electric response.

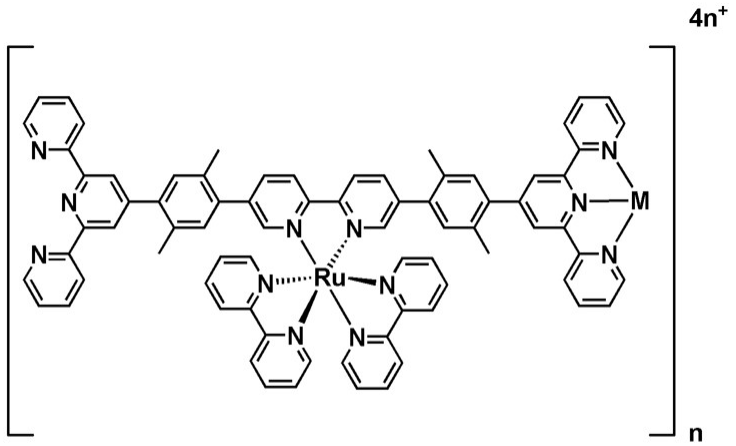

M = Fe^{2+} [28]$^{4n+}$
M = Cr^{2+} [29]$^{4n+}$

Figure 4.6: One-dimentional bimetallic polymer based on $[Ru(bpy)_3]^{2+}$ and terpyridyl complex of either Fe^{2+} of Cr^{2+}

4.2 $[Ru(bpy)_3]^{2+}$/$[Fe(tpy)_2]^{2+}$ bimetallic polymer

4.2.1 Synthesis

The described complex **[5]**$^{2+}$ namely [Ru-(ϕ-tpy)$_2$] is used for the construction of the alternating $[Ru(bpy)_3]^{2+}$ and $[Fe(tpy)_2]^{2+}$ polymer **[28]**$^{4n+}$. The rigid backbone ensured by the phenylene linkers enables us to obtain linear one dimensional assemblies. The polymer was prepared using two different methods. As a start the soluble coordination polymer was synthesized by refluxing one molar equivalent of $[Fe(H_2O)_6].2BF_4$ salt and one molar equivalent of the building block [Ru-(ϕ-tpy)$_2$] in acetonitrile **figure 4.7**. The polymer is then isolated as a hexafluorophosphate salt and purified by recrystallization from a mixture of CH_3CN : Et_2O. Alternately, **[28]**$^{4n+}$ is also prepared *in situ* by adding equimolar amounts of the $[Fe(H_2O)_6].2BF_4$ and [Ru-(ϕ-tpy)$_2$] in a solution of CH_3CN and 0.1 M TBAP. In both cases, the polymer self assembles by coordinating the Fe^{2+} to the free terpyridine coordination site of the ruthenium complex. The addition of the iron salt is accompanied by a fast change in color from red to purple which certifies the presence of the $[Fe(tpy)_2]^{2+}$. The formation and composition of **[28]**$^{4n+}$ is assessed by NMR, MALDI-TOF, CV, absorption and emission spectra.

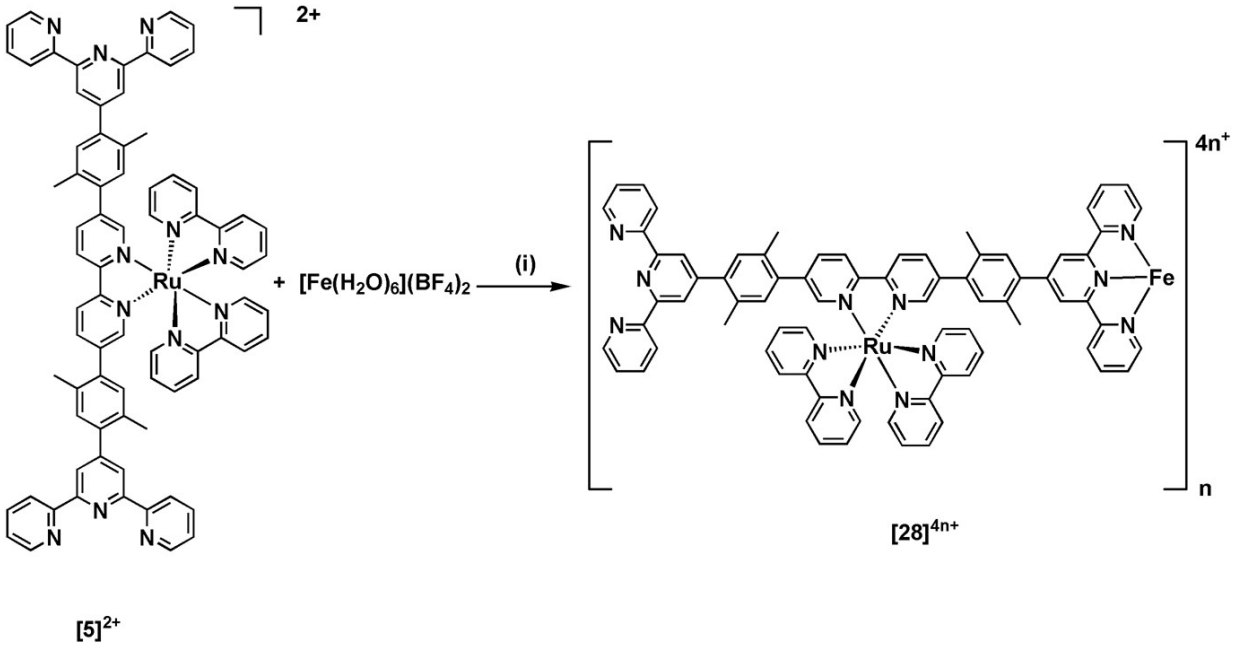

Figure 4.7: Synthesis of the polymer **[28]**$^{4n+}$ (i) CH_3CN, 80 °*C*, 2 h

This coordination polymer is characterized by the ^{1}H NMR and ^{1}H DOSY NMR spectra **figure 4.8**. Upon addition of one equivalent of $[Fe(H_2O)_6].2BF_4$ salt, there is a significant broadening of the set of signals which are found in the aromatic region. Since the solution remains clear and no precipitation is evidenced, this broadening can be associated with the

formation of the coordination polymer. Generally, the NMR data allows the estimation of the number of repeating units in a polymer chain upon integration of the protons in the repeating units and those found in the extremity of the polymer namely end groups. Nonetheless, in our case the peaks are attributed to the superimposition of the proton chemical shifts of the terpyridine and the bipyridine ligands. Thus it is difficult to distinguish the chemical shift of the protons of the complexed terpyridine units from those of the free ones present at the extremity of the polymer (end groups), making it difficult to estimate the molar mass of **[28]**$^{4n+}$ using this technique. To further affirm the formation of oligomeric and polymeric species, diffusion ordered spectroscopy ^{1}H DOSY NMR experiments were carried out. This two dimensional NMR technique correlates the ^{1}H NMR signals with the diffusion coefficient of the species present in solution. The diffusion coefficient **(D)** is related to the radii of the molecules as expressed by "Stokes Einstein Equation" **equation 4.1**:

$$\mathrm{D} = \frac{k_B T}{6\pi\eta r} \tag{4.1}$$

where D stands for the diffusion coefficient, k_B is the Boltzmann constant, T is the absolute temperature, η the dynamic viscosity, and r the radius.

As it is obvious from this equation, the diffusion coefficient is inversely proportional to the radius of the molecule. The DOSY NMR spectrum of the metallo-ligand [Ru-(ϕ-tpy)$_2$] is shown in **figure 4.8.a**. Since [Ru-(ϕ-tpy)$_2$] in itself is a large species with a molecular weight = 1530 g.mol^{-1}, it appears at a relatively small diffusion coefficient (log D = –8.5). Upon formation of **[28]**$^{4n+}$, the diffusion coefficient significantly shifts to a value (log D = –9.5) which is one order of magnitude smaller than that recorded for [Ru-(ϕ-tpy)$_2$] **figure 4.8.b**. This clearly shows the formation of a different species with a higher molecular weight. Assuming that we are in a dilute solution and that T and η are similar in both cases referring to the temperature and viscosity of the solvent CD_3CN respectively, and taking into consideration that both species, [Ru-(ϕ-tpy)$_2$] and **[28]**$^{4n+}$ are in a constant circular motion when present in solution, the ratio of the diffusion coefficient of both species can be expressed by the following relation **equations 4.2** and **4.3**:

$$\frac{D_{[5]^{2+}}}{D_{[28]^{4n+}}} = \frac{r_{[28]^{4n+}}}{r_{[5]^{2+}}} \tag{4.2}$$

$$r_{[28]^{4n+}} = 10\, r_{[5]^{2+}} \tag{4.3}$$

This would mean, that the radius of **[28]**$^{4n+}$ is 10 times higher than that of [Ru-(ϕ-tpy)$_2$], assuming that we approximately have 10 repeating units of the monomer. This methods gives us an estimation of the composition of the polymer present in solution. Nonetheless, it has to be further validated with different experiments.

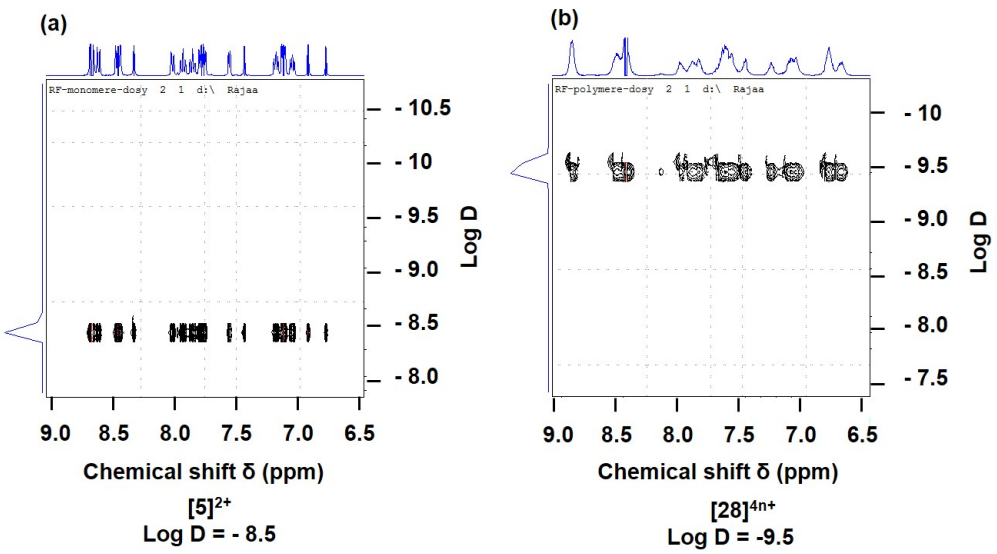

Figure 4.8: Aromatic region of the ^{1}H DOSY NMR spectra (a) of the metallo ligand [Ru-(ϕ-tpy)$_2$] **[5]**$^{2+}$ and (b) polymer **[28]**$^{4n+}$ in CH_3CN. The diffusion coefficients, D ($m^2.s^{-1}$) are plotted in a logarithmic scale *vs.* the chemical shift

In general, mass spectroscopy is not useful for obtaining structural information on a metallo-supramolecular polymer, since the polymer backbone is formed by coordination bonds which are readily broken by the laser of the mass spectroscopy during measurement. Still, Matrix-assisted laser desorption/ionization (MALDI) is a soft ionization technique used in mass spectrometry, and allows the analysis of large organic molecules (such as polymers, dendrimers and other macromolecules), which tend to be fragile and fragment when ionized by more conventional ionization methods.

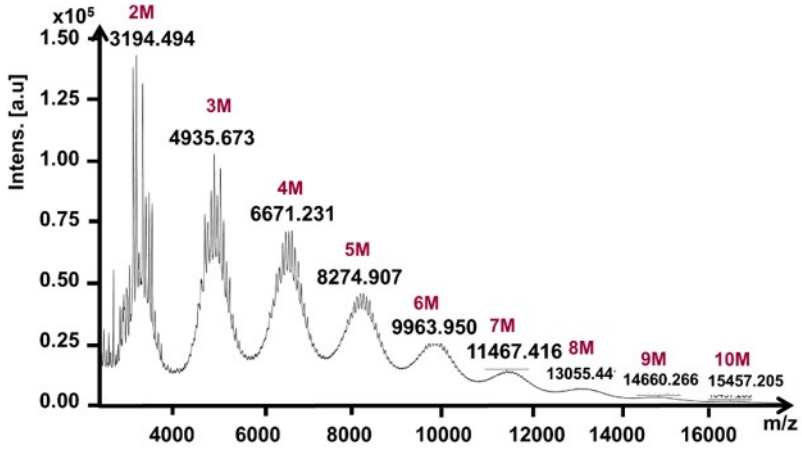

Figure 4.9: Partial MALDI-TOF mass spectrum of the polymer **[28]**$^{4n+}$, M corresponds to the monomer with the formula [Ru-(ϕ-tpy)$_2$-Fe]$^{4+}$

Indeed, we were able to detect several signals, but more importantly with a consistent pattern corresponding to the masses of the oligomers of up to 10 repeating units of the monomeric

species [Ru-(ϕ-tpy)$_2$-Fe] **figure 4.9**. This indicates that the polymer backbone contains at least 10 alternating units of both iron and ruthenium fragments. The lack of higher molecular weight peaks was also evidenced in similar cases in the literature and was explained by the opening of the iron bis terpyridine complexes under the MALDI conditions or insufficient desorption.[16]

4.2.2 Electrochemistry

Electrochemistry in Solution

The cyclic voltammogram of **[28]**$^{4n+}$ was recorded for the isolated and *in situ* prepared polymers, and they both showed similar behaviors. In the positive region, the CV is the sum of the electroactivity of both metallic centers (Ru and Fe) without modification of the oxidation potentials with respect to the unconnected complexes **figure 4.10**. The potentials for both [Ru-(ϕ-tpy)$_2$] and **[28]**$^{4n+}$ are collected in **table 4.1**. Thus, the wave recorded at 0.81 V is attributed to the Fe^{3+}/Fe^{2+} couple, and the peak in the more positive region 1.03 V to the ruthenium center. In the negative region, all the waves are highly distorted, and it is difficult to assign the $E_{1/2}$ values. This could be explained by the deposition of the reduced form of the polymer on the electrode.

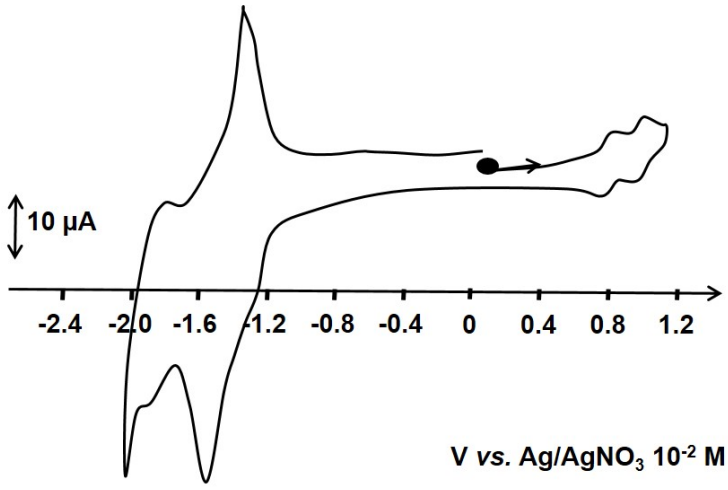

Figure 4.10: CV of **[28]**$^{4n+}$ (10^{-3} M) in CH_3CN with 0.1 M $[Bu_4N]ClO_4$ recorded on a carbon electrode (diameter = 5 mm) at a scan rate = 100 mV/s

Another interesting feature of the CV is the proportionality of the peak between the Fe and Ru centers which suggests the 1:1 composition of the **[28]**$^{4n+}$. This was further confirmed by the RDE experiment **figure 4.11.b** (black line), by which the height of the peak under both oxidation waves is equivalent. Moreover, the absorption spectrum of the initial **[28]**$^{4n+}$ contains the signatures of both the Ru and Fe MLCT at 459 and 563 nm respectively, with the height of

the latter being almost as twice of that of the ruthenium. Taking into account that the extinction coefficient of the Fe MLCT (25 000) is twice of that of the Ru (13 000), this also confirms the 1:1 ratio. The shift at the level of the absorption maxima of the Ru MLCT (459 with respect to 453 nm for [Ru-(ϕ-tpy)$_2$]) is most probably due to the electron withdrawing effect of the [Fe(tpy)$_2$]$^{2+}$ which lowers the π^* of bpy-tpy ligand slightly.

Table 4.1: Redox potentials of **[5]**$^{2+}$ "[Ru-(ϕ-tpy)$_2$] " and **[28]**$^{4n+}$ in CH_3CN + 0.1 M $[Bu_4N]ClO_4$ recorded on a carbon electrode (diameter = 5 mm) at a scan rate = 100 mV/s. The potentials are referred to $Ag/AgNO_3$ (10^{-2} M)

Complex	$E_{1/2}^{oxidation}$, V (ΔEp, mV)		$E_{1/2}^{reduction}$, V (ΔEp, mV)		
	Ru^{3+}/Ru^{2+}	Fe^{3+}/Fe^{2+}	L.C 1	L.C 2	L.C 3
$[5]^{2+}$	1.03 (60)	-	- 1.51 (60)	-1.74 (80)	-2.0 (100)
$[28]^{4n+}$	1.03 (60)	0.81 (60)	-	-	-

We have also studied the stability of the polymer under different oxidation states by performing exhaustive electrolysis at 0.9 and 1.2 V during which we have recorded the RDE voltammogram and the absorption spectra **figure 4.11**.

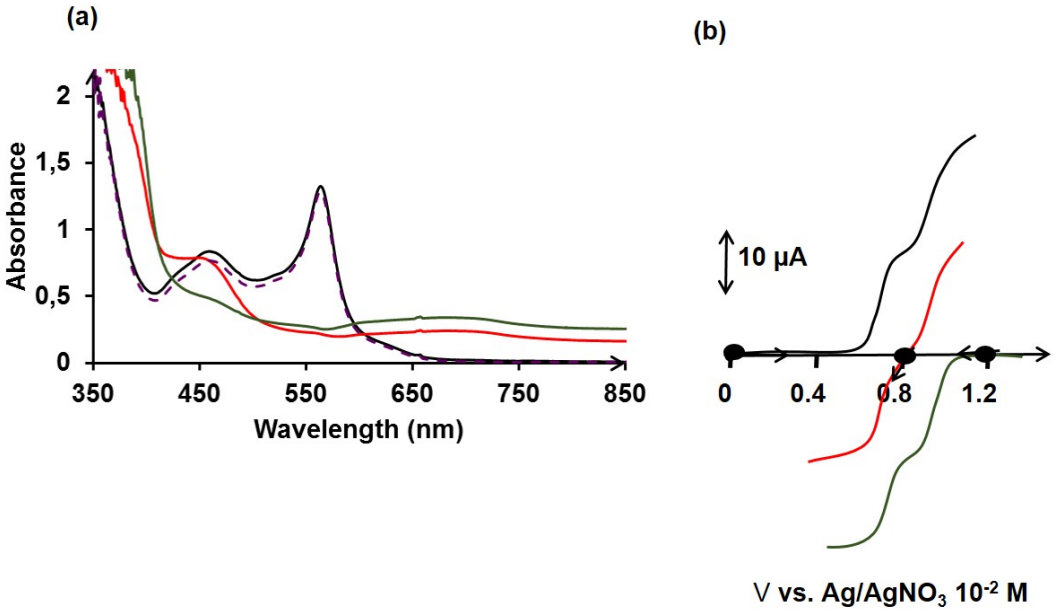

Figure 4.11: (a) Absorption spectra of **[28]**$^{4n+}$ initial solution (black) after electrolysis carried out at 0.9 V (red) after electrolysis at 1.2 V (green) and after cathodic electrolysis at 0 V; (b) RDE voltammogram of **[28]**$^{4n+}$ (10^{-3} M) in an CH_3CN solution containing 0.1 M $[Bu_4N]ClO_4$ at a scan rate = 5 mV/s initial solution (black) after electrolysis at 0.9 V, (red) and after electrolysis at 1.2 V (green)

At this level, we will not detail the electrolysis experiment since similar system **[6]**$^{6+}$ was already described in **Chapter 1**. Briefly, we can safely say that **[28]**$^{4n+}$ is stable under different

oxidation states of $Fe^{3+/2+}$ and $Ru^{3+/2+}$ in solution as evidenced by the conservation of the proportionality of the height of the peak under the Fe and Ru centers in the RDE voltammogram **figure 4.11.b**. Moreover, we were able to recover the initial absorption spectrum after the consecutive electrolysis of Fe and Ru **figure 4.11**. This is of a particular importance for proceeding sections.

Fabrication of Modified Electrodes

As shown in the CV of **[28]**$^{4n+}$ in solution, the reduction waves in the negative region are completely distorted due to adsorption of the reduced species. We took advantage of this behavior, in order to deposit our polymer on different types of surfaces (carbon, platinum and ITO) upon successive cycling in the negative region.[17;18] By cycling only the potential including the first reduction wave no film growth was observed, while cycling between 0 and –1.8 V containing the first two reductions showed an inefficient deposition. However, if the potential range includes the three reduction waves (between 0 and –2.1 V), the three waves grow in as a consequence of the deposition of the conductive film on the surface of the electrode **figure 4.12.a**.

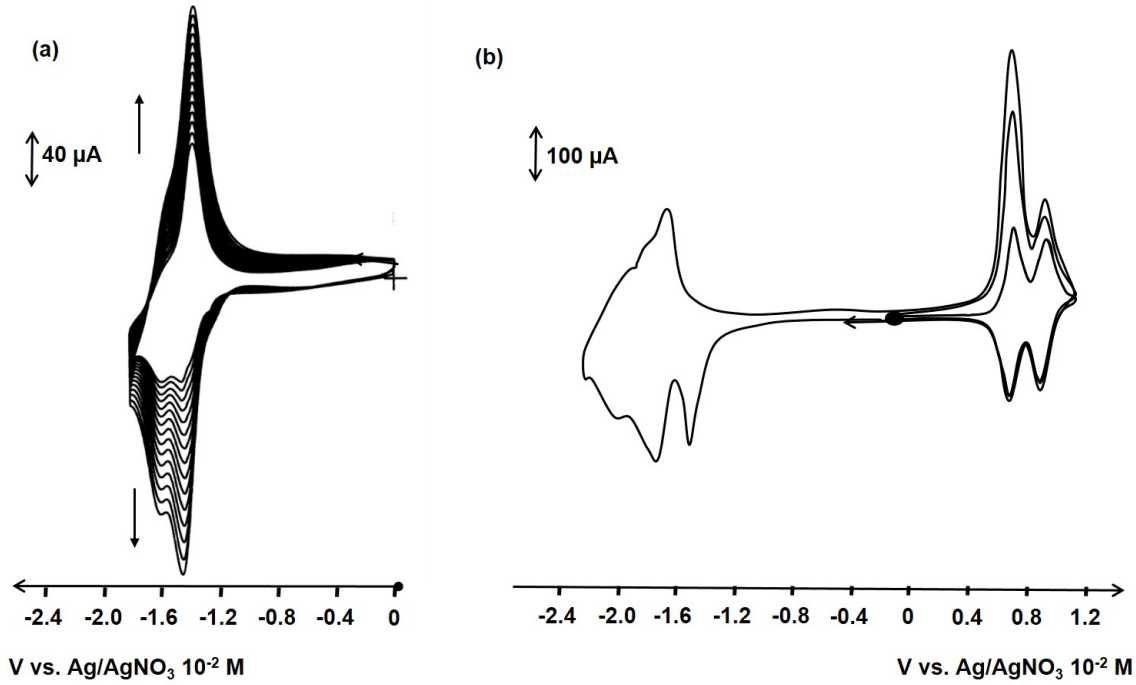

Figure 4.12: (a) Deposition of **[28]**$^{4n+}$ (10^{-3} M) on ITO electrode by successive cycling between 0 and –2.0 V *vs.* $Ag/AgNO_3$ (10^{-2} M) in an CH_3CN solution ν = 50 mV.s^{-1} (b) CV of the modified surface in an CH_3CN solution containing 0.1 M $[Bu_4N]ClO_4$ *vs.* at ν = 50 mV.s^{-1}.

Then the functionalized electrodes are transferred into a blank solution containing CH_3CN and 0.1 M $[Bu_4N]ClO_4$. For instance, after 15 successive cycles including the three reduction

systems, the CV of a modified electrode will look as follows **figure 4.12.b**. Initially, in the negative window, we are able to detect the reduction of the terpyridine and bipyridine ligands at similar potentials than those of **[28]**$^{4n+}$ in solution. Regarding the oxidation, three consecutive cycles are needed in order to obtain a stable signal, and get rid of the capacitive current by allowing proper penetration of the electrolyte inside the film.

From the CVs of the modified electrodes in oxidation, two peaks with a value of $E_{1/2}$ = 0.8 and 1.0 V are recorded and correspond to the Fe^{2+}/Fe^{3+} and Ru^{2+}/Ru^{3+} couples respectively. Moreover, we can assure that the grafted polymer has a 1:1 ratio of ruthenium and iron from the proportionality of the peaks underneath the oxidation waves of both metals. We can also estimate the surface coverage upon grafting on an ITO electrode to 4×10^{-9} mol.cm^{-2} after 10 cycles. These values are way more significant (>100) than those reported for the monolayers (3×10^{-11} mol.cm^{-2}) discussed in **Chapter 2**. This difference arises from the fact that during polymerization several layers are deposited above each other, contrary to the stepwise coordination approach that lead to monolayer.

In order to test the reproduciblity of the preparation of the films, we plotted the thickness of the adsorbed layers (nm) *vs.* the number of cycles **figure 4.13**. As for the thickness, the modified electrode are scratched with a needle and the difference of altitudes was measured in the tapping mode of atomic force microscopy (AFM). As expected, a linear relationship was obtained, which shows that the thickness of the film increases steadily upon increasing the number of cycles.

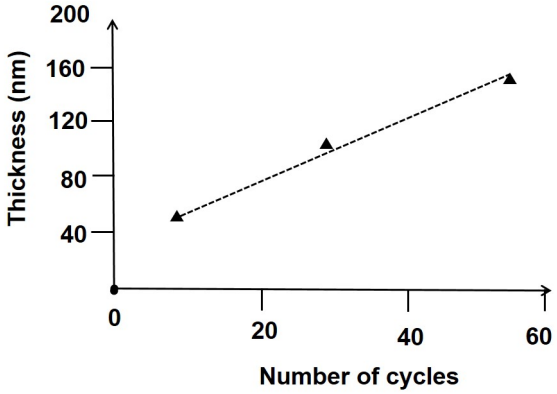

Figure 4.13: Variation of the thickness of the modified surface upon increasing the number of cycles for deposition of the polymer on ITO surfaces.

The morphology of the ITO covered by the coordination polymer **[28]**$^{4n+}$ was investigated using AFM **figure 4.14**. The topography of the modified electrode appears nodular, inhomogeneous, typical of an electrodeposited film.[19] Moreover, we couldn't detect a specific lamella pattern of the polymer on the surface in contrast to long polymers based on alternating iron bis terpyridine and poly(ethylene oxide).[16] This could imply that the length of the polymer chain

in our case is short.

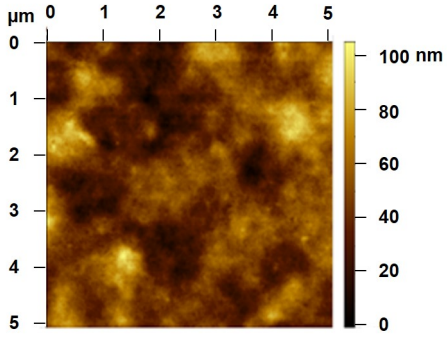

Figure 4.14: AFM images of an ITO coated with polyRuFe after 55 cycles of deposition

4.2.3 Photophysics

In order to further investigate the properties of this bimetallic polymer, steady state and time-resolved emission of **[28]**$^{4n+}$ were recorded in deoxygenated CH_3CN solution as shown in **table 4.2**.

Table 4.2: Luminescence lifetime of the monomeric and polymeric species recorded in deoxygenated CH_3CN + 0.1 M $[Bu_4N]ClO_4$ solution at 25 °C. ϕ_{em} represents the emission quantum yield of the complexes

Complex	λ_{em} (nm)	Lifetime	τ (ns)	k_q (s^{-1})	ϕ_{em}	ϕ_{em}/ϕ_0 (%)
		τ_1 ns (%)	τ_2 ns (%)			
$[5]^{2+}$	616		1000	-	0.058	-
$[28]^{2+}$	616	3 (95)	888 (5)	3×10^8	0.0085	15

Upon excitation at 450 nm, **[28]**$^{4n+}$ exhibited a poor luminescence around 616 nm. This luminescence lies in the same region as that of [Ru-(ϕ-tpy)$_2$], and could be attributed to the ruthenium core. The poor quantum yield (ϕ_{em} = 0.0085) which constitutes only 15% of the emission of the parent molecule (0.058) is attributed to a strong deactivation pathway of the excited state of ruthenium. Indeed, this was also observed for the trimetallic complex **[6]**$^{6+}$ in **Chapter 1**, and was rationalized to be the result of an energy transfer from the ruthenium to the iron center as governed by the strong overlap between the emission of the ruthenium and absorption of iron.

Like for **[6]**$^{6+}$, the luminescence intensity decay can be fitted by a bi-exponential equation, while the short component τ_1 is attributed to the quenched species and the longer lifetime τ_2 is believed to correspond to the unquenched Ru center. In the case of the bimetallic polymer, the lifetime τ_1 is slightly shorter compared to the trimetallic system as a probable consequence

of the polymer structure which maintains the different metallic centers in a close environment. This most probably leads to an additional deactivation pathway of the Ru^* by self quenching with adjacent Ru center.

The quenching rate constants (k_q) occurring in **[28]**$^{4n+}$ is estimated to 3×10^8 s^{-1} . This value is similar to polymer systems containing alternating ruthenium and iron centers with ethyl bridges connecting the counter parts in the 4,4' position of the bipyridine **figure 4.5** .[15] This suggests that energy transfer takes place with similar rates whether ethyls or phenylenes are introduced as bridges.

4.2.4 Electrochromism

During continuous cycling between +0.65 and +1.5 V, the film shows a multi-color electrochromic properties, upon varying the oxidation states of the metals **figure 4.15**.

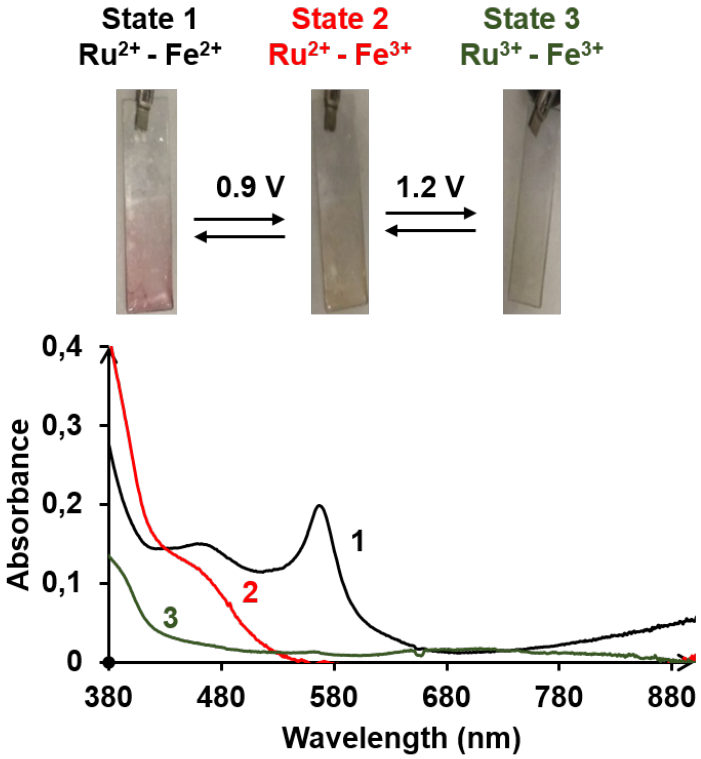

Figure 4.15: Absorption spectra of **[28]**$^{4n+}$: Black: applied potential = 0 V; Red: applied potential = 0.9 V; Green: applied potential =1.2 V

Intially at +0.65 V, the color of the film is purple which is due to the presence of Fe^{2+} and Ru^{2+}, during which the absorption spectrum is dominated by the MLCT of Ru and Fe in the visible region 457 and 570 nm. The latter absorption is indeed responsible for the purple color. Upon increasing the applied potential to +0.9 V which is 100 mV higher than the oxidation

potential of Fe^{3+}/Fe^{2+} couple, this induces the electrolysis of the iron to generate Fe^{3+}, accompanied by a change of color to brown (mixture of green Fe^{3+} and red Ru^{2+}), along with the disappearance of the Fe(II) MLCT (red spectrum). Finally applying a potential of 1.2 V , 200 mV higher than the oxidation potential of the Ru^{3+} Ru^{2+} couple, a green film is obtained due to the formation of Fe^{3+} and Ru^{3+}. This is consistent with the absorption spectrum by which the Ru MLCT at 450 nm disappears and is accompanied by the appearance of a broad peak around 700 nm.

It is, however, difficult to discuss the relationship between the applied potentials to the electrode and the redox potentials of the metal ions in the polymer due to internal resistance of the device and other factors. Nonetheless, such delay has been also reported in the literature.[12;15]

4.2.5 Cathodic Photocurrent in the presence of ArN_2^+

In this work we prepared several electrodes with surface coverages varying between 9×10^{-9} and 13×10^{-9} mol.cm^{-2} upon increasing the number of polymerization cycles from 20 to 50.

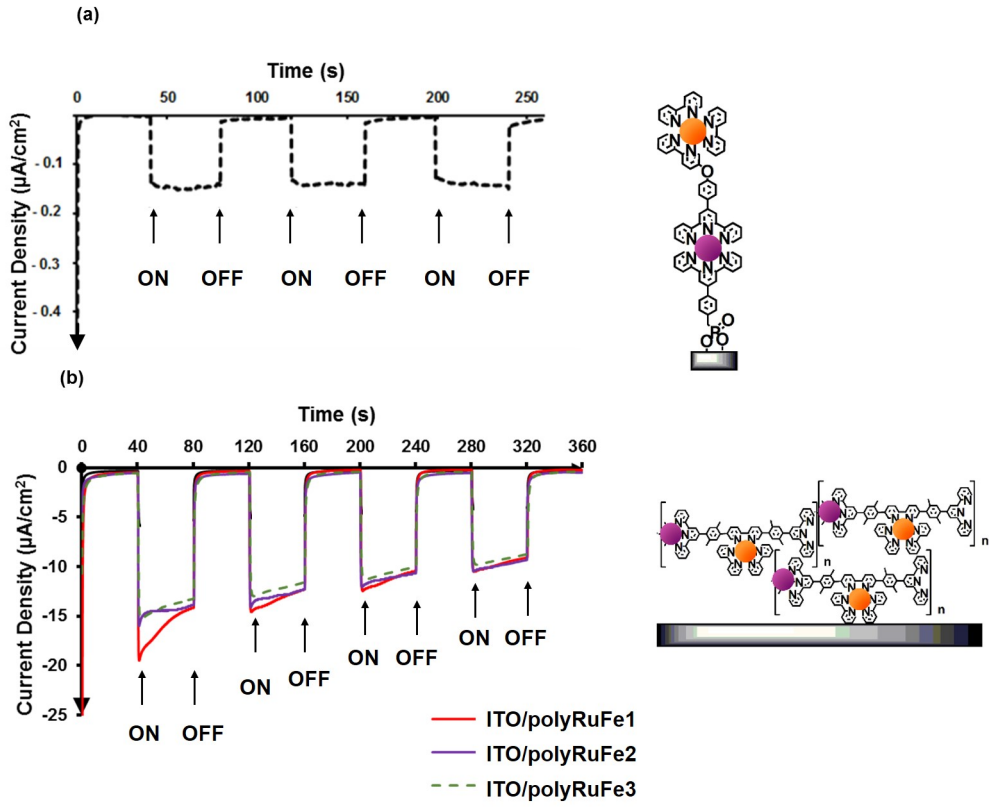

Figure 4.16: Photo-response upon irradiation with a Xenon Lamp of the modified electrode in CH_3CN in the presence of 15 mM ArN_2^+ (a) ITO/$[Fe(tpy)_2]O[Ru(bpy)_3]$ (b) ITO modified with the $[28]^{4n+}$ with varying surface coverage values: ITO/polyRuFe1 $\Gamma = 9 \times 10^{-9}$ mol.cm^{-2}, ITO/polyRuFe2 $\Gamma = 10 \times 10^{-9}$ mol.cm^{-2}, ITO/polyRuFe3 $\Gamma = 13 \times 10^{-9}$ mol.cm^{-2}

We have also tested the ability of the polymer modified electrodes to generate photocurrent upon irradiation in an CH_3CN solution containing 0.1 M $[Bu_4N]ClO_4$ and 15 mM of a sacrificial electron acceptor namely (ArN_2^+) with an applied bias of 0.4 V. A light gated response was obtained for modified electrodes upon successive cycles as shown in **figure 4.16.b**.

Before commenting on the values of the obtained photocurrent, it is important to understand its origin. Undoubtedly, the ruthenium unit is the photoactive center as evidenced earlier with monolayers of ITO/$[Fe(tpy)_2]O[Ru(bpy)_3]$. Yet, there is a significant difference in the architecture of both surfaces. While ITO/$[Fe(tpy)_2]O[Ru(bpy)_3]$ exhibits a linear and controlled growth of the dyads on the ITO surfaces, films prepared with electrodeposition of the polymer on the ITO lack orientation. The electron transfer in ITO/$[Fe(tpy)_2]O[Ru(bpy)_3]$ can be simply explained by the vectorial electron transfer from the electrode to the solution as shown in **figure 4.17.a** and discussed earlier in **Chapter 2**.

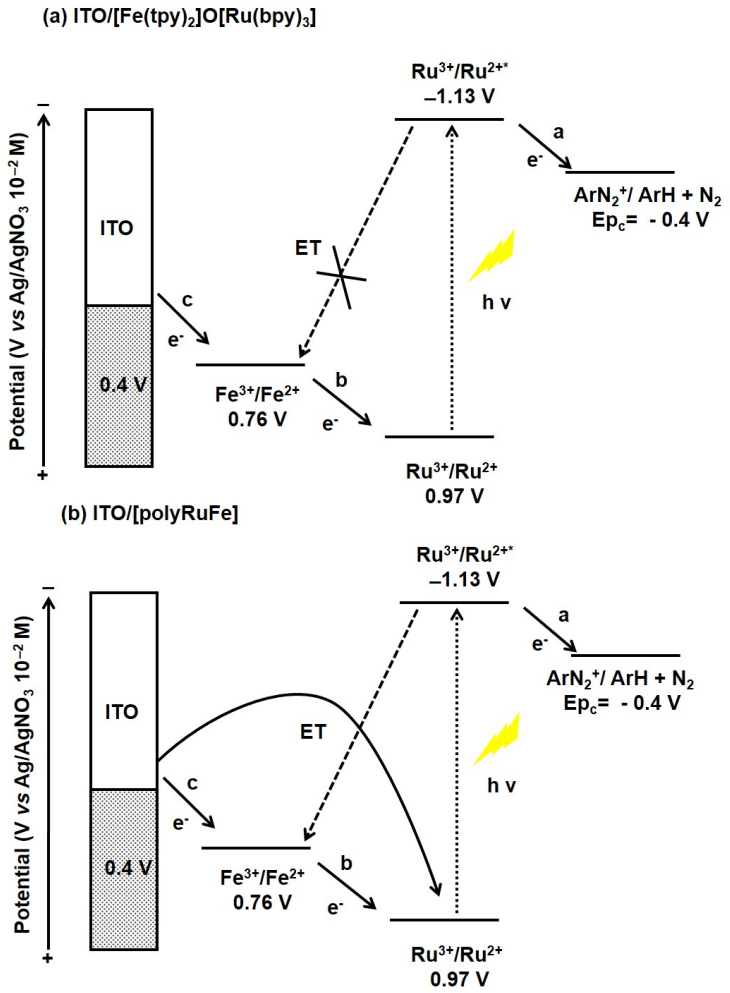

Figure 4.17: Proposed mechanism for the electron transfer

Whereas for polymers, in addition to the described mechanism, we can also imagine that the excited state of ruthenium directly accepts an electron from the electrode without using

the iron as a relay **figure 4.17.b**. Importantly, we can expect an increase of the quenching of the excited state of ruthenium with adjacent iron moieties due to highly packed structure. Despite all of these side reactions that are more probable to take place, the recorded cathodic current remain significant yet unstable when compared to dyad ITO/[Fe(tpy)$_2$]O[Ru(bpy)$_3$]. The magnitude of the photocurrent along with the surface coverage is collected in **table 4.3**. ITO's modified with polymer record a current intensity with a value $\simeq 10\ \mu A$ which is 25 times higher than that obtained with ITO/[Fe(tpy)$_2$]O[Ru(bpy)$_3$] under the same conditions. This is also accompanied by an increase of $\simeq 100$ times of surface coverage. Thus, despite the more engineered assemblies in ITO/[Fe(tpy)$_2$]O[Ru(bpy)$_3$], the superior values of surface coverage lead to a significant enhancement of the photocurrent. This unquestionably sheds light on the importance of increasing the surface coverage values in order to get more significant photoelectric response.

Table 4.3: Variation of the magnitude of photocurrent with different surface coverage values

Modified ITO	Γ ($mol.cm^{-2}$)	Photocurrent ($\mu A.cm^{-2}$)
ITO/[Fe(tpy)$_2$]O[Ru(bpy)$_3$]	3×10^{-11}	0.15
ITO/polyRuFe1	9×10^{-9}	10^a
ITO/polyRuFe2	10×10^{-9}	10^a
ITO/polyRuFe3	13×10^{-9}	10^a

[a] This value was calculated after three cycles.

By careful examination of the photo response of the different ITO electrodes, we observe that the magnitude of the photocurrent varies slightly upon changing the surface coverage. This could be either due to slower rate of charge propagation through a thicker polymer film, or due to the fact that only part of the electrodeposited material is photoactive because of the inaccessibility of the redox mediator. Moreover, the current drops significantly during the on/off cycles accompanied by loss of $\simeq 70$ % of the deposited polymer as evidenced from the decrease of Γ which is calculated from the recorded CV after five cycles of irradiation. This can be explained by the instability of the deposition under light or heat. On the contrary, the dyads ITO/[Fe(tpy)$_2$]O[Ru(bpy)$_3$] display a small photocurrent intensity (0.15 μA.cm^{-2}) under the same conditions yet with a much superior stability. This is governed by the presence of the covalent linkages which maintains the attachement of the molecules on the electrode.

4.3 $[Ru(bpy)_3]^{2+}$/$[Cr(tpy)_2]^{2+}$ bimetallic polymer

4.3.1 Synthesis

The previously described complex Ru-(ϕ-tpy)$_2$ **[5]**$^{2+}$ is used for the construction of the polymer **[29]**$^{4n+}$, holding both $[Cr(ttpy)_2]^{2+}$ and $[Ru(bpy)_3]^{2+}$ **figure 4.18**. Polymer **[29]**$^{4n+}$ is synthesized by refluxing one equivalent of $CrCl_2$ salt and one equivalent of the building block Ru-(ϕ-tpy)$_2$ in methanol for 4 hours during which the polymer precipitates. Ammonium hexafluorophosphate is added in order to induce the full precipitation of **[29]**$^{4n+}$. Then **[29]**$^{4n+}$ is oxidized by exhaustive electrolysis in a glove box to yield **[29]**$^{5n+}$. The following study is performed with the air stable **[29]**$^{5n+}$ form of the polymer.

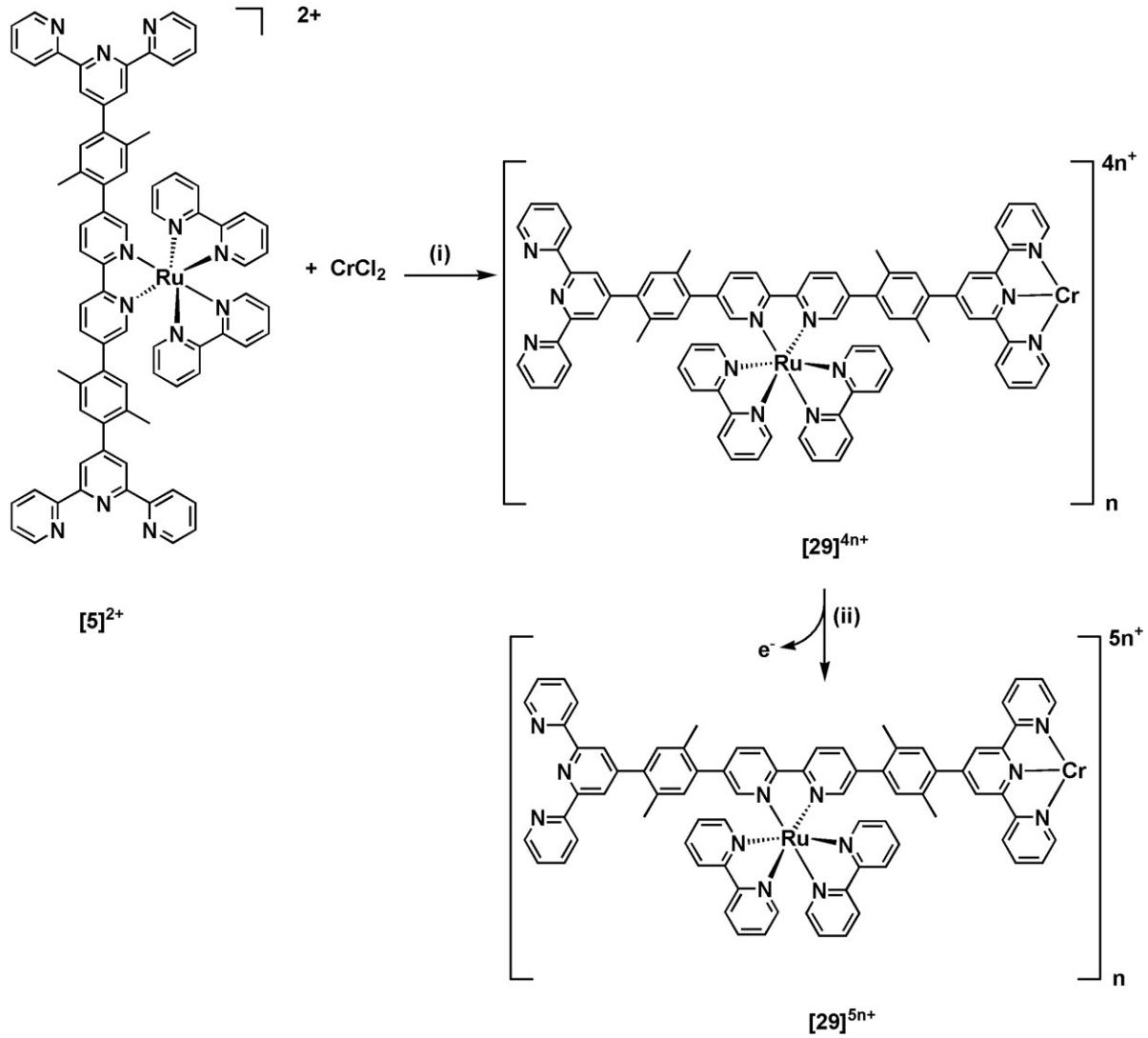

Figure 4.18: Synthesis of the chromium-ruthenium bimetallic polymer **[29]**$^{4n+}$, (i) $CrCl_2$, MeOH, 65 °C, 4 h, NH_4PF_6; (ii) oxidation by exhaustive electrolysis at 0 V *vs.* $Ag/AgNO_3$ in CH_3CN + 0.1 M $[Bu_4N]ClO_4$ to yield **[29]**$^{5n+}$.

4.3.2 *Electrochemistry*

Electrochemistry in Solution

The CV of the polymer **[29]**$^{5n+}$ is the superimposition of the electroactivity of the two subunits [Ru-(ϕ-tpy)$_2$] and [Cr(ttpy)$_2$]$^{3+}$ in their 1:1 stoichiometry **figure 4.19.A**. The redox potentials are collected in **table 4.4**. We can thus assign the $E_{1/2}$ at 1.00 V to the oxidation of the ruthenium center, and the first three reductions at –0.45, –0.82 and –1.3 V to the succesive monoelectronic reductions of the terpyridine ligands of the [Cr(ttpy)$_2$]$^{3+}$. The reductions at more negative potentials (–1.52, –1.72 V) are associated to the successive reductions of the bipyridine ligands of the [Ru(bpy)$_3$]$^{2+}$ domain. Unfortunately it is difficult to comment on the proportionality of the two subunits from the RDE voltammograms due to the poor solubility of the latter in CH_3CN in the form of BF_4^-, ClO_4^- and PF_6^- salt. Indeed, the deposition of the polymer **[29]**$^{5n+}$ in reduction is evident in the RDE voltammogram, by which the third reduction peak show an adsorption on the electrode **figure 4.19.B**.

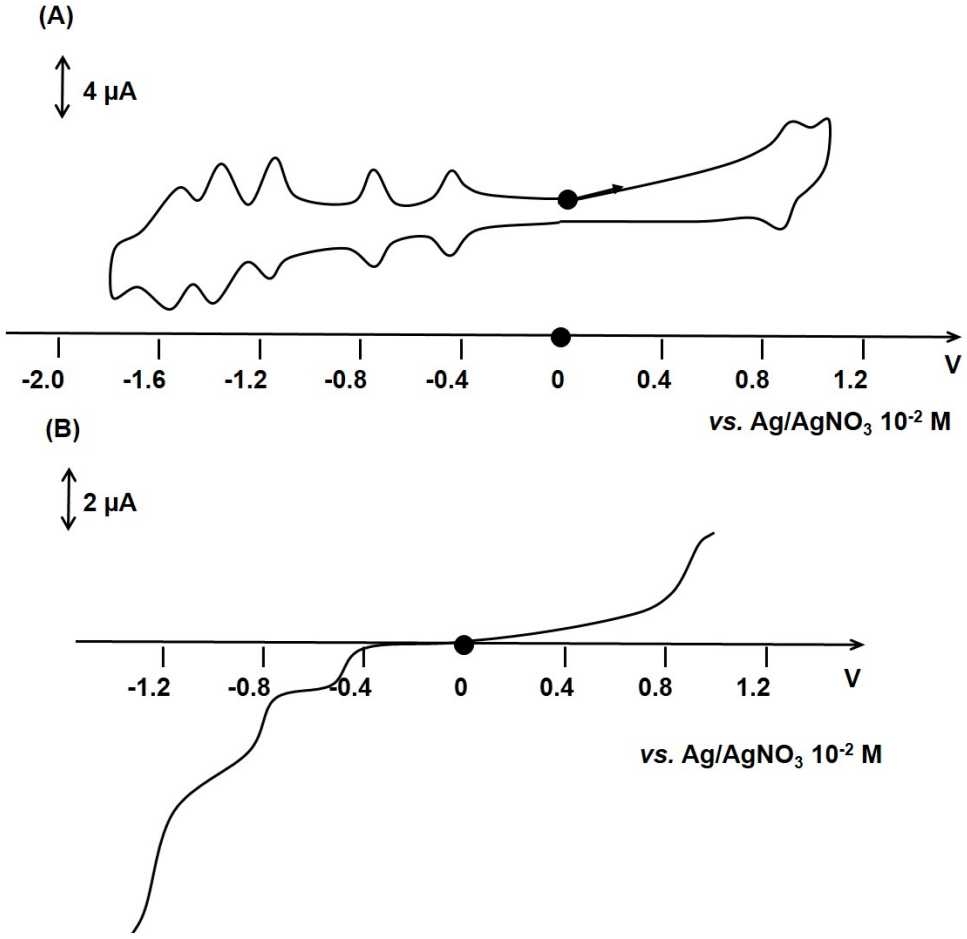

Figure 4.19: (A) CV of **[29]**$^{5n+}$(10^{-5} M) in CH_3CN + 0.1 M [Bu_4N]ClO_4 at a carbon electrode of 0.5 mM solution; scan rate: 100 mV.s^{-1} ; (B) Voltammogram at a carbon RDE in CH_3CN + 0.1 M [Bu_4N]BF_4, ω = 600 rpm, scan rate: 5 mV.s^{-1}.

Table 4.4: Redox potentials of **[5]**$^{2+}$ [Ru-(ϕ-tpy)$_2$], **[24]**$^{3+}$ and **[29]**$^{5n+}$ in CH_3CN + 0.1 M $[Bu_4N]ClO_4$ at scan rate = 100 mV/s. The potentials are reported with respect to $Ag/AgNO_3$ (10^{-2} M)

Complex	$E_{1/2}^{oxidation}$, V (ΔEp, mV)	$E_{1/2}^{reduction}$, V (ΔEp, mV)				
	Ru^{3+}/Ru^{2+}	L.C 1	L.C 2	L.C 3	L.C 4	L.C 5
$[5]^{2+}$	1.03 (60)	- 1.51 (60)	-1.74 (80)	-2.0 (100)	-	-
$[24]^{3+}$	-	–0.41 (60)	–0.77 (60)	–1.27 (60)	-	-
$[29]^{5n+}$	1.00 (40)	–0.45 (45)	–0.82 (40)	–1.3 (30)	–1.52 (40)	–1.72 (40)

The different oxidation states of the polymer **[29]**$^{xn+}$ are obtained by exhaustive electrolysis in CH_3CN + 0.1 M $[Bu_4N]BF_4$ during which the absorption spectra are recorded **figure 4.20**.

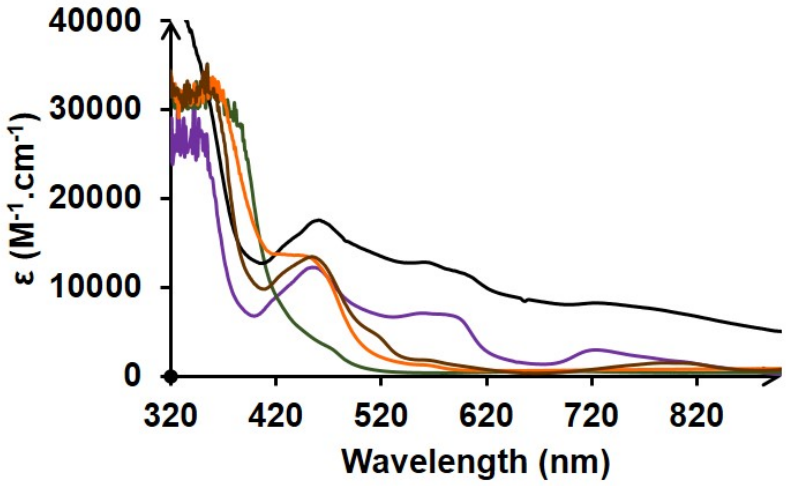

Figure 4.20: Absorption spectra of the different oxidation states of complex **[29]**$^{xn+}$ in CH_3CN + 0.1 M $[Bu_4N]BF_4$, black line represents **[29]**$^{2n+}$, purple line represents **[29]**$^{3n+}$; brown line represents **[29]**$^{4n+}$; red line represents **[29]**$^{5n+}$; green line represents **[29]**$^{6n+}$.

It is noteworthy, that we worked in very dilute solutions (10^{-5} M) in order to ensure the full solubility of **[29]**$^{5n+}$, nonetheless, **[29]**$^{2n+}$ and **[29]**$^{3n+}$ (black and purple lines) were poorly soluble under these conditions. Different solubility profiles have been indeed evidenced for the distinct oxidation states of the $[Cr(ttpy)_2]^{n+}$ complex as discussed earlier. The spectrscopic signatures are collected in **table 4.5**. It is difficult to comment on the proportion of chromium and ruthenium centers from the present absorption spectra due to the overlap of the signals of both centers and the low solubility of the complex. Nonetheless, comparison of the absorption bands for **[29]**$^{5n+}$ 380 nm (27 500), 445 nm (13 500) is consistent with the presence of 1:1 ratio of both $[Ru(bpy)_3]^{2+}$ and $[Cr(ttpy)_2]^{3+}$. However, this proportionality is not maintained through the different oxidation states of the polymer. This is presumed to be the result of the breaking of the polymer during the reduction processes.

Table 4.5: Absorption signatures of **[5]**$^{2+}$, **[24]**$^{3+}$, **[24]**$^{2+}$, **[29]**$^{6n+}$, **[29]**$^{5n+}$, **[29]**$^{4n+}$ and **[29]**$^{3n+}$ in deoxygenated CH_3CN + 0.1 M $[Bu_4N]BF_4$

Complex	λ_{abs} ($M^{-1}.cm^{-1}$)
$[5]^{2+}$	380 (3 200) ,453 (12 900)
$[24]^{3+}$	380 (25 000), 441 (3 500), 475 (1 500)
$[24]^{2+}$	500 (7 700), 584 (2 600), 800 (2 800)
$[29]^{6n+}$	380 (30 900), 441 (5 500), 680 (470)
$[29]^{5n+}$	380 (27 500), 445 (13 500)
$[29]^{4n+}$	445 (13 100), 523 (3 800), 800 (1 700)
$[29]^{3n+}$	445 (11 700), 572 (7 000), 720 (2 900)

Fabrication of Modified Electrodes

Similarly to the RuFe polymer **[28]**$^{4n+}$, polymer **[29]**$^{5n+}$ was deposited onto different electrodes (carbon, ITO and platinum) by electrodeposition . The low solubility of the **[29]**$^{5n+}$ in CH_3CN facilitated the deposition by which successive reduction cycles between 0 and –1.6 V (including the three reductions of $[Cr(tpy)_2]^{3+}$ and the first reduction of the bipyridine of $[Ru(bpy)_3]^{2+}$) were sufficient to ensure the deposition of the **[29]**$^{5n+}$. However, more efficient and uniform films were obtained by reduction between 0 and –2 V **figure 4.21**.

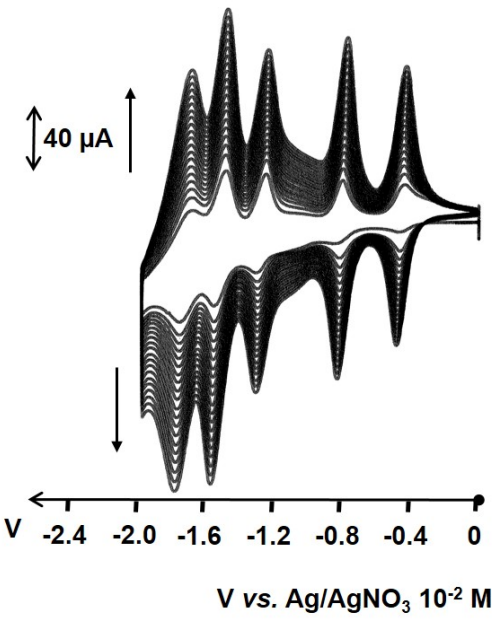

Figure 4.21: Deposition of **[29]**$^{5n+}$ (10^{-5} M) on ITO electrode by successive cycling between 0 and –2.0 V *vs.* $Ag/AgNO_3$ (10^{-2} M) in an CH_3CN solution 0.1 M $[Bu_4N]ClO_4$ ν = 50 $mV.s^{-1}$

The modified electrodes were then transferred to a clean solution of CH_3CN + 0.1 M $[Bu_4N]ClO_4$ and several cyclic voltammograms are recorded in reduction and in oxidation in order to obtain a stable signal **figure 4.22**. The CV of the modified surfaces consist of the superimposition of the electroactivity of $[Ru(bpy)_3]^{2+}$ and that of $[Cr(tpy)_2]^{3+}$ complexes in their 1:1 ratio. The surface coverage values were estimated to 8×10^{-10} after 10 reduction cycles which is lower to the values obtained for the polyRuFe films (4×10^{-9}) with the same number of cycles.

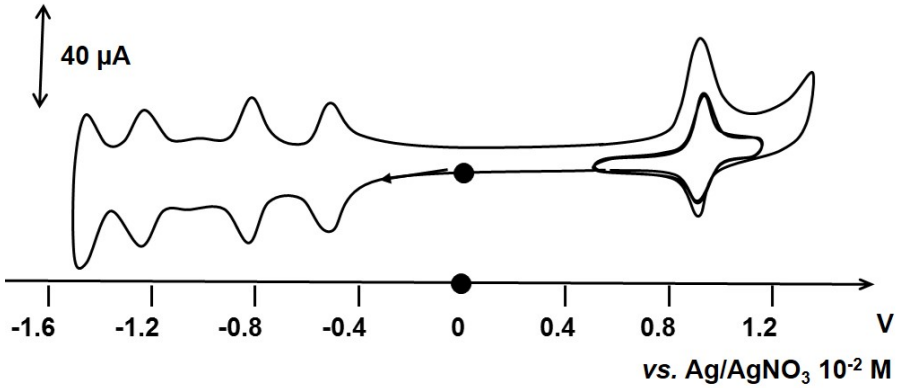

Figure 4.22: CV of the ITO surface coated with **[29]**$^{5n+}$ in an CH_3CN solution containing 0.1 M $[Bu_4N]ClO_4$ at ν = 50 mV.s^{-1}.

4.3.3 Photophysics

The photophysical properties of this bimetallic polymer **[29]**$^{xn+}$ were studied in order to further quantify the interaction between the metallic centers. Steady state and time-resolved emission of **[29]**$^{5n+}$ and **[29]**$^{4n+}$ were recorded in deoxygenated CH_3CN solution as shown in **table 4.6**.

Table 4.6: Luminescence lifetime of the monomeric and polymeric species recorded in deoxygenated CH_3CN + 0.1 M $[Bu_4N]BF_4$ solution at 25 °C. ϕ_{em} represents the emission quantum yield of the complexes

Complex	λ_{em} (nm)	Lifetime	τ (ns)	k_q (s^{-1})	ϕ_{em}	ϕ_{em}/ϕ_0 (%)
		τ_1 ns (%)	τ_2 ns (%)			
$[5]^{2+}$	616		1000	-	0.058	-
$[29]^{5n+}$	616	5.6 (98)	1060 (2)	1.8×10^8	0.009	15
$[29]^{4n+}$	616	5.2 (98)	1380 (2)	1.9×10^8	0.013	23

Upon excitation at 450 nm, **[29]**$^{4n+}$ and **[29]**$^{5n+}$ exhibited a poor luminescence around 616 nm. This luminescence lies in the same region as that of [Ru-(ϕ-tpy)$_2$] and is attributed to the ruthenium core. The poor quantum yield of the emission for **[29]**$^{5n+}$ and **[29]**$^{4n+}$ with respect

to the parent molecule is attributed to a strong deactivation pathway of the excited state of ruthenium. Indeed, this was also observed for the trimetallic complexes Ru-Cr-Ru in **Chapter 3**. The quenching is rationalized to be the result of an electron transfer in the case of **[29]**$^{5n+}$ ($\Delta G = -0.66$ eV). Regarding **[29]**$^{4n+}$, several deactivation pathways are possible. Briefly, energy transfer is possible as shown by the overlap of the emission spectrum of $[Ru(bpy)_3]^{2+}$ and the absorption of $[Cr(tpy)_2]^{2+}$ in addition to electron transfer which is exergonic with $\Delta G = -0.3$ and -0.79 eV for reductive and oxidative quenching respectively. It is noteworthy, that despite the multiple deactivation pathways for **[29]**$^{4n+}$ with respect to **[29]**$^{5n+}$, a more efficient quenching takes place in the latter as evident by the lower quantum yield of emission (0.009 with respect to 0.013). The same behavior was also observed in trimetallic complexes Ru-Cr-Ru **[25]**$^{n+}$.

The luminescence intensity decay can be fitted by a bi-exponential equation, while the short component τ_1 is attributed to the quenched species and the longer lifetime τ_2 is believed to correspond to the unquenched Ru center. In the case of the bimetallic polymer, the lifetime τ_1 is slightly shorter compared to the trimetallic system as a probable consequence of the polymer structure which maintains the different metallic centers in a close environment. This most probably leads to an additional deactivation pathway of the Ru^* by quenching with adjacent Ru or Cr centers.

The quenching rate constants (k_q) in **[29]**$^{5n+}$ and **[29]**$^{4n+}$ are similar and estimated to 2×10^8 s^{-1}, which are in the same order of magnitude for trimetallic Ru-Cr-Ru complexes.

4.3.4 Electrochromism

Several bias between –1.1 and 1.2 V were applied to the modified ITO/polyRuCr in order to induce the oxidation or the reduction of the different metal center during which the absorption spectra are recorded **figure 4.23**. Applying a potential of –1.1 V lead to the formation of a purple film due to the presence of Ru^{2+} and $[Cr(tpy)_2]^0$ redox state, during which the absorption spectrum is dominated by the transitions in the visible region between 500 and 800 nm. Changing the potential to –0.9 V lead to the formation of a pale purple film in accordance with the absorption band around 445 nm of $[Ru(bpy)_3]^{2+}$ along with the emergence of two bands at 570 nm and 720 nm consistent with the formation of $[Cr(tpy)_2]^+$. Applying a potential of –0.5 V lead to the formation of $[Cr(tpy)_2]^{2+}$ as evidenced by the broad absorption around 800 nm and the change of the color of the film to reddish brown. Electrolysis at 0 V induced the formation of $[Cr(tpy)_2]^{3+}$, as governed by the increase in the absorption in the visible-infrared region of the spectrum changing the color of the surface to orange. Finally by applying a potential of 1.2 V, a yellow-green film is obtained due to the formation of Cr^{3+} and Ru^{3+}. This is consistent with the absorption spectrum by which the Ru MLCT at 450 nm disappears and is accompanied by the appearance of a broad peak around 700 nm.

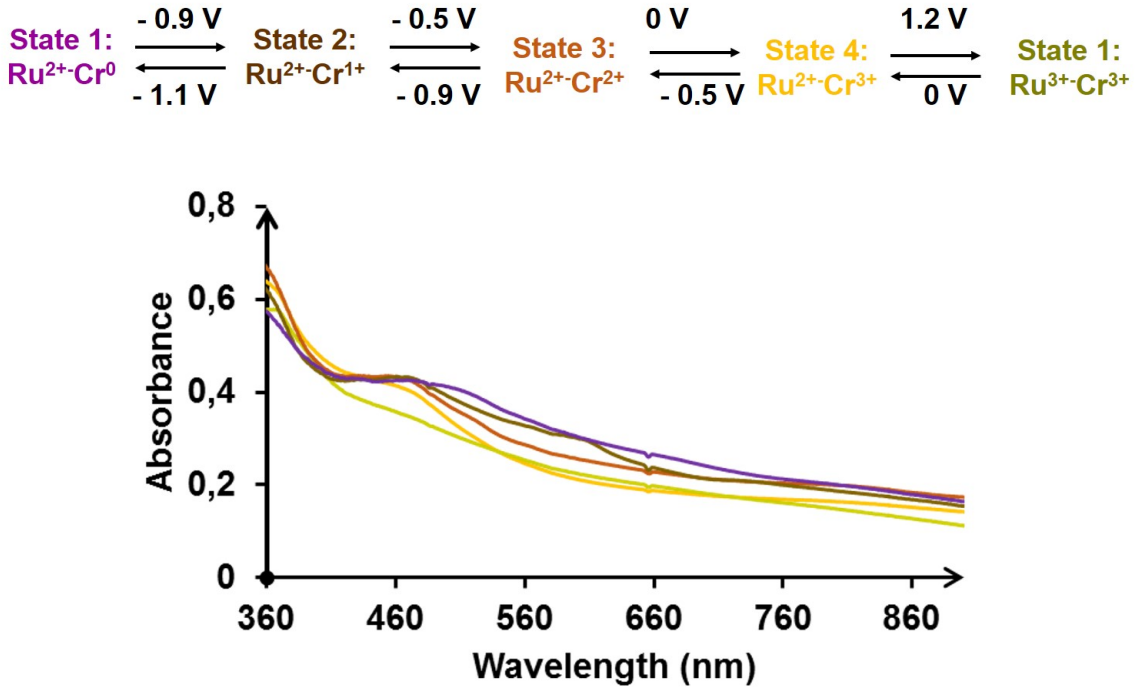

Figure 4.23: Absorption spectra of ITO coated with $\mathbf{[29]}^{5n+}$ in CH_3CN: Purple: applied potential = –1.1 V; brown: applied potential = –0.9 V; Red: applied potential = –0.5 V, Orange: applied potential = 0 V; Green: applied potential =1.2 V

4.3.5 *Anodic Photocurrent in the Presence of TEOA*

Several electrodes coated with **[29]**$^{5n+}$ with varying surface coverage's namely ITO/polyRuCr1, ITO/polyRuCr2 and ITO/polyRuCr3 were prepared upon varying the number of deposition cycles from 10 to 30 to 50. All of these electrodes were successful in generating an anodic photocurrent in CH_3CN + 0.1 M $[Bu_4N]ClO_4$ in the presence of TEOA (15 mM) with an applied bias of 0 or –0.5 V *vs.* $Ag/AgNO_3$ **figure 4.24**.

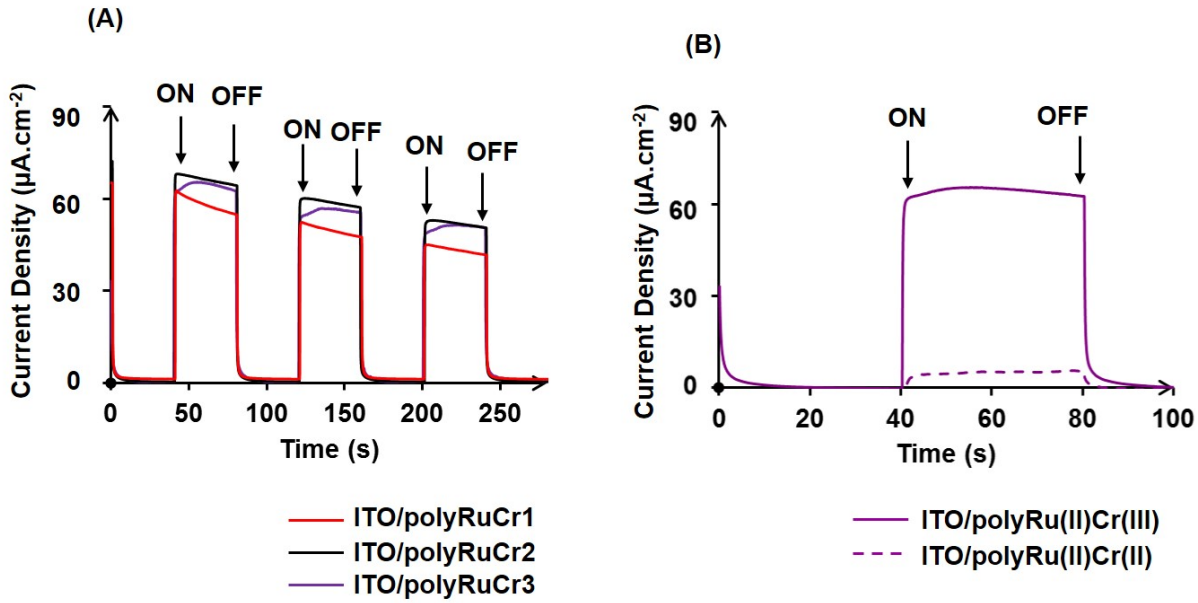

Figure 4.24: Photo-response upon irradiation of the modified electrode in CH_3CN in the presence of 15 mM TEOA (A) ITO modified with the **[29]**$^{5n+}$ with varying surface coverage values: ITO/polyRuCr1 $\Gamma = 8 \times 10^{-10}$ mol.cm^{-2}, ITO/polyRuCr2 $\Gamma = 1 \times 10^{-9}$ mol.cm^{-2}, ITO/polyRuCr3 $\Gamma = 3 \times 10^{-9}$ mol.cm^{-2} with an applied bias of 0 V. (B) Photo-response upon irradiation of the modified electrode in CH_3CN in the presence of 15 mM TEOA of ITO/polyRuCr3 $\Gamma = 3 \times 10^{-9}$ mol.cm^{-2} with an applied bias of 0 V (full line) and applied bias of –0.5 V dashed line.

The presence of an anodic photocurrent can be explained by a hole injected from the immobilized photo-reduced species. Interestingly, the rich electroactivity of the $[Cr(tpy)_2]^{n+}$ complexes allows us to modulate the applied bias, thus selecting the desired redox couple of $[Cr(tpy)_2]^{n+}$. For instance, applying a bias of 0 V *vs.* $Ag/AgNO_3$ will ensure the formation of $[Cr(tpy)_2]^{3+}$, while that of –0.5 V will lead to the formation of $[Cr(tpy)_2]^{2+}$. Nonetheless, due to the random deposition of the polymer on the electrode, several pathways can result in the generation of the photocurrent which makes it challenging to deduce the most favorable one. Regarding ITO/polyRu(II)Cr(III), several scenarios may be responsible for the generation of photoresponse resulting in a high magnitude of photocurrent **figure 4.25.A**. Upon light irradiation, both units $[Cr(tpy)_2]^{3+}$ and $[Ru(bpy)_3]^{2+}$ can absorb photons generating their excited

state. Both excited states can inject an electron to the electrode if found in a close proximity and their fundamental state can thus be regenerated from the TEOA present in solution. Moreover, we can also expect a multistep electron transfer from the $[Ru(bpy)_3]^{2+*}$ core to the $[Cr(tpy)_2]^{3+}$ unit (ΔG = –0.66 eV) which can eventually donate an electron to the electrode or passing through the $[Cr(tpy)_2]^{3+*}$ which can give an electron to $[Ru(bpy)_3]^{2+}$ upon UV excitation.

In the case of ITO/polyRu(II)Cr(II), the anodic current can be explained by oxidative quenching of $[Ru(bpy)_3]^{2+*}$ unit by the $[Cr(tpy)_2]^{2+}$ complex generating $[Cr(tpy)_2]^{1+}$ which further injects and electron to the electrode (ΔG = –0.3 eV), or direct quenching with the electrode. In all cases $[Ru(bpy)_3]^{2+}$ is regenerated from TEOA found in the solution.

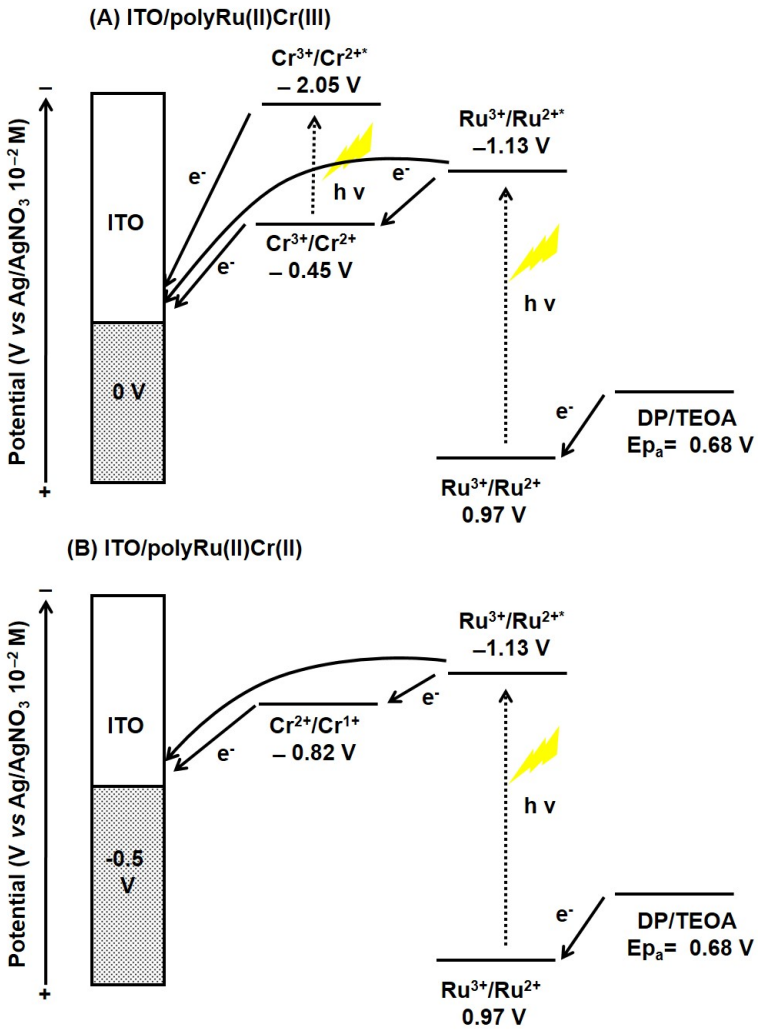

Figure 4.25: Proposed mechanism for the photo-induced electron transfer (A) ITO/polyRu(II)Cr(III); (B) ITO/polyRu(II)Cr(II).

Upon light irradiation with an applied bias of 0 V, the magnitude of the photocurrent varies slightly for surfaces ITO/polyRuCr1, ITO/polyRuCr2 and ITO/polyRuCr3 despite the significant change of surface coverage's **table 4.7**. This has also been evidenced for ITO/polyRuFe

and is explained by the difficulty of charge propagation in the thicker films, suggesting that only the outer layer is participating in the current generation.

Table 4.7: Variation of the magnitude of photocurrent with different surface coverage values

Modified ITO	Γ $(mol.cm^{-2})$	Photocurrent $(\mu A.cm^{-2})$
ITO/polyRuCr1	8×10^{-10}	65[a]
ITO/polyRuCr2	1×10^{-9}	65[a]
ITO/polyRuCr3	3×10^{-9}	65[a], 5.3[b]

[a] This value was calculated after three cycles with an applied bias of 0 V *vs* $Ag/AgNO_3$.
[b] This value was calculated after three cycles with an applied bias of –0.5 V *vs* $Ag/AgNO_3$.

Moreover, the photoresponse is rather unstable showing the instability of the polymer under light and heat **figure 4.26**. For instance, after 9 cycles of irradiation of ITO/polyRuCr3, the current density decreases from 80 to 30 μA.cm^{-2}. Upon decreasing the bias to –0.5 V, the ITO/polyRu(II)Cr(II) generates an anodic current of 5.3 μA. Although, this value is rather insignificant when compared to those obtained with ITO/polyRu(II)Cr(III) (65 μA), the presence of both systems allow increasing the energy stockage from 0.68 V to 1.18 V. This suggests that both couples $[Cr(tpy)_2]^{3+}$ and $[Cr(tpy)_2]^{2+}$ can take part in the photocurrent generation.

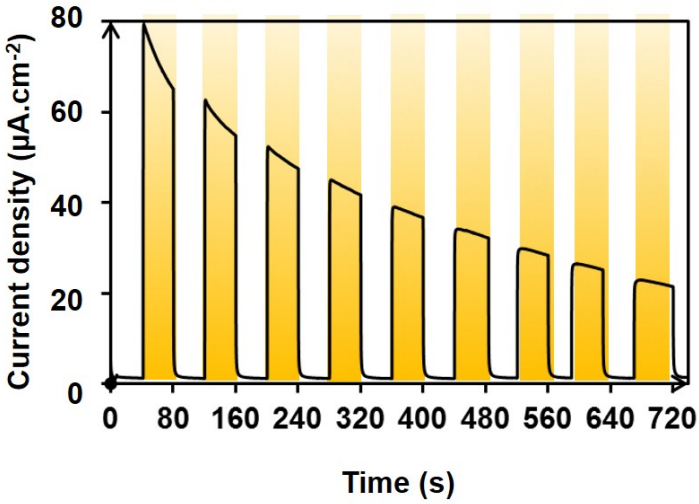

Figure 4.26: Photoresponse of ITO/polyRuCr3 upon successive on off cycles in CH_3CN + 0.1 M $[Bu_4N]ClO_4$, TEOA (15 mM), applied bias = 0 V *vs.* $Ag/AgNO_3$. The irradiated regions are highlighted in yellow

4.4 Conclusion

During this chapter we have demonstrated the ability of the fabrication and characterization of one dimensional bimetallic polymers based on ruthenium and either iron or chromium by a simple coordination reaction. The metallo ligand Ru-(ϕ-tpy)$_2$ offers an interesting linear structure that allows the synthesis of polymer chains with around 10 units and minimizes the formation of macrocycles. These polymers were electro-deposited onto several type of electrodes (carbon, platinum and ITO) by simple cycling between 0 and –2 V. The modified ITO electrodes are both electro and photoactivable, by which they showed a rich multi-electrochromic behavior when the voltage applied was changed from 0.6 to 1.5 V in the case of ITO/polyRuFe and between –1.1 and 1.2 for ITO/polyRuCr. Moreover, we demonstrated that the deposited polymer ITO/polyRuFe can as a photocathode while ITO/polyRuCr can act as a photoanode upon visible light irradiation for a photochemical cell. This study demonstrates the importance of increasing the number of accessible photo-active molecules on the surface for the increase of the output of photocurrent. The case of ITO/polyRuCr is particularily interesting since it couples two photoredox subunits leading to cooperative effect. In addition, it shows the importance of covalently grafting the molecules on the surface for an optimized stability. Thus, for more efficient photoactivable systems, we can imagine introducing suitable functionalities on the polymer backbone that can help anchor them covalently on surfaces.

Bibliography

[1] D. Ray, C.-K. Liang, N. D. McClenaghan, D. M. Bassani, *Curr.Phys.Chem* **2011**, *1*, 169–180.

[2] P. M. Beaujuge, J. M. J. Fréchet, *J. Am. Chem. Soc.* **2011**, *133*, 20009–20029.

[3] H. Maeda, R. Sakamoto, H. Nishihara, *Polymer* **2013**, *54*, 4383 – 4403.

[4] S. C. Yu, X. Gong, W. K. Chan, *Macromolecules* **1998**, *31*, 5639–5646.

[5] S. C. Yu, S. Hou, W. K. Chan, *Macromolecules* **2000**, *33*, 3259–3273.

[6] E. Puodziukynaite, J. L. Oberst, A. L. Dyer, J. R. Reynolds, *J. Am. Chem. Soc.* **2012**, *134*, 968–978.

[7] B. Happ, A. Winter, M. D. Hager, U. S. Schubert, *Chem. Soc. Rev.* **2012**, *41*, 2222–2255.

[8] D.-C. Jeong, J. Lee, Y. Lee, C. Satheeshkumar, C. Song, *Macromolecules* **2015**, *48*, 1621–1626.

[9] Kim, J. M. Beebe, C. Olivier, S. Rigaut, D. Touchard, J. G. Kushmerick, X.-Y. Zhu, C. D. Frisbie, *J. Phys. Chem. C* **2007**, *111*, 7521–7526.

[10] A. Wild, A. Winter, F. Schlutter, U. S. Schubert, *Chem. Soc. Rev.* **2011**, *40*, 1459–1511.

[11] T. Sato, M. Higuchi, *Chem. Commun.* **2013**, *49*, 5256–5258.

[12] M. D. Hossain, J. Zhang, R. K. Pandey, T. Sato, M. Higuchi, *Eur. J. Inorg. Chem.* **2014**, *2014*, 3763–3770.

[13] M. Higuchi, *J. Mater. Chem. C* **2014**, *2*, 9331–9341.

[14] A. Gasnier, J.-M. Barbe, C. Bucher, C. Duboc, J.-C. Moutet, E. Saint-Aman, P. Terech, G. Royal, *Inorg. Chem.* **2010**, *49*, 2592–2599.

[15] J. Lombard, D. A. Jose, C. E. Castillo, R. Pansu, J. Chauvin, A. Deronzier, M.-N. Collomb, *J. Mater. Chem. C* **2014**, *2*, 9824–9835.

[16] S. Schmatloch, A. M. J. van den Berg, A. S. Alexeev, H. Hofmeier, U. S. Schubert, *Macromolecules* **2003**, *36*, 9943–9949.

[17] J. Lombard, J.-C. Lepretre, D. Jouvenot, A. Deronzier, M.-N. Collomb, *New J. Chem.* **2008**, *32*, 1117–1123.

[18] K. Gorgy, M.-N. Collomb, J.-C. Leprêtre, A. Deronzier, C. Duboc-Toia, S. Ménage, M. Fontecave, *Electrochem. Commun.* **2001**, *3*, 686 – 691.

[19] Y. Lattach, J. F. Rivera, T. Bamine, A. Deronzier, J.-C. Moutet, *ACS Appl. Mater. Interfaces* **2014**, *6*, 12852–12859.

General Conclusion

Résumé:

Dans cette thèse, nous avons cherché à mimer les processus de transfert multi-électrons réalisés par l'appareil photosynthétique pour la conversion de l'énergie lumineuse en énergie chimique. Dans ce but, l'unité photosensible $[Ru(bpy)_3]^{2+}$ a été associée à différents complexes de coordination qui agissent en tant que donneurs et accepteurs d'électrons. En particulier, nous avons synthétisé une série de complexes à base de $[Ru(bpy)_3]^{2+}$ portant soit un soit deux ligands terpyridine sur la même bipyridine. Trois types de couplage différents ont été utilisés avec succès pour introduire les sites de coordination terpyridiniques, conduisant à la formation de ponts amide, éther et phénylène. Bien que les ponts amide aient été souvent incorporés au noyau $[Ru(bpy)_3]^{2+}$ pour construire des systèmes supramoléculaires, nos résultats ont montré que la présence de la liaison amide a une influence considérable sur le rendement quantique et la durée de vie de l'émission du $[Ru(bpy)_3]^{2+*}$. Les systèmes contenant des ponts éther et phénylène apparaissent comme une meilleure approche et préservent les propriétés photophysiques du noyau $[Ru(bpy)_3]^{2+}$.

Le fragment $[Ru(bpy)_3]^{2+}$ monosubstitué portant une terpyridine libre a été utilisé pour accéder à des complexes trimétalliques du type Ru-M-Ru avec M = Fe(II), Co(III) et Cr(III), tandis que l'unité $[Ru(bpy)_3]^{2+}$ portant deux terpyridines libres permet la formation de polymères alternés bimétalliques $(Ru\text{-}M)_n$ et des structures hétéro-trimétalliques.

En ce qui concerne le système associant les noyaux $[Ru(bpy)_3]^{2+}$ et $[Fe(tpy)_2]^{2+}$, nos résultats montrent que sous irradiation visible le processus de transfert d'énergie qui a lieu de l'état excité du $[Ru(bpy)_3]^{2+*}$ vers le fer peut être efficacement court-circuité par un transfert d'electron vers un accepteur sacrificiel. Ce la conduit à la formation de l'espèce $[Ru(bpy)_3]^{3+}$ qui induit l'oxydation du centre $[Fe(tpy)_2]^{2+}$.

Dans le cas des systèmes construits par l'association de $[Ru(bpy)_3]^{2+}$ avec $[Co(tpy)_2]^{3+}$ ou $[Cr(tpy)_2]^{3+}$, l'irradiation visible induit une réaction de transfert de charge intramoléculaire conduisant à l'oxydation du photosensibilisateur. La réaction a été mise en évidence sous irradiation continue en présence de PPh_3 ou TEOA comme donneurs d'électrons sacrificiels. Nous avons notamment montré que $[Cr(tpy)_2]^{3+}$ peut être réduit au moins deux fois par ces cycles photorédox. Ce processus permet le stockage de deux électrons sur le centre $[Cr(tpy)_2]^{3+}$, qui pourraient potentiellement servir pour des processus de réduction bi-électroniques.

Après avoir clarifié la nature de la communication entre $[Ru(bpy)_3]^{2+*}$ et les différents centres métalliques de Co, Cr et Fe, nous avons étudié la possibilité de greffer ces systèmes sur la surface d'une électrode. Dans ce contexte, nous avons assemblé la première triade trimétallique basée sur un fragment $[Ru(bpy)_3]^{2+}$ portant des sous-unités $[Co(tpy)_2]^{3+}$ et $[Fe(tpy)_2]^{2+}$ comme

accepteur et donneur d'électrons respectivement. La construction de ces surfaces photoactivables est possible par une approche de chimie de coordination étape par étape sur les électrodes, afin de minimiser la labilité des systèmes. Ces assemblages sont capables de photogénérer un courant en présence d'un médiateur sacrificiel. La nature du photocourant est expliquée par un transfert vectoriel photoinduit d'électrons ou de trous, de l'électrode jusqu'à la solution en passant par l'assemblage. Nos expériences ont montré l'importance de la présence d'un relais d'électron supplémentaire sur l'efficacité de la génération de photocourant : en effet une amélioration de 40% a été atteinte avec une triade par rapport à une architecture plus simple de diade. La photoréponse a également montré une forte dépendance à la fois à la densité de surface et à la puissance d'irradiation.

Enfin, nous avons également obtenu des polymères de coordination unidimensionnels avec une structure alternée $[Ru(bpy)_3]^{2+}$/ $[M(tpy)_2]^{n+}$ (M = Fe(II) et Cr(III)) bien organisée. Cette classe de polymères de coordination couple les propriétés photorédox du noyau $[Ru(bpy)_3]^{2+}$ avec les propriétés redox du métal. Les polymères ont été déposés en films minces sur des électrodes. Dans une cellule photochimique lors de l'irradiation par la lumière visible ces polymères se comportent comme une photocathode dans le cas de $[Ru(bpy)_3]^{2+}$/ $[Fe(tpy)_2]^{2+}$ et comme une photoanode dans le cas de $[Ru(bpy)_3]^{2+}$/ $[Cr(tpy)_2]^{3+}$. Néanmoins, l'exposition prolongée à la lumière conduit à la désorption du film. Ces résultats prouvent l'importance d'une liaison covalente entre l'électrode et la couche photo-active pour la stabilité à long terme. De plus, nous avons démontré que l'épaisseur de ces assemblages polymères n'a qu'une faible influence sur l'amplitude du photocourant résultant.

Ce travail ouvre plusieurs perspectives, notamment avec la complexation du Cr(III) par la terpyridine. Nos expériences préliminaires suggèrent l'utilisation possible de ces complexes comme électrocatalyseurs ou photocatalyseurs pour la réduction à deux électrons de H^+ à H_2. On peut aussi penser que l'utilisation d'une antenne $[Ru(bpy)_3]^{2+}$ favoriserait la photogénération de H_2 par irradiation dans le visible. La suite de ce travail de recherche inclura le remplacement des surfaces conductrices plates par des électrodes mésoporeuses pour augmenter la densité de recouvrement de la surface active. En plus de l'application en photocatalyse, ce travail permet l'accès à des dispositifs électroniques moléculaires photoactifs. Dans ce domaine, les triades inorganiques pourraient être incorporées entre deux électrodes afin de former des jonctions moléculaires photo-activables, en tirant profit de la structure rigide et linéaire apportée par les ligands terpyridine.

GENERAL CONCLUSION

In this thesis we aimed to mimic the multi-electron transfer processes realized by the photosynthetic machinery for the light to chemical energy conversion. In this purpose, the $[Ru(bpy)_3]^{2+}$ photosensitive unit has been associated to different coordination complexes acting as electron donors and acceptors. In particular, we have synthesized a series of complexes based on $[Ru(bpy)_3]^{2+}$ core holding one or two terpyridine pending ligands on the same bipyridine. Three different types of coupling have been successfully used in order to introduce the terpyridine coordination sites resulting in the formation of amide, ether and phenylene bridges. Although amide bridges have been excessively incorporated to $[Ru(bpy)_3]^{2+}$ cores to build supramolecular systems, our results showed that the presence of the amide linkage have a drastic influence on the quantum yield and emission lifetime of $[Ru(bpy)_3]^{2+*}$. Systems containing ether and phenylene bridges appear as a better approach and preserve the photophysical properties of the $[Ru(bpy)_3]^{2+}$ core.

The monosubstituted $[Ru(bpy)_3]^{2+}$ moiety bearing a free terpyridine arm has been used to gain access to trimetallic complexes of the type Ru-M-Ru with M = Fe(II), Co(III) and Cr(III), while the $[Ru(bpy)_3]^{2+}$ unit bearing two free terpyridines allows the formation of alternated bimetallic polymers $(Ru\text{-}M)_n$ and hetero-trimetallic structures.

Regarding the system which associates the $[Ru(bpy)_3]^{2+}$ and the $[Fe(tpy)_2]^{2+}$ cores our results show that under visible irradiation the energy transfer process which takes place from the excited state of $[Ru(bpy)_3]^{2+*}$ to the iron can be efficiently short circuited by an electron transfer process toward an external electron acceptor. This reaction lead to the formation of the $[Ru(bpy)_3]^{3+}$ species that induces the oxidation of the $[Fe(tpy)_2]^{2+}$ counterpart.

In the case of the systems constructed by the association of the $[Ru(bpy)_3]^{2+}$ with the $[Co(tpy)_2]^{3+}$ or $[Cr(tpy)_2]^{3+}$, visible irradiation induced an intramolecular charge transfer re-

action leading to the oxidation of the photosensitizer. The reaction has been evidenced under continuous irradiation in the presence of TEOA or PPh_3 as sacrificial electron donors. We have notably shown that the $[Cr(tpy)_2]^{3+}$ can be reduced at least twice by these photoredox cycles. This process allows the storage of two electrons at the $[Cr(tpy)_2]^{3+}$ counterpart, that could potentially serve for bi-electronic reduction processes.

After clarifying the nature of the communication between $[Ru(bpy)_3]^{2+*}$ and the different Co, Cr and Fe metallic centers, we studied the possibility of coating these systems on the surface of an electrode.

In such, we have assembled the first trimetallic triad built on a $[Ru(bpy)_3]^{2+}$ moiety, bearing $[Co(tpy)_2]^{3+}$ and $[Fe(tpy)_2]^{2+}$ units as an electron acceptor and donor respectively. These photoactivable surfaces were only feasible by the stepwise construction approach on electrodes in order to minimize the lability of the system. Indeed, these assemblies were successful to photogenerate current in the presence of a sacrificial mediator. The nature of the photocurrent was explained by a vectorial photoinduced electron or hole transfer from the electrode passing by the built assembly to the solution. Our experiments showed the importance of the presence of an electron relay on the result of the output of the photocurrent, by which a 40% enhancement was achieved with a triad architecture compared to more simple dyads. The photoresponse also showed a strong dependence on both the surface coverage and power of irradiation.

Finally, we also obtained one dimensional coordination polymers with a well organized alternated $[Ru(bpy)_3]^{2+}/[M(tpy_2)]^{n+}$ structure (M = Fe(II) and Cr(III)). This class of coordination polymer couples the photoredox properties of the $[Ru(bpy)_3]^{2+}$ core with the redox properties of the second metal used for the coordination reaction. The polymers were also deposited as thin films on electrodes behaving as a photocathode in the case of $[Ru(bpy)_3]^{2+}/[Fe(tpy)_2]^{2+}$ and as a photoanode in the case of $[Ru(bpy)_3]^{2+}/[Cr(tpy)_2]^{3+}$ upon visible light irradiation for a photochemical cell. Nonetheless, the prolonged exposure to light lead to the desorption of the film. These results prove the importance of a covalent linkage between the electrode and the photoactive layer for long-term stability. Moreover, we have demonstrated that the thickness of these polymeric assemblies has only a small influence on the magnitude of the resulting photocurrent.

This work opens several perspectives, notably with the complexation of Cr(III) in the terpyridine site. Our preliminary experiments suggest the possible use of such complexes as electrocatalysts or photocatalyst for the two electron reduction of H^+ to H_2. It is expected that using $[Ru(bpy)_3]^{2+}$ antenna would even favor the photogeneration of H_2 by visible irradiation. An extension of this research must include the anchoring of the system on a mesoporous electrodes to increase the active surface coverage value.

Beside the photocatalysis application, this work also allows accessing photoactive molec-

ular electronic devices. In this field the inorganic triads could be incorporated between two electrodes in order to form photo-activable molecular junctions taking advantage of the rigid and linear backbone thanks to the terpyridine ligands.

EXPERIMENTAL PART

Apparatus:

Nuclear Magnetic Resonace: ^{1}H NMR and ^{13}C NMR and Diffraction Ordered Spectroscopy NMR ^{1}H DOSY were recorded at room temperature on Bruker Avance 400 or 500 MHz spectrometers. ^{1}H chemical shifts were referenced to residual solvent peaks. Coupling constants value (J) are given in hertz and chemical shift (δ) in ppm. The abbreviations used are: s=singlet, d= doublet, dd= doublet of doublet, t= triplet and m=multiplet, dt= doublet of triplet, q= quartet.

Mass Spectroscopy: The electrospray ionization mass spectrometry (ESI-MS) experiments were performed on a triple quadrupole mass spectrometer Quattro II (microlass, Altrincham, UK). The ESI source was heated to 80 °C. The sampling cone voltage was set within the range 14 - 18 V. Complex in solution (1-2 mg.mL^{-1} in CH_3CN) were injected using a syringe pump at a flow rate in the range of 5 μL.min^{-1} . The electrospray probe (capillary voltage was optimized in the range 2.9 - 3.30 KV for positive ion electrospray and in the range of () for a negative ion electrospray. Matrix assisted laser desorption/ionization time-of-flight MALDI-TOF were recorded on a Bruker-Daltonics Maldi-ToF-ToF Speed.

Atomic Force Microscopy AFM: AFM images were recorded on a Veeco dimension 3100 atomic force microscope. The probes used were RTSP probe and the DNP-20 probe for tapping mode and contact mode, respectively. For these experiments, the functionalized electrodes on ITO, SiO_2 were rinsed and images were recorded under air with a scan rate of 0.9 Hz. The scan sizes were 3 μm^2 and 500 nm^2 for the tapping and contact mode, respectively.

UV-Vis absorption spectroscopy: UV-vis spectra were recorded on a Varian Cary 100 or on a MCS 500 UV-NIR Zeiss spectrophotometer or on a Perkin-Elmer Lambda 650 using conventional quartz cells or all-quartz immersion probes (Hellma Inc.).

Luminescence measurements: The steady state emission spectra were recorded on a Cary Eclipse spectro-fluorometer. Samples for luminescence experiments at room temperature were solubilized in CH_3CN and degassed directly in the 1 cm quartz cell used for the recording. Emission quantum yields ϕ_s were determined using the following equation:

$$\phi_s = \phi_{ref} \times \frac{A_{ref}}{A_S} \times \frac{I_S}{I_{ref}} \times \left(\frac{\eta_S}{\eta_{ref}}\right)^2 \tag{4.4}$$

where ϕ_{ref} is the quantum yield of the reference compound, I is the emission intensity, was calculated from the spectrum area $\int I(\lambda)d\lambda$, A represents the absorption at the excitation wavelength. η is the refractive index of the solvents used. The superscripts "S" and "ref" refer respectively to the sample and to the standard, usually the later was a CH_3CN solution of $[Ru(bpy)_3](PF_6)_2$ ($\phi_{ref} = 0.062$).[1]
The luminescence lifetime of the complexes were measured after irradiation at $\lambda = 400$ nm, obtained by the second harmonic of a Titanium:Sapphire laser (picosecond Tsunami laser spectra physics 3950-M1BB). The Fluotime 200 from AMS Technologies is used for decay acquisition. It consists of a GaAs michrochannel plate photomultiplier tube (Hamamatsu model R3809U-50) coupled to a time-correlated single photon counting system from Picoquant (PisoHarp300). The optimized time resolution of the system was as low as 30 ps.
Time-resolved luminescence lifetime experiments on films were performed using a space and time-correlated photon-counting photomultiplier (Q_A) from EuroPhoton GmbH mounted onto a microscope. The setup was available at the "Laboratoire de Photophysique et Photochimie Supramoleculaire et Macromoleculaire" (Cachan-France). The excitation source is an argon-ion laser pumped mode-locked Ti/sapphire laser (Tsunami, by Spectra Physics) with a pulse-picker and frequency-doubled. The excitation source was 495 nm. The luminescence lifetime given correspond to the global emission decay of the analyzed area.

EPR spectroscopy: X and Q band EPR spectra were recorded with a Bruker EMX, equipped with the ER-4192 ST Bruker and ER-4121 VT for the X-band at 100 K experiments and the ER-5106 QTW Bruker cavity and an Oxford Instruments ESR-900 continuous-flow helium cryostat for the Q-band at 4.5 K experiments.

Electrochemistry: The electrochemical measurements were run under an argon atmosphere at room temperature. Electrolytes were purchased and used without further purification (minimum purity 99%): tetra-n-butylammonium perchlorate (TBAP, Fluka puriss), tetra-n- butylammonium hexafluorophosphate ($TBAPF_6$, Aldrich), tetra-n- butylammonium tetrafluoroborate ($TBABF_4$, Fluka puriss), silver nitrate ($AgNO_3$, Prolabo).
When dry CH_3CN or CH_2Cl_2 were used as solvents, the electrochemical measurements were performed in a dry glove box. Cyclic voltammetry (CV) and rotating disc electrode (RDE) experiments were recorded using a CHI-620b potentiostat (CH Instruments) or using an EG&F model 173 potentiostat/galvanostat equipped with a PAR model universal prograller and a PAR

mode179 digital coulometer. A standard three-electrode electrochemical cell was used. Potentials were referred to an Ag/0.01 M $AgNO_3$ reference electrode in CH_3CN + 0.1 M electrolyte. Potentials referred to that system can be converted to the ferrocene/ferricinium couple by subtracting 87 mV, to SCE by adding 298 mV or to NHE reference electrode by adding 548 mV. The a vitreous carbon disk (5 mm in diameter), or ITO/FTO surfaces were used as working electrodes, and was polished with a 2 μm diamond paste (Mecaprex Presi). (E_{pa}, anodic peak potential; E_{pc}, cathodic peak potential ; $E_{1/2}$ = (E_{pa}+ E_{pc}/2; Ep = E_{pa} E_{pc}). The auxiliary electrode was a Pt wire in CH_3CN + 0.1 M electrolyte.
Spectroelectrochemical measurements were carried out at 25 °C under an argon atmosphere (glove box) in a standard one-compartment, three-electrodes electrochemical cell equipped with a EG&F model. The light sources are halogen (CLH 500 20 W) and deutreium lamps (CLD 500) equipped with optic fibers (041.002).

Photocurrent Measurements: A specific flat cell consisting of Ag/$AgNO_3$, platinum wire and the modified surface as the reference, counter and working electrode respectively were used with the distances between the electrodes maintained small, and ohmic losses were neglected. For the photocurrent experiments, an electron mediator (15 mM) was added to a solution of CH_3CN + 0.1 M TBAP. The samples were illuminated with a Mercury-Xenon lamp (Hamamatsu L9588) operated at maximum power. The electrochemical cell was held 4 cm above the lamp for every measurement. In these conditions, the radiant power landing on the surface of the electrode is 1.79 W.cm^{-2}. During this experiment, the light was alternatively switched on and off leading to the generation of photocurrent. ICPE values were measured using a laser diode (LD-WL206) (λ = 445 nm, P = 0.33 W.cm^{-2}) as excitation light. Photoaction spectrum was recorded using a monochromator (Jobin Yvon HR250) between the lamp and the electrochemical cell.

Chemicals:

Solvent and reagents: Acetonitrile (Rathburn, HPLC grade), DMSO (Acros, anhydrous 99.7%), DMF (Acros, anhydrous 99.8%), ethylene glycol (Prolab), chloroform (Carlo Erba, HPLC grade), diethyl ether (Aldrich, 99.8%), hexane (95%), pentane (Carlo Erba), dichloromethane (SDS anhydrous, analytical grade), methanol (SDS anhydrous, analytical grade), ethanol (SDS anhydrous, analytical grade), acetone(Aldrich, 99.5) were purchased and used as received. Dry solvents were obtained by distillation from suitable desiccants under argon. All other chemicals are purchased from commercial sources and used without further purification unless noted. Column chromatography was carried out on silica gel 60[Merck, 70-230 mesh]. Thin layer chromatography (TLC) was performed on plates coated with silica gel 60 F_{254}.

General Methods:

Synthesis of air sensitive reactions were performed in oven-dried glassware attached to a

vacuum line with Schlenck techniques, or using a glove box. Every case will be detailed separately.

Synthesis protocol:

4,4'-(bromophenyl)-2,2':6,2"-terpyridine,[2] 4,4'-(bromomethylphenyl)-2,2':6,2"-terpyridine,[3] 5-methyl-2-2'-bipyridine,[4], 4-bromo-2,5-dimethylbenzaldehyde,[5] 5-carboxy-2,2'-bipyridine **(8)**,[6] 5,5'-dicarboxy-2,2'-bipyridine **(10)**,[6] 5,5'-dibromo-2,2'-bipyridine **(14)**,[7] 4'-(4- Hydroxophenyl) -2,2':6,2"-terpyridine **(20)**,[2] 4'-(4-Mercaptophenyl)-2,2':6,2"-terpyridine **(21)**[8] were synthesized according to previously described procedures.

$[1]^{2+}$: $[9]^{2+}$ (50 mg, 0.055 mmol) was heated at reflux for 24 h in 2 mL of freshly distilled thionyl chloride. Excess $SOCl_2$ was removed under vacuum. The resulting solid was suspended in 10 mL of dry CH_2Cl_2 to which a 10 mL dry CH_2Cl_2 solution containing **17** (19 mg, 0.055 mmol) and a catalytic amount of 4-(N,N-dimethylamino)pyridine were added slowly. This reaction mixture was left to stir at room temperature for 24 h under Ar. The solvent was evaporated under reduced pressure and the resulting solid was purified by flash chromatography with a gradient of CH_3CN-H_2O-sat. aq. KNO_3 (100:5:0.5-100:10:1-100:20:2-100:30:4) to obtain $[1]^{2+}$ as a red powder (49 mg, 0.038 mmol) (70%). ^{1}H NMR: (400 MHz, CD_3CN) δ : 9.90 (s, 1H), 8.90-8.80 (m, 4H), 8.70-8.60 (m, 8), 8.50 (s, 2H), 8.15-8.07 (m, 10 H), 7.94 (q, ^3J = 8.0 Hz, 4 H), 7.65-7.50 (m, 10 H) ppm. ESI-MS: *m/z* calculated for $C_{56}H_{50}F_{12}N_{10}OP_2Ru$: $[M\text{-}PF_6]^+$ = 1125.29, found 1124.80, $[M\text{-}2PF_6]^{2+}$ = 468.13, found 470.01.

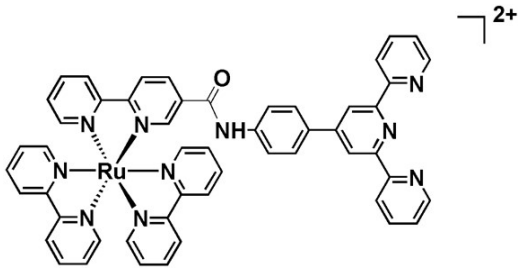

$[2]^{2+}$: The diacid **$[11]^{2+}$** (31 mg, 0.033 mmol) was refluxed in 6 mL of freshly distilled $SOCl_2$ for 5 h. The solution was evaporated and the dark black solid was dried under vacuum for 2 h. The formed product is then solubilized in 5 mL of dry CH_3CN along with **17** (50 mg, 0.154 mmol) and refluxed under Ar for 24 h. The solution was evaporated to dryness, and the resulting red powder, is solubilized by the minimum amount of CH_3CN and precipitated with a sat.aq.KPF_6 solution. The solution was filtered over cotton, and the precipitate was dissolved in acetone, evaporated to dryness and recrystallized from and CH_3CN:Et_2O yielding $[2]^{2+}$ (43 mg, 0.026 mmol) (80%) ^{1}H NMR: (400 MHz, CD_3CN) δ: 9.8 (s, 2H), 8.98 (d, ^3J = 9 Hz, 2H), 8.82-8.73 (m, 18), 8.70 (d,^3J = 8 Hz, 2), 8.40 (d, ^4J = 2 Hz, 2H), 8.20-8.10 (m, 12 H), 8.03 (d, ^3J

= 6 Hz, 2H), 7.95 (d, ^3J = 9 Hz, 4H), 7.83 (d, ^3J = 9 Hz, 4H), 7.56 (d.t, ^3J = 7 Hz, ^4J= 1 Hz, 2H), 7.50 (d.t, ^3J = 7 Hz, ^4J= 1 Hz, 2H) ppm. ESI-MS: *m/z* calculated for $C_{77}H_{61}F_{12}N_{14}O_2P_2Ru$ $[M\text{-}PF_6]^+$ = 1460.38, found 1460.20, $[M\text{-}2PF_6]^{2+}$ = 643.19, found 643.31.

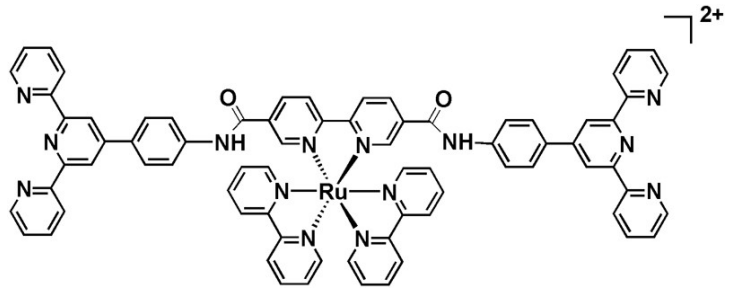

[3]$^{2+}$: [13]$^{2+}$ (183 mg, 0.195 mmol), **20** (84 mg, 0.256 mmol), and K_2CO_3 (71 mg, 0.5122 mmol) were dissolved in 100 mL of acetonitrile and refluxed overnight under argon. The reaction mixture was concentrated to 10 mL and precipitated with a saturated solution of KPF_6. The solution was filtered over a cotton, and the precipitate was dissolved in acetone, evaporated to dryness and submitted to a chromatography on a silica using $CH_3CN/H_2O/KNO_3$sat (100:5:0.5) affording the desired compound **[3]**$^{4+}$ (141 mg, 0.119 mmol) as an orange powder (60%). ^{1}HNMR: (400 MHz, CD_3CN) δ: 8.77-8.73 (m, 8H), 8.48 (m, 4H), 8.41 (d, ^{3}J = 8.17 Hz, 1H), 8.36 (d, ^4J = 8.02 Hz, 1H), 8.12-7.98 (m, 6H), 7.89-7.83 (m, 4H), 7.79-7.67 (m, 4H), 7.57(d, ^3J = 5.58 Hz, 1H), 7.49-7.34 (m, 6H), 7.22 (t, ^3J = 6.45 Hz, 1H), 7.13 (d, ^3J = 8.53 Hz, 2H), 7.07 (d, ^4J = 2.37 Hz, 1H) ppm. ^{13}CNMR: (100 MHz, CD_3CN) δ: 157.85, 157.52, 157.47, 157.37, 157.22, 156.96, 156.25, 155.16, 152.45, 152.33, 152.19, 152.05, 151.93, 150.02, 149.55, 139.95, 138.58, 139.42, 138.38, 137.94, 136.88, 129.96, 128.29, 128.18, 128.11, 127.93, 127.50, 126.79, 125.98, 125.01, 124.92, 124.85, 124.63, 124.23, 121.72, 121.68, 119.12 ppm. ESI-MS: *m/z* calculated for $C_{51}H_{37}F_{12}N_9OP_2Ru$ $[M\text{-}PF_6]^+$ = 1038.13, found 1038.30, $[M\text{-}2PF_6]^{2+}$ = 446.61, found 446.8.

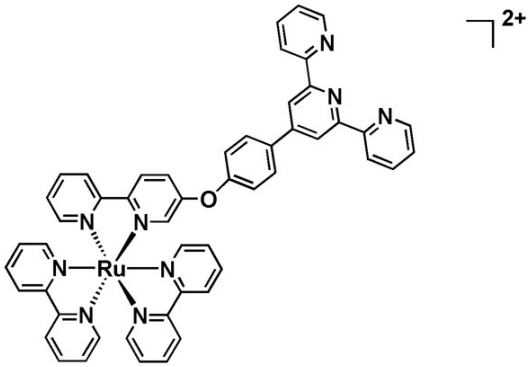

[4]$^{2+}$: [15]$^{2+}$ (150 mg, 0.147 mmol), **20** (106 mg, 0.325 mmol) and K_2CO_3 (150 mg, 1.086 mmol) were dissolved in 75 mL of acetonitrile and refluxed for 48 h under argon. The reaction mixture was concentrated to 10 mL and precipitated with a saturated solution of KPF_6. The

solution was filtered over a cotton, and the precipitate was dissolved in acetone, evaporated to dryness and purified on a silica using $CH_3CN/H_2O/KNO_3$sat (100:5:0.5) affording the desired compound **[4]**$^{2+}$ (145 mg, 0.095 mmol) as an orange powder (65%). ^{1}HNMR: (400 MHz, CD_3CN) δ: 8.71 (d, ^4J = 4 Hz, 2H), 8.66 (m, 10H), 8.45 (d, ^3J = 8 Hz, 2H), 8.36 (d, ^3J = 9 Hz, 2H),8.28 (d, ^3J = 8 Hz, 2H), 8.09 (t.d, ^3J = 8 ^4J = 1.09 Hz, 2H), 7.98 (t.d, ^3J = 7.5 ^4J = 1.57 Hz, 2H), 7.84 (d, ^3J = 5.3 Hz, 2H), 7.82-7.77 (m, 6H), 7. 71(d.d, ^3J = 9, ^4J = 2.5 Hz, 6H), 7.54 (d, ^3J = 5.38 Hz, 2H), 7.52 (m, 2H), 7.45 (m, 4H), 7.19 (m, 2H), 7.08 (d, ^3J = 8.7 Hz, 4H), 7.00 (d, ^4J = 2.7 Hz, 2H) ppm. ESI-MS: *m/z* calculated for $C_{72}H_{50}F_{12}N_{12}O_2P_2Ru$ $[M\text{-}PF_6]^+$ = 1361.29, found 1361.3, $[M\text{-}2PF_6]^{2+}$ = 608.16, found 608.3.

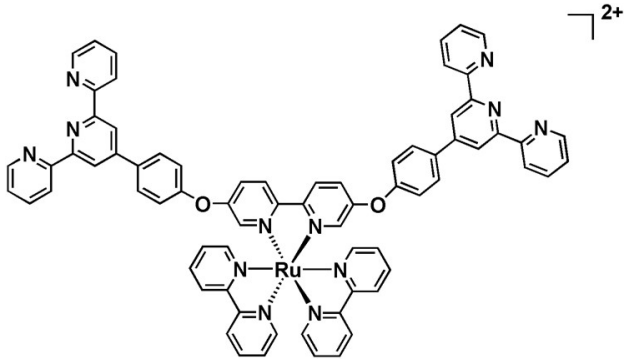

[5]$^{2+}$**:** **[15]**$^{2+}$ (100 mg, 0.098 mmol), **19** (253 mg, 0.480 mmol) and K_2CO_3 (34 mg, 0.246 mmol) were solubilized in 20 mL of dry and degassed DMF under argon in a schlenk. $[Pd(PPh_3)_4]$ (16 mg, 5%) was added and the reaction mixture was heated at 100 °C overnight. The DMF was removed under vacuum and the resulting solid is purified on silica using $CH_3CN/H_2O/KNO_3$ sat (100:25:2.5) as an eluent affording compound **[5]**$^{2+}$ (92 mg, 0.058 mmol) as a red powder (60%) ^{1}H NMR: (400 MHz, CD_3CN) δ: 8.72-8.70 (m, 8H), 8.65 (d, ^3J = 8 Hz, 2H), 8.55-8.51 (t.d, ^3J = 8 Hz, ^3J = 2 Hz, 4 H), 8.43 (s, 4H), 8.18 (dd, ^3J = 7 Hz, ^4J = 2 Hz, 2H), 8.11 (d.t, ^3J = 8 Hz ^3J = 2 Hz, 2H), 8.05 (d.t, ^3J = 7 ^3J = 2 Hz, 2H), 7.90-7.97 (m, 6H), 7.81(d, ^3J = 7 Hz, 2H), 7.70 (d, ^4J = 2 Hz, 2H), 7.50 (d.t, ^3J = 6 Hz, ^4J = 2 Hz, 2 H), 7.49-7.44 (m, 4H), 7.40 (t.d, ^3J = 8 Hz, ^4J = 1 Hz, 2H), 7.39 (s, 2H), 7.18(s, 2H), 2.3 (s, 6H), 2.05 (s, 6H) ppm. ^{13}CNMR: (100 MHz, CD_3CN) δ: 157.726, 157.580, 156.127, 155.940, 152.621, 152.539, 151.601, 151.388, 149.888, 140.985, 140.941, 138.906, 138.024, 138.630, 138.594, 138.024, 135.962, 134.080, 133.956, 132.963, 132.513, 128.398, 128.303, 124.996, 124.906, 124.657, 121.578, 121.638, 19.548, 19.510 ppm. ESI-MS: *m/z* calculated for $C_{76}H_{58}F_{12}N_{12}P_2Ru$ $[M\text{-}PF_6]^+$ = 1385.36, found 1385.5, $[M\text{-}2PF_6]^{2+}$ = 627.1, found 620.3.

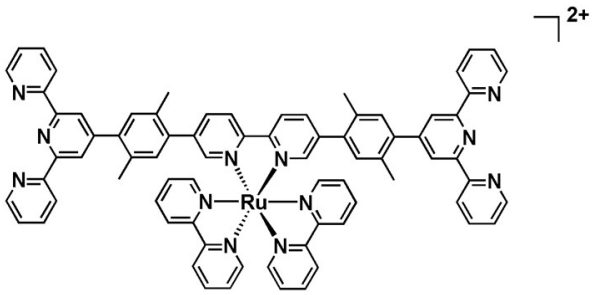

[6]$^{6+}$**:** [Ru-O-tpy] **[3]**$^{2+}$ (50 mg, 0.042 mmol) and [Fe(H_2O)$_6$].2BF_4 (7 mg, 0.021 mmol) were refluxed in 10 mL of CH_3CN for 1 h. The solution was cooled to room temperature, solubilized in the minimum amount of acetone and precipitated with a concentrated aqueous solution of KPF_6. The resulting solid is re-precipitated from a mixture of CH_3CN:Et_2O affording **[6]**$^{6+}$ (114 mg, 0.042 mmol) as a purple solid (95%) ^{1}H NMR (400 MHz, CD_3CN) δ: 9.17 (s, 4H), 8.68(d, ^3J = 8 Hz, 4H), 8.59-8.45 (m, 12H), 8.35 (d, ^3J = 8 Hz, 4H), 8.17-8.05 (m, 8 H), 7.96-7.92 (m, 7 H), 7.82 (d, ^3J = 7 Hz, 4H), 7.77 (d, ^3J = 6 Hz, 2H), 7.72 (t, ^3J = 6 Hz, 4H), 7.51 (m, 4H), 7.41-7.37 (m, 10H), 7.29 (d, ^4J = 2 Hz, 2H), 7.23(d, ^3J = 6 Hz, 4H), 7.1(t, ^3J = 7 Hz, 4H) ppm. ESI-MS: *m/z* calculated for $C_{102}H_{74}F_{36}FeN_{18}O_2P_6Ru_2$ [M-PF_6]$^{2+}$ = 1211.11, found 1211.10, [M-2PF_6]$^{3+}$ = 759.08, found 759.1, [M-2PF_6]$^{4+}$ = 529.83, found 533.1.

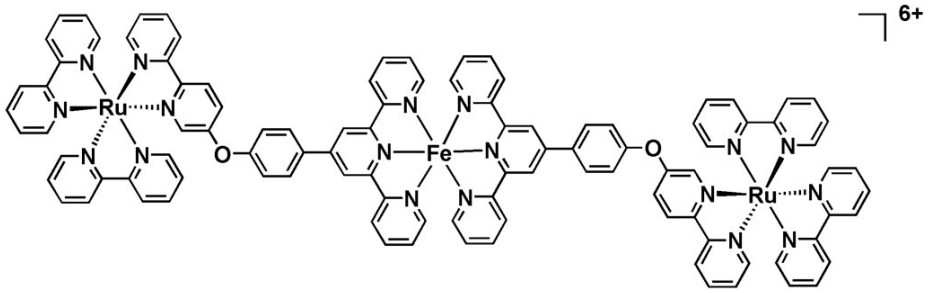

[7]$^{6+}$**:** [Ru-O-tpy] **[3]**$^{2+}$ (50 mg, 0.042 mmol) and [Co(OAc)$_2$] (3.7 mg, 0.021 mmol) were refluxed in 20 mL of MeOH for 2 h. The solution was cooled to room temperature, solubilized in the minimum amount of acetone and precipitated with a concentrated aqueous solution of KPF_6. The resulting solid is re-precipitated from a mixture of CH_3CN:Et_2O affording **[7]**$^{6+}$ (103 mg, 0.038 mmol) as an orange solid (90%). ESI-MS: *m/z* calculated for $C_{102}H_{74}CoF_{36}N_{18}O_2P_6Ru_2$ [M-PF_6]$^{2+}$ = 1212.61, found 1212.17, [M-2PF_6]$^{4+}$ = 533.82, found 533.9.

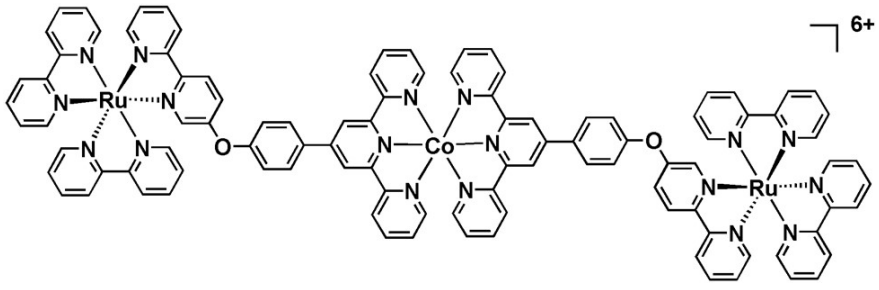

[9]$^{2+}$: 5-carboxy-2,2'-bipyridine **8** (46 mg, 0.230 mmol) and [Ru(bpy)$_2$Cl$_2$].2H$_2$O (100 mg, 0.190 mmol) were heated at reflux for 4 h in a mixture of ethanol:water (8:2) (10 mL). The reaction was left to cool down, then the ethanol was evaporated. Addition of few drops of a saturated solution of ammonium hexafluorophosphate lead to the precepitation of the **[9]$^{2+}$** (175 mg, 0.1900 mmol) as a red-orange powder. (100%). ^{1}HNMR (400 MHz, acetone d^6) δ: 7.66 (m, 5H), 8.00-8.33 (m, 10H), 8.36 (s, 1H) 8.62 (d, ^3J = 5 Hz, 1H), 8.80-8.94 (m, 6H) ppm.

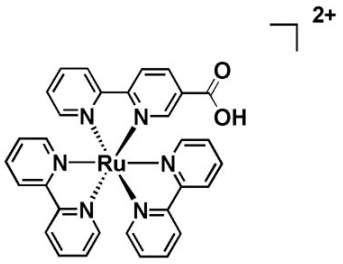

[11]$^{2+}$: 5,5'-dicarboxy-2,2'-bipyridine **10** (150 mg, 0.614 mmol) and [Ru(bpy)$_2$Cl$_2$].2H$_2$O (260 mg, 0.500 mmol) were heated at 120 ° for 2 h in 5 mL of ethylene glycol. The reaction was left to cool down, then the ethanol was evaporated. Addition of few drops of a saturated solution of ammonium hexafluorophosphate lead to the precepitation of the [11]$^{2+}$ (474 mg, 0.500 mmol) as a red-orange powder. (100%). ^{1}HNMR (400 MHz, acetone d^6) δ: 9.05 (d, ^3J = 9 Hz, 2H), 8.88-8.83(m, 4 H), 8.66 (dd, ^3J = 9 Hz, ^4J = 2 Hz, 2H), 8.42 (d, ^4J = 2 Hz, 2H), 8.3 (d.t, ^3J = 8 Hz, ^4J = 2 Hz, 2H), 8.25 (d.t, ^3J = 10 Hz, ^4J = 2 Hz, 2H), 8.19 (d, ^3J = 6 Hz, 2H), 8.13(d, ^3J = Hz, 2H), 7.66 (d.t, ^3J = 6 Hz, ^4J = 1 Hz, 2H), 7.56 (d.t, ^3J = 7 Hz, ^4J = 1 Hz, 2H) ppm.

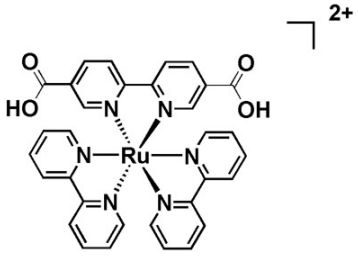

12: Freshly distilled 2-bromopyridine (0.61 mL, 6.30 mmol) was added to 30 mL of dry diethyl ether and maintained at –78 °C under argon, followed by a dropwise addition of *n*-BuLi (3.45 ml, 2M, 6.93 mmol) over a period of 15 min. The mixture turned immediately red, and was stirred for 2 h at –78 °C. The reaction mixture was warmed up to room temperature and then deceased again to –78 °C during which ClSnMe$_3$ (1.51 g, 7.6 mmol) in toluene (5 mL) was carefully added. The reaction was stirred for an additional hour at –78 °C and overnight at room temperature. The solution was then concentrated under vacuum, redissolved in 5 mL of n-hexane, were non soluble products were filtered off and the filtrate was evaporated to dryness. The resulting yellow oil and 5-bromo-2-iodopyridine (1.78 g, 6,34 mmol) were dissolved in 35

mL dry toluene. The solution was degassed for 1 h, [$Pd(PPh_3)_4$] (502 mg, 0.34 mmol) was added, and the solution was refluxed overnight. Pd black was filtered off and the solvent was evaporated to dryness. The resulting solid was submitted to chromatography on deactivated silica using ethyl acetate: pentane (6:4) as an eluent to afford 5-bromobipyridine (885 mg, 3.78 mmol) as a beige solid (60%). ^{1}H NMR: (400 MHZ, $CDCl_3$) δ: 8.64 (d, ^4J = 2.11 Hz, 1H), 8.58 (d, ^3J = 4.9 Hz, 1H), 8.29 (d, ^3J = 8.0 Hz, 1H), 8.24 (d, ^3J = 8.4 Hz, 1H), 7.84 (dd, ^3J = 8.5 Hz, ^4J= 2.5 Hz, 1H), 7.72 (dt, ^3j = 7.8 Hz, ^4J = 1.3 Hz, 1H), 7.26-7.21 (m, 1H) ppm.

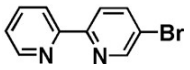

[13]$^{2+}$: 11 (100 mg, 0.428 mmol), and [$Ru(bpy)_2Cl_2$].$2H_2O$ (185 mg, 0.356 mmol) were suspended in 4 mL of ethylene glycol and heated for 90 min at 120 °C. The reaction mixture was cooled down and precipitated with a saturated solution of KPF_6. The solution was filtered over a cotton, and the precipitate was dissolved in acetone, evaporated to dryness and submitted to a chromatography on a silica using $CH_3CN/H_2O/KNO_3$sat (100:10:1) affording the desired compound **[13]**$^{2+}$ (254 mg, 0.27 mmol) as red powder (76%). ^{1}HNMR: (400 MHZ, acetone-d^6) δ: 8.84 (m, 5H), 8.77 (d, ^3J = 8.6 Hz, 1H), 8.29 (d, ^3J = 8.06 Hz, 1H), 8.41 (dd, ^3J = 8.55 Hz, ^4J = 2.10 Hz, 1H), 8.26-8.20 (m, 6H), 8.11 (d, ^4J = 2.00 Hz, 1H), 8.09-8.00 (m, 4H), 7.61-7.56 (m, 5H) ppm.

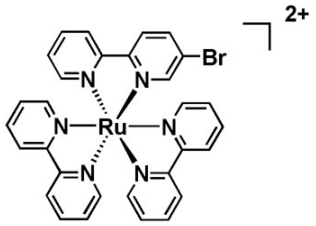

[15]$^{2+}$: 10 (150 mg, 0.48 mmol), and [$Ru(bpy)_2Cl_2$].$2H_2O$ (192 mg, 0.37 mmol) were suspended in 5 mL of ethylene glycol and heated for 90 min at 120 °C. The reaction mixture was cooled down and precipitated with a saturated solution of KPF_6. The solution was filtered over a cotton, and the precipitate was dissolved in acetone, evaporated to dryness and submitted to a chromatography on a silica using $CH_3CN/H_2O/KNO_3$sat (100:20:2) affording the desired compound **[15]**$^{2+}$ (384 mg, 0.36 mmol) as red powder (98%). ^{1}HNMR (400 MHZ, acetone-d^6) δ: 8.82 (d, ^3J = 8 Hz, 4H), 8.76 (d, ^3J = 8.8 Hz, 2H), 8.29 (d.d, ^3J = 8.6 Hz, 2H), 8.26-8.17 (m, 6H), 8.10 (d, ^3J = 8.06, 2H), 8.02 (d, ^3J = 6 Hz, 2H), 7.61-7.56 (m, 4H) ppm.

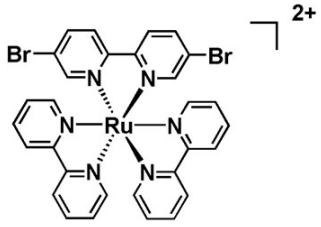

16: 2-acetylpyridine (7.4 g, 61.3 mmol) and 4-acetomidebenzaldehyde (5 g, 30.6 mmol) were dissolved in 250 mL of MeOH. A solution of KOH (5 g in 30 mL of H_2O) and 250 mL of NH_4OH were added and the reaction mixture was left to stir at room temperature for 3 days. The white-yellowish precipitate was filtered of to afford **16** (4.5 g, 12.24 mmol) (40%). ^{1}H NMR: (400 MHz, $CDCl_3$) δ: 8.73-8.71 (m, 4H), 8.66 (d, ^3J = 8 Hz, 2H), 7.9-7.85 (m, 4H), 7.66 (d, ^3J = 9 Hz, 2H) , 7.36-7.35 (m, 2H), 2.21 (s, 3H) ppm.

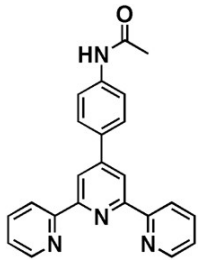

17: Compund **16** (710 mg, 1.93 mmol) was heated to reflux in a 50 mL solution of HCl. H_2O 1:1 overnight. The reaction mixture was left to cool down, and then it was neutralized by the addition of a sodium hydroxide solution leading a yellow precipitate. The precipitate was filtered of and dried under vacuum to afford **17** (594 mg, 1.83 mmol) (95%). ^{1}H NMR: (400 MHz, $CDCl_3$) δ: 8.73(d.d, ^3J = 6 Hz, ^4J = 1 Hz, 2H), 8.68 (s, 2H), 8.65 (d, ^3J = 8 Hz, 2H), 7.86 (d.t, ^3J = 8 Hz, ^4J= 2 Hz, 2H), 7.78 (dd, ^3J = 10 Hz, ^4J = 1 Hz, 2H), 7.35-7.32 (m, 2H), 6.80 (d, ^3J = 9 Hz, 2H) ppm.

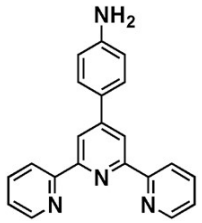

18: 2-acetylpyridine (1.7 g, 14.8 mmol), 4-bromo-2,5-dimethylbenzaldehyde (1.5 g, 7.9 mmol) and KOH (830 mg, 14.8 mmol) were refluxed in a mixture of NH_4OH (50 mL) and EtOH (30 mL) for 1 day. The beige precipitate was filtered of (1.3 g, 3.17 mmol) (45%). ^{1}H NMR: (400 MHz, $CDCl_3$) δ: 8.7-8.65 (m, 4H), 8.41 (s, 2H), 7.86 (d.t, ^3J = 8 Hz, ^4J = 2 Hz, 2H), 7.48 (s, 1H), 7.36 (d.t, ^3J = 6 Hz, ^4J = 3 Hz, 2H), 7.23 (s, 1H), 2.40 (s, 3H), 2.30 (s, 3H) ppm.

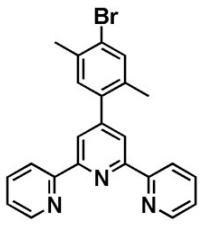

19: Compound **18** (200 mg, 0.48 mmol), bis(pinacolato)diboron (270 mg, 1.05 mmol), Pd(dppf)Cl_2 (24 mg, 0.028 mmol) and KOAc (283 mg, 2.88 mmol) were heated at 90 °C in 8 mL of dry DMSO under Ar overnight. The reaction was quenched with H_2O (10 mL) and extracted with toluene (2 × 20 mL). The organic phase is evaporated yielding a brown oil. Pentane is added and the formed brown solid is filtered off. The filtrate is concentrated under vacuum to yield a yellow oil which soldifies with time. Compound **19** is used in the next step without further purification. ^{1}H NMR: (400 MHz, $CDCl_3$) δ: 8.7-8.62 (m, 4H), 8.45 (s, 2H), 7.87 (d.t, ^3J = 9 Hz, ^4J = 2 Hz, 2H), 7.69 (s, 1H), 7.33 (d.t, ^3J = 6 Hz, ^4J = 3 Hz, 2H), 7.18 (s, 1H), 2.54 (s, 3H), 2.32 (s, 3H), 1.38 (s, 12H) ppm.

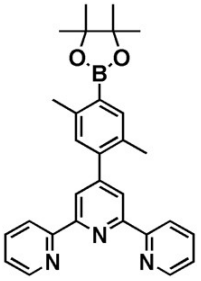

22: 4'-(4-bromomethylphenyl)-2,2':6',2"-terpyridine (163 mg, 0.40 mmol) was dissolved in 3 mL of triethyl phosphite and heated at 160 °C overnight. The reaction mixture was cooled down, and triethyl phosphite was removed under reduced pressure. The beige powder was then triturated in *n*-hexane to afford the desired product pure (165 mg, 0.33 mmol) (90%). The NMR data are in agreement with the literature. ^{1}HNMR: (400 MHz, $CDCl_3$) δ: 8.78(s, 2H), 8.76 (d, ^4J = 3.8 Hz, 2H), 8.71 (d, ^3J = 7.8 Hz, 2H), 7.96-7.89 (m, 4H), 7.45 (dd, ^3J = 8.4 Hz, ^4J = 2.5 Hz, 2H), 7.40 (t, ^3J = 6.35, 2H), 4.06 (m, 4H), 3. (d, ^3J = 22.10 Hz, 2H), 1.29 (t, ^3J= 7.15 Hz ,6H) ppm. ^{31}PNMR: (162 MHz, $CDCl_3$) δ: 25.76 ppm.

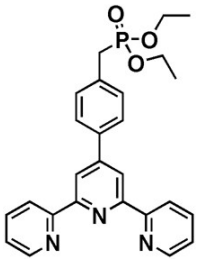

23: 22 (170 mg, 0.37 mmol) was dissolved in 3 mL of dry dichloromethane. TMSBr (227 mg, 1.48 mmol) was added dropwise under Ar and the reaction mixture was stirred overnight. After evaporation, the brown solid was stirred in 15 mL of methanol for 2 h. The precipitate was filtered, washed with acetone to afford the desired product as a white powder (119 mg, 0.29 mmol) (80%). ^{1}HNMR: (400 MHzS, H_2O) δ: 8.39 (d, ^4J = 4.25 Hz, 2H), 8.14 (m , 2H), 8.04 (m, 2H), 7.68 (m, 4H), 7.68 (t, ^3J = 5.93 Hz, 2H), 7.60 (s, 2H), 7.04 (d, ^3J = 7.88 Hz, 2H), 6.90 (d, ^3J = 7.31 Hz, 2H), 2.90 (d, ^3J = 21.4 Hz, 2H) ppm. ^{31}PNMR: (162 MHz, H_2O) δ: 19.45

ppm ESI-MS: *m/z* calculated for $C_{22}H_{18}N_3O_3P$ ($[M+H]^+$) = 403.11 , found = 404.1, $[M-H]^-$ = 402.11, 401.7

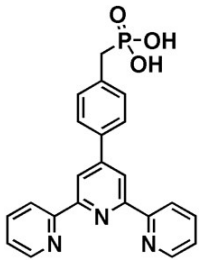

[24]$^{3+}$: A 5 mL solution of $CrCl_2$ (32 mg, 0.26 mmol) was added to a suspension of 4,4'-(methylphenyl)-2,2':6,2"-terpyridine (250 mg, 0.77 mmol) in 50 mL of H_2O in a glove box. Few drops of EtOH are added accompanied by the formation of a purple color. The solution was left to stirr for 1 h at 25 °C. Addition of $LiClO_4$ leads to the precipitation of **[24]**$^{2+/1+}$ as a purple powder (100%). Bubbling oxygen for 30 min to a suspension of **[24]**$^{2+}$ lead to the formation of a yellow suspension. Then the obtained yellow precipitate is filtered and recrystallized from a mixture of EtOH:H_2O to yield **[24]**$^{3+}$ (87 mg, 0.10 mmol) (40%). $E_{1/2}$ = 1.07, –0.41 , –0.77, –1.27 V *vs.* Ag/$AgNO_3$ in CH_3CN + 0.1 mM $TBABF_4$. Absorbance in CH_3CN = 370 (35 397), 445 (26771).

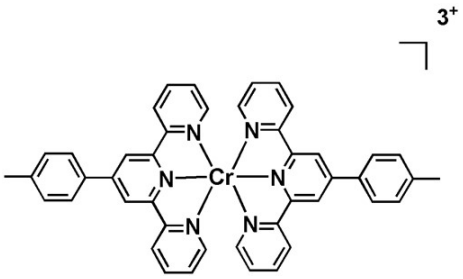

[25]$^{6+}$: [Ru-O-tpy] **[3]**$^{3+}$ (80 mg, 0.06 mmol) and $CrCl_2$ (4 mg, 0.03 mmol) were refluxed in 20 mL MeOH in a glove box for 4 h. NH_4PF_6 was added to the resulting brown solution, and the brown precipitate was filtered and recrystallized from CH_3CN:Et_2O to yield **[25]**$^{6+}$ (57 mg, 0.021 mmol) (70%). $E_{1/2}$ = –0.37 , –0.77, –1.23 V *vs.* Ag/$AgNO_3$ in CH_3CN + 0.1 mM TBAP. Absorbance in CH_3CN = 370 (36 465), 441 (3 460), 475 (1 487).

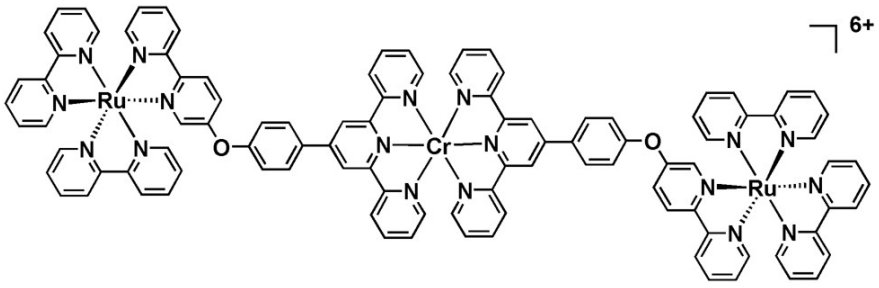

[26]:[9] Anhydrous $CrCl_3$ (185 mg, 1.15 mmol) and 4,4'-(methylphenyl)-2,2':6,2"-terpyridine (484 mg, 1.50 mmol) were suspended in EtOH (10 mL). The reaction mixture was heated to reflux and then granulated zinc (21 mg, 0.32 mmol) was added. After a short time, the mixture turned black and a green precipitate formed. The reaction mixture was then heated at reflux for over night, after which it was filtered, leaving excess zinc in the reaction flask. The green precipitate of **[26]** (508 mg, 1.05 mmol) was collected on the filter-frit, washed with EtOH and used in the next step without further purification (92%).

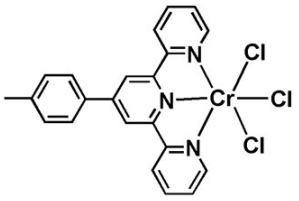

[27]:[9] Complex **[26]** (150 mg, 0.10 mmol) was dissolved in CF_3SO_3H (1.63 mL, 4 mmol) and the dark red solution stirred overnight at room temperature. The reaction was then cooled to 0 ° and Et_2O (20 mL) was added, yielding a dark red precipitate. The solid was separated by filtration, washed with Et_2O and **[27]** (44 mg, 0.05 mmol) was isolated as brown solid (54%). ESI-MS: *m/z* calculated for $C_{25}H_{17}CrF_9N_3\ O_9S_2$ $[M\text{-}OTf]^+$ = 672.99 found 673.1, $[Cr(ttpy)(OTf)_3{+}Na]^+$ = 845.09 found 845.1, $[Cr(ttpy)(OTf)_3{+}OTf]^-$ = 844.91 found 845.1.

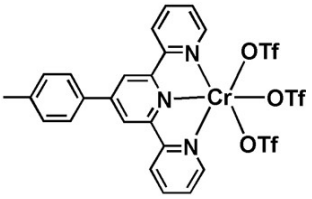

[28]$^{4n+}$: Metallo ligand **[5]**$^{2+}$ (50 mg, 0.033 mmol) and $[Fe(H_2O)_6].2BF_4$ (11 mg, 0.033 mmol) were refluxed in 10 mL CH_3CN for 2 h. KPF_6 is added and the polymer **[28]**$^{4n+}$ is precipitated as a purple solid (50%); $E_{1/2}$ = 0.81, 1.03 V *vs.* $Ag/AgNO_3$ in CH_3CN + 0.1 mM TBAP. Absorbance in CH_3CN = 449 (14 000), 569 (23 700).

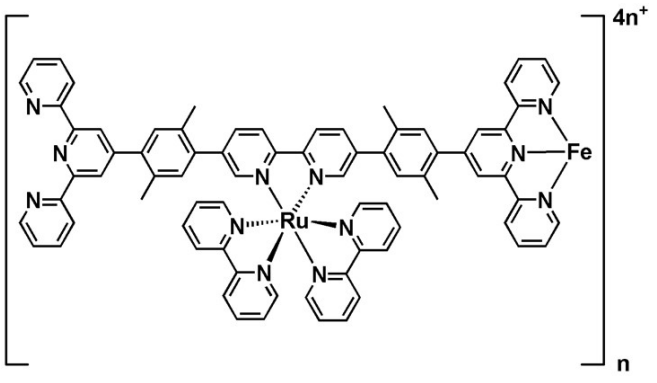

[29]$^{4n+}$**:** Metallo ligand **[5]**$^{2+}$ (50 mg, 0.033 mmol) and $CrCl_2$ (4 mg, 0.033 mmol) were refluxed in 20 mL of MeOH for 4 h under Ar. KPF_6 is added and the polymer **[29]**$^{4n+}$ is precipitated as a brown solid (20%); $E_{1/2}$ = 0.97, –0.45, –0.82, –1.28 V *vs.* $Ag/AgNO_3$ in CH_3CN + 0.1 mM TBAP.

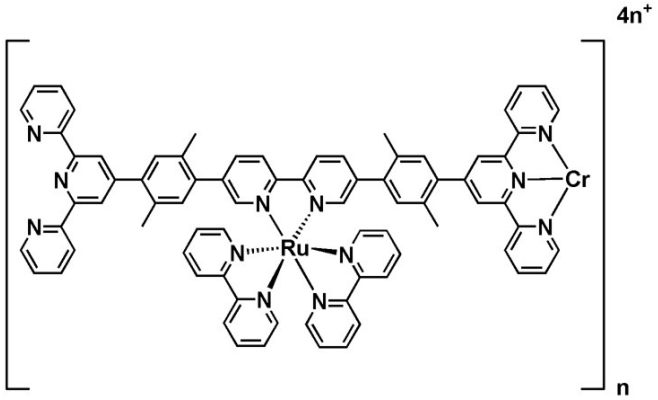

Bibliography

[1] J. V. Caspar, T. J. Meyer, *J. Am. Chem. Soc.* **1983**, *105*, 5583–5590.

[2] J. Wang, G. S. Hanan, *SynLett* **2005**, *8*, 1251–1254.

[3] O. Johansson, M. Borgström, R. Lomoth, M. Palmblad, J. Bergquist, L. Hammarström, L. Sun, B. Åkermark, *Inorg. Chem.* **2003**, *42*, 2908–2918.

[4] K. T. Potts, P. A. Winslow, *J. Org. Chem.* **1985**, *50*, 5405–5409.

[5] C. Houarner-Rassin, F. Chaignon, C. She, D. Stockwell, E. Blart, P. Buvat, T. Lian, F. Odobel, *J. Photochem. Photobiol.* **2007**, *192*, 56 – 65.

[6] F. Venema, H. F. M. Nelissen, P. Berthault, N. Birlirakis, A. E. Rowan, M. C. Feiters, R. J. M. Nolte, *Chem. Eur. J* **1998**, *4*, 2237–2250.

[7] J.-F. Ayme, J. E. Beves, D. A. Leigh, R. T. McBurney, K. Rissanen, D. Schultz, *J. Am. Chem. Soc.* **2012**, *134*, 9488–9497.

[8] T. Kurita, Y. Nishimori, F. Toshimitsu, S. Muratsugu, S. Kume, H. Nishihara, *J. Am. Chem. Soc.* **2010**, *132*, 4524–4525.

[9] E. C. Constable, C. E. Housecroft, M. Neuburger, J. Schonle, J. A. Zampese, *Dalton Trans.* **2014**, *43*, 7227–7235.

Résumé:

Dans ce manuscrit, nous présentons la synthèse de divers assemblages construits autour d'un photosensibilisateur de type $[Ru(bpy)_3]^{2+}$ lié à différentes sous-unités métalliques servant de relais d'électrons afin de mimer les processus photosynthétiques naturels de transformation de l'énergie lumineuse en énergie chimique. Nous nous sommes intéressés à des complexes bis-terpyridines de cobalt(III) ou de chrome(III) comme accepteurs d'électrons potentiels et de fer(II) comme donneur d'électron. Dans ce contexte, un motif $[Ru(bpy)_3]^{2+}$ a été connecté à un ou deux ligands terpyridines à l'aide de ponts de différentes nature afin d'assembler les centres métalliques. Cela a permis d'accéder à des systèmes hétérobimétalliques soit de type trinucleaire tels que $[Ru(bpy)_3]^{2+}$-$[M(tpy)_2]^{2+/3+}$-$[Ru(bpy)_3]^{2+}$ soit sous la forme de polymère $[Ru(bpy)_2(bpy\text{-}tpy)M]_n{}^{4n+}$. Des triades trimétalliques ont aussi été obtenues sur surface par une approche étape par étape associant autour du $[Ru(bpy)_3]^{2+}$, le $[Co(tpy)_2]^{2+}$ en tant qu'accepteur d'électron et le $[Ru(bpy)_3]^{2+}$ comme donneur. Les propriétés électrochimiques et les processus de tranfert d'énergie et /ou d'electron photoinduits des différentes architectures ont été étudiés en détails. En outre, nous avons examiné la capacité des différents systèmes immobilisés (polymères, triades) de produire un courant électrique lors d'une irradiation dans le visible et en présence d'un réactif sacrificiel. Dans son ensemble, cette étude donne un aperçu de certains des paramètres essentiels qui gouvernent l'efficacité de la conversion photo-électrique.
Mots clés: Fonctionalisation de surface, polymère de coordination, photocourant

Abstract:

In this thesis, we present the synthesis of various assemblies constructed around a photosensitive $[Ru(bpy)_3]^{2+}$ core and different metallic subunits serving as electron relays in order to mimic the photosynthetic machinery for the light to chemical energy transformation. In particular we were interested in terpyridyl complexes of cobalt(III) or chromium(III) as potential electron acceptors and iron(II) as an electron donor. In this context, a $[Ru(bpy)_3]^{2+}$ motif was connected to either one or two terpyridine arms with the help of different bridges in order to assemble the different metallic centers. This allowed to access heterobimetallic systems either in trinuclear assemblies of the type $[Ru(bpy)_3]^{2+}$+ -$[M(tpy)_2]^{2+/3+}$ -$[Ru(bpy)_3]^{2+}$ or in the polymer form $[Ru(bpy)_2(bpy\text{-}tpy)M]_n{}^{4n+}$. More engineered linear trimetallic triads based on $[Co(tpy)_2]^{3+}$ as an electron acceptor $[Ru(bpy)_3]^{2+}$ as a photosensitizer and $[Fe(tpy)_2]^{2+}$ as an electron donor were also constructed in a stepwise mode on an electrode. The electrochemical properties and photoinduced electron and/or energy transfer processes of the various architectures were carefully studied. Furthermore, we have examined the ability of the different immobilized systems (polymer, triads) to produce an electric current upon irradiation and in the presence of a sacrificial reagent. All in all, this study gives insight into some of the essential parameters that should be modulated in order to obtain more efficient photo-electric conversion.
Keywords: Surface functionalization, coordination polymer, photocurrent